NONLINEAR FINITE ELEMENT MODELING OF REINFORCED CONCRETE STRUCTURAL WALLS

by

Muhammet Fethi Güllü

B.S., Civil Engineering, Istanbul Technical University, 2009

M.S., Civil Engineering, Boğaziçi University, 2013

Submitted to the Institute for Graduate Studies in
Science and Engineering in partial fulfillment of
the requirements for the degree of
Doctor of Philosophy

Graduate Program in Civil Engineering

Boğaziçi University

2019

NONLINEAR FINITE ELEMENT MODELING OF REINFORCED CONCRETE STRUCTURAL WALLS

APPROVED BY:

Assoc. Prof. Kutay Orakçal (Thesis Supervisor) .....

Prof. Hilmi Luş .....

Prof. Alper İlki .....

Assoc. Prof. Özer Çinicioğlu .....

Assist. Prof. Zeynep Tuna Değer .....

DATE OF APPROVAL: 31.05.2019

To my family

ACKNOWLEDGEMENTS

I would also like to express my sincere gratitude to my thesis supervisor Associate Professor Kutay Orakçal for his invaluable guidance and support throughout my studies. I am also grateful to him for his endless patience and positive attitude during preparation of this thesis.

I would like to express my special thanks to my thesis committee members Professor Hilmi Luş and Professor Alper İlki for their support and suggestions and I would also thank to Associate Professor Özer Çinicioğlu, Assistant Professor Zeynep Tuna Değer and Associate Professor Serdar Soyöz for their interest and time in evaluating my thesis and participating in my thesis jury.

I would like to thank to Professor Uğur Ersoy for his advisory guidance during my studies.

I am grateful to TÜBİTAK – Turkish Technological and Scientific Research Institute – for their financial support during my PhD thesis.

I am indebted to my father Ali Murtaza Güllü for endless support and encouragement he has given me throughout my life. I cannot forget the support of my dear wife Ebrar Güllü whose patience and encouragement throughout this study have meant so much to me. Lastly, my daughter, Fatma Zehra, whose innocent, restless attitude always stimulates and refreshes me for the accomplishment of my study.

ABSTRACT

NONLINEAR FINITE ELEMENT MODELING OF REINFORCED CONCRETE STRUCTURAL WALLS

A relatively simple finite element modeling approach–referred to as the Fixed-Strut-Angle Finite Element (FSAFE) Model–is proposed in this thesis for simulating the hysteretic lateral load behavior of reinforced concrete (RC) structural walls with both flexural and shear controlled responses. The behavioral characteristics of the constitutive panel elements incorporated in the model formulation are based on a fixed-crack-angle modeling methodology. Improvements are made on the constitutive panel model formulation, with the implementation of simple behavioral models for shear-aggregate-interlock in concrete and dowel action on reinforcing bars. Model response predictions were first compared with experimentally-measured global and local responses of wall specimens with varying behavioral characteristics; including relatively slender (shear span-to-depth ratios between 2.3 and 3.0) flexure-controlled walls with rectangular and T-shaped cross-sections, as well as medium-rise walls (shear span-to-depth ratios between 1.5 and 2.0) with coupled shear-flexural responses. The FSAFE model formulation was further refined for improved simulation of walls with shear-controlled responses, with modifications made on the hysteresis rules of the shear aggregate interlock and dowel action models, as well as by incorporating cyclic degradation parameters in their constitutive formulation. The FSAFE model formulation was also modified for consideration of strain penetration effect within the wall foundation, and for limiting the strain localization effect. The improved model was validated against tests on RC squat wall specimens (shear span-to-depth ratios between 0.44 and 1.15) with shear-dominant responses, incorporating a variety of behavioral characteristics at global and local response levels. The proposed FSAFE model is shown to be a relatively simple yet accurate and reliable modeling approach for simulating nonlinear wall behavior, which can be used towards improvement of performance-based seismic design and assessment of methods for building structures incorporating RC walls.

ÖZET

BETONARME PERDE DUVARLARIN DOĞRUSAL OLMAYAN SONLU ELEMANLAR YÖNTEMİYLE MODELLENMESİ

Bu tezde, eğilme ve kayma kontrollü eylem gösteren betonarme perde duvarların çevrimsel yükleme koşulları altında davranış modellemesi için Sabit Payanda Açılı Sonlu Elemanlar (FSAFE) metodu olarak adlandırılan görece basit bir sonlu eleman yöntemi önerilmektedir. Analitik modeli oluşturan panel elemanlarının davranışı için sabit çatlak yönlü modelleme yaklaşımı benimsenmiştir. Panel model formülasyonu, çatlaklarda agrega kenetlenmesi ve donatıda kama etkisi mekanizmaları basit davranış modelleriyle temsil edilerek geliştirilmiştir. Analitik model öncelikli olarak farklı davranış karakteristiklerine sahip eğilme kontrollü davranış gösteren görece narin (kesme açıklığı 2.3 ile 3.0 arasında) dikdörtgen ve T-şeklinde kesitli ve kesme-eğilme etkileşimi gösteren orta narinlikte (kesme açıklığı 1.5 ile 2.0 arasında) perde duvar numunelerinin deney sonuçları ile karşılaştırılmıştır. Sonrasında, baskın olarak kesme etkileri altında davranış gösteren perde duvarların daha kapsamlı bir biçimde modellemesine yönelik olarak FSAFE model formülasyonu üzerinde geliştirmeler yapılmış, bu kapsamda agrega kenetlenmesi ve kama etkisini temsil eden davranış modellerinin çevrimsel çalışma prensipleri, çevrimsel azalma bağıntıları da dikkate alınarak iyileştirilmiştir. Model formülasyonu ayrıca duvar temelinde gözlemlenen gerinim penetrasyonu etkisini dikkate almak ve şekil değiştirme lokalizasyonu etkilerini en aza indirmek için geliştirilmiştir. Geliştirilen analitik model birçok karakteristik özelliği kapsayan kesme baskın davranış gösteren betonarme bodur (kesme açıklığı 0.44 ile 1.15 arasında) perde duvar deneyleri ile doğrulanmıştır. Bu tez çalışması kapsamında geliştirilmiş olan FSAFE modelinin, betonarme perde duvarlar içeren yapılar için performansa dayalı tasarım ve değerlendirilmesi yöntemlerinin geliştirilmesi kapsamında, perdelerin doğrusal olmayan davranışlarının modellenmesi amacıyla kullanılabilecek görece basit ancak güvenilir ve doğruluk payı yüksek bir modelleme yaklaşımı olduğu düşünülmektedir.

TABLE OF CONTENTS

ACKNOWLEDGEMENTS iv
ABSTRACT v
ÖZET vi
LIST OF FIGURES x
LIST OF TABLES xxi
LISY OF SYMBOLS xxii
LIST OF ACRONYMS/ABBREVIATONS xxviii
1. INTRODUCTION 1
1.1. General 1
1.2. Literature Review 2
1.2.1. Macroscopic Modeling Approaches 3
1.2.2. Microscopic Modeling Approaches 12
1.3. Objectives and Scope 17
1.4. Thesis Outline 19
2. MODEL DESCRIPTION 20
2.1. The Proposed Fixed Sturt Angle Finite Element (FSAFE) Model Description 20
2.1.1. General Model Description 21
2.1.2. Description of Rigid Body Constraint and Support Conditions 26
2.2. The Constitutive Fixed Strut Angle Model (FSAM) for RC Panels 30
2.3. Material Constitutive Models 33
2.3.1. Concrete 33
2.3.2. Reinforcing Steel 36
2.3.3. Compression Softening in Concrete 39
2.3.4. Tension Stiffening Effect on Concrete and Steel 40
2.3.5. Biaxial Damage on Concrete 42
2.4. Shear Aggregate Interlock on Crack Surfaces 43
2.5. Dowel Action on Reinforcement 45
2.6. Overview 48

3. EXPERIMENTAL VALIDATION OF THE MODEL FOR WALLS WITH FLEXURAL OR COUPLED SHEAR-FLEXURAL RESPONSES 50
3.1. Description of Test Specimens 50
3.2. Definition of Model Parameters for the Wall Specimens 56
3.2.1. Model Geometry 56
3.2.2. Material Model Parameters 57
3.3. Comparison of Model Responses with Test Data 62
3.3.1. Lateral Load vs. Top Displacement Responses 62
3.3.2. Lateral Load vs. Flexural and Shear Deformation Responses 68
3.3.3. Deformation Profiles along Wall Height 72
3.3.4. Wall Vertical Growth 74
3.3.5. Crack Patterns and Principal Compressive Stress Contours 81
3.3.6. Vertical Normal Strain Profiles at Wall Base 84
3.3.7. Other Local Response Predictions 90
3.4. Mesh Sensitivity Analysis 93
3.5. Overview 95
4. REFINEMENT AND EXPERIMENTAL VALIDATION OF THE MODEL FOR WALLS WITH SHEAR CONTROLLED RESPONSES 107
4.1. General 107
4.2. Refinements on the FSAFE Model for Simulation of Squat Walls 110
4.2.1. Implementation of a Robust Shear Aggregate Interlock Model 110
4.2.2. Implementation of a Robust Dowel Action Model 112
4.2.3. Implementation of Cyclic Degradation Parameters 114
4.2.4. Implementation of a Rotational Spring for Strain Penetration 114
4.3. Description of Squat Wall Specimens Used for Model Validation 116
4.4. Modeling Parameters for Squat Wall Specimens 120
4.4.1. Model Geometry 120
4.4.2. Material Model Parameters 124
4.4.3. Strain Penetration Spring Stiffness 128
4.4.4. Regularization of the Constitutive Model for Concrete in Compression 128
4.5. Comparison of Model Responses with Test Data 131
4.5.1. Lateral Load vs. Top Displacement Responses 131

4.5.2. Lateral Load vs. Flexural and Shear Deformation Responses 136
4.5.3. Local Responses 137
4.6. Parametric Sensitivity Studies on Model Results 142
4.6.1. Consideration of a Rotational Strain Penetration Spring 142
4.6.2. Consideration of a Regularization Method to Minimize Strain Localization 144
4.6.3. Mesh Sensitivity Analysis 145
4.6.4. Effect of Predefining a Sliding Crack for the Wall with Sliding Shear Failure 146
4.7. Global Response Predictions of the Model for the Entire Squat Wall Database 157
4.8. Overview 162
5. SUMMARY AND CONCLUSIONS 164
5.1. Summary 164
5.2. Conclusions on FSAFE Model Characteristics 165
5.2.1. Walls with Flexural or Coupled Shear Flexural Responses 165
5.2.2. Walls with Shear Controlled Responses 167
5.3. Suggested Improvements and Recommendations for Future Studies 169
REFERENCES 171

LIST OF FIGURES

Figure 1.1. Multiple-Vertical-Line-Element Model (MVLEM) (Vulcano *et al.*, 1988). . 4

Figure 1.2. MVLEM (Orakcal *et al.*, 2004).. 5

Figure 1.3. Shear wall element: (a) vertical axial bending, (b) concrete shear, and (c) typical material backbone relation (Computers and Structures Inc., 2006). . 6

Figure 1.4. Element models: (a) MVLEM element, (b) coupled model element (Massone *et al*., 2009). 6

Figure 1.5. Fiber element with nonlinear shear deformations: (a) fiber strain field, (b) concrete fiber strains, (c) micro-planes, and (d) tributary transverse steel reinforcement (Jiang and Kurama, 2010). 7

Figure 1.6. RC wall and wall panel truss model (Panagiotou *et al.*, 2012).. 8

Figure 1.7. Improved MVLEM formulation: (a) multiple horizontal springs in upgraded MVLEM, (b) horizontal shear spring at each MVLEM macro-fiber, and (c) mechanisms of shear force transfers over the cracks (Fischinger *et al.*, 2012). 9

Figure 1.8. SFI-MVLEM formulation: (a) model element, (b) RC panel behavior, (c) concrete struts, (d) shear aggregate interlock, (e) steel behavior, and (f) reinforcement dowel action (Kolozvari *et al.*, 2018a). 10

Figure 1.9. Force based fiber section nonlinear beam-column element: (a) simulation of flexural behavior, (b) simulation of shear behavior (Kolozvari *et al.*, 2018a).. 11

Figure 1.10. Illustration of the numerical model (Lu and Henry, 2017). 14

Figure 1.11. Overview of CSMM for reinforced concrete (Luu *et al.*, 2017). 15

Figure 1.12. a) Membrane element global DOF, b) A typical rectangular layered membrane section (Rojas *et al.*, 2016). 16

Figure 1.13. Curved shell element: a) in-plane interpolation, b) three-point integration scheme over the element thickness (Dashti *et al.*, 2017a). 17

Figure 2.1. Modeling of wall specimens in FSAFE: (a) Rectangular, (b) Non-rectangular (T-shaped) 21

Figure 2.2. Displacement along nodal DOFs in FSAFE model. 21

Figure 2.3. FSAFE model element: (a) Forces along nodal DOF, (b) Equilibrium of nodal forces and average internal stresses. 23

Figure 2.4. (a) Without body constraint, (b) With body constraint. 28

Figure 2.5. Illustration of the implemented solution strategy for a single DOF system (Clarke and Hancock, 1990). 29

Figure 2.6. Iterative strategy and residual displacements (Clarke and Hancock, 1990). 30

Figure 2.7. Constitutive Fixed-Strut-Angle Model (FSAM): (a) strain field on panel element, (b) concrete stresses along fixed struts, (c) shear aggregate interlock stresses along cracks, (d) uniaxial stresses in reinforcement, (e) dowel stresses in reinforcement. 31

Figure 2.8. Behavior of uncracked concrete in FSAM. 31

Figure 2.9. Behavior of concrete after formation of first crack in FSAM. 32

Figure 2.10. Behavior of concrete after formation of second crack in FSAM 33

Figure 2.11. Constitutive model for concrete (Chand and Mander, 1994). 34

Figure 2.12. Hysteretic parameters of the model by Chand and Mander (1994). 36

Figure 2.13. Constitutive model for reinforcing steel (Menegotto and Pinto, 1973). . . 37

Figure 2.14. Degradation of cyclic curvature (Menegotto and Pinto, 1973). 38

Figure 2.15. Compression softening effect with Model B (Ulugtekin, 2010). 40

Figure 2.16. Average stress–strain relationship by Belarbi and Hsu (1994) for concrete in tension. 41

Figure 2.17. Average stress–strain relationship by Belarbi and Hsu (1994) for reinforcing bars embedded in concrete.. 42

Figure 2.18. Shear aggregate interlock mechanism along crack surfaces. 44

Figure 2.19. Dowel action mechanism on reinforcement.. 47

Figure 3.1. Wall cross sections and reinforcement details for specimens: (a) RW2, (b) TW2, (c) R2, (d) WSH6. 53

Figure 3.2. Wall cross sections and reinforcement details for specimens: (a) RW-A20-P10- S38, (b) RW-A20-P10-S63, (c) RW-A15-P10-S51, (d) RW-A15-P10-S78, (e) S6. 54

Figure 3.3. Calibrated unconfined and confined concrete material stress-strain model in compression for specimen WSH6. 58

Figure 3.4. Calibrated concrete material stress-strain model in tension for specimen WSH6.. 59

Figure 3.5. Lateral load vs. top displacement responses for specimens: (a) RW2, (b) TW2.. 63

Figure 3.6. Lateral load vs. top displacement responses for specimen WSH6.. 64

Figure 3.7. Lateral load vs. top displacement response for specimen R2.. 65

Figure 3.8. Lateral load vs. top displacement responses for specimens: (a) RW-A20-P10-S38, (b) RW-A20-P10-S63, (c) RW-A15-P10-S51, (d) RW-A15-P10-S78.. 67

Figure 3.9. Lateral load vs. top displacement responses for specimen S6. 67

Figure 3.10. Lateral load vs. flexural and shear deformation responses for specimens: (a) RW2, (b) TW2.. 69

Figure 3.11. Lateral load vs. flexural and shear deformation responses for specimens: (a) RW-A20-P10-S38, (b) RW-A20-P10-S63. 70

Figure 3.12. Lateral load vs. flexural and shear deformation responses for specimens: (a) RW-A15-P10-S51, (b) RW-A15-P10-S78. 71

Figure 3.13. Lateral load vs. flexural and shear deformation responses for specimen S6. 72

Figure 3.14. Displacement profiles along the height of specimen RW2: (a) total displacement, (b) displacement due to flexural deformation, (c) displacement due to shear deformation. 75

Figure 3.15. Displacement profiles along the height of specimen RW-A20-P10-S38: (a) total displacement, (b) displacement due to flexural deformation, (c) displacement due to shear deformation. 76

Figure 3.16. Displacement profiles along the height of specimen RW-A20-P10-S63: (a) total displacement, (b) displacement due to flexural deformation, (c) displacement due to shear deformation. 77

Figure 3.17. Displacement profiles along the height of specimen RW-A15-P10-S51: (a) total displacement, (b) displacement due to flexural deformation, (c) displacement due to shear deformation. 78

Figure 3.18. Displacement profiles along the height of specimen RW-A15-P10-S78: (a) total displacement, (b) displacement due to flexural deformation, (c) displacement due to shear deformation. 79

Figure 3.19. Vertical growth vs. top displacement for specimens: (a) RW-A20-P10-S38, (b) RW-A20-P10-S63. 80

Figure 3.20. Vertical growth vs. top displacement for specimens: (a) RW-A15-P10-S51, (b) RW-A15-P10-S78. 80

Figure 3.21. Crack patterns for specimen RW2 at 2.0% drift: (a) Test (b) Model. . . . 82

Figure 3.22. Crack patterns for specimens: (a) RW-A20-P10-S38 at 1.5% drift, (b) RW-A20-P10-S63 at 1.5% drift, (c) RW-A15-P10-S51 at 3.0% drift, (d) RW-A15-P10-S78 at 2.0% drift.. 83

Figure 3.23. Concrete principal compressive stress contours for specimen RW2 at 2.0% drift.. 84

Figure 3.24. Concrete principal compressive stress contours for specimens: (a) RW-A20-P10-S38 at 2.2% drift, (b) RW-A20-P10-S63 at 2.0% drift, (c) RW-A15-P10-S51 at 1.5% drift, (d) RW-A15-P10-S78 at 2.0% drift. 85

Figure 3.25. Vertical normal strain profiles at wall base for specimen RW2. 86

Figure 3.26. Vertical normal strain profiles at wall base for specimens: (a) RW-A20-P10-S63, (b) RW-A15-P10-S51, (c) RW-A15-P10-S78. 87

Figure 3.27. Vertical normal strain profiles at wall base for specimen TW2: (a) along the web when the flange is in compression, (b) along the web when the flange is in tension, (c) along the flange when the flange is in tension. . . 89

Figure 3.28. Specimen WSH6: (a) vertical strains at wall boundaries along wall height under positive displacements, (b) vertical strains at wall boundaries along wall height under negative displacements. 91

Figure 3.29. Specimen WSH6: (a) curvature profile along wall height, (b) cumulative contribution of flexural deformations along wall height to top flexural displacement, (c) shear deformation to flexural deformation ratio.. 92

Figure 3.30. Shear deformation contribution to top displacement for specimen S6. . . 93

Figure 3.31. Lateral load vs. shear distortion along the bottom 1830mm (40%) of wall height for specimen R2 93

Figure 3.32. Sensitivity of model lateral load vs. top displacement responses to number of model elements used in horizontal (*m*) and vertical directions (*n*): (a) *m*=6, *n*=9 (b) *m*=12, *n*=18, (c) *m*=24, *n*=36. 96

Figure 3.33. Sensitivity of model lateral load vs. flexural and shear deformation responses to number of model elements used in horizontal (*m*) and vertical (*n*) directions: (a) *m*=6, *n*=9 (b) *m*=12, *n*=18, (c) *m*=24, *n*=36. . . 97

Figure 3.34. Sensitivity of model total displacement profile along wall height responses to number of model elements used in horizontal (*m*) and vertical (*n*) directions: (a) *m*=6, *n*=9 (b) *m*=12, *n*=18, (c) *m*=24, *n*=36. . . 98

Figure 3.35. Sensitivity of model flexural displacement profile along wall height responses to number of model elements used in horizontal (*m*) and vertical (*n*) directions: (a) *m*=6, *n*=9 (b) *m*=12, *n*=18, (c) *m*=24, *n*=36. . . 99

Figure 3.36. Sensitivity of model shear displacement profile along wall height responses to number of model elements used in horizontal (*m*) and vertical (*n*) directions: (a) *m*=6, *n*=9 (b) *m*=12, *n*=18, (c) *m*=24, *n*=36. . . 100

Figure 3.37. Sensitivity of model vertical growth vs. top displacement responses to number of model elements used in horizontal (*m*) and vertical (*n*) directions: (a) *m*=6, *n*=9 (b) *m*=12, *n*=18, (c) *m*=24, *n*=36. 101

Figure 3.38. Sensitivity of model crack patterns for specimen RW-A15-P10-S51 at 3.0% drift with various model elements in horizontal and vertical directions: (a) *m*=6, *n*=9, (b) *m*=12, *n*=18, (c) *m*=24, *n*=36. 102

Figure 3.39. Sensitivity of model concrete principal compressive stress contours for specimen RW-A15-P10-S51 at 1.5% drift with various model elements in horizontal and vertical directions: (a) *m*=6, *n*=9, (b) *m*=12, *n*=18, (c) *m*=24, *n*=36. 102

Figure 3.40. Sensitivity of model vertical normal strain profiles at wall base responses to number of model elements used in horizontal (*m*) and vertical (*n*) directions: (a) *m*=6, *n*=9 (b) *m*=12, *n*=18, (c) *m*=24, *n*=36. 103

Figure 4.1. Shear aggregate interlock on crack surfaces. 112

Figure 4.2. Dowel action on reinforcement.. 113

Figure 4.3. Interface crack and rotational spring (Massone *et al*., 2009): (a) single curvature, (b) double curvature. 115

Figure 4.4. Wall geometry and reinforcement details for specimens (Terzioglu *et al*., 2018): (a) Type 1, (b) Type 2. Note: All units are in mm. 117

Figure 4.5. Wall geometry and reinforcement details for specimens (Orakcal *et al.*, 2009): (a) wall spandrel (Type 1), (b) wall pier (Type 5). 118

Figure 4.6. Longitudinal reinforcement ratios for typical wall boundary conditions (ACI318-14, 2014): 119

Figure 4.7. Compression fracture energy for (a) Non-regularized stress-strain model (based on standard cylinder test results), (b) Regularized stress-strain model 130

Figure 4.8. Lateral load vs. top displacement responses for specimens: (a) SW-T4-S1 -6, (b) SW-T2-S3-4, (c) SW-T6-S1-8, (d) SW-T1-S1-2, (e) SW-T1-S2-9, (f) SW-T1-N10-S1-11.. 133

Figure 4.9. Lateral load vs. top displacement responses for specimens: (a) WS-T1-S1, (b) WS-T2-S1. 134

Figure 4.10. Lateral load vs. top displacement responses for specimens: (a) WP-T5--N5-S1, (b) WP-T5-N10-S1.. 135

Figure 4.11. Lateral load vs. flexural and shear deformation responses for specimens: (a) SW-T4-S1-6, (b) SW-T6-S1-8. 136

Figure 4.12. Shear displacement profile along the height of the specimens: (a) WP-T5-N5-S1, (b) WP-T5-N10-S1 138

Figure 4.13. Vertical growth vs. top displacement for specimens: (a) WP-T5-N5-S1, (b) WS-T2-S1. 139

Figure 4.14. Average horizontal normal strain profiles along wall height for specimens: (a) SW-T2-S3-4, (b) SW-T1-N10-S1-11 140

Figure 4.15. Concrete principal compressive stress contours for specimens: (a) SW-T2-S3-4 at 0.6% drift, (b) WP-T5-N10-S1 at 0.4% drift. 141

Figure 4.16. Open and closed crack orientations for specimen SW-T6-S1-8 at 0.8% drift: (a) Test, (b) Model. 142

Figure 4.17. Open and closed crack orientations for specimens SW-T2-S3-4 at 0.6% drift: (a) Test, (b) Model. 142

Figure 4.18. Sensitivity of the model results to consideration of rotational spring for the specimens: (a) SW-T6-S1-8, (b) WS-T1-S1. 143

Figure 4.19. Sensitivity of the model results to consideration of regularization for specimens: (a) SW-T2-S3-4, (b) SW-T1-N10-S1-11. 144

Figure 4.20. Sensitivity of model lateral load vs. top displacement responses to number of model elements used in horizontal (m) and vertical (n) directions for specimen SW-T2-S3-4: (a) m=7, n=3 (b) m=12, n=6, (c) m=24, n=12. 147

Figure 4.21. Sensitivity of model lateral load vs. top displacement responses to number of model elements used in horizontal (m) and vertical (n) directions for specimen WP-T5-N5-S1: (a) m=7, n=5 (b) m=11, n=10, (c) m=22, n=20. 148

Figure 4.22. Sensitivity of model lateral load vs. flexural and shear deformation responses to number of model elements used in horizontal (m) and

vertical (*n*) directions for specimen SW-T2-S3-4: (a) *m*=7, *n*=3, (b) *m*=12, *n*=6, (c) *m*=24, *n*=12. 149

Figure 4.23. Sensitivity of model lateral load vs. flexural and shear deformation responses to number of model elements used in horizontal (*m*) and vertical (*n*) directions for specimen WP-T5-N5-S1: (a) *m*=7, *n*=5, (b) *m*=11, *n*=10, (c) *m*=22, *n*=20. 150

Figure 4.24. Sensitivity of model shear displacement profile along wall height responses to number of model elements used in horizontal (*m*) and vertical (*n*) directions for specimen WP-T5-N5-S1: (a) *m*=7, *n*=5, (b) *m*=11, *n*=10, (c) *m*=22, *n*=20. 151

Figure 4.25. Sensitivity of model vertical growth vs. top displacement responses to number of model elements used in horizontal (*m*) and vertical (*n*) directions for specimen WP-T5-N5-S1: (a) *m*=7, *n*=5, (b) *m*=11, *n*=10, (c) *m*=22, *n*=20. 152

Figure 4.26. Sensitivity of model average horizontal normal strain profiles along wall height responses to number of model elements used in horizontal (*m*) and vertical (*n*) directions for specimen SW-T2-S3-4. 153

Figure 4.27. Sensitivity of model average horizontal normal strain profiles along wall height responses to number of model elements used in horizontal (*m*) and vertical (*n*) directions for specimen WP-T5-N5-S1. 153

Figure 4.28. Sensitivity of model crack patterns for specimen SW-T2-S3-4 at 0.6% drift with various model elements in horizontal and vertical directions: (a) *m*=7, *n*=3, (b) *m*=12, *n*=6, (c) *m*=24, *n*=12. 154

Figure 4.29. Sensitivity of model concrete principal compressive stress contours for specimen SW-T2-S3-4 at 0.6% drift with various model elements in

horizontal and vertical directions: (a) m=7, n=3, (b) m=12, n=6, (c) m=24, n=12. 155

Figure 4.30. Lateral load vs. top displacement response for specimen SW-T3-S1-5: (a) sliding shear crack not enforced (b) sliding shear crack enforced. . . . 157

Figure 4.31. Description of the significant parameters in lateral load vs. top displacement envelope. 158

Figure 4.32. Hysteretic energy dissipation capacity of specimen SW-T6-S1-8 for the first loading cycle to 1.2% drift: (a) Test, (b) Model.. 158

Figure 4.33. Comparison of lateral load capacities for squat walls with: (a) different failure modes, (b) different shear-span-to-depth ratios, (c) different levels of axial load. 159

Figure 4.34. Comparison of drift capacities for squat walls with: (a) different failure modes, (b) different shear-span-to-depth ratios, (c) different levels of axial load. 160

Figure 4.35. Comparison of cumulative hysteretic energy dissipation capacities for squat walls with: (a) different failure modes, (b) different shear-span-to-depth ratios, (c) different levels of axial load. 161

LIST OF TABLES

Table 3.1. Properties of wall specimens.. 55

Table 3.2. Material and response characteristics of wall specimens. 56

Table 3.3. Definition of wall model geometry. 57

Table 3.4. Material model parameters for confined and unconfined concrete in compression. 60

Table 3.5. Material model parameters for concrete in tension. 60

Table 3.6. Material model parameters for reinforcing bars.. 61

Table 4.1. Properties of squat walls. 121

Table 4.2. Material and response characteristics of squat walls. 122

Table 4.3. Definition of wall geometry. 123

Table 4.4. Material model parameters for concrete in compression and tension. 125

Table 4.5. Material model parameters for confined concrete of specimen SW-T1-S2-9.. 125

Table 4.6. Material model parameters for reinforcing bars in wall boundary regions. . 126

Table 4.7. Material model parameters for reinforcing bars in wall web. 127

Table 4.8. Rotational (strain penetration) spring stiffness for wall specimens.. 129

LISY OF SYMBOLS

A_{bar}	Reinforcing steel area of a single bar
A_g	Gross concrete cross sectional area
a_1 and a_2	Experimentally determined parameters that represent the degradation of the curvature within subsequent cycles
B	Tension stiffening parameter for reinforcing steel
b	Steel strain hardening ratio
c	Neutral axis depth
$\{D\}$	Global displacement vector
d_{bar}	Bar diameter
D_{fl}	Lateral flexural displacement
D_{sh}	Lateral shear displacement
D_{top}	Top lateral displacement
$[E]$	Tangent stiffness (partial derivative) matrix
E_c	Elastic modulus for concrete
E_{new}	New concrete tangent modulus upon return to unloading point on monotonic envelope
E_{pl}	Concrete plastic modulus upon unloading from monotonic envelope
E_s	Elastic modulus for steel
E_{sec}	Concrete secant modulus upon unloading from monotonic envelope
E_0	Elastic modulus for steel
E_1	Strain hardening modulus for steel
$\{F\}$	Global internal force vector
f'_c	Peak concrete compressive strength
f_{cr}	Concrete tensile strength
f_{new}	New concrete stress upon return to unloading point on monotonic envelope
f_{re}	Concrete stress at point of return to monotonic envelope
f_t	Concrete tensile strength
f_y	Yield strength of the bare reinforcing steel bars
$f_{y,boundary}$	Yield strength of the bare reinforcing steel bars in boundary region

f_{yeff}	Effective (reduced) average yield strength of bars embedded in cracked concrete
$f_{y,web}$	Yield strength of the bare reinforcing steel bars in web region
f_{un}	Concrete stress at unloading point from monotonic envelope
G	Shear modulus
$G_{f,c}$	Fracture energy
h	Height of mesh
h_w	Height of wall
I_s	Moment of inertia of the rebar cross-section
$[K]$	Global stiffness matrix
k_c	Foundation modulus of surrounding concrete
k_θ	Rotational spring stiffness
k_ϕ	Curvature stiffness
L_e	Length of concrete fixed strut
L_p	Length of concrete cylinder specimen
l	Effective dowel length
l_d	Development length of reinforcing steel bar
l_w	Length of wall
M	Section moment
m	Mesh number in horizontal direction
N	Applied axial load
n	Mesh number in vertical direction
P_{ax}	Axial load at top level of rectangular wall
P_{lat}	Lateral load
R	Parameter that influences the curvature of the transition curve between the two asymptotes
R_0	The value assigned to the parameter R for initial (or monotonic) loading,
r	Parameter defining shape of monotonic stress-strain curve for concrete
s	Nominal crack spacing
s_x	Distance between horizontal reinforcing bars
s_y	Distance between vertical reinforcing bars
$[T]$	Transformation matrix for body constraint
t	Thickness of wall

x_{crn}	Non-dimensional critical strain on concrete tension envelope
x_{crp}	Non-dimensional critical strain on the concrete compression envelope curve (used to define a tangent line up to the spalling strain)
V	Section shear force
V_{dow}	Dowel force acting on the horizontal and vertical reinforcing steel bars
$V_{dow,deg}$	Cyclic degradation parameter in dowel force
$V_{n,ACI}$	Nominal shear capacity per ACI
$V_{n,ACI-FLEX}$	Nominal moment capacity per ACI
w	Width of mesh
Δ	Slip deformation
Δ_{dow}	Dowel deformations acting on the horizontal and vertical reinforcing steel bars
Δ_{el}	Elongation at reinforcing bar
Δf	Reloading stress offset for concrete
$\Delta\varepsilon$	Reloading strain offset for concrete
Δ_{crack}	Slip deformation along the crack surface
Δ_s	Shear deformation
Δ_f	Flexural deformation
Δ_{max}	Maximum slip deformation through the experienced loading history
Δ_u	Lateral drift capacity
$\Delta\lambda$	The initial load increment
$\Delta\delta_n$	The initial displacement increment
$\Delta\delta$	Displacement increment
$\Delta\delta_R$	Residual displacement increment
α	Cyclic degradation parameter
β_m	Compression softening coefficient
β_{damage}	Biaxial damage coefficient
ε'_c	Monotonic strain at peak concrete compressive stress
ε_x	Normal strain in x direction
ε_y	Normal strain in y direction
$\varepsilon_{x'}$	Normal strain transformed to x' direction

$\varepsilon_{y'}$	Normal strain transformed to y' direction
ε_1	Normal strain in principal direction 1
ε_2	Normal strain in principal direction 1
ε_{cr}	Peak strain at tensile strength of concrete
ε_{cr}	Concrete strain where monotonic stress-strain relation starts following a straight line
ε_{c0}	Concrete strain at which the cyclic tension envelope originates
ε_0	Steel strain at intersection of elastic and yield asymptotes
ε_0	Strain at peak concrete compressive stress
ε_{pl}	Plastic strain upon unloading
ε_n	Strain at intersection of the elastic and plastic lines for steel bars embedded in concrete
ε_r	Concrete strain at point of return to monotonic envelope
ε_r	Monotonic strain where concrete stress reaches to zero
ε_r'	Regularized monotonic strain where concrete stress reaches to zero
ε_{re}	Strain at the point of strain reversal
ε_s	Maximum tensile strain at reinforcing steel
ε_t	Concrete tensile strain at peak tension stress
ε_{un}	Concrete strain at unloading point from monotonic envelope
ε_y	Strain at monotonic yield point
$\varepsilon_{\perp max}$	Maximum value of the compressive strain experienced
γ_{crack}	Shear strain along crack surface
γ_{xy}	Shear strain
$\gamma_{x'y'}$	Shear strain transformed to x'y' direction
$\gamma_{x'y'A}$	Shear strain along first fixed strut direction
$\gamma_{x'y'B}$	Shear strain along second fixed strut direction
σ_{cx}	Concrete normal stress in x direction
$\sigma_{cx'}$	Concrete normal stress in x' direction
$\sigma_{cx'A}$	Concrete normal stress in first fixed strut direction
σ_{cy}	Concrete normal stress in y direction
$\sigma_{cy'}$	Concrete normal stress in y' direction

$\sigma_{cy'B}$	Concrete normal stress in second fixed strut direction
σ_{sx}	Reinforcing steel stress in x direction
σ_{sy}	Reinforcing steel stress in y direction
σ_{x}	Total normal stress in x direction
σ_{y}	Total normal stress in x direction
$\sigma_{c\perp}$	Compressive stress in concrete in perpendicular direction to the crack
σ_{c1}	Concrete stress in principal direction 1
σ_{c2}	Concrete stress in principal direction 2
$\sigma_{dow,1}$	Dowel tensile stress in perpendicular to crack direction
σ_{r}	Steel stress at reversal point
σ_{y}	Steel yield stress
$\sigma_{\perp}$	Total normal stress in perpendicular direction to the crack
σ_{0}	Steel stress at intersection of elastic and yield asymptotes
σ_{1}	Concrete principal compressive stress
τ_{crack}	Shear aggregate interlock stress along crack surface
$\tau_{crack,deg}$	Cyclic degradation parameter in shear aggregate interlock stress
τ_{cxy}	Concrete shear stress
$\tau_{cx'y'}$	Concrete shear stress along x'y' direction
$\tau_{cx'y'A}$	Concrete shear stress along first fixed strut direction
$\tau_{cx'y'B}$	Concrete shear stress along second fixed strut direction
τ_{dow}	Dowel stress along crack surface
$\tau_{dow,12}$	Dowel shear stress in parallel to crack direction
τ_{xy}	Total shear stress
θ	Crack angle
θ_{rot}	Rotation at crack interface
θ_{crA}	Concrete crack direction A or first fixed strut direction
θ_{crB}	Concrete crack direction B or second fixed strut direction
ρ	Steel reinforcement ratio
ρ_{b}	Steel reinforcement ratio in boundary region
ρ_{web}	Steel reinforcement ratio in web region

ξ	The absolute strain difference between the current asymptote intersection point and the previous maximum or minimum strain reversal point
η	Friction coefficient
ϕ	Section curvature
$\Sigma\Delta$	Cumulative slip deformation through the experienced loading history

LIST OF ACRONYMS/ABBREVIATONS

ACI	American Concrete Institute
AESM	Axial Element in Series Model
ASCE	American Society of Civil Engineers
BR	Bar Rupture
CB	Concrete Crushing/Bar Buckling
CSMM	Cyclic Softened Membrane Model
DC	Diagonal Compression
DOF	Degree of Freedom
DSFM	Disturbed Stress Field Theory
DT	Diagonal Tension
FA-STM	Fixed Angle Softened Truss Model
FEM	Finite Element Model
FL	Flexure
FSAM	Fixed Strut Angle Model
FSAFE	Fixed Strut Angle Finite Element
FWE	Force Wall Element
LI	Lateral Instability
MCFT	Modified Compression Field Theory
MCPM	Multiple Component Parallel Model
MVLEM	Multiple Vertical Line Element Model
NLTM	Nonlinear Truss Model
OOHM	Origin Oriented Hysteresis Model
QLMEDD	Quadrilateral Layered Membrane Element with Drilling Degrees of Freedom
RA-STM	Rotating Angle Softened Truss Model
RC	Reinforced Concrete
SFI	Shear-Flexure-Interaction
SMM	Softened Membrane Model
SS	Sliding Shear
TVLEM	Three Vertical Line Element Model

1. INTRODUCTION

1.1. General

Reinforced concrete (RC) structural walls are commonly used in design due to their significant contribution to resistance against lateral actions, including wind loads and earthquake effects, imposed on building structures. Presence of structural walls has considerable impact on the lateral stiffness and strength characteristics of a building, reducing both the elastic displacement demands on the structural system under wind loads or service-level earthquakes, as well as the inelastic displacement (or ductility) demands under severe earthquakes. Improving the seismic performance of reinforced concrete (RC) building-type structures with means to enhance their lateral stiffness and lateral load capacity, promotes the use of structural walls. Structural walls are designed and detailed to provide adequate stiffness and strength, as well as sufficient ductility to attain favorable structural performance under both moderate and severe earthquake demands. Seismic design codes and recommendations enforce slender walls to exhibit ductile flexural behavior, by incorporating specially-detailed boundary regions and providing sufficient shear capacity for preventing brittle failures, whereas shear-controlled walls or wall segments (e.g., wall piers and spandrels) are designed to possess the necessary shear strength to experience limited levels of ductility demand under severe earthquake actions. However, obtaining reliable predictions for local responses (e.g., amplification of compressive strain at wall boundary regions and plane sections not remaining plane due to shear lag effects created by nonlinear shear deformations), as well as important shear response characteristics (e.g., influence of axial load on shear capacity, definition of a realistic value for the effective shear stiffness) are still topics of interest for even slender structural walls. Robust characterization and analytical representation of the behavior of slender walls with different cross-sectional geometries, as well as medium-rise and squat walls under earthquake actions, is a significant area of research towards more reliable seismic design and performance assessment of RC buildings.

The aspect (height-to-width) ratio is commonly used to classify structural walls. Shear behavior governs the response of structural walls with aspect ratios less than 1.0-1.5

(squat walls), whereas for structural walls with aspect ratios exceeding 2.5-3.0 (slender walls), flexural actions predominantly control the wall response. For walls with moderate aspect ratios (between 1.5 and 2.5), both flexural yielding and nonlinear shear deformations (which are usually coupled) contribute to wall behavior. For such walls, nonlinear shear deformations can constitute up to 30% to 50% of lateral wall displacements, as investigated experimentally by Tran and Wallace (2015). Reliable behavioral modeling of such structural walls with predominant shear-flexure interaction (SFI) behavior is of particular interest, especially because fiber-based modeling methodologies commonly used in practice for performance-based design of buildings typically consider uncoupled shear and flexural response components. However, analytical models with uncoupled flexural and shear responses are shown by previous research to underestimate compressive strains even in relatively slender RC walls controlled by flexure (Orakcal and Wallace, 2006), and overestimate the lateral load capacity of RC walls with moderate aspect ratios (Kolozvari *et al.*, 2015a,b) and low aspect ratios (Massone *et al.*, 2009). Shear-controlled squat walls (with aspect ratios typically less than 1.5) are also common in low-rise construction and at lower levels of tall buildings (for example, parking-level walls or basement walls), as well as in perimeter walls with window and door openings, in the form of wall piers and spandrels (wall segments). For low aspect-ratio walls or wall segments, behavior is often dominated by nonlinear shear responses, as well as the modeling parameters selected for shear stiffness and strength can have a significant impact on the predicted building performance. For performance-based design and evaluation of RC systems with structural walls, there is still a need for simple yet robust modeling approaches that capture coupled axial, shear, and flexural responses of walls with various aspect ratios and response characteristics.

1.2. Literature Review

Simulation of the nonlinear seismic response of structural walls can be accomplished by using phenomenological (macroscopic) or finite element (microscopic) modeling approaches. In this section, an overview of the macroscopic and microscopic modeling methods available in literature are presented.

1.2.1. Macroscopic Modeling Approaches

In macroscopic (or macro-element) modeling approaches for RC walls, phenomenological model elements with constitutive force displacement or stress-strain relationships are assembled together (using behavioral assumptions such as plane-sections-remain plane), generally for simulation of axial-flexural behavior, while shear behavior is represented by implementation of a shear spring defined by a simple hysteresis model (e.g., origin oriented). Due to their modeling assumptions, interaction between the axial-flexural and shear behaviors is often neglected. Hence, macro-element models are also developed for simulation of the coupled behavior of axial-flexural and shear responses, which is deemed significant even in modeling of slender RC walls. The majority of the well-known macroscopic models in the literature, considering uncoupled or coupled axial-flexural and shear responses, are summarized herein.

Vulcano *et al.* (1988), proposed the so-called Multi-Component-Parallel Model (MCPM, also known as Multiple-Vertical-Line Element Model MVLEM), for better simulation of the nonlinear inelastic behavior of RC walls that represents flexural controlled responses. The model was derived by improving the axial-element-in-series model (AESM), firstly proposed by Vulcano and Bertero (1986), with the implementation of more robust constitutive material models and with modifying the geometry of wall model. AESM was obtained by modifying the axial stiffness hysteresis model of Three-Vertical-Line-Element Model (TVLEM), which was originally proposed by Kabeyasawa *et al.* (1983) based on a seven-story RC frame wall building test results. For simulation of axial-flexural behavior of an RC wall, MVLEM was described by two vertical elements in the boundary regions while more than two vertical elements in the web regions (Figure 1.1). A horizontal shear spring was also incorporated similar to the model TVLEM to represent the nonlinear shear response of walls. Hysteresis rules in vertical line elements were defined with the axial force deformation relationship which was also used in AESM, and hysteresis rules of shear spring was described by the origin-oriented hysteresis model (OOHM) originally defined in the study by Kabeyasawa *et al*. (1983). Development of MVLEM also includes redefining the axial behavior of uncracked concrete and tension stiffening effect. Finally, the model was found to be reliable in reproducing the nonlinear

response of flexural controlled walls; however, in predicting the nonlinear responses of walls representing shear controlled behavior, the model was not reliable.

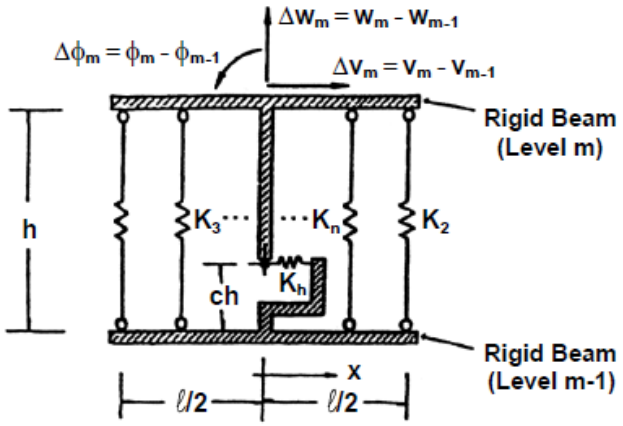

Figure 1.1. Multiple-Vertical-Line-Element Model (MVLEM) (Vulcano *et al.*, 1988).

Orakcal *et al*. (2004) and Orakcal and Wallace (2006) improved MVLEM with the implementation of the state-of-the-art uniaxial constitutive material models in its formulation (Figure 1.2). Sensitivity analyses were conducted for identifying the parameters in the constitutive material models and for presenting the effects of these parameters to model accuracy. The aim of this study was to provide better simulation of RC walls in both global and local response levels. The improved model was verified against the test results of the slender walls with rectangular and non-rectangular (T-shaped) cross-sections. The model well represented the nonlinear hysteretic response characteristics of relatively slender RC walls. However, SFI and nonlinear shear responses of even slender walls was not simulated by the model, due to the uncoupled modeling assumption for the axial-flexural and shear behaviors in the formulation of the model. Additionally, although the model reasonably captured the tensile strain profile, the discrepancy between the model and test results in compressive strain profile was significantly observed.

Perform-3D (Computers and Structures Inc. 2006) is one of the most the well-known software for nonlinear modeling of RC walls. Two different element types are available in Perform-3D, which are shear wall element and general wall element. Shear wall element is mostly used ones for modeling of RC walls with incorporation of a fiber section to

simulate the axial/flexural responses (Figure 1.3a) and a layer section to represent shear behavior (Figure 1.3b). Although Perform-3D is a publicly-available commercial software, it does not consider the SFI in modeling of walls. Additionally, plane section remains plane in the formulation of Perform-3D, which is not an observed behavioral response for RC walls.

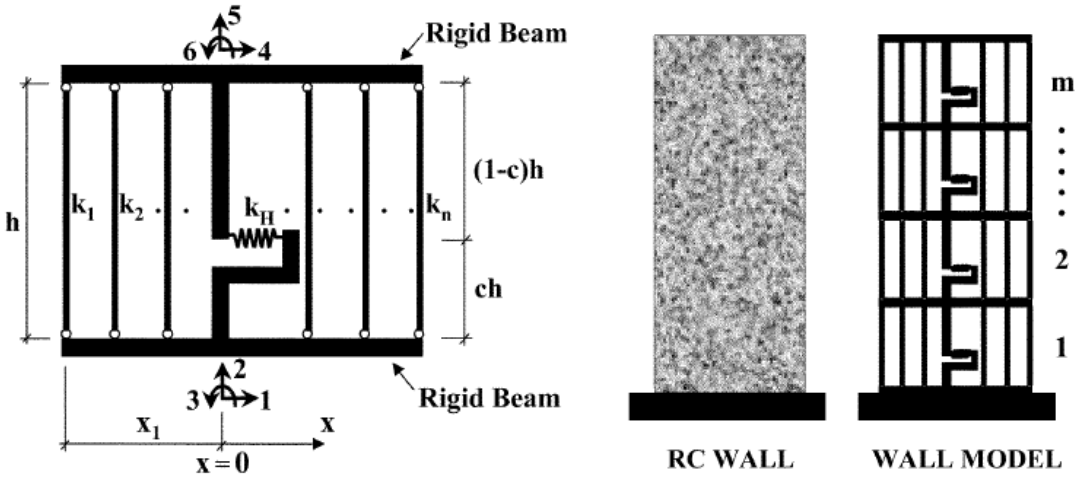

(a) MVLEM element (b) Model of a wall

Figure 1.2. MVLEM (Orakcal *et al.*, 2004).

Massone *et al.* (2009) modified the MVLEM with the implementation of shear springs for each uniaxial elements to capture the SFI responses of RC walls (Figure 1.4). This modeling approach was assumed similar to the implementation of a RC panel element into a fiber-based modelling approach, which was primarily developed by Petrangeli (1999). Simulation of RC panel elements in the formulation of modified MVLEM was achieved by a rotating angle modeling approach. Shear strains across the cross-section of the wall was assumed uniformly distributed in the model formulation. The model was validated against experimental results of squat walls. Model was only capable of simulating the envelope response of RC walls due to not defining the cyclic material models in its formulation, which is the main limitation of the modified MVLEM. The assumption of the uniformly distributed shear strains across the cross-section of the walls resulted in not well estimating test results with decreasing shear-span-to-depth ratios.

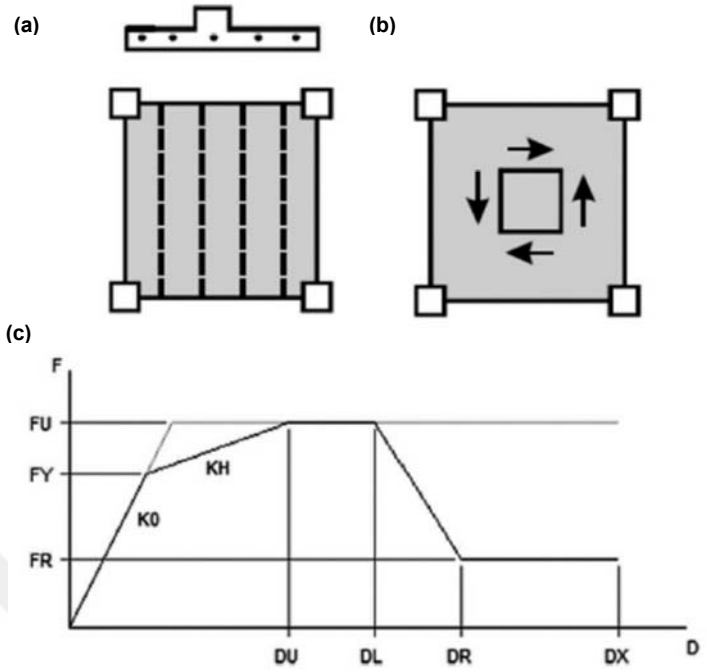

Figure 1.3. Shear wall element: (a) vertical axial bending, (b) concrete shear, and (c) typical material backbone relation (Computers and Structures Inc., 2006).

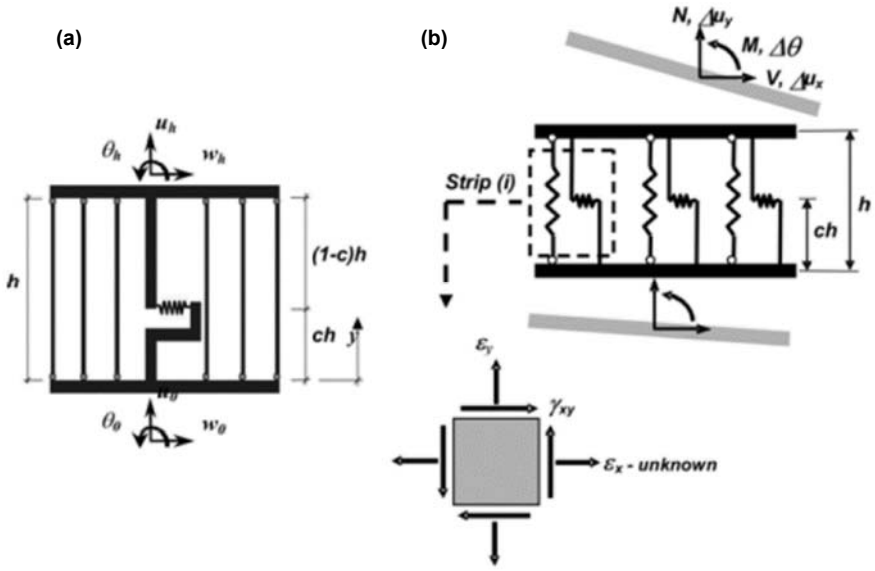

Figure 1.4. Element models: (a) MVLEM element, (b) coupled model element (Massone *et al*., 2009).

Jiang and Kurama (2010) also developed an analytical model considering the coupled effects of axial, flexural and shear responses for RC walls (Figure 1.5) based on the micro-plane fiber modeling approach primarily proposed by Petrangeli (1999). The study mainly focused on the global and local response predictions of medium-rise walls and the proposed model was not validated against squat walls with shear critical responses. The model was also found to be sensitive to the determination of Gauss integration points in the formulation. The model needs further verification with the wall specimens from different experimental programs.

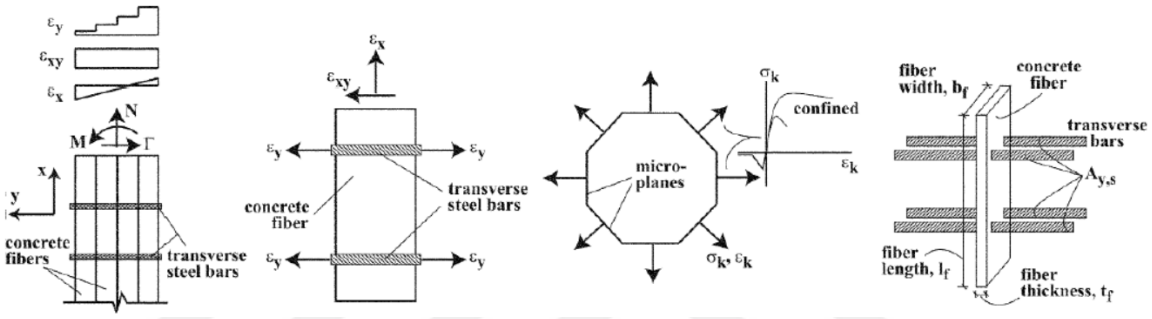

(a) (b) (c) (d)

Figure 1.5. Fiber element with nonlinear shear deformations: (a) fiber strain field, (b) concrete fiber strains, (c) micro-planes, and (d) tributary transverse steel reinforcement (Jiang and Kurama, 2010).

A strut and tie model, called Nonlinear-Truss-Model (NLTM), was proposed Panagiotou *et al.* (2012) to predict the shear-flexural interaction responses of RC walls. The model was implemented in OpenSees (McKenna *et al.*, 2000) platform by the authors. Wall modeling in NLTM was accomplished by definition of nonlinear vertical, horizontal and diagonal elements connected at nodes. Cyclic uniaxial material models were described for concrete and steel in the model (Figure 1.6). In the modeling approach, SFI was considered by incorporating a reduction factor in concrete compressive strength related to the transverse tensile strain. The NLTM was compared with test results of the wall specimens having significant SFI responses. Pre-cracking stiffness and strength values of the wall specimens was over-predicted by the NLTM due to overlaps in the concrete strut areas that were oriented in the vertical, horizontal and diagonal directions. The model was also found to be sensitive to the size of the elements especially in predicting the local responses.

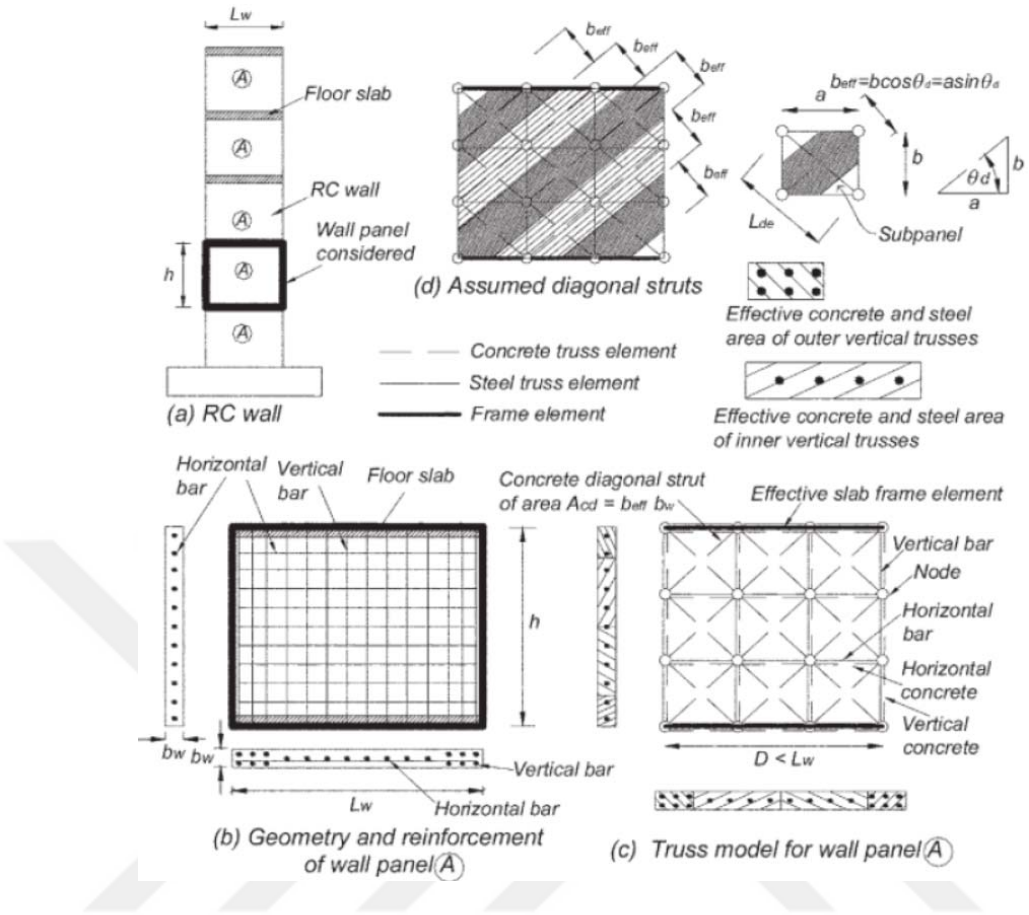

Figure 1.6. RC wall and wall panel truss model (Panagiotou *et al.*, 2012).

Similar to the model formulations proposed by Petrangeli (1999) and Massone *et al.* (2009), Fischinger *et al.* (2012) improved the MVLEM (originally developed by Fischinger *et al.*, 1990) to consider the SFI in nonlinear response of walls. In this modeling approach, three horizontal shear springs were assigned for each of the uniaxial element (Figure 1.7a). These horizontal springs (Figure 1.7b) were employed for simulation of shear aggregate interlock (HSA), dowel action on vertical reinforcing bars (HSD) and axial resistance of horizontal reinforcing bars (HSS) (Figure 1.7c). Semi-empirical models developed by Rejec (2011) were employed for definition of the constitutive models for each of the horizontal springs. Model was only compared with the test results of a five-story coupled wall specimen subjected to biaxial dynamic loading on the shaking table. Model accurately simulated the failure modes of the pier specimen as well as the base shear response; however, validation of the model for a broad range of wall specimens was not presented.

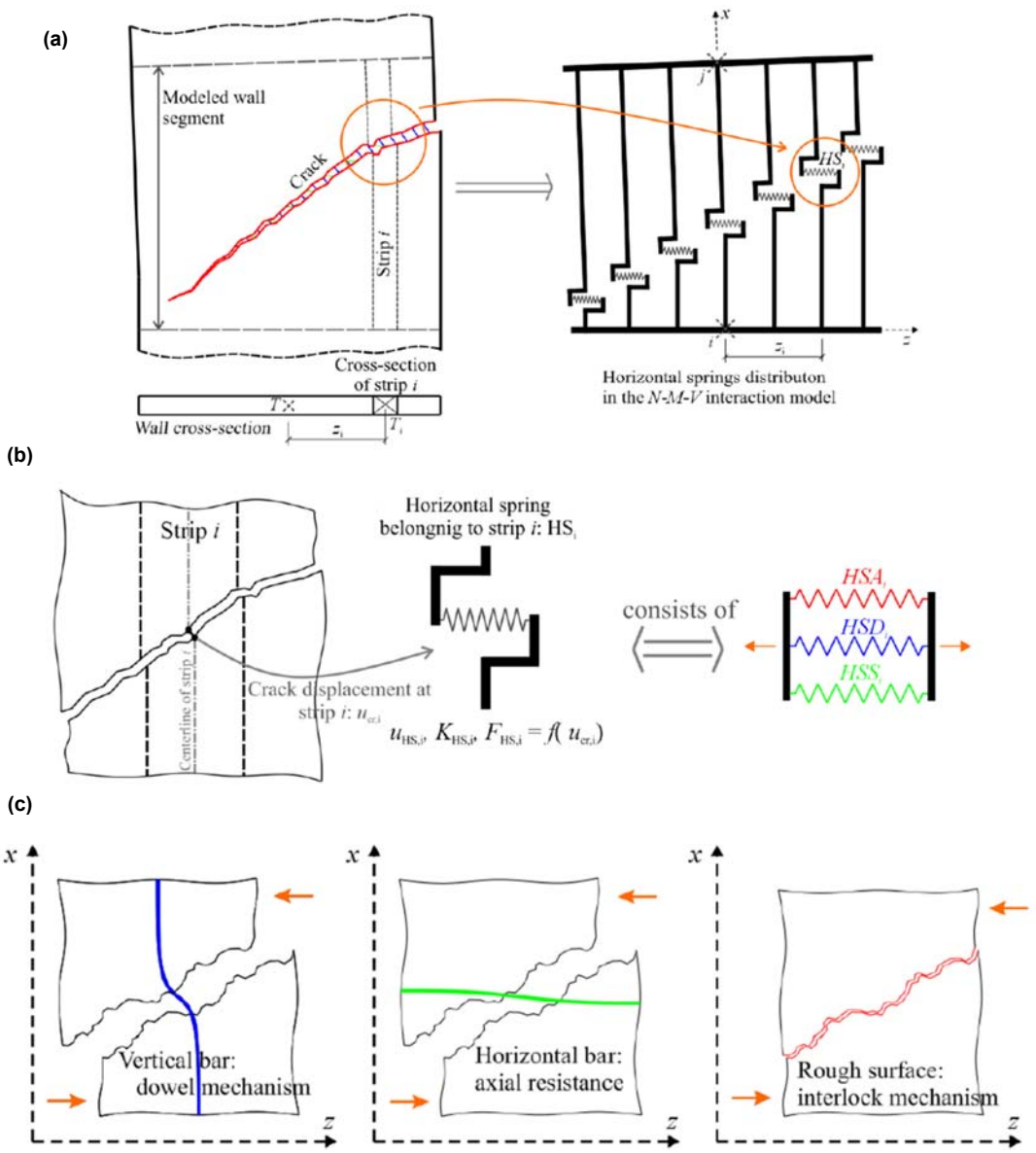

Figure 1.7. Improved MVLEM formulation: (a) multiple horizontal springs in upgraded MVLEM, (b) horizontal shear spring at each MVLEM macro-fiber, and (c) mechanisms of shear force transfers over the cracks (Fischinger *et al.*, 2012).

Kolozvari *et al.* (2015a, b) also developed a fiber-based model called SFI-MVLEM, which was obtained by modifying the model formulation of the MVLEM –originally described by Orakcal *et al.* (2004)– to consider the coupled shear-flexural interaction behavior in the nonlinear responses of medium-rise RC walls (Figure 1.8). Uniaxial fiber elements in MVLEM was treated as RC panel elements with the description of the Fixed-Strut-Angle-Model (FSAM) (Orakcal *et al.*, 2012) for each of the uniaxial elements

(Figure 1.8a). Shear aggregate interlock (Figure 1.8d) and dowel action (Figure 1.8f) mechanisms along the crack interface also incorporated by the model. Experimentally obtained global and local responses of five medium rise walls were compared with model predictions. Modeling parameters for shear aggregate interlock and dowel action mechanisms dominated the analytical model predictions, indicating that the model is sensitive to the parameters defined in the formulation of these mechanisms. Hence, these parameters need to be further calibrated for confirmation. Model was also unable to capture the degradation in lateral load capacity due to not representing the failure mechanisms associated with the buckling of reinforcing bars and out-of-plane deformation in boundary regions as well as the shear sliding close to the base of the walls.

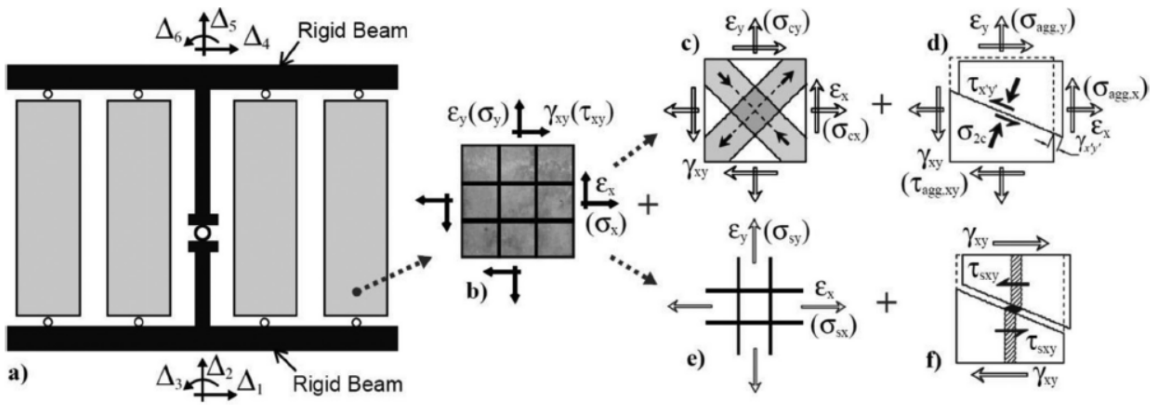

Figure 1.8. SFI-MVLEM formulation: (a) model element, (b) RC panel behavior, (c) concrete struts, (d) shear aggregate interlock, (e) steel behavior, and (f) reinforcement dowel action (Kolozvari *et al.*, 2018a).

Vásquez *et al.* (2016) developed the force-based Force-Wall-Element (FWE) model based on the fiber-based nonlinear beam-column element. Uniaxial elements were employed for simulation of the axial and flexural behavior of the walls (Figure 1.9a) similar to other fiber-based modeling approaches. Cyclic stress-strain material models were defined in the formulation of FWE for simulating the behavior of uniaxial elements. Shear deformations were represented by horizontal shear sections (Figure 1.9b) incorporating a stress deformation curve with a monotonic envelope defined by Gérin and Adebar (2009). The regularization method proposed by Coleman and Spacone (2001) was also incorporated in the model formulation to obtain analysis results insensitive to mesh

size, which is significant in predicting the descending region of load vs. displacement responses. Model was only validated against a rectangular and two non-rectangular (U-shaped and T-shaped) wall specimens from literature. Comparison of local response predictions of the model against test results were not presented in this study. Coupled interaction of shear and flexural deformations were not considered in the model formulation. The FEW model is required to be improved in simulating the nonlinear shear responses of non-rectangular walls.

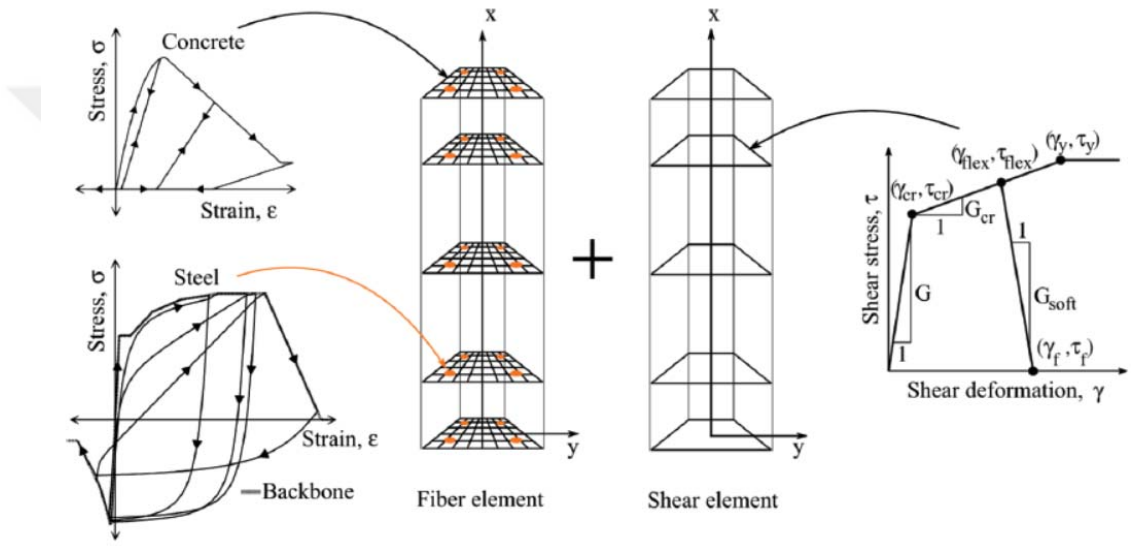

(a) (b)

Figure 1.9. Force based fiber section nonlinear beam-column element: (a) simulation of flexural behavior, (b) simulation of shear behavior (Kolozvari *et al.*, 2018a).

As discussed in previous paragraphs, macroscopic models are developed based on the observed behavior of structural walls (during experiments or after earthquakes), and their formulations are typically characterized by simplifying assumptions (e.g., plane-sections-remain-plane, uncoupling of flexural and shear responses, assumption of uniformly distributed shear strains along the wall cross-section). Due to their relatively simple formulations, macro-models are effective computational tools that are relatively easy to implement in analysis, and many have been shown to be efficient and reasonably accurate in predicting important hysteretic response characteristics of RC structural walls. However, the applicability of these models is typically limited to cases for which the assumptions implemented in the model formulations are valid. Although macroscopic

modeling approaches used commonly in performance-based design applications, they fail to capture shear-flexure interaction effects that have been observed experimentally for not only medium-rise walls (Tran and Wallace, 2015) but for slender walls also (Massone and Wallace, 2004). Fiber-based models also cannot simulate other important response attributes of walls, including plane-sections not remaining plane, which results in amplification of compressive strains in concrete, as well as salient characteristics of nonlinear shear behavior, including effective shear stiffness, influence of axial load on shear strength, shear ductility, and shear failure type depending on whether or not horizontal web reinforcement yields. There is still a need for simple and computationally-manageable yet robust modeling approaches that can incorporate such behavioral characteristics of walls in the analysis, for more reliable performance-based seismic design applications.

1.2.2. Microscopic Modeling Approaches

Microscopic (finite element models), although are more computationally-demanding, provide more general solutions towards simulating the nonlinear seismic response of walls, since their formulation is based on a detailed definition of local behavior. To describe local behavior in finite element modeling approaches, various constitutive model formulations for monotonic (e.g., Vecchio and Collins, 1986; Pang and Hsu, 1995, 1996; Vecchio, 2000; Hsu and Zhu, 2002) and cyclic (e.g., Ohmori *et al.*, 1989; Stevens *et al.*, 1991; Vecchio, 1999; Palermo and Vecchio, 2003; Mansour and Hsu, 2005; Gérin and Adebar, 2009) loading have been proposed for representing the nonlinear behavior of the constitutive RC panel (membrane) elements. As well, numerous research efforts on finite element modeling of structural walls are available in the literature with those constitutive models, of which only the more well-known or recent studies will be summarized here.

Finite element analysis software incorporating hysteretic formulations of the Modified Compression Field Theory (MCFT) (Vecchio and Collins, 1986) and the Disturbed Stress Field Model (DSFM) (Vecchio, 2000) is available online (http://vectoranalysisgroup.com), and the VecTor software is widely used in modeling and analysis of RC walls, although for research purposes mostly. For example, Palermo and Vecchio (2007) used VecTor2 (Vecchio, 1989), with the MCFT (Vecchio and Collins,

1986) as the constitutive panel (membrane) model, for analysis of both slender and squat walls with rectangular or non-rectangular cross-sections, as well as rectangular walls with openings. However, walls with non-rectangular sections were modeled in two-dimensions only, therefore neglecting the out-of-plane shear lag effects (non-uniform longitudinal strain distribution) in the wall flanges perpendicular to the loading direction. The developed analytical model does not consider the effect of dowel action and bar buckling. In addition to lateral load vs. top displacement response comparisons for wall specimens investigated, deformed shape and concrete crushing results for only one specimen was presented. Local response predictions of the model were not validated against the experimentally-measured local results.

Lu and Henry (2017) used VecTor2 (Vecchio, 1989) to conduct finite element analysis of lightly reinforced walls (Figure 1.10) using the DSFM (Vecchio, 2000) as the constitutive model. Dowel action and buckling effect for reinforcing bars were also incorporated in the formulation of the analytical model. Experimental validation of the model was conducted using six test specimens with varying shear-span-to-depth ratios, axial load levels, and anti-buckling tie details. This study focused on prediction of the global lateral load vs. top displacement response of lightly-reinforced walls with rectangular cross-sections only, and their drift capacity at the initiation of reinforcement buckling. Accuracy of the model in estimating the distribution of vertical strains at wall boundaries along wall height was also evaluated. Eleven additional walls were modeled with various wall dimensions and material properties to conduct research on significant parameter of lightly reinforced concrete walls. However, although the walls investigated had various shear-span-to-depth ratios, they were all relatively slender walls with flexure-controlled responses, with shear deformations contributing to wall lateral displacements by less than 5%. In addition, mesh discretization in the analytical model formulation was found to be significant for estimating the crack patterns of wall specimens.

Pang and Hsu (1996) and Hsu and Zhang (1997) introduced a Fixed-Angle-Softened-Truss-Model (FA-STM) for simulating the in-plane membrane behavior. The model was developed over the Rotating-Angle-Softened-Truss-Model (RA-STM) (Hsu, 1988; Belarbi and Hsu, 1994, 1995) with the assumption of that, cracks are fixed at an angle for consideration of the contribution of concrete behavior to shear stress along crack

directions. Since RA-STM and FA-STM were insufficient for modeling of post-peak responses in membrane elements, Hsu and Zhu (2002) introduced Softened-Membrane-Model (SMM) with applying two significant modifications on the FA-STM. One of these modifications was the implementation of Hsu/Zhu ratios developed by Zhu and Hsu (2002) used for simulation of the smeared stress-strain behavior of RC membrane elements upon cracking. The second modification was the implementation of a shear stress-strain material model proposed by Zhu *et al.* (2001). Mansour and Hsu (2005) introduced Cyclic-Softened-Membrane-Model (CSMM) as an extension of SMM with the implementation of constitutive material models and a cyclic damage coefficient for simulation of cyclic response characteristics. Although the CSMM has been implemented in the open-source computational platform OpenSees (McKenna *et al.*, 2000), studies on simulating the nonlinear response of structural walls using the CSMM are limited. Upon implementing the CSMM as a quadrilateral element in OpenSees, Mo *et al.* (2008) analyzed nine two-dimensional wall-frame assemblies tested in the laboratory, incorporating walls with identical aspect ratios but with various reinforcement configurations and axial load levels applied. Model predictions and test results for shear force vs. total drift responses only compared for validation of the model. Luu *et al.* (2017) implemented a layered shell finite element formulation of the CSMM (Figure 1.11) in OpenSees, and validated it against test results conducted on one U-shaped wall specimen and one cylindrical tank specimen. However, accuracy of the CSSM in predicting local (e.g., strain) response characteristics of walls was not evaluated in the studies by Mo *et al.* (2008) or Luu *et al.* (2017).

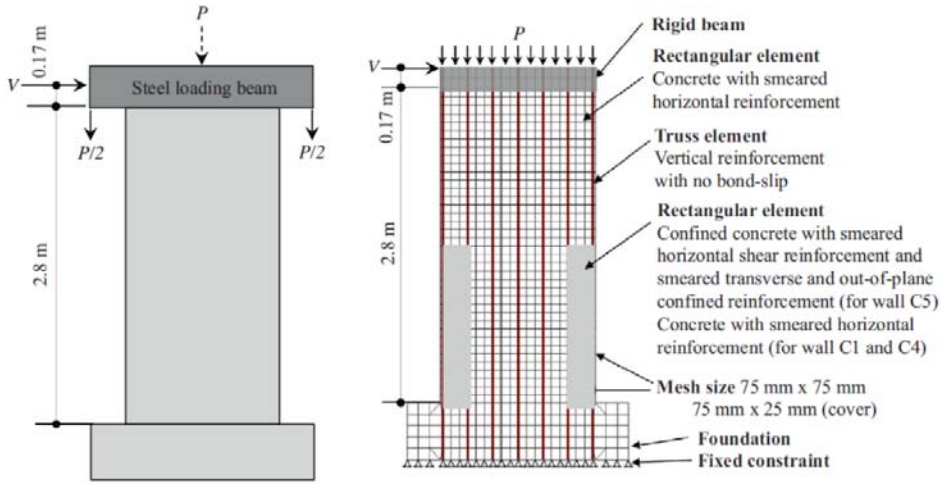

Figure 1.10. Illustration of the numerical model (Lu and Henry, 2017).

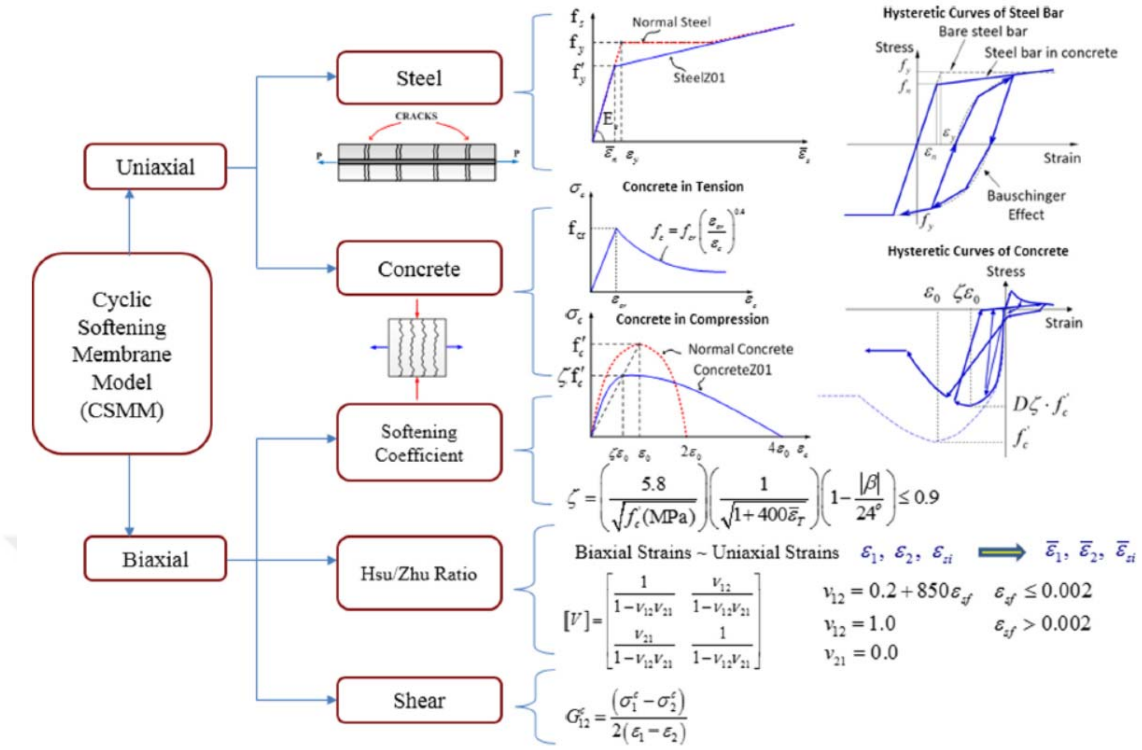

Figure 1.11. Overview of CSMM for reinforced concrete (Luu *et al.*, 2017).

Rojas *et al.* (2016) proposed the Quadrilateral Layered Membrane Element with Drilling Degrees of Freedom (QLMEDD) (Figure 1.12) for finite element modeling of walls with a rotating-crack constitutive modeling approach for the membrane elements. As illustrated in Figure 1.12a, the model had twelve in-plane DOFs, four of which were rotational DOFs, allowing the proposed model to be connected to frame type elements. The layered formulation (Figure 1.12b) also provided variations in steel and concrete material models along the thickness of the walls. In the formulation of the QLMEDD, a uniaxial concrete material model was employed along the principal stress directions and Poisson ratios of concrete after cracking were neglected. Analytical model formulation also incorporated a uniaxial steel stress-strain relationship including bar buckling proposed by Massone and Moroder (2009).The model was validated against test results for a total of ten wall specimens with various aspect ratios and failure modes, but having rectangular cross-sections only. Seven of these wall specimens were tested under monotonic loading, while three of these wall specimens were subjected to cyclic loading. This study focused more on prediction of the global lateral load vs. displacement responses of walls, and only limited

local response comparisons (vertical strain profiles along the base of two wall specimens) were provided to assess the accuracy of the model in predicting local deformations.

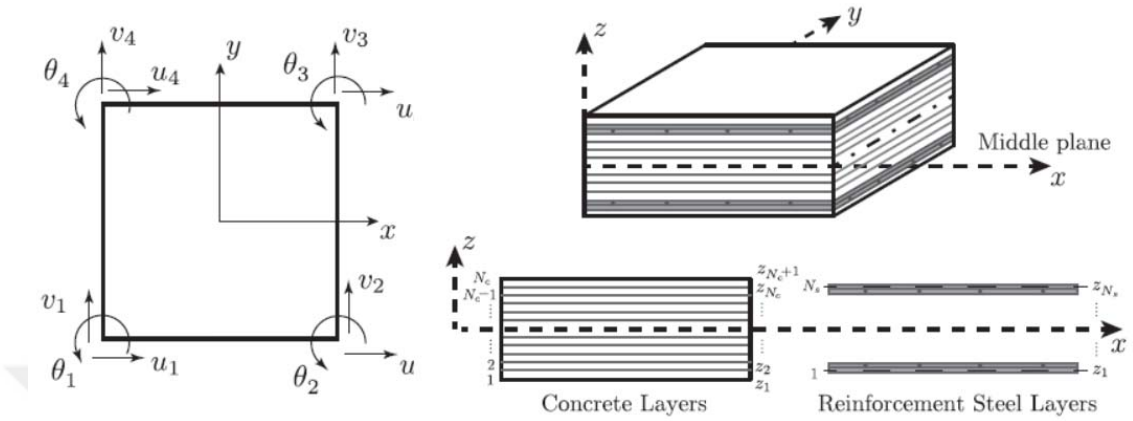

(a) (b)

Figure 1.12. a) Membrane element global DOF, b) A typical rectangular layered membrane section (Rojas *et al.*, 2016).

Another recent study on finite element modeling of walls was conducted by Dashti *et al.* (2017a) using the commercial analysis software DIANA (2011). The modeling approach adopted in this study involved using curved shell elements (Figure 1.13), which consider out-of-plane deformations that can develop even under in-plane loading conditions, and therefore allow capturing of the out-of-plane instability behavior of walls. In the model formulation, 2x2 Gauss integration point was employed along the area of the elements, while three integration points were used along the thickness of the elements, which contributes the model in simulating the out-of-plane deformations. The Total Strain Crack Model available in DIANA, with a rotating-crack angle formulation, was used as the constitutive model to describe the in-plane behavior of the model elements. Experimental validation of the model was carried out using test results of six wall specimens with rectangular cross-sections only, but having different shear-span-to-depth ratios, cross-sectional aspect ratios, and failure mechanisms. Two of the wall specimens investigated were subjected to monotonic loading whereas four of them were tested under cyclic loading. Accuracy of the model was evaluated in terms of global lateral load vs. top displacement responses of the walls, as well as out-of-plane instability behavior, crack patterns, and vertical strain profiles at wall base. However, model accuracy in predicting the flexural and shear deformation contributions on the wall response was not assessed.

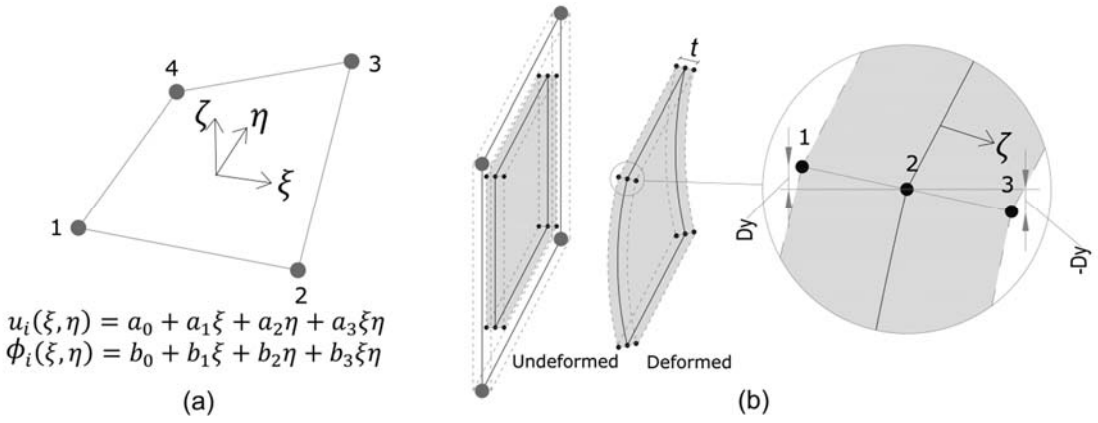

Figure 1.13. Curved shell element: a) in-plane interpolation, b) three-point integration scheme over the element thickness (Dashti *et al.*, 2017a).

LS-DYNA, another commercial software, is generally used as a finite element analysis tool for RC walls (Murray, 2007). Composite-layered shell element is used for simulation of RC walls. Material layers are employed along the thickness of the walls for representing cover concrete, vertical reinforcing bars and horizontal reinforcing bars (with two layers) as well as core concrete (with one layer). Concrete layers are represented using a smeared fixed-crack-approach with the material model MAT_CONCRETE_EC2, while simulation of reinforcing bars are achieved by the MAT HYSTERETIC REINFORCEMENT material model along their oriented directions. Since fixed-crack-approach is employed in the model formulation, shear resisting and dowel action mechanisms are also incorporated. Although LS-DYNA is a publicly-available and commonly-used software, it has not been adequately validated for prediction of nonlinear hysteretic response characteristics of RC walls.

1.3. Objectives and Scope

The aim of this study is to develop and experimentally-validate a novel finite element model formulation for effectively simulating the hysteretic nonlinear response characteristics of RC structural walls with various configurations and behavioral features.

A recently-developed constitutive model with a relatively simple formulation (named as the Fixed Strut Angle Model, FSAM, Orakcal *et al.*, 2012) is used as a baseline

formulation, for describing the nonlinear stress vs. strain behavior of the membrane (panel) elements used in the finite element model formulation developed, since the FSAM was previously shown to provide accurate response (stress vs. strain) predictions for individual RC panel specimens with various reinforcement configurations (Orakcal *et al.*, 2012).

The FSAM formulation is first improved in this study, via implementation of both simple (for slender and medium-rise walls) and refined (for squat walls) constitutive relationships for representing shear stress transfer across cracks in concrete, as well as dowel action on reinforcing steel bars. A quadrilateral model element formulation is then generated, using a simple approach incorporating linear strain interpolation functions and a single Gauss integration point for each model element. The model elements are then assembled together, using a direct stiffness assembly procedure, for constructing a finite element model formulation for a RC wall, also with the necessary numerical manipulations implemented to simulate support conditions, loading conditions, and rigid body constraints, as well as for consideration of strain penetration effects and strain localization effects in the analysis results.

The developed finite element model formulation (named as the Fixed Strut Angle Finite Element–FSAFE–Model) is also validated extensively, against test results on RC walls with a broad range of configurations and response attributes. It must be mentioned that analytical studies available in the literature on finite element modeling of walls with both rectangular and non-rectangular cross-sections, in which the model is validated against experimental results for walls with various response characteristics (flexure-controlled, shear controlled, shear-flexure interaction) at both global (load vs. displacement) and local (shear and flexural deformations, strains, etc.) response levels are extremely limited (e.g., Rojas *et al.*, 2016; Dashti *et al.,* 2017a). Therefore, the FSAFE model is experimentally-validated against test results obtained from seven different experimental programs in the literature, on thirty-four selected wall specimens with varying levels of flexural and shear deformation contributions on wall response. Model response predictions are compared with experimentally-measured responses of walls with various geometry and reinforcement attributes; including relatively slender (aspect ratio of 3.0) flexure-controlled walls with rectangular and T-shaped cross-sections, medium-rise walls (aspect ratios of 1.5 and 2.0) with coupled shear-flexural responses, and squat walls

(shear span-to-depth ratios ranging from 0.44 and 1.15) with shear-predominant responses. Accuracy of the model in simulating the experimentally-observed wall responses is evaluated not only in terms of global lateral load vs. displacement behavior, but also with regards to relative contributions of nonlinear flexural and shear deformations to wall lateral displacements, as well as local deformation characteristics including the magnitudes and distribution of nonlinear deformations and local strains (both longitudinal and transverse) developing in the walls investigated.

1.4. Thesis Outline

This thesis includes five chapters. Chapter 1 presents a general introduction and a review of previously-developed macroscopic and microscopic modeling approaches for walls, as well as the objectives and scope of this study. Details on the formulation of the Fixed-Strut-Angle Finite Element (FSAFE) Model is provided in Chapter 2. Chapter 3 presents the details on experimental validation of the FSAFE model for selected wall specimens with flexural or coupled shear-flexural responses. Chapter 4 provides details on refinement of the FSAFE model formulation for improved simulation of squat walls with shear controlled responses, as well as validation of the FSAFE model against test results for numerous squat wall specimens. In Chapter 5, the analytical findings are summarized and concluding remarks on the capabilities and limitations of the FSAFE model, as well as recommendations for future studies, are presented.

2. MODEL DESCRIPTION

2.1. The Proposed Fixed Sturt Angle Finite Element (FSAFE) Model Description

The Fixed Strut Angle Finite Element (FSAFE) model is an assembly of rectangular four-node membrane elements with only in-plane translational degrees of freedom defined at the nodes. The main assumption of the FSAFE model is that each model element incorporates linear strain interpolation functions and only a single Gauss integration point (located at the centroid of the model element). The constitutive behavior of a single model element in the FSAFE model is defined by a single average strain field (ε_x, ε_y, γ_{xy}) corresponding to a single average stress field (σ_x, σ_y, τ_{xy}). The constitutive axial/shear behavior of the model elements under plane-stress (σ_x, σ_y, τ_{xy}) loading follows the so-called Fixed Strut Angle Model (FSAM) formulation (Orakcal *et al.,* 2012). Mechanical principles of the FSAM and the constitutive material models implemented in its formulation are summarized in the following sections. Although not mandatory, this approach was preferred in order to facilitate convergence and to reduce analysis time of the model.

Figure 2.1a shows the nodes and nodal degrees of freedom of an individual model element, and also illustrates typical model meshing for a rectangular wall specimen in the FSAFE model formulation. Although the model elements are 4-node membrane elements with only in-plane translational degrees of freedom, through a simple direct stiffness assembly, they can be assembled to construct a model for a wall with a non-rectangular cross-section. For a T-shaped wall specimen (Figure 2.1b), upon lateral loading along the direction of the wall web, the model elements defined along the wall flange will contribute to the overall lateral stiffness and nonlinear lateral load behavior of the wall, due to the in-plane deformations and in-plane restoring forces developing in these model elements. However, this approach neglects the contribution of the out-of-plane flexural stiffness of the wall flange to the overall response, since the model elements defined along the wall flange remain to be membrane elements with no out-of-plane stiffness.

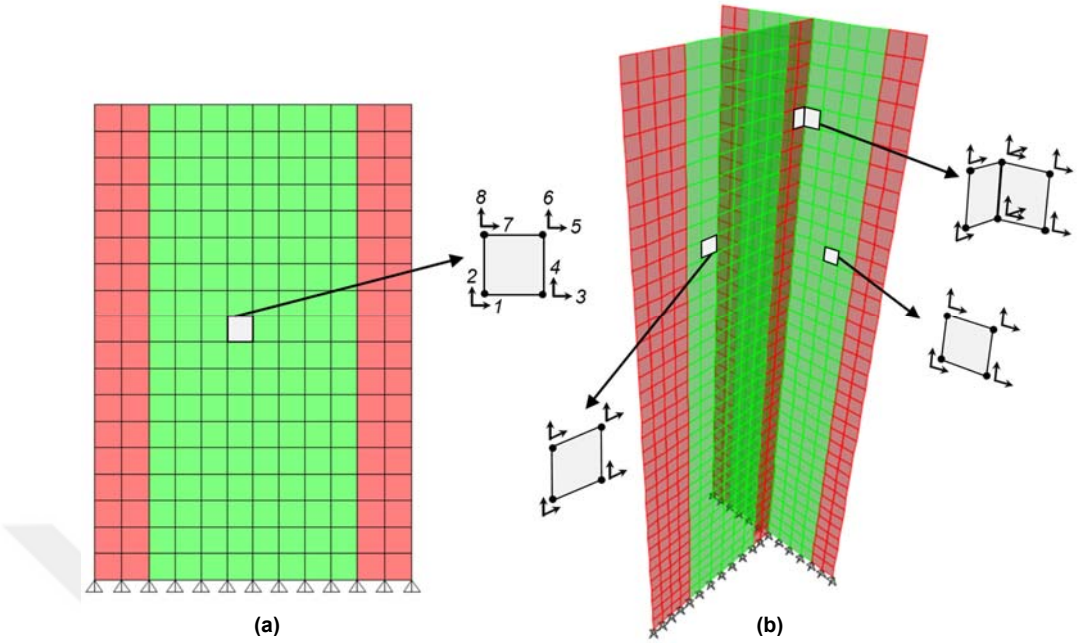

Figure 2.1. Modeling of wall specimens in FSAFE: (a) Rectangular, (b) Non-rectangular (T-shaped).

2.1.1. General Model Description

The FSAFE model of a RC wall is simply generated using a direct stiffness assembly of rectangular four-nodes with eight-degree freedoms membrane elements. The numbering of degree of freedoms (DOFs) in the formulation of the model increases in the counter-clockwise direction (Figure 2.2).

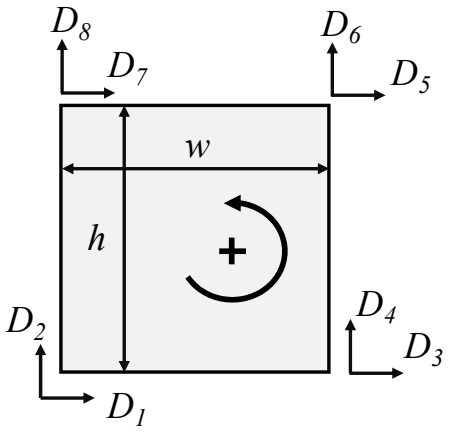

Figure 2.2. Displacement along nodal DOFs in FSAFE model.

The average strain field on each model element is first calculated using the nodal displacements $\{D\}$ along the elements degrees of freedom (Figure 2.2) with the following kinematic transformation:

$$\begin{Bmatrix} \varepsilon_x \\ \varepsilon_y \\ \gamma_{xy} \end{Bmatrix} = \begin{bmatrix} -1/2w & 0 & 1/2w & 0 & 1/2w & 0 & -1/2w & 0 \\ 0 & -1/2h & 0 & -1/2h & 0 & 1/2h & 0 & 1/2h \\ -1/2h & -1/2w & -1/2h & 1/2w & 1/2h & 1/2w & 1/2h & -1/2w \end{bmatrix} \begin{Bmatrix} D_1 \\ D_2 \\ D_3 \\ D_4 \\ D_5 \\ D_6 \\ D_7 \\ D_8 \end{Bmatrix} \quad (2.1)$$

where w and h are the width and height of model element, respectively. The average strain element, as well as the tangent stiffness (partial derivative) matrix [E] of the model element at the stress–strain level, using the constitutive behavior described by the Fixed-Strut-Angle model (FSAM).

$$\begin{Bmatrix} \varepsilon_x \\ \varepsilon_y \\ \gamma_{xy} \end{Bmatrix} \xrightarrow{\text{FSAM}} \begin{Bmatrix} \sigma_x \\ \sigma_y \\ \tau_{xy} \end{Bmatrix}, \begin{bmatrix} \frac{\partial \sigma_x}{\partial \varepsilon_x} & \frac{\partial \sigma_x}{\partial \varepsilon_y} & \frac{\partial \sigma_x}{\partial \gamma_{xy}} \\ \frac{\partial \sigma_y}{\partial \varepsilon_x} & \frac{\partial \sigma_y}{\partial \varepsilon_y} & \frac{\partial \sigma_y}{\partial \gamma_{xy}} \\ \frac{\partial \tau_{xy}}{\partial \varepsilon_x} & \frac{\partial \tau_{xy}}{\partial \varepsilon_y} & \frac{\partial \tau_{xy}}{\partial \gamma_{xy}} \end{bmatrix} \quad (2.2)$$

Components of the 8×1 internal (restoring) force vector $\{F\}$ of a single model element (Figure 2.3a) is calculated using equilibrium of forces along the nodal degrees of freedom with the average stresses in the model element (Figure 2.3b), as:

$$F_1 = -\sigma_x \frac{ht}{2} - \tau_{xy} \frac{wt}{2} \quad (2.3)$$

$$F_2 = -\sigma_y \frac{wt}{2} - \tau_{xy} \frac{ht}{2} \tag{2.4}$$

$$F_3 = \sigma_x \frac{ht}{2} - \tau_{xy} \frac{wt}{2} \tag{2.5}$$

$$F_4 = -\sigma_y \frac{wt}{2} + \tau_{xy} \frac{ht}{2} \tag{2.6}$$

$$F_5 = \sigma_x \frac{ht}{2} + \tau_{xy} \frac{wt}{2} \tag{2.7}$$

$$F_6 = \sigma_y \frac{wt}{2} + \tau_{xy} \frac{ht}{2} \tag{2.8}$$

$$F_7 = -\sigma_x \frac{ht}{2} + \tau_{xy} \frac{wt}{2} \tag{2.9}$$

$$F_8 = \sigma_y \frac{wt}{2} - \tau_{xy} \frac{ht}{2} \tag{2.10}$$

where t is the thickness of the model element (wall thickness).

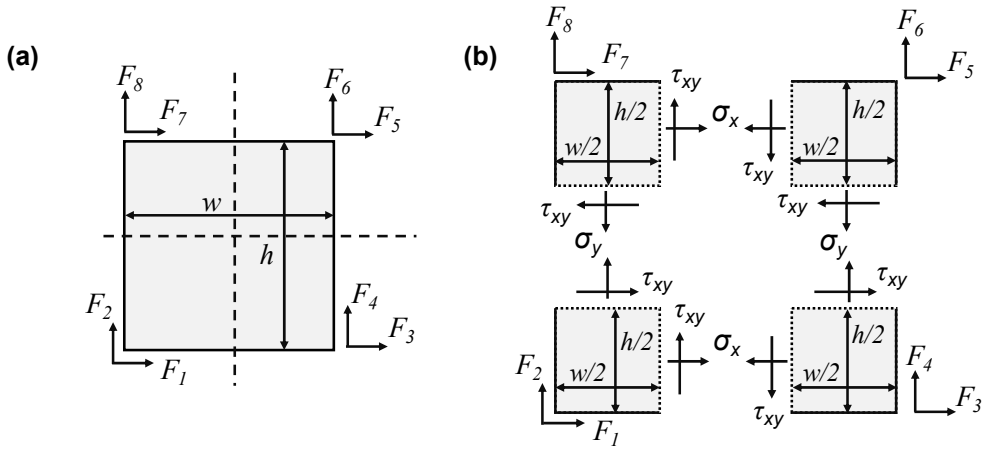

Figure 2.3. FSAFE model element: (a) Forces along nodal DOF, (b) Equilibrium of nodal forces and average internal stresses.

Terms in the 8×8 tangent stiffness matrix [*K*] of a model element can then be computed using partial derivatives of the restoring forces with respect to the displacements along the element nodal degrees of freedom, as:

$$[K]=\begin{bmatrix} K_{11} & K_{12} & \cdots & K_{18} \\ K_{21} & K_{22} & \cdots & K_{28} \\ \vdots & \vdots & \ddots & \vdots \\ K_{81} & K_{82} & \cdots & K_{88} \end{bmatrix}=\begin{bmatrix} \frac{\partial F_1}{\partial D_1} & \frac{\partial F_1}{\partial D_2} & \cdots & \frac{\partial F_1}{\partial D_8} \\ \frac{\partial F_2}{\partial D_1} & \frac{\partial F_2}{\partial D_2} & \cdots & \frac{\partial F_2}{\partial D_8} \\ \vdots & \vdots & \ddots & \vdots \\ \frac{\partial F_8}{\partial D_1} & \frac{\partial F_8}{\partial D_2} & \cdots & \frac{\partial F_8}{\partial D_8} \end{bmatrix} \tag{2.11}$$

where the chain rule can be applied in calculation of the partial derivatives. As example, the first four terms K_{11}, K_{12}, K_{21} and K_{22} in the element tangent stiffness matrix are obtained as:

$$\begin{aligned} K_{11}=\frac{\partial F_1}{\partial D_1}=\frac{\partial F_1}{\partial \sigma_x}&\left(\frac{\partial \sigma_x}{\partial \varepsilon_x}\frac{\partial \varepsilon_x}{\partial D_1}+\frac{\partial \sigma_x}{\partial \varepsilon_y}\cancelto{0}{\frac{\partial \varepsilon_y}{\partial D_1}}+\frac{\partial \sigma_x}{\partial \gamma_{xy}}\frac{\partial \gamma_{xy}}{\partial D_1}\right) \\ &+\cancelto{0}{\frac{\partial F_1}{\partial \sigma_y}}\left(\frac{\partial \sigma_y}{\partial \varepsilon_x}\frac{\partial \varepsilon_x}{\partial D_1}+\frac{\partial \sigma_y}{\partial \varepsilon_y}\cancelto{0}{\frac{\partial \varepsilon_y}{\partial D_1}}+\frac{\partial \sigma_y}{\partial \gamma_{xy}}\frac{\partial \gamma_{xy}}{\partial D_1}\right) \\ &+\frac{\partial F_1}{\partial \tau_{xy}}\left(\frac{\partial \tau_{xy}}{\partial \varepsilon_x}\frac{\partial \varepsilon_x}{\partial D_1}+\frac{\partial \tau_{xy}}{\partial \varepsilon_y}\cancelto{0}{\frac{\partial \varepsilon_y}{\partial D_1}}+\frac{\partial \tau_{xy}}{\partial \gamma_{xy}}\frac{\partial \gamma_{xy}}{\partial D_1}\right) \\ &=\frac{ht}{4w}\frac{\partial \sigma_x}{\partial \varepsilon_x}+\frac{t}{4}\frac{\partial \sigma_x}{\partial \gamma_{xy}}+\frac{t}{4}\frac{\partial \tau_{xy}}{\partial \varepsilon_x}+\frac{wt}{4h}\frac{\partial \tau_{xy}}{\partial \gamma_{xy}} \end{aligned} \tag{2.12}$$

$$
\begin{aligned}
K_{12} = \frac{\partial F_1}{\partial D_2} = \frac{\partial F_1}{\partial \sigma_x} & \left(\frac{\partial \sigma_x}{\partial \varepsilon_x} \cancelto{0}{\frac{\partial \varepsilon_x}{\partial D_2}} + \frac{\partial \sigma_x}{\partial \varepsilon_y} \frac{\partial \varepsilon_y}{\partial D_2} + \frac{\partial \sigma_x}{\partial \gamma_{xy}} \frac{\partial \gamma_{xy}}{\partial D_2} \right) \\
& + \cancelto{0}{\frac{\partial F_1}{\partial \sigma_y}} \left(\frac{\partial \sigma_y}{\partial \varepsilon_x} \cancelto{0}{\frac{\partial \varepsilon_x}{\partial D_2}} + \frac{\partial \sigma_y}{\partial \varepsilon_y} \frac{\partial \varepsilon_y}{\partial D_2} + \frac{\partial \sigma_y}{\partial \gamma_{xy}} \frac{\partial \gamma_{xy}}{\partial D_2} \right) \\
& + \frac{\partial F_1}{\partial \tau_{xy}} \left(\frac{\partial \tau_{xy}}{\partial \varepsilon_x} \cancelto{0}{\frac{\partial \varepsilon_x}{\partial D_2}} + \frac{\partial \tau_{xy}}{\partial \varepsilon_y} \frac{\partial \varepsilon_y}{\partial D_2} + \frac{\partial \tau_{xy}}{\partial \gamma_{xy}} \frac{\partial \gamma_{xy}}{\partial D_2} \right) \\
& = \frac{ht}{4w} \frac{\partial \sigma_x}{\partial \gamma_{xy}} + \frac{t}{4} \frac{\partial \sigma_x}{\partial \varepsilon_y} + \frac{t}{4} \frac{\partial \tau_{xy}}{\partial \gamma_{xy}} + \frac{wt}{4h} \frac{\partial \tau_{xy}}{\partial \varepsilon_y}
\end{aligned}
\tag{2.13}
$$

$$
\begin{aligned}
K_{21} = \frac{\partial F_2}{\partial D_1} = \cancelto{0}{\frac{\partial F_2}{\partial \sigma_x}} & \left(\frac{\partial \sigma_x}{\partial \varepsilon_x} \frac{\partial \varepsilon_x}{\partial D_1} + \frac{\partial \sigma_x}{\partial \varepsilon_y} \cancelto{0}{\frac{\partial \varepsilon_y}{\partial D_1}} + \frac{\partial \sigma_x}{\partial \gamma_{xy}} \frac{\partial \gamma_{xy}}{\partial D_1} \right) \\
& + \frac{\partial F_2}{\partial \sigma_y} \left(\frac{\partial \sigma_y}{\partial \varepsilon_x} \frac{\partial \varepsilon_x}{\partial D_1} + \frac{\partial \sigma_y}{\partial \varepsilon_y} \cancelto{0}{\frac{\partial \varepsilon_y}{\partial D_1}} + \frac{\partial \sigma_y}{\partial \gamma_{xy}} \frac{\partial \gamma_{xy}}{\partial D_1} \right) \\
& + \frac{\partial F_2}{\partial \tau_{xy}} \left(\frac{\partial \tau_{xy}}{\partial \varepsilon_x} \frac{\partial \varepsilon_x}{\partial D_1} + \frac{\partial \tau_{xy}}{\partial \varepsilon_y} \cancelto{0}{\frac{\partial \varepsilon_y}{\partial D_1}} + \frac{\partial \tau_{xy}}{\partial \gamma_{xy}} \frac{\partial \gamma_{xy}}{\partial D_1} \right) \\
& = \frac{ht}{4w} \frac{\partial \tau_{xy}}{\partial \varepsilon_x} + \frac{t}{4} \frac{\partial \sigma_y}{\partial \varepsilon_x} + \frac{t}{4} \frac{\partial \tau_{xy}}{\partial \gamma_{xy}} + \frac{wt}{4h} \frac{\partial \sigma_y}{\partial \gamma_{xy}}
\end{aligned}
\tag{2.14}
$$

$$
\begin{aligned}
K_{22} = \frac{\partial F_2}{\partial D_2} = \cancelto{0}{\frac{\partial F_2}{\partial \sigma_x}} & \left(\frac{\partial \sigma_x}{\partial \varepsilon_x} \cancelto{0}{\frac{\partial \varepsilon_x}{\partial D_2}} + \frac{\partial \sigma_x}{\partial \varepsilon_y} \frac{\partial \varepsilon_y}{\partial D_2} + \frac{\partial \sigma_x}{\partial \gamma_{xy}} \frac{\partial \gamma_{xy}}{\partial D_2} \right) \\
& + \frac{\partial F_2}{\partial \sigma_y} \left(\frac{\partial \sigma_y}{\partial \varepsilon_x} \cancelto{0}{\frac{\partial \varepsilon_x}{\partial D_2}} + \frac{\partial \sigma_y}{\partial \varepsilon_y} \frac{\partial \varepsilon_y}{\partial D_2} + \frac{\partial \sigma_y}{\partial \gamma_{xy}} \frac{\partial \gamma_{xy}}{\partial D_2} \right) \\
& + \frac{\partial F_2}{\partial \tau_{xy}} \left(\frac{\partial \tau_{xy}}{\partial \varepsilon_x} \cancelto{0}{\frac{\partial \varepsilon_x}{\partial D_2}} + \frac{\partial \tau_{xy}}{\partial \varepsilon_y} \frac{\partial \varepsilon_y}{\partial D_2} + \frac{\partial \tau_{xy}}{\partial \gamma_{xy}} \frac{\partial \gamma_{xy}}{\partial D_2} \right) \\
& = \frac{ht}{4w} \frac{\partial \tau_{xy}}{\partial \gamma_{xy}} + \frac{t}{4} \frac{\partial \sigma_y}{\partial \gamma_{xy}} + \frac{t}{4} \frac{\partial \tau_{xy}}{\partial \varepsilon_y} + \frac{wt}{4h} \frac{\partial \sigma_y}{\partial \varepsilon_y}
\end{aligned}
\tag{2.15}
$$

As illustrated in the equations above, tangent stiffness parameters K_{12} equals to K_{21}, representing the symmetry in the tangent stiffness matrix [K] of the model element at force-deformation level, considering that tangent stiffness (partial derivative) matrix [E] of the model element at the stress–strain level is also symmetric. Finally, the 8×1 restoring force vectors and the 8×8 tangent stiffness matrices of the model elements are assembled, using a standard direct stiffness assembly, for obtaining the global restoring force vector and the global tangent stiffness matrix of the FSAFE model generated for a wall.

The formulation described above becomes equivalent to a standard finite element model formulation, in which linear strain interpolation functions and only a single Gauss integration point (located at the element centroid) are used for each model element.

2.1.2. Description of Rigid Body Constraint and Support Conditions

In the FSAFE model formulation, rigid body constraints are defined at the top of the walls for simulating test conditions of the wall specimens used for validation of the model. In all experimental programs employed for validation of the model, a RC or steel load transfer beam at the top of the walls, for transferring the horizontal loads and the axial loads (whenever present), was used. To incorporate the influence of these load transfer beams, rigid body constraints are defined at the top of the walls in the FSAFE model formulation. Implementation of body constraints in the model formulation is achieved by defining a displacement transformation matrix [T]. DOFs of each panel element at the top of the walls are enforced to undergo equal horizontal displacements in horizontal direction and coupled vertical displacements in the vertical direction with the implementation of transformation matrix. Additionally, the body constraint relates the top vertical displacements to a global rotational DOF since vertical DOFs at the top of the walls are eccentrically located from the geometric center of the walls.

Translation of an illustrative wall model with four model elements (Figure 2.4a) into a wall model having a body constraint at the top (Figure 2.4b) is presented herein, as an explanation of the implementation of the rigid body constraint in the FSAFE model formulation. First, the displacement transformation matrix [T] of the wall model is defined for transformation of the 15×1 displacement vector to the 18×1 displacement vector

(Equation 2.16). Derivation of the 15×15 stiffness matrix and 15×1 restoring force vector, following the assignment of the top rigid body constraint, is obtained by multiplying both sides of Equation 2.17 with the transpose of the displacement transformation matrix. Finally, the tangent stiffness matrix, restoring force vector, and displacement vector with the assigned rigid body constraint at the top are calculated as shown in Equation 2.20.

$$[T]_{18x15} = \begin{bmatrix} 1 & 0 & 0 & 0 & 0 & 0 & 0 & 0 & 0 & 0 & 0 & 0 & 0 & 0 & 0 \\ 0 & 1 & 0 & 0 & 0 & 0 & 0 & 0 & 0 & 0 & 0 & 0 & 0 & 0 & 0 \\ 0 & 0 & 1 & 0 & 0 & 0 & 0 & 0 & 0 & 0 & 0 & 0 & 0 & 0 & 0 \\ 0 & 0 & 0 & 1 & 0 & 0 & 0 & 0 & 0 & 0 & 0 & 0 & 0 & 0 & 0 \\ 0 & 0 & 0 & 0 & 1 & 0 & 0 & 0 & 0 & 0 & 0 & 0 & 0 & 0 & 0 \\ 0 & 0 & 0 & 0 & 0 & 1 & 0 & 0 & 0 & 0 & 0 & 0 & 0 & 0 & 0 \\ 0 & 0 & 0 & 0 & 0 & 0 & 1 & 0 & 0 & 0 & 0 & 0 & 0 & 0 & 0 \\ 0 & 0 & 0 & 0 & 0 & 0 & 0 & 1 & 0 & 0 & 0 & 0 & 0 & 0 & 0 \\ 0 & 0 & 0 & 0 & 0 & 0 & 0 & 0 & 1 & 0 & 0 & 0 & 0 & 0 & 0 \\ 0 & 0 & 0 & 0 & 0 & 0 & 0 & 0 & 0 & 1 & 0 & 0 & 0 & 0 & 0 \\ 0 & 0 & 0 & 0 & 0 & 0 & 0 & 0 & 0 & 0 & 1 & 0 & 0 & 0 & 0 \\ 0 & 0 & 0 & 0 & 0 & 0 & 0 & 0 & 0 & 0 & 0 & 1 & 0 & 0 & 0 \\ 0 & 0 & 0 & 0 & 0 & 0 & 0 & 0 & 0 & 0 & 0 & 0 & 1 & 0 & 0 \\ 0 & 0 & 0 & 0 & 0 & 0 & 0 & 0 & 0 & 0 & 0 & 0 & 0 & 1 & -b \\ 0 & 0 & 0 & 0 & 0 & 0 & 0 & 0 & 0 & 0 & 0 & 0 & 1 & 0 & 0 \\ 0 & 0 & 0 & 0 & 0 & 0 & 0 & 0 & 0 & 0 & 0 & 0 & 0 & 1 & 0 \\ 0 & 0 & 0 & 0 & 0 & 0 & 0 & 0 & 0 & 0 & 0 & 0 & 1 & 0 & 0 \\ 0 & 0 & 0 & 0 & 0 & 0 & 0 & 0 & 0 & 0 & 0 & 0 & 0 & 1 & b \end{bmatrix} \tag{2.16}$$

$$[K]_{18x18} \times \{D\}_{18x1} = \{F\}_{18x1} \tag{2.17}$$

$$[K]_{18x18} \times [T]_{18x15} \times \{D\}_{15x1} = \{F\}_{18x1} \tag{2.18}$$

$$\boxed{[T]^T_{18x15} \times [K]_{18x18} \times [T]_{18x15}} \times \{D\}_{15x1} = \boxed{[T]^T_{18x15} \times \{F\}_{18x1}} \tag{2.19}$$

$$[K]_{15x15} \times \{D\}_{15x1} = \{F\}_{15x1} \tag{2.20}$$

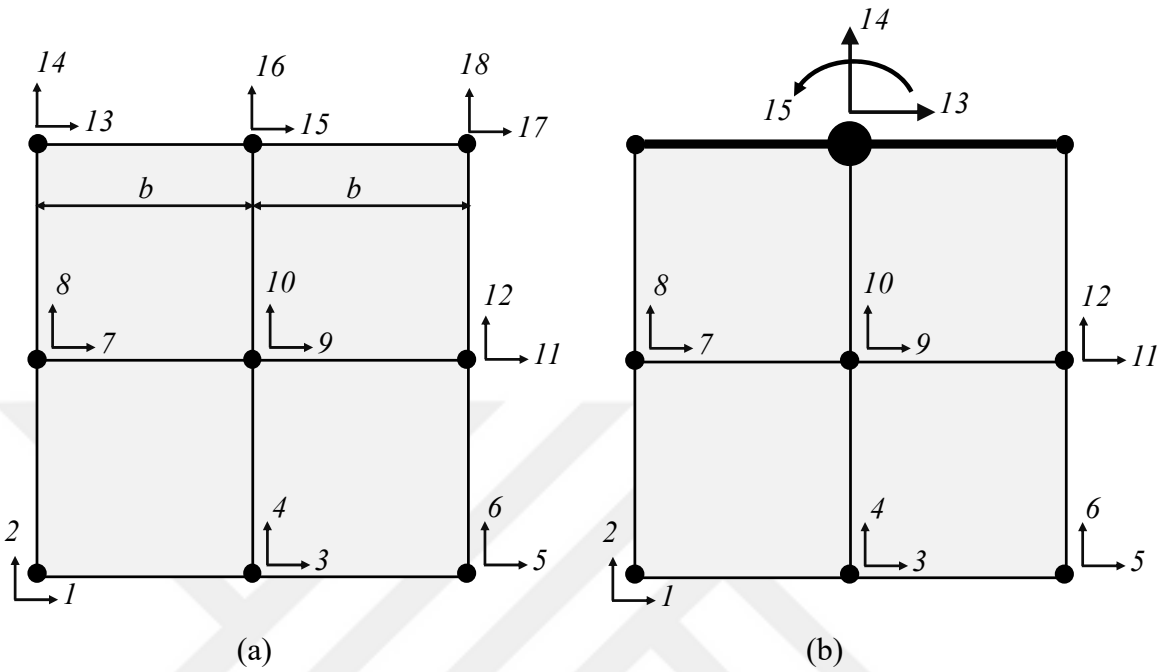

Figure 2.4. (a) Without body constraint, (b) With body constraint.

It must be stated that the wall model using four elements is only a simple illustration for the implementation of top body constraint. Using more elements for accurately simulating the response of RC wall specimens is inherently necessary, as discussed in the following chapter through sensitivity analysis with various mesh discretizations.

Furthermore, wall specimens investigated in the present study incorporate a RC pedestal at the bottom for connection of the walls to the strong floor, providing fixed support at the bottom of the walls. For simulation of the zero displacements along the bottom pedestal of the walls, the DOFs at the bottom (e.g., the DOFs from 1 to 6 in Figure 2.4) are enforced to have zero displacement in the FSAFE model formulation. Solving the equilibrium equations is accomplished via partitioning of the equations. Support reactions are then calculated using the known (zero) displacements and the unknown (which are calculated with the known nodal forces) displacements of the wall formulation in the FSAFE model.

The model formulation is implemented in MatLab (2012) together with a displacement-controlled nonlinear analysis solution strategy (Clarke and Hancock 1990), which allows direct comparison of model response predictions with test results available in literature on RC wall specimens subjected to drift-controlled loading protocols. The employed solution strategy incorporates the load incrementation and equilibrium stages. At the former stage (denoted by "*i*"), incrementation of the applied target displacement is performed on the model, whereas at the later stage (denoted by "*j*"), model displacements are iterated for balancing the difference between the external and internal forces within an acceptable error margin. Figure 2.5 and Figure 2.6 present the employed nonlinear solution strategy, details of which are available in the study by Gullu (2013).

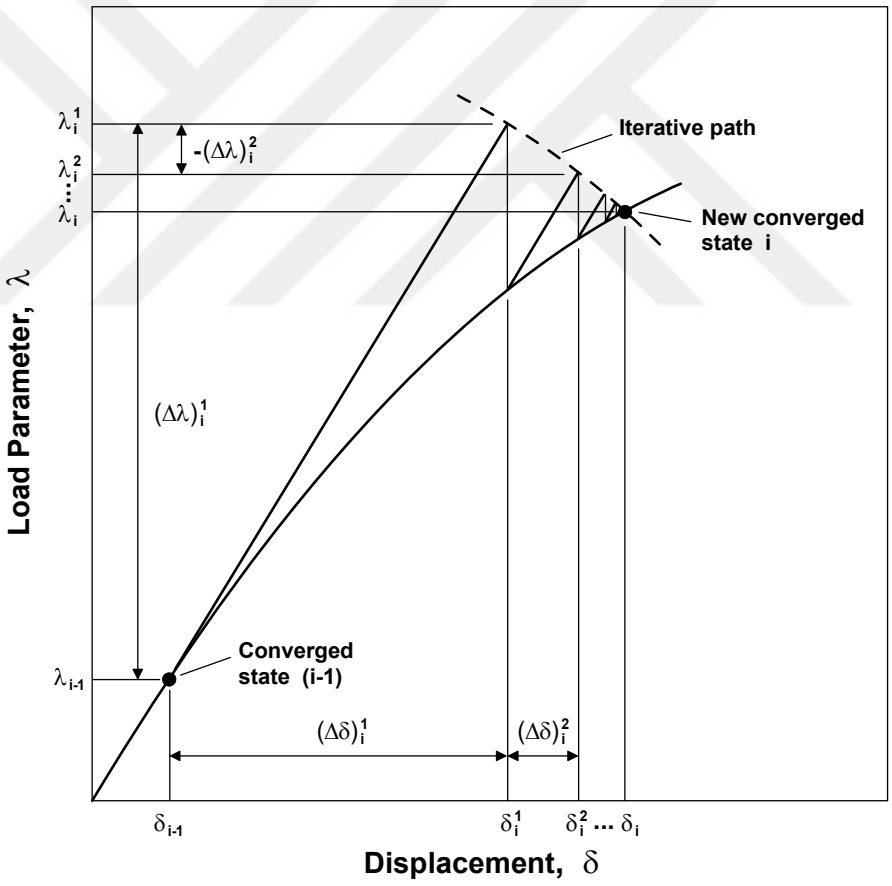

Figure 2.5. Illustration of the implemented solution strategy for a single DOF system (Clarke and Hancock, 1990).

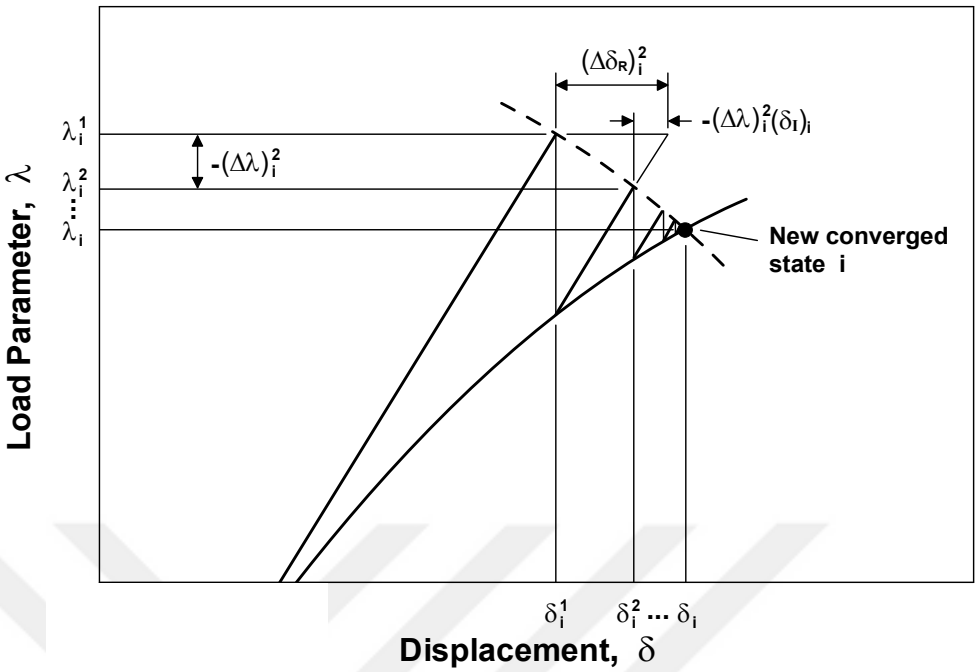

Figure 2.6. Iterative strategy and residual displacements (Clarke and Hancock, 1990).

2.2. The Constitutive Fixed Strut Angle Model (FSAM) for RC Panels

The Fixed-Strut-Angle Model (FSAM) (Orakcal *et al.*, 2012) is adopted and improved in this study, for representing the constitutive smeared stress vs. average strain behavior of the RC membrane elements in the FSAFE model assembly. In the formulation of the FSAM, normal stresses in cracked concrete are calculated along fixed crack (strut) directions. Shear stresses developing along crack surfaces, which are calculated using a simple friction-based constitutive relationship, are superimposed with the concrete stresses along the struts, for obtaining the total stress field in concrete. The behavior of reinforcing steel is described using a uniaxial stress-strain relationship applied along the orthogonal rebar directions. As well, in this study, a simple constitutive relationship that considers a smeared stress approach is implemented in the formulation of the FSAM to represent the dowel effects (shear stress) on both horizontal and vertical reinforcing bars. Superposition of stresses developing in concrete (normal stresses along strut directions and shear stresses along crack surfaces) with smeared stresses in reinforcing steel (uniaxial and dowel stresses developing in reinforcing bars) gives the resultant average stresses on the panel element (Figure 2.7).

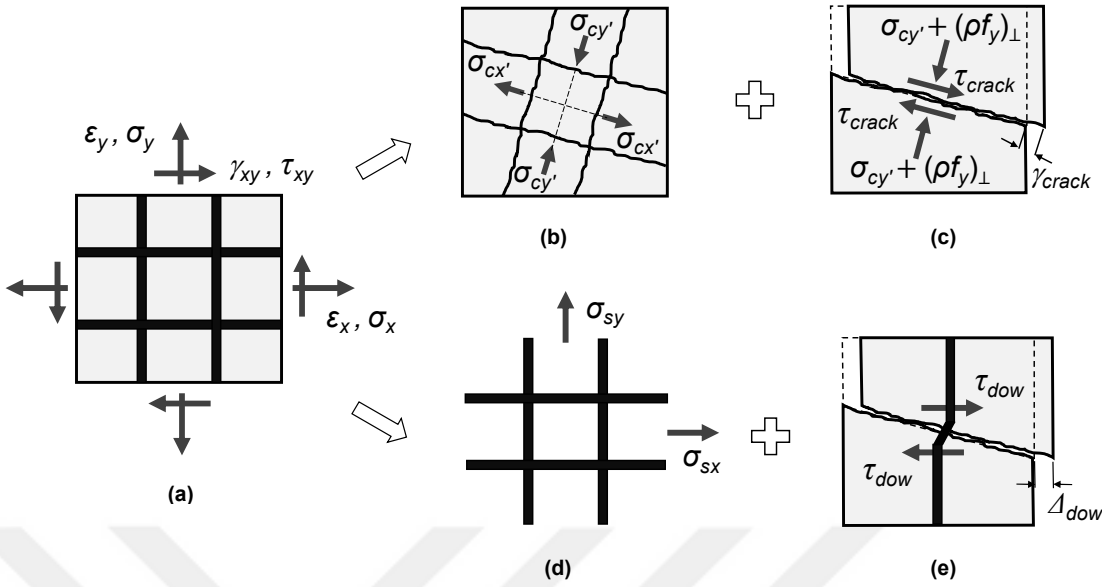

Figure 2.7. Constitutive Fixed-Strut-Angle Model (FSAM): (a) strain field on panel element, (b) concrete stresses along fixed struts, (c) shear aggregate interlock stresses along cracks, (d) uniaxial stresses in reinforcement, (e) dowel stresses in reinforcement.

Before cracking, the stress vs. strain behavior of concrete in the FSAM is simulated using a rotating-principal-stress-direction approach (e.g., Vecchio and Collins, 1986; Pang and Hsu, 1995). The strain field applied on concrete is transformed into principal strain directions and a uniaxial stress–strain relationship for concrete is applied along the principal strain directions, for obtaining the principal stresses in concrete (Figure 2.8). The principal strain directions imposed on the panel element are therefore assumed to coincide the with principal stress directions in concrete. A monotonic stress–strain relationship is adopted for concrete in the uncracked state, since the monotonic and hysteretic stress–strain behavior of concrete in a panel element subjected hysteretic loading can be assumed to not differ significantly prior to first cracking.

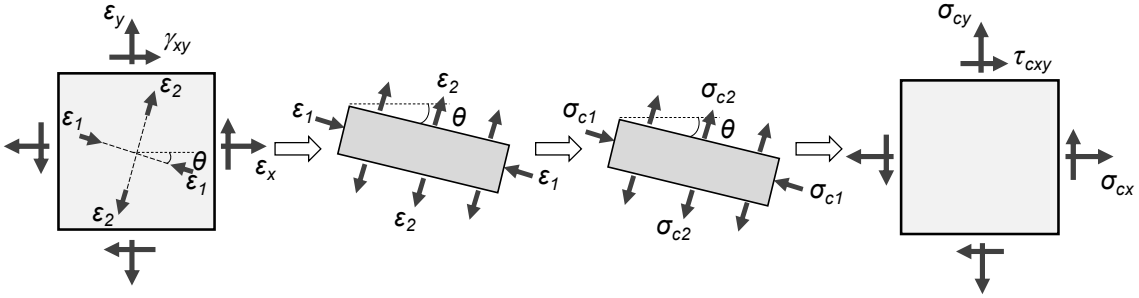

Figure 2.8. Behavior of uncracked concrete in FSAM.

At the instant when the principal tensile strain in concrete first exceeds the concrete cracking strain (ε_t in Figure 2.11), the first crack develops, and the principal strain direction corresponding to first cracking is assigned as the first "fixed strut" (first crack) direction in the panel (θ_{crA} in Figure 2.9). After the first crack forms, while principal strain directions continue to rotate based on the applied strain field, the directions of the principal stresses in concrete are assumed to be fixed, as parallel and perpendicular to the first fixed strut direction. This implies that the first crack (or strut) direction coincides with the principal stress directions in concrete, under the condition that zero shear stress develops along the crack. The analysis continues following a single fixed-strut mechanism until the second crack forms, at which stage the second strut is activated in the panel model.

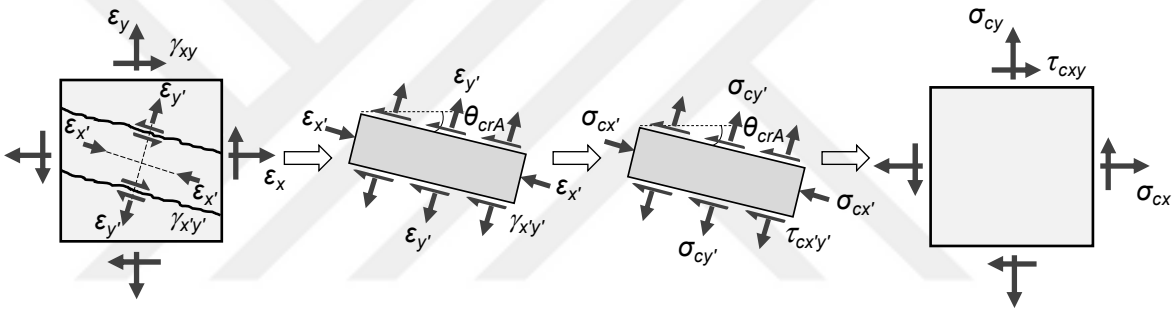

Figure 2.9. Behavior of concrete after formation of first crack in FSAM.

When the normal strain along the first strut first exceeds the concrete cracking strain upon unloading from the compression envelope ($\varepsilon_{c0}+\varepsilon_t$ in Figure 2.11), the second crack develops. Not considering the shear (aggregate interlock) stress developing on the crack surface allows the simplification that the second crack will form in perpendicular direction to the first crack, according to a principal-stress-based cracking criterion. Although various other cracking criteria may be used for definition of the second crack direction, this approach was selected for its simplicity. At the instant of the second crack formation, the second "fixed strut" will develop in parallel direction to the second crack (in perpendicular direction to the first strut). During further loading, the concrete stress field comprises two independent struts, working under interchanging compression and tension (Figure 2.10), based on the applied strain field. While the principal direction of the applied strain field continues to rotate during subsequent loading, the principal stress directions in concrete are

assumed to be fixed along the two strut directions, again when the shear stresses are developing along the two crack surfaces are ignored. Since both strut directions are fixed, the hysteretic stress–strain relationship adopted for concrete can be applied along the first and second strut directions (θ_{crA} and θ_{crB} in Figure 2.10). It must be mentioned that although the concrete stress–strain relationship to be used in the FSAM formulation is fundamentally uniaxial in nature, it should also incorporate parameters to consider biaxial softening effects under plane stress loading.

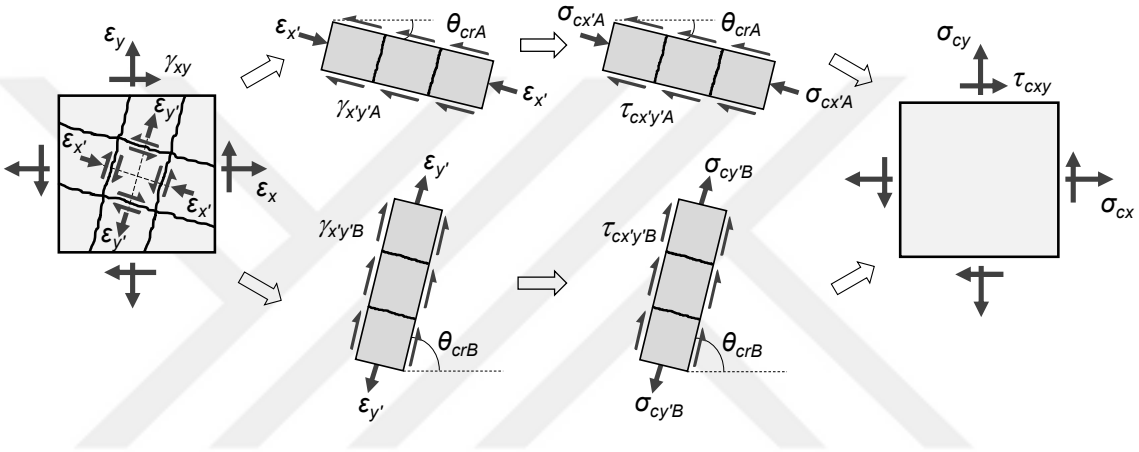

Figure 2.10. Behavior of concrete after formation of second crack in FSAM.

2.3. Material Constitutive Models

2.3.1. Concrete

The state-of-the-art hysteretic uniaxial constitutive model by Chang and Mander (1994) was implemented in the original formulation of the FSAM (Orakcal *et al.*, 2012) for representing the uniaxial stress vs. strain behavior of concrete (Figure 2.11). The model formulation reflects important behavioral characteristics of concrete such as the hysteretic transition from compression to tension and vice versa, the progressive degradation of stiffness of the unloading and reloading curves for increasing values of strain, gradual crack closure, and tension stiffening (post-crack tensile behavior).

The monotonic envelope parameters and the key hysteretic parameters for the compression response of concrete employed in the model formulation is summarized

herein. Monotonic envelope of concrete stress–strain relationship in tension is defined in accordance with the study by Belarbi and Hsu (1994). The parameters that represents the behavioral characteristics of concrete in tension is summarized in Section 2.3.4. Chang and Mander (1994) have introduced empirical relationships for the slope of the stress strain behavior at the origin (E_c), the strain at peak stress (ε'_c), and the shape of the pre-peak branches (r) (defined by Tsai, 1988) of the stress–strain behavior related to the unconfined concrete peak stress f'_c (MPa).

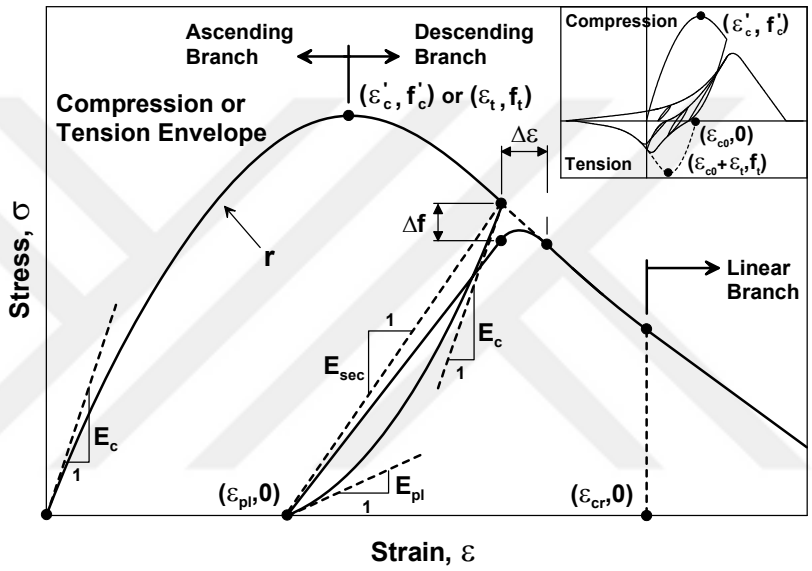

Figure 2.11. Constitutive model for concrete (Chand and Mander, 1994).

The empirical relationships for the monotonic envelope of the unconfined concrete model is presented in Equations 2.21 to 2.23.

$$E_c = 8200 f'^{(3/8)}_c \tag{2.21}$$

$$\varepsilon'_c = \frac{f'^{(1/4)}_c}{28} \tag{2.22}$$

$$r = \frac{f'_c}{5.2} - 1.9 \tag{2.23}$$

In order to represent the cyclic characteristics of the stress–strain behavior, the model employs empirical equations for key hysteretic parameters such as those for secant stiffness (E^{-}_{sec}) and plastic stiffness (E^{-}_{pl}) upon unloading from the envelope, and stress and strain offsets (Δf^{-} and $\Delta\varepsilon^{-}$) upon return to the compression envelope (Figure 2.12). The hysteretic parameters are calculated by the following equations:

$$E^{-}_{\text{sec}} = E_c \left(\frac{\left| \frac{f^{-}_{un}}{E_c \varepsilon'_c} \right| + 0.57}{\left| \frac{\varepsilon^{-}_{un}}{\varepsilon'_c} \right| + 0.57} \right) \tag{2.24}$$

$$E^{-}_{pl} = 0.1 E_c \, exp\left(-2 \left| \frac{\varepsilon^{-}_{un}}{\varepsilon'_c} \right| \right) \tag{2.25}$$

$$\Delta f^{-} = 0.09 f^{-}_{un} \sqrt{\left| \frac{\varepsilon^{-}_{un}}{\varepsilon'_c} \right|} \tag{2.26}$$

$$\Delta\varepsilon^{-} = \frac{\varepsilon^{-}_{un}}{1.15 + 2.75 \left| \frac{\varepsilon^{-}_{un}}{\varepsilon'_c} \right|} \tag{2.27}$$

where ε'_c is the strain at peak compressive stress, E_c is the slope of the stress–strain behavior at the origin, and f^{-}_{un} and ε^{-}_{un} are the unloading stress and strain parameters, respectively.

In the Chang and Mander (1994) model, the envelope curves for compression and tension can be defined using test results or empirical relationships, for the slope of the stress–strain behavior at the origin and the shape of both the pre-peak and post-peak

branches of the stress–strain behavior, while keeping the values of the peak stress and the strain at peak stress constant. The model formulation was implemented in the FSAM also with modifications to reflect the behavioral characteristics of concrete associated with biaxial softening behavior under plane stress loading conditions, as well as smeared post-crack behavior in tension, by incorporating compression softening (Model B by Vechio and Collins, 1993), hysteretic biaxial damage (Mansour *et al.*, 2002), and tension stiffening (Belarbi and Hsu, 1994) relationships into its formulation. The modification parameters are explained in the following sections.

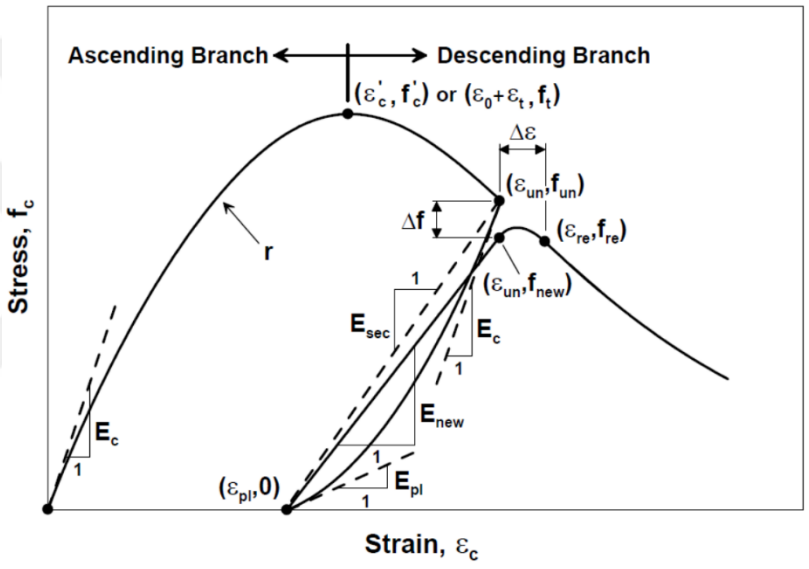

Figure 2.12. Hysteretic parameters of the model by Chand and Mander (1994).

2.3.2. Reinforcing Steel

The uniaxial stress–strain relationship implemented in the FSAM for reinforcing steel bars is the widely-used hysteretic model by Menegotto and Pinto (1973), extended by Filippou *et al.* (1983) for representing isotropic strain hardening behavior, and further extended by Kolozvari *et al.* (2018b) to remedy stress overshooting upon strain reversals with small magnitude. This model, despite its relatively simple formulation, has been shown to accurately represent test results on individual rebar specimens. In the Menegotto and Pinto (1973) model, the hysteretic stress–strain relationship follows curved transitions, each from a straight-line asymptote with slope E_0 (modulus of elasticity) to another

straight-line asymptote with slope $E_1=bE_0$ (yield modulus), where the parameter b is the strain hardening ratio (Figure 2.13).

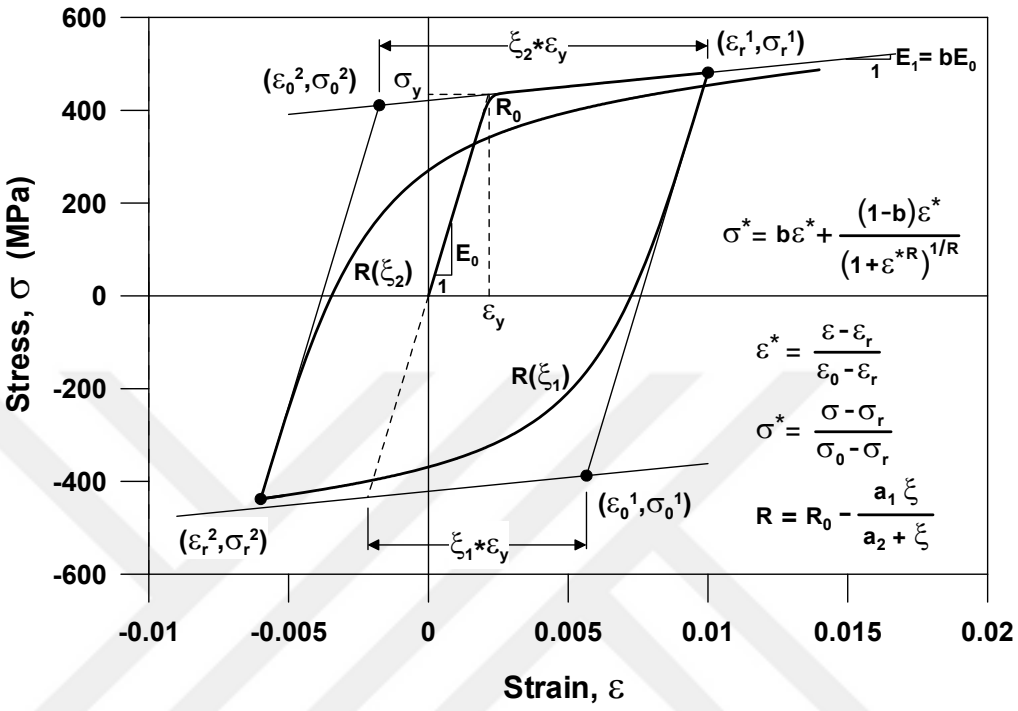

Figure 2.13. Constitutive model for reinforcing steel (Menegotto and Pinto, 1973).

The uniaxial stress–strain (σ–ε) relationship in Menegotto and Pinto (1973) is defined by the following expression:

$$\sigma^* = b\varepsilon^* + \frac{(1-b)\varepsilon^*}{\left(1+\varepsilon^{*R}\right)^{1/R}} \tag{2.28}$$

where

$$\varepsilon^* = \frac{\varepsilon - \varepsilon_r}{\varepsilon_0 - \varepsilon_r} \tag{2.29}$$

$$\sigma^* = \frac{\sigma - \sigma_r}{\sigma_0 - \sigma_r} \tag{2.30}$$

and where the parameters σ_r and ε_r are the stress and strain at the point of reversals, while the parameters σ_0 and ε_0 are the stress and strain at the point of intersection of the two asymptotes. The curvature of the transition curve between the two asymptotes is governed by a cyclic curvature parameter (R), which depends on the strain history and represents the so-called Bauschinger's effect (Figure 2.14). The cyclic curvature parameter is defined by the following equation:

$$R = R_0 - \frac{a_1 \xi}{a_2 + \xi} \tag{2.31}$$

in which, R_0 is the parameter defined for monotonic loading, a_1 and a_2 are assigned in accordance with the experimental results for simulation of the degradation in the curvature under following loading cycles, and ξ is a parameter that describes the absolute strain differences between the current asymptote intersection point and the previous maximum or minimum strain reversal point.

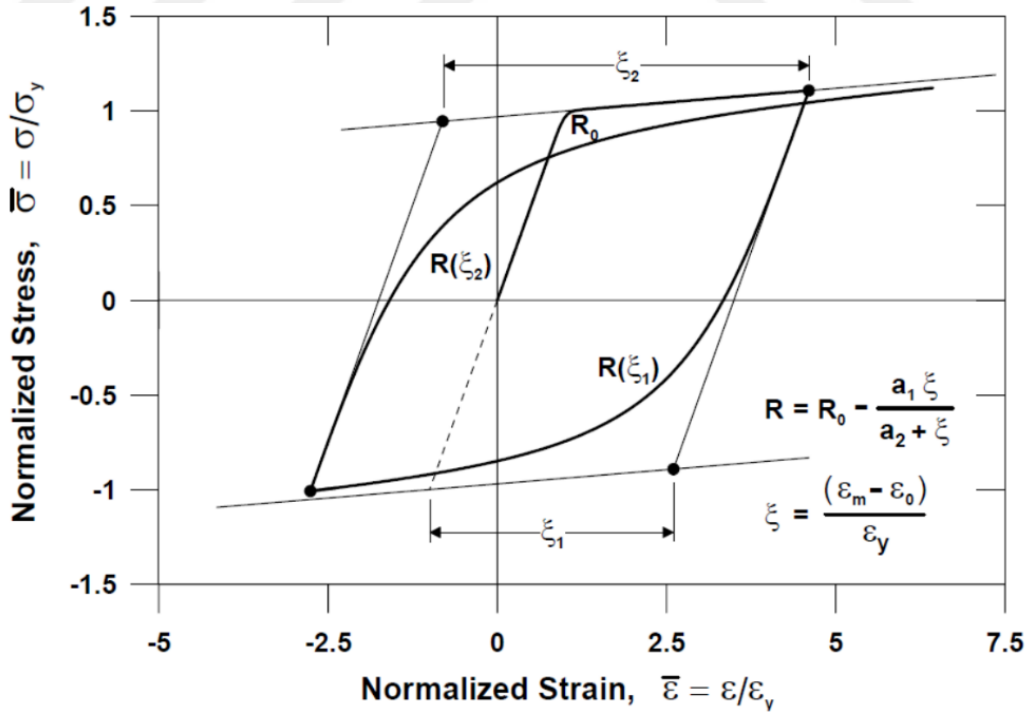

Figure 2.14. Degradation of cyclic curvature (Menegotto and Pinto, 1973).

During the implementation of the Menegotto and Pinto (1973) model in the FSAM, the tensile yield strength and strain-hardening parameters of the model were defined also considering the empirical relationships proposed by Belarbi and Hsu (1994), to include the effect of tension stiffening on the smeared stress–strain behavior of reinforcing bars embedded in concrete. However, the present model formulation does not yet incorporate rebar buckling, low-cycle fatigue, or fracture behavior.

2.3.3. Compression Softening in Concrete

An important consideration in modeling the behavior of a RC panel element under membrane actions is incorporating the compression softening effect. The softening effect for the behavior of concrete under biaxial stress state has been experimentally observed by many researchers, (e.g., Vecchio and Collins, 1986), and has been represented by analytical models mainly in the form of reduction (softening) in the compressive stresses in concrete along the principal compression direction of RC panels, due to presence of tensile strains in the perpendicular principal direction.

In this study, the so-called “Model B” by Vecchio and Collins (1993), which considers only a reduction in peak compressive stress (Figure 2.15), was used, since Vecchio and Collins (1993) observed that more complicated models (including also reduction in the strain at peak stress) are only marginally better for incorporating the compression softening effect, and also due to the simplicity of Model B for implementation into a cyclic panel model. In this approach, only compressive stress along the principal compression direction is reduced by the β_m coefficient, providing a simpler model implementation. The softening coefficient β_m is defined in this case as:

$$\beta_m = \frac{1}{1 + 0.27 \cdot \left(\frac{\varepsilon_t}{\varepsilon'_c} - 0.37 \right)} \tag{2.32}$$

where ε_t is the tensile strain in the principal tensile stress direction and ε'_c is the strain corresponding to peak stress of concrete in compression.

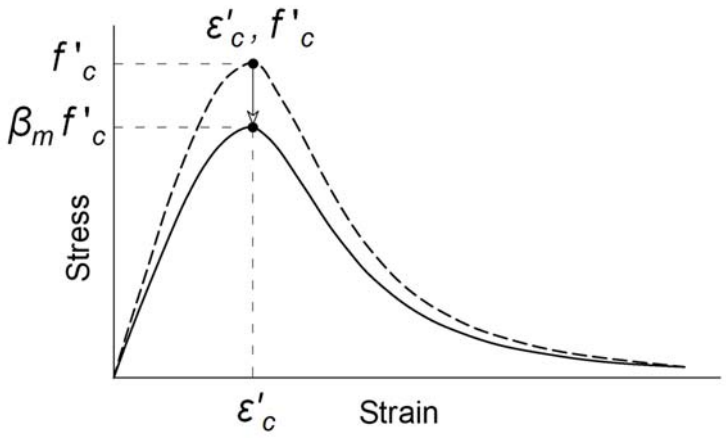

Figure 2.15. Compression softening effect with Model B (Ulugtekin, 2010).

2.3.4. Tension Stiffening Effect on Concrete and Steel

The contribution of cracked concrete to the tensile resistance of RC members is known as the effect of tension stiffening. The concrete between the cracks, which is still bonded to the reinforcing steel bars, contributes to the tensile resistance of the member. The tension stiffening phenomenon plays a significant role in reducing the post-cracking deformations of reinforced concrete structures, and has been proven by researchers (e.g., Pang and Hsu, 1995) to influence considerably the post-cracking stiffness, yield capacity and shear behavior of reinforced concrete members.

In formulation of the FSAM, the tension stiffening model by Belarbi and Hsu (1994) is incorporated. As investigated in detail by Belarbi and Hsu (1994), modeling of the tension stiffening phenomenon must consider two effects simultaneously. First, an average (smeared) tensile stress-strain curve must be considered for cracked concrete; and second, the stress-strain curve of bare mild steel bars must be replaced by an average (smeared) stress-strain curve for steel bars stiffened by concrete between cracks. In the Belarbi and Hsu (1994) model, the tensile stress-strain (σ_c, ε_c) behavior of concrete is considered as linear up to cracking (f_{cr}, ε_{cr}) and, a descending curve is defined for the post-cracked stress-strain region with the following equation:

$$\sigma_c = f_{cr}\left(\varepsilon_{cr}/\varepsilon_c\right)^{0.4} \tag{2.33}$$

where f_{cr} is the tensile strength of concrete and ε_{cr} is the peak strain at tensile strength of concrete (Figure 2.16).

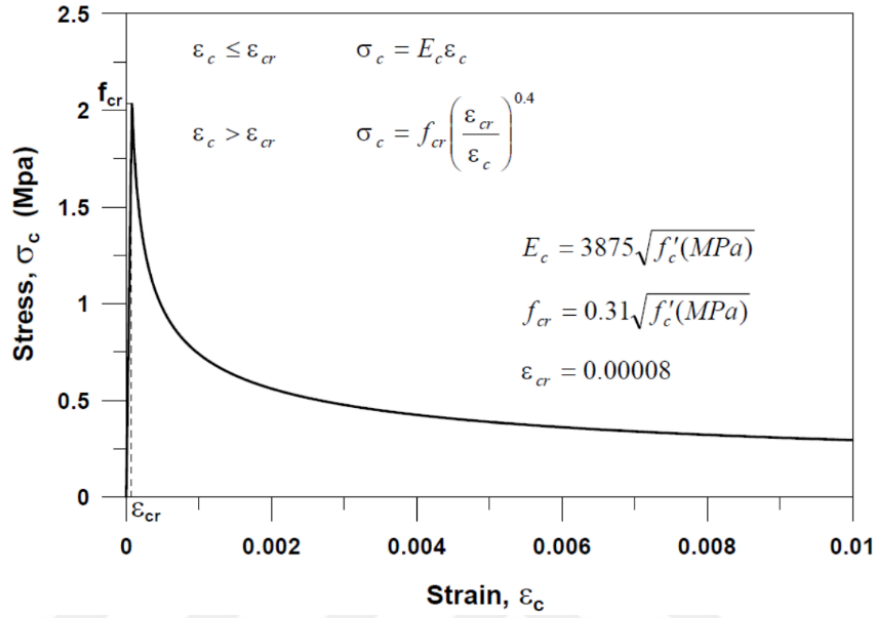

Figure 2.16. Average stress–strain relationship by Belarbi and Hsu (1994) for concrete in tension.

Belarbi and Hsu (1994) also identified how the average stress-strain relationship of reinforcing steel bars surrounded by concrete is different than the stress-strain relationship of bare steel bars (Figure 2.17). The most important difference was found to be the lowering of the yield stress, as yielding of a reinforced concrete element occurs when the steel stress at the cracked section reaches the yield strength of the bare bar. At the same time, the average steel stress smeared along the length of the element reaches a level lower than that of the yield stress of the bare bar. Based on experimental data from the RC panels, the effective (reduced) yield stress (f_{yeff}) for embedded reinforcing bars is expressed, in terms of the elastic modulus ratio n (E_s/E_c), the reinforcement ratio ρ, concrete cracking stress f_{cr}, and bare bar yield stress σ_y, as:

$$f_{yeff} = f_y \cdot \left[1 - 1.314 \cdot \frac{n^{0.434}}{\rho^{1.084}} \cdot \left(\frac{f_{cr}}{f_y}\right)^{1.517}\right] \tag{2.34}$$

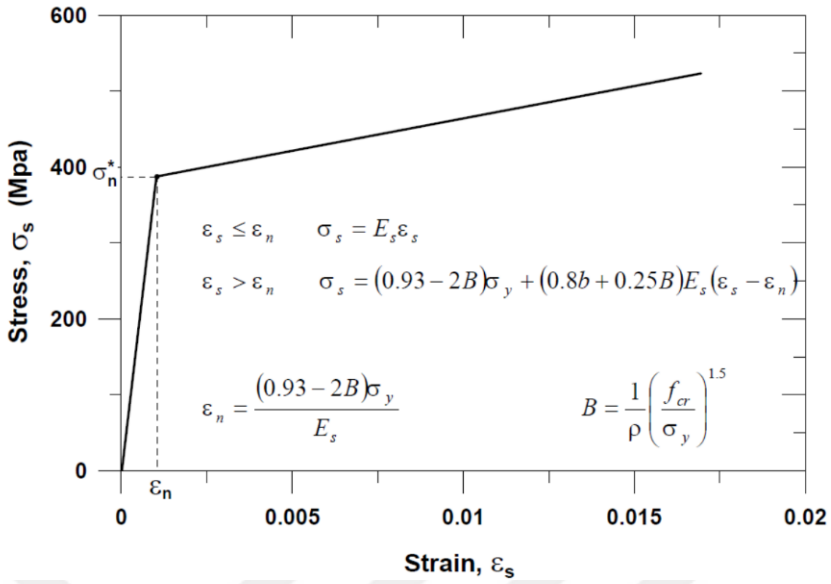

Figure 2.17. Average stress–strain relationship by Belarbi and Hsu (1994) for reinforcing bars embedded in concrete.

2.3.5. Biaxial Damage on Concrete

An important consideration in modeling the behavior of a RC panel element under membrane actions is incorporating the cyclic damage effects on concrete subjected to biaxial loading. This cyclic damage on concrete is represented via a damage coefficient. Unlike compression softening and tension stiffening parameters, the damage coefficient is a cyclic-strain-history-dependent parameter, and is not considered in analysis of concrete under monotonic loading.

The damage coefficient is a parameter that considers the effect of the history of compressive strains, which are in perpendicular direction to a specific compressive stress direction considered (e.g., along a compression strut) for concrete. The damage coefficient is therefore defined for biaxial loading, and does not apply for uniaxial concrete stress-strain behavior. The damage coefficient, similar to the compression softening coefficient, is applied as a multiplier to the concrete compressive stress, softening the stress-strain behavior of concrete in compression. In formulation of the FSAM, for simulation of the damage coefficient model by Mansour *et al*. (2002) was implemented. The biaxial damage formulation proposed by Mansour *et al*. (2002) uses the ratio of the maximum value of the

compressive strain experienced in the direction perpendicular to the compressive (strut) direction considered, to the peak compressive stress, (ε'_c) in concrete, as:

$$\beta_{damage} = \left(1 - 0.4\varepsilon_{\perp max} / \varepsilon'_c\right) \tag{2.35}$$

The final softening parameter used in this study considering both compression softening and biaxial damage parameters takes the form of $\beta = \beta_m \cdot \beta_{damage}$.

2.4. Shear Aggregate Interlock on Crack Surfaces

As described in Section 2.2, the baseline formulation of the FSAM considers that when shear stresses transferred across cracks are neglected (i.e., when the crack surfaces are assumed frictionless), the concrete principal stress directions and crack directions coincide. However, the FSAM formulation also allows implementing a constitutive (shear stress vs. shear strain) relationship for representing shear stress transfer across cracks. In RC members, sliding along cracks is known to develop shear aggregate interlock action, resulting in shear stresses developing along crack surfaces.

Therefore, on top of the baseline formulation of the FSAM, a simple friction-based constitutive relationship for shear aggregate interlock is implemented in this study, which relates the maximum shear stress developing along a crack surface to the compressive stress in concrete in perpendicular direction to the crack $\sigma_{c\perp}$, as well as the smeared "clamping stress" created by the perpendicular component of the yield strength of the reinforcement spanning the crack $(\rho f_y)_\perp$, using a friction coefficient (η) (Figure 2.18). In this model, the shear stress capacity along a crack is bounded by the product of the friction coefficient (η) and the normal stress perpendicular to the crack ($\sigma_\perp$). The normal stress perpendicular to the crack is taken as the sum of the compressive stress in concrete (which changes during loading) and the clamping stress capacity of the reinforcement (which is assumed constant), similarly to the shear friction capacity approach used in ACI 318-14. The contribution of concrete is reduced to zero when the normal stress in concrete perpendicular to the crack is tensile (due to tension stiffening) or zero; that is, when the crack is open. In order to describe the hysteretic characteristics of this friction-based

constitutive relationship, peak-oriented hysteresis rules are implemented in the present model formulation, where the unloading from the shear (friction) stress vs. shear (sliding) strain envelope follows the initial elastic stiffness (which can be taken as a large value; a value of $0.4E_c$ representing the elastic shear modulus of concrete was adopted), zero stress is maintained until the origin, and reloading to the envelope in the opposite direction is oriented towards the previous peak (Figure 2.18).

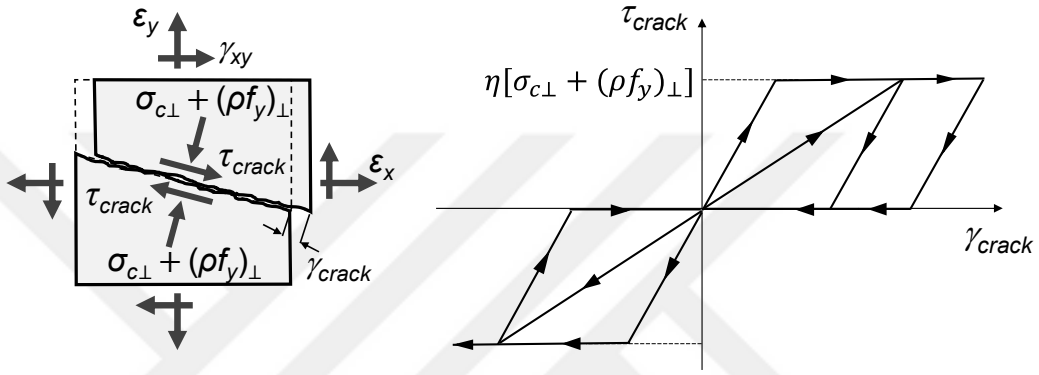

Figure 2.18. Shear aggregate interlock mechanism along crack surfaces.

It must be mentioned that in the original formulation of the FSAM (Orakcal *et al.*, 2012), which was validated against test results on isolated panel specimens subjected to uniformly distributed strain and stress states, the friction-based constitutive relationship used to represent shear aggregate interlock behavior along cracks followed elasto-plastic hysteresis rules (similarly to the stress–strain behavior of reinforcing steel with no strain hardening), and the contribution of the clamping effect of reinforcing steel bars on the interlock shear stress capacity was not considered, as suggested by Tassios and Vintzeleou (1987) for interfaces (cracks) with smooth surfaces. For finite element modeling of structural walls using the FSAFE model, the contribution of clamping on the interlock shear stress capacity is considered in this study, as also recommended by Tassios and Vintzeleou (1987) for modeling of shear aggregate interlock across rough crack surfaces. As well, the peak-oriented hysteresis rules described above are adopted as a simplification of more detailed hysteresis models presented in the literature (e.g., Vassilopoulou and Tassios, 2003; Thermou *et al.*, 2014) for rough crack surfaces. In the present model formulation, a friction coefficient value of $\eta = 0.50$ is adopted, similarly to the value of $\eta = 0.44$ recommended by Tassios and Vintzeleou (1987). Although more refined

constitutive models for shear aggregate interlock along crack surfaces (which also consider crack width and the hysteretic degradation of interlock shear stress capacity) (Vassilopoulou and Tassios, 2003; Thermou *et al.*, 2014) or other various empirical relationships for representing shear stress transfer across cracks (summarized in Zhu *et al.*, 2001) are available in the literature, the friction-based constitutive model described above was used in the present FSAM, due to its simplicity and its compatibility with a smeared stress vs. strain formulation.

2.5. Dowel Action on Reinforcement

The original FSAM (Orakcal *et al.,* 2012) formulation assumed that no shear stress is resisted by the reinforcing steel bars in their transverse direction, implying no dowel action on the reinforcement.

In the FSAM formulation implemented in this study in the FSAFE model, a relatively simple constitutive relationship developed by He and Kwan (2001) using a smeared stress and strain approach, is incorporated for representing the dowel effects on both horizontal and vertical reinforcing bars. In the constitutive model formulation by He and Kwan (2001), shear (γ_{12}) and tensile (ε_1) strains in a RC panel element parallel and perpendicular to a crack are first transformed into dowel deformations ($\Delta_{dow,x}$, $\Delta_{dow,y}$) acting on the horizontal and vertical reinforcing steel bars, using the following strain transformation equations and an empirically-defined "effective dowel length (l_x, l_y)".

$$\Delta_{dow,x} = l_x \left(\varepsilon_1 \cos\theta \sin\theta + \gamma_{12} \cos^2\theta \right) \tag{2.36}$$

$$\Delta_{dow,y} = l_y \left(\varepsilon_1 \cos\theta \sin\theta - \gamma_{12} \cos^2\theta \right) \tag{2.37}$$

The effective dowel length was derived by He and Kwan (2001) using a semi-infinite beam on an elastic foundation analogy for reinforcing bars embedded in concrete, and depends empirically on parameters including the elastic modulus of reinforcing steel (E_s), the compressive strength of concrete (f'_c), rebar diameter (d_{bar}), and the moment of inertia of the rebar cross-section (I_s). The effective dowel length is given by:

$$l = \frac{\pi}{\lambda} \tag{2.38}$$

where,

$$\lambda = \sqrt[4]{\frac{k_c d_{bar}}{4 E_s I_s}} \tag{2.39}$$

and in which k_c simulates the foundation modulus of surrounding concrete related with a concrete compressive strength, diameter of one bar and an empirical coefficient "c_1"as:

$$k_c = \frac{127 c_1 \sqrt{f'_c}}{d_{bar}^{2/3}} \tag{2.40}$$

The elasto-plastic envelope of the constitutive model (Figure 2.19), which relates the dowel (shear) force on a single rebar with the dowel deformation, starts with a linear elastic region, the slope of which is also defined empirically, based on the aforementioned parameters. The plastic region of the model represents the dowel (shear force) capacity of a single rebar, which depends on the bar diameter (d_{bar}), the compressive strength of concrete (f'_c), and the yield strength of reinforcement (f_y).

Dowel forces calculated on the horizontal and vertical reinforcing bars using this empirical approach are then converted into smeared dowel stresses with the following equations, considering the reinforcement ratios (ρ_x, ρ_y) in the two orthogonal rebar directions.

$$\tau_{dow,x} = \frac{\rho_x}{A_{bar,x}} V_{dow,x} \tag{2.41}$$

$$\tau_{dow,y} = \frac{\rho_y}{A_{bar,y}} V_{dow,y} \tag{2.42}$$

Lastly, these dowel stresses are back-transformed, using stress transformation equations, into shear ($\tau_{dow,12}$) and tensile ($\sigma_{dow,1}$) stresses developed due to shear and tensile strains in the panel element, in parallel and perpendicular directions to a crack as follows:

$$\sigma_{dow,1} = \left(\tau_{dow,x} + \tau_{dow,y}\right)\cos\theta\sin\theta \tag{2.43}$$

$$\tau_{dow,12} = \tau_{dow,x}\cos^2\theta - \tau_{dow,y}\sin^2\theta \tag{2.44}$$

In the present FSAM formulation, the origin-oriented rules shown in Figure 2.19 are adopted to represent the hysteretic characteristics of the dowel force (or stress) vs. dowel deformation behavior of reinforcing steel bars (upon unloading from and reloading to the elasto-plastic envelope by He and Kwan (2001)), as a simplification of more detailed hysteretic models (Vintzēleou and Tassios, 1986) presented in the literature. Although more refined constitutive models for dowel action have been developed (e.g., Vintzēleou and Tassios, 1986), their working principles are similar, and the envelope by He and Kwan (2001) with origin-oriented hysteresis rules was selected as the simplest and the most suitable approach for implementation into the smeared stress and strain formulation of the FSAM.

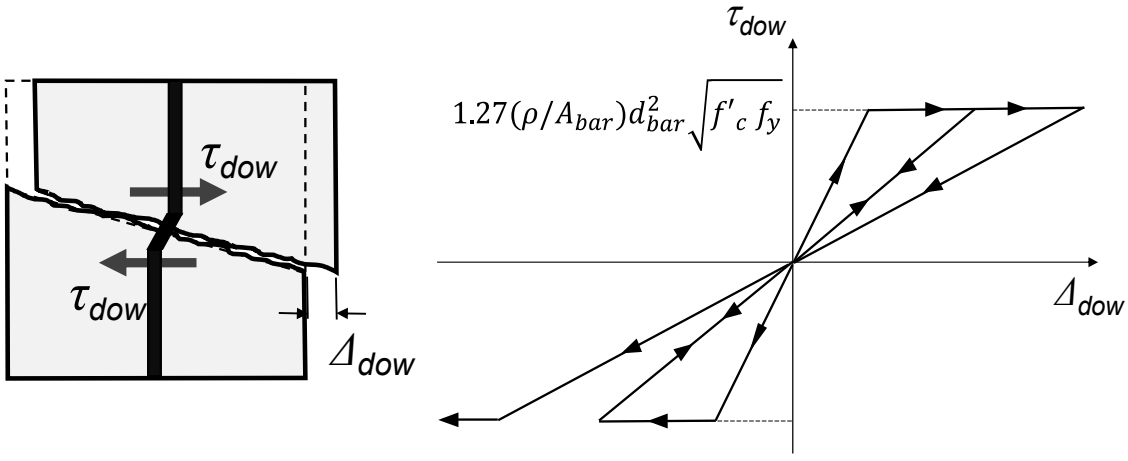

Figure 2.19. Dowel action mechanism on reinforcement.

2.6. Overview

Description of the proposed FSAFE model for simulation of hysteretic behavioral response characteristics of walls with both rectangular and non-rectangular cross sections was presented in this chapter. The FSAM model with material constitutive models originally proposed by Orakcal *et al.* (2012) was also summarized.

In the original FSAM, the response of stress vs. strain in panel elements was described with rotating-principal-stress-direction approach before cracking. After formation of cracks (struts), principal stress directions were fixed along strut directions in the FSAM formulation. Uniaxial constitutive concrete material model by Chang and Mander (1994) was employed along strut directions and superimposed with shear stresses obtained from a peak-oriented shear stress vs. shear strain model along crack surfaces, for calculation of the total concrete stresses. Uniaxial stress-strain relationship by Menegotto and Pinto (1973) was used along the orthogonal reinforcement directions for simulation of the behavior of reinforcing steel bars in panel elements. Parameters for compression softening (Model B by Vecchio and Collins, 1993), hysteretic biaxial damage (Mansour *et al.*, 2002), and tension stiffening (Belarbi and Hsu, 1994) implemented in the original FSAM were also briefly described.

In this study, the FSAM formulation was modified with implementation of a peak-oriented stress vs. strain model for representing the influence of shear aggregate interlock mechanism along crack surfaces and an origin-oriented stress vs. strain model on behalf of the observed dowel action mechanisms on reinforcing bars embedded in concrete. Shear aggregate interlock model with the hysteretic rules and shear stress capacity, as well as the dowel action model with the hysteretic rules, shear stress capacity and smeared stress-strain approach employed in the model formulation were described in this chapter.

Nonlinear behavioral characteristics of the model elements were represented with the implementation of FSAM in the FSAFE model formulation. Derivation of average strain fields were first calculated with the applied nodal displacements. Using the implemented FSAM, average stress fields and tangent stiffness (partial derivative) matrix of the model element at the stress–strain level were calculated for each of the panel elements. Average

stress fields obtained from FSAM were used with the equilibrium equations for definition of 8×1 internal force vectors for each of the panel element. Partial derivative of internal force parameters with respect to nodal displacements provided the 8×8 tangent stiffness (partial derivative) matrix of each model elements at the force–displacement level. Assembly of the 8×1 internal force vectors and 8x8 tangent stiffness matrix were lastly performed for generation of a wall model. Furthermore, at the top of the wall specimens modeled, rigid body constraints were defined in the FSAFE model formulation for representing the load transfer beams used for transmitting the horizontal loads and the axial loads (if any) during the experiments. The DOFs at the bottom of wall models were also restrained for simulation of fixed support conditions at the bottom.

The Fixed-Strut-Angle Finite Element (FSAFE) model formulation, incorporating the baseline Fixed-Strut-Angle Model (FSAM) formulation, the material constitutive relationships, as well as the constitutive models for shear aggregate interlock and dowel action described in this chapter, was implemented in Matlab (2012) together with a displacement-based nonlinear analysis solution strategy (Clarke and Hancock, 1990), in order to correlate model results with results of drift-controlled lateral load tests on RC wall specimens. In the following chapters, validation of the proposed FSAFE model for wall specimens with flexural controlled and shear controlled responses at global and local response levels is presented.

3. EXPERIMENTAL VALIDATION OF THE MODEL FOR WALLS WITH FLEXURAL OR COUPLED SHEAR-FLEXURAL RESPONSES

In this section, the model is experimentally-validated against test results obtained from the literature for a total of nine wall specimens, tested as part of four different experimental programs. The reason behind the selection of these particular specimens is that they represent various global response characteristics (flexure-controlled and shear-flexure interaction responses), due to their varying aspect ratios (ranging from 3.0 to 1.26); however, they were all designed to yield in flexure prior to reaching nominal shear capacity, as prescribed in seismic design codes. One of the slender wall specimens investigated in this study had a non-rectangular (T-shaped) cross-section. As well, all specimens were densely-instrumented during testing, allowing detailed local response comparisons between model response predictions and local deformation measurements. Information on the characteristics of the wall specimens, definition of the model parameters for representing the wall specimens, and comparison of model results and test data at both global and local response levels are presented in the following subsections.

3.1. Description of Test Specimens

Wall specimens used for experimental validation of the FSAFE model include Specimens RW2 and TW2 (Thomsen and Wallace 1995); Specimen R2 (Oesterle *et al.* 1976); Specimen WSH6 (Dazio *et al.* 2009); Specimens RW-A20-P10-S38, RW-A20-P10-S63, RW-A15-P10-S51 and RW-A15-P10-S78 (Tran and Wallace 2015); and Specimen S6 (Vallenas *et al.* 1979). These wall specimens were selected to encompass a broad range of test parameters and various important response characteristics for planar walls designed to yield in flexure; including wall aspect ratio (or shear span-to-depth ratio), wall length-to-thickness ratio in plan, axial load level, average shear stress demand at nominal flexural capacity, and failure mode. One additional wall specimen with non-rectangular cross section, Specimen TW2 (Tran and Wallace 2015), is also included in the response comparisons presented in this study for demonstrating the capability of the FSAFE model

in simulating the nonlinear response of non-rectangular walls. The aspect ratio of the walls ranged from 1.26 to 3.00, while their shear span-to-depth ratios varied between 1.50 and 3.00, due to the different loading configurations applied during testing.

Two of the relatively slender wall specimens (aspect ratio of 3.0) tested by Thomsen and Wallace (1995, 2004), one having a rectangular cross-section (RW2), and one with a T-shaped cross-section (TW2), were first used for experimental validation of the FSAFE model (Figure 3.1a, b). Concrete with compressive strength of 43MPa and reinforcement with yield strength ranging from 434MPa to 448MPa were used in the construction of the specimens. The walls were designed to exhibit ductile flexural behavior, with a capacity design approach used to provide sufficient shear capacity to resist the shear force corresponding to the wall probable moment capacity. Thereby, the nominal shear strength of specimen RW2 reached almost twice its nominal flexural capacity. Well-detailed boundary elements were provided at the boundary regions of the walls. A constant axial load of approximately 0.07–0.08$A_g f'_c$ was applied on the walls throughout the duration of the tests. Failure of specimen RW2 was initiated by spalling of cover concrete, followed by buckling of longitudinal reinforcement and crushing of confined concrete in the boundary regions. For specimen TW2, failure was due to spalling of cover concrete followed by initiation of crushing of confined concrete and global buckling (over several tie spacings) of longitudinal reinforcement within the web boundary region of the wall, leading to out-of-plane instability of the web boundary.

Validation of the model was also carried out against the experimental results of the wall specimens R2 (Figure 3.1c) and WSH6 (Figure 3.1d) from two different experimental program tested by Oesterle *et al.* (1976) and Dazio *et al.* (2009), respectively. The aspect ratio of the specimen R2 is 2.34 (shear span-to-depth ratio of 2.4) while the aspect ratio of WSH6 is 2.02 (shear span-to-depth ratio of 2.26). Concrete compressive strength of specimen R2 is 46MPa and reinforcement yield strengths were ranged from 450 to 535 MPa at boundary. Specimen R2 is varied from the previously described specimens with zero axial load applied during test. Strength degradation of the specimen was started with crushing of concrete at earlier stages of loading, resulting in buckling of reinforcement at wall boundary and lateral instability of the compression zone. The concrete compressive strength of specimen WSH6 was 45.6 MPa, and the reinforcing bar yield strengths were

ranged from 519 MPa to 584 MPa. Specimen WSH6 was subjected to a constant axial load level of $0.11A_g f'_c$ thorough the experiment. Strength loss of specimen WSH6 was similar to specimen RW2, which was triggered by spalling of cover concrete at earlier stages of loading. At subsequent loading stages, a number of confining hoops crushed and the longitudinal boundary reinforcements buckled leading to crushing of the compression boundary zone.

The model was also validated against experimental results for four of the five medium-rise rectangular wall specimens tested by Tran and Wallace (2012, 2015) (Figure 3.2a, b, c and d), two with an aspect ratio of 2.0 (RW-A20-P10-S38, RW-A20-P10-S63), and the others with an aspect ratio of 1.5 (RW-A15-P10-S51, RW-A15-P10-S78). The walls were subjected to an axial load of approximately $0.10A_g f'_c$ during testing. For these specimens, the measured compressive strength of concrete ranged from 47MPa to 56MPa, and the yield strength of reinforcement varied from 473MPa to 516MPa. The walls incorporated specially-detailed boundary regions, and were designed to yield in flexure at a lateral load of approximately 80%–90% of their nominal shear strength. These wall specimens exhibited coupled shear and flexural responses (shear-flexure-interaction behavior), with shear deformations contributing significantly to wall lateral displacements. For the specimens RW-A20-P10-S38 and RW-A15-P10-S51, strength degradation was initiated by crushing of confined concrete and buckling of longitudinal reinforcement at the wall boundaries, followed by progressive degradation associated with diagonal tension failure along two major diagonal cracks, while diagonal-compression-related failures (crushing of concrete under combined shear-flexural effects) observed for specimens RW-A20-P10-S63, RW-A15-P10-S78.

Final validation of the model was conducted with the medium rise wall specimen S6 (Figure 3.2e) tested by Vallenas *et al.* (1979) with an aspect ratio of 1.26 (shear-span-to-depth ratio of 1.60). The specimen subjected to axial load level of $0.05A_g f'_c$. Concrete with compressive strength of 35MPa and reinforcement with yield strength ranging from 482MPa to 507MPa were used in the construction of the specimens. Failure of specimen S6 was triggered by the spalling of concrete cover on only one side of the boundary element, which resulted in out-of-plane buckling of the wall boundary, after spalling of the concrete cover.

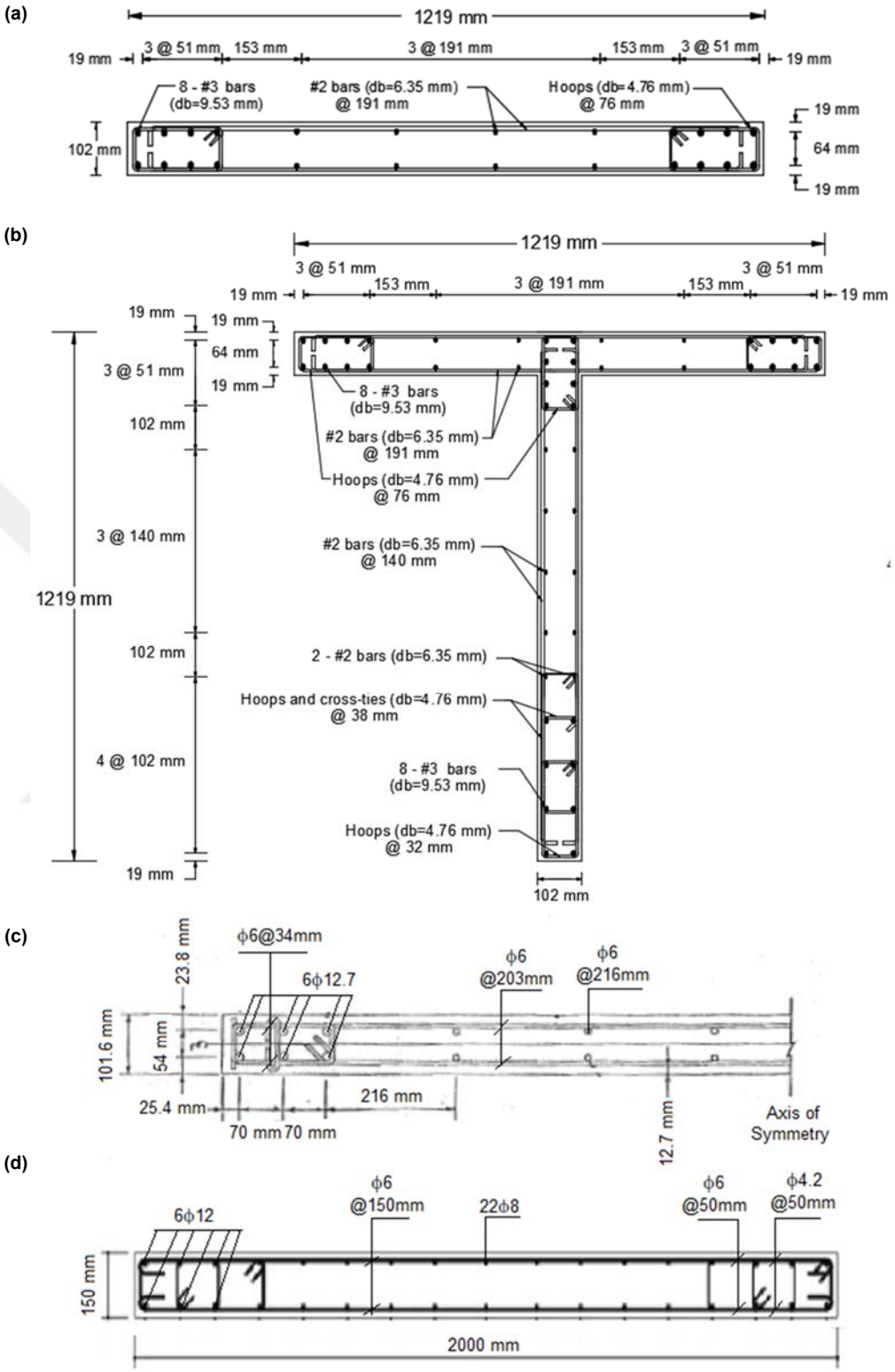

Figure 3.1. Wall cross sections and reinforcement details for specimens: (a) RW2, (b) TW2, (c) R2, (d) WSH6.

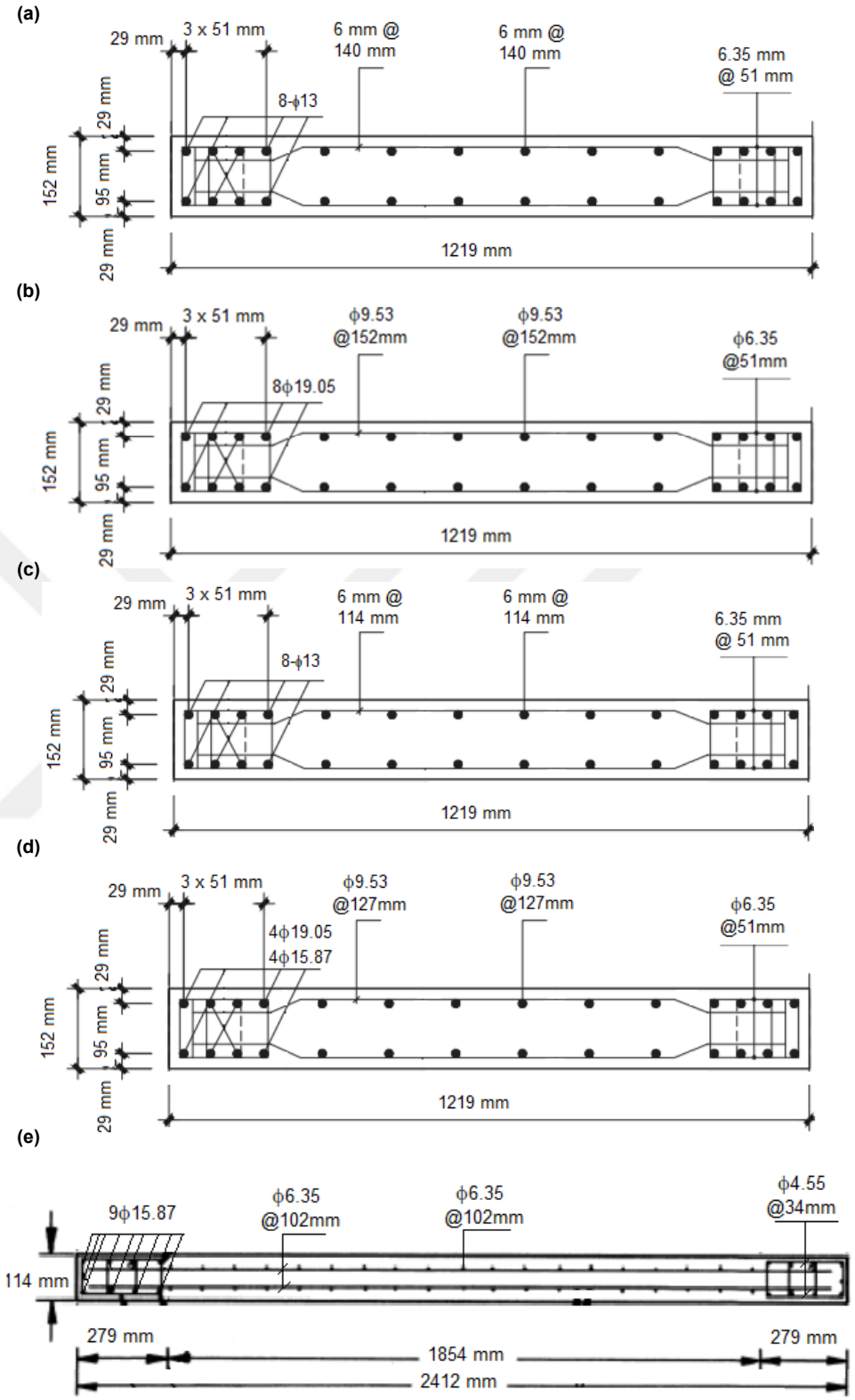

Figure 3.2. Wall cross sections and reinforcement details for specimens: (a) RW-A20-P10-S38, (b) RW-A20-P10-S63, (c) RW-A15-P10-S51, (d) RW-A15-P10-S78, (e) S6.

Geometric and reinforcement characteristics of the wall specimens are listed in Table 3.1 , whereas specimen cross-sections at wall base are shown in Figure 3.1 and Figure 3.2. Important material parameters of the wall specimens, including concrete compressive strength (f'_c) and reinforcing steel yield strength (f_y) are listed in Table 3.2. The experimentally-observed failure models of the walls and the average shear stress levels on the walls at their lateral load capacities are also reported in Table 3.2. All wall specimens were tested as vertical cantilevers. They incorporated a RC pedestal at the bottom for connection of the specimen to the strong floor, and a RC or steel load transfer beam at the top for connection to a horizontal actuator. Only specimen S6 was subjected to a proportional lateral load pattern imposed using three transverse actuators mounted on the wall at representative story levels (1.22 m, 2.13 m, and 3.05 m from the wall base), and a bending moment applied at the top of the wall using two longitudinal actuators, as described by Vallenas *et al.* (1979). Axial load was applied on the walls using hydraulic jacks mounted on the load transfer beams.

Table 3.1. Properties of wall specimens.

Experimental Program	Specimen ID		l_w (mm)	h_w (mm)	t (mm)	$\frac{l_w}{t}$	$\frac{h_w}{l_w}$	$\frac{M}{Vl_w}$	$\frac{P_{ax}}{A_g f'_c}$	Web Reinforcement (Transverse/Longitudinal)		Boundary Reinforcement	
										Rebar	ρ_{web} (%)	Rebar	ρ_b (%)
Thomsen and Wallace (1995, 2004)	RW2		1220	3660	102	12	3.00	3.00	0.07	ϕ6.35@191mm	0.33	8ϕ9.53	2.93
	TW2	Web	1220	3660	102	12	3.00	3.00	0.08	ϕ6.35@140mm	0.44	8ϕ9.53	2.93
		Flange								ϕ6.35@191mm	0.33	8ϕ9.53	2.93
Oesterle *et al.* (1976)	R2		1905	4470	102	19	2.34	2.40	0.00	ϕ6.35@203mm ϕ6.35@216mm	0.31/0.25	6ϕ12.7	4.00
Dazio *et al.* (2009)	WSH6		2000	4030	150	13	2.02	2.26	0.11	ϕ6@150mm ϕ8@125mm	0.25/0.46	6ϕ12 2ϕ8	1.54
Tran and Wallace (2012, 2015)	RW-A20-P10-S38		1220	2440	152	8	2.00	2.00	0.10	ϕ6@140mm	0.27	8ϕ12.7	3.23
	RW-A20-P10-S63		1220	2440	152	8	2.00	2.00	0.10	ϕ9.53@152mm	0.61	8ϕ19.05	7.11
	RW-A15-P10-S51		1220	1830	152	8	1.50	1.50	0.10	ϕ6@114mm	0.32	8ϕ12.7	3.23
	RW-A15-P10-S78		1220	1830	152	8	1.50	1.50	0.10	ϕ9.53@ 127mm	0.73	4ϕ19.05 4ϕ15.87	6.06
Vallenas *et al.* (1979)	S6		2412	3048	114	21	1.26	1.60	0.05	ϕ6.35@102mm	0.55	9ϕ15.87	5.60

Table 3.2. Material and response characteristics of wall specimens.

Specimen ID		f'_c (MPa)	$f_{y,web}$ (Transverse/Longitudinal) (MPa)	$f_{y,boundary}$ (MPa)	$\frac{V_{max}}{A_{CV}\sqrt{f'_c}}$	Behavior Mode(1)	Failure Mode(2)
RW2		42.8	448	434	0.20	FL	CB
TW2	Web	42.8	448	434	0.34	FL	CB/LI
	Flange						
R2		46.4	535	450	0.16	FL	CB/BR/LI
WSH6		45.6	519/584	576	0.29	FL	CB
RW-A20-P10-S38		47.1	450/516	472	0.36	SFI/DT	CB
RW-A20-P10-S63		48.6	443	477	0.57	SFI/DC	CB/LI
RW-A15-P10-S51		48.8	450/516	472	0.46	SFI/DT	CB
RW-A15-P10-S78		55.8	443	477	0.61	SFI/DC	CB/LI/SS
S6		34.7	507	482	0.53	SFI/DC	CB/LI

(1) FL: flexure; SFI: shear/flexure interaction; DT: diagonal tension; DC: diagonal compression

(2) CB: concrete crushing/bar buckling; LI: lateral instability; BR: bar rupture; SS: sliding shear

3.2. Definition of Model Parameters for the Wall Specimens

3.2.1. Model Geometry

FSAFE model assemblies generated for the wall specimens were geometrically-discretized using an appropriate number of constitutive model elements, so that the model elements had approximately equal width and height, and the locations of local deformation measurements on the specimens were captured. As a standardization, two model elements (side-by-side) were used to define each boundary region of the specimens incorporating confined boundary zones, with the exception of four model elements used to define the longer web boundary of specimen TW2. As an example, specimen RW-A15-P10-S51 (with an aspect ratio of 1.5) was divided into 12 model elements in the horizontal direction and 18 elements in the vertical direction, resulting in a total of 216 approximately square-shaped model elements. Similarly, both the web and the flange of the T-shaped wall specimen TW2 (with an aspect ratio of 3.0) was divided into 12 model elements in the horizontal direction and 36 elements in the vertical direction, resulting in a total of 432

model elements for the web and 432 model elements for the flange. Figure 2.1 shows the nodes and nodal degrees of freedom of an individual model element, and also illustrates representative model discretizations for the rectangular wall specimen RW-A15-P10-S51 and the T-shaped wall specimen TW2. Table 3.3 presents the mesh dimensions and mesh numbers in both horizontal and vertical directions for wall specimens investigated. It was observed that using a larger number of model elements did not significantly alter the model response predictions for the wall specimens investigated in this study, other than the rate of degradation in lateral load after the wall lateral load capacity is reached. Sensitivity of the model responses to number of model elements is scrutinized in Section 3.4.

Table 3.3. Definition of wall model geometry.

Specimen ID		Mesh (Element) Dimensions (mm)			Number of Meshes (Elements)		
		Horizontal		Vertical	Horizontal (m)		Vertical (n)
		Boundary	Web		Boundary	Web	
RW2		95.5	104.6	101.6	4	8	36
TW2	Web	76.1	114.3	101.6	7	6	36
	Flange	95.5	104.6	101.6	4	8	36
R2		95.3	95.3	95.3	4	16	48
WSH6		130	148	150.7	4	10	30
RW-A20-P10-S38		105	100	101.7	4	8	24
RW-A20-P10-S63		105	100	101.7	4	8	24
RW-A15-P10-S51		105	100	101.7	4	8	18
RW-A15-P10-S78		105	100	101.7	4	8	18
S6		139.5	154.5	152.4	4	12	20

3.2.2. Material Model Parameters

The constitutive material parameters used in the FSAFE model formulation were assigned values that match the as-tested properties of the materials employed in the construction of the specimens (whenever detailed material test results pertaining to the wall specimens were available), or based on well-established empirical relationships presented in the literature. The material parameters were not adjusted to fit the model predictions with experimentally-obtained responses of the wall specimens. The monotonic envelope of

the stress–strain model by Chang and Mander (1994) for unconfined concrete in compression was defined to agree with concrete stress–strain curves obtained from cylinder specimens of concrete used in the construction of the wall specimens, wherever reported. In cases where only the concrete compressive strength was reported, the empirical equations proposed by Chang and Mander (1994) were used to define the ascending region of the envelope. For generating the ascending region of the stress–strain envelope for confined concrete, the confinement model by Mander *et al.* (1988) was used. The descending (post-peak) slope of the stress–strain envelopes for both confined and unconfined concrete were defined to match the explicitly-defined descending slope of the Saatcioglu and Razvi (1992) model as shown in Figure 3.3. Unconfined and confined concrete constitutive modeling parameters for all specimens are presented in Table 3.4. The Concrete compressive strength (f'_c), elastic modulus (E_c), strain at peak compressive stress (ε'_c), a parameter for description of the shape of the envelope curve (r) and the normalized critical strain value (parameter defines the slope of the descending region) (x_{crn}) for all wall specimens are reported in the table.

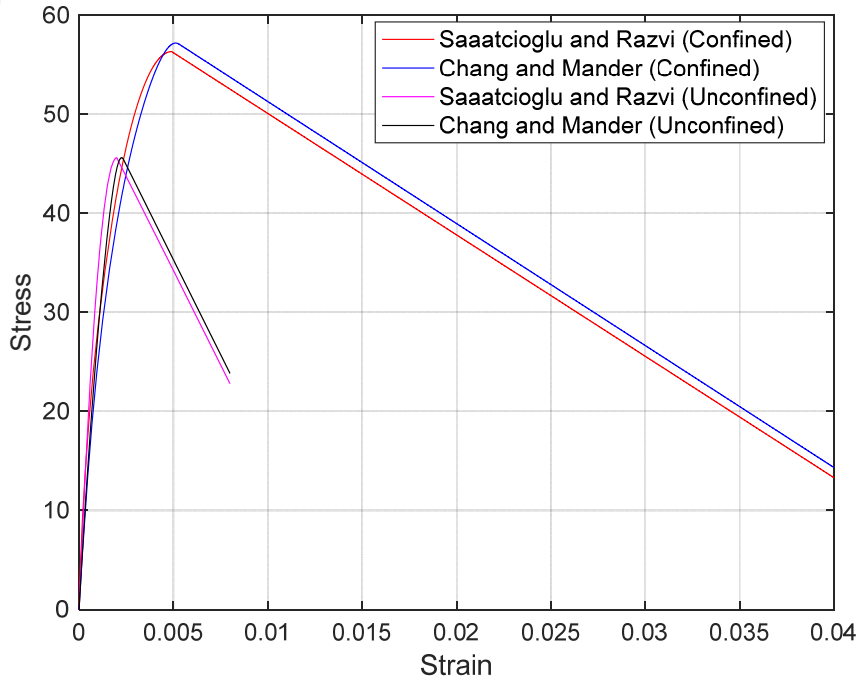

Figure 3.3. Calibrated unconfined and confined concrete material stress-strain model in compression for specimen WSH6.

Concrete tensile strength was determined from the relationship $f_t = 0.31\sqrt{f'_c}$ (MPa), and a value of 0.00008 was selected for the strain (ε_t) at peak tensile strength (Figure 2.11), as suggested by Belarbi and Hsu (1994) for RC panels. The shape of the tensile stress–strain envelope was also defined to match the average post-crack stress–strain relationship of by Belarbi and Hsu (1994), which considers the effects of tension stiffening on the smeared stress–strain behavior of concrete. Figure 3.4 presents an illustrative definition of the envelope of concrete material model in tension for specimen WSH6 using the material model proposed by Belarbi and Hsu (1994). Table 3.5 illustrates the constitutive modeling parameters of all specimens for concrete in tension.

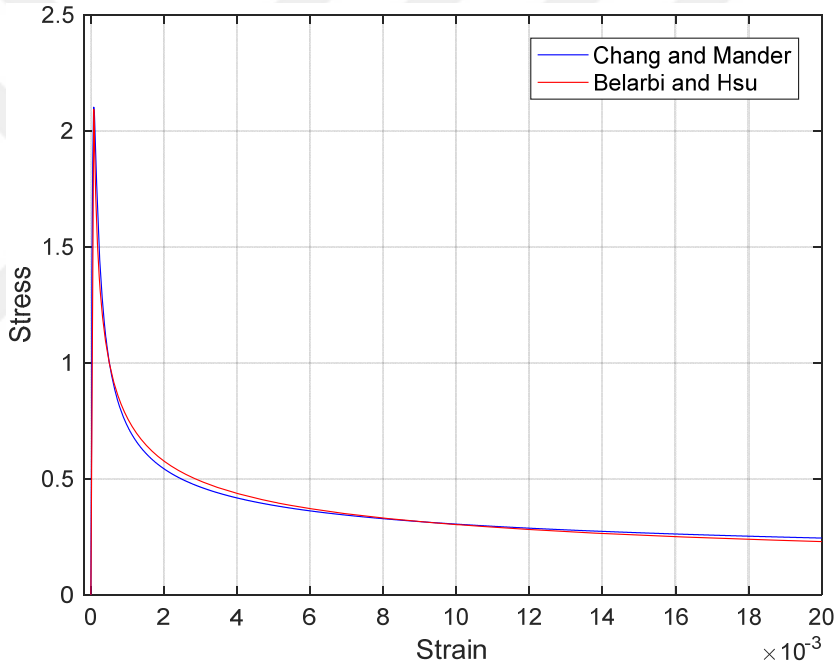

Figure 3.4. Calibrated concrete material stress-strain model in tension for specimen WSH6.

The monotonic parameters of the constitutive stress–strain model by Menegotto and Pinto (1973), including the yield strength and strain hardening ratio, were assigned values that represent the stress–strain curve obtained from coupon samples of reinforcing steel bars used in the construction of the wall specimens. The tensile yield strength and tensile strain-hardening parameters were modified according to the empirical relationships by Belarbi and Hsu (1994), to consider the effect of tension stiffening on the behavior of

reinforcing bars embedded in concrete. Constitutive modeling parameters for reinforcing steel bars are shown in Table 3.6. The yield strength (f_y) and strain hardening ratio (b) of reinforcing bars in compression are equal to the test results for bare bars. These parameters; however, are not identical in tension and compression, due to consideration of tension stiffening effect in the definition of reinforcing bars in tension.

Table 3.4. Material model parameters for confined and unconfined concrete in compression.

Specimen ID			Boundary (Confined)					Web (Unconfined)				
			f'_c (MPa)	E_c (MPa)	ε'_c	r	x_{crn}	f'_c (MPa)	E_c (MPa)	ε'_c	r	x_{crn}
RW2			47.60	31026	0.0033	1.9	1.121	42.8	31026	0.0021	7.0	1.039
TW2	Web	Web	57.10	31026	0.0056	1.5	1.304	42.8	31026	0.0021	7.0	1.048
		Web-Flange Intersection	43.90	31026	0.0024	3.8	1.042					
	Flange		43.90	31026	0.0024	3.8	1.042	42.8	31026	0.0021	7.0	1.048
R2			81.60	26890	0.0144	13.9	1.015	46.4	26890	0.0030	7.1	1.056
WSH6			57.36	34543	0.0052	9.2	1.035	45.6	34543	0.0023	6.9	1.045
RW-A20-P10-S38			62.22	38596	0.0060	3.4	1.071	47.1	34965	0.0023	7.2	1.045
RW-A20-P10-S63			65.65	39379	0.0055	2.2	1.118	48.6	35378	0.0020	7.5	1.032
RW-A15-P10-S51			63.97	38999	0.0056	2.3	1.107	48.8	35433	0.0022	7.5	1.032
RW-A15-P10-S78			72.86	40949	0.0060	2.2	1.113	55.8	37259	0.0024	8.9	1.026
S6			51.30	26000	0.0088	8.0	1.041	34.7	26000	0.0026	4.8	1.087

Table 3.5. Material model parameters for concrete in tension.

Specimen ID		f_t (MPa)	E_c (MPa)	ε_t	r_t	x_{crp}
RW2		2.03	31026	0.00008	1.2	10000
TW2	Web	2.03	31026	0.00008	1.2	10000
	Flange	2.03	31026	0.00008	1.2	10000
R2		2.12	26890	0.00008	1.15	10000
WSH6		2.1	34543	0.00008	1.23	10000
RW-A20-P10-S38		2.13	34965	0.00008	1.23	10000
RW-A20-P10-S63		2.16	35378	0.00008	1.23	10000
RW-A15-P10-S51		2.17	35433	0.00008	1.23	10000
RW-A15-P10-S78		2.32	37259	0.00008	1.23	10000
S6		1.83	26000	0.00008	1.18	10000

The parameters describing the cyclic stiffness degradation characteristics of the constitutive model were defined as R_0 = 20, a_1 = 18.5, and a_2 = 0.15 (Figure 2.13), as proposed originally by Menegotto and Pinto (1973). An exception was made for specimens RW2 and TW2, for which a value of a_2 = 0.0015 was used in the definition, based on the results of previous analytical studies (e.g., Orakcal and Wallace, 2006) conducted on these specimens.

Table 3.6. Material model parameters for reinforcing bars.

Specimen ID		Rebar Orientation	Boundary					Web				
			ϕ (mm)	Rebar in Compression		Rebar in Tension		ϕ (mm)	Rebar in Compression		Rebar in Tension	
				f_y (MPa)	b	f_y (MPa)	b		f_y (MPa)	b	f_y (MPa)	b
RW2		Horizontal	4.76	425	0.01	354	0.01	6.35	448	0.02	336	0.035
		Vertical	9.53	434	0.02	395	0.0185	6.35	448	0.02	336	0.035
TW2	Web	Horizontal	4.76	425	0.01	354	0.01	6.35	448	0.02	336	0.035
		Vertical	9.53	434	0.02	387	0.02	6.35	448	0.02	356	0.0295
	Flange	Horizontal	4.76	425	0.01	354	0.01	6.35	448	0.02	336	0.035
		Vertical	9.53	434	0.02	395	0.0185	6.35	448	0.02	336	0.035
R2		Horizontal	6.35	535	0.0064	483	0.0085	6.35	535	0.0064	411	0.0255
		Vertical	12.7	450	0.0107	411	0.0106	6.35	535	0.0064	389	0.0306
WSH6		Horizontal	6	519	0.0038	447	0.0116	6	519	0.0038	376	0.0287
		Vertical	12	576	0.0071	521	0.0088	8	584	0.0071	521	0.0088
RW-A20-P10-S38		Horizontal	6	423	0.003	393	0.0025	6	450	0.02	417	0.0163
		Vertical	12.7	472	0.0104	439	0.0084	6	516	0.0033	479	0.0029
RW-A20-P10-S63		Horizontal	6	423	0.003	393	0.0025	9.53	443	0.017	412	0.0137
		Vertical	19.05	477	0.0103	444	0.0083	9.53	443	0.017	412	0.0137
RW-A15-P10-S51		Horizontal	6	423	0.003	393	0.0025	6	450	0.02	417	0.0163
		Vertical	12.7	472	0.0104	439	0.0084	6	516	0.0033	479	0.0029
RW-A15-P10-S78		Horizontal	6	423	0.003	393	0.0025	9.53	443	0.017	412	0.0137
		Vertical	15.87	474	0.0100	441	0.0081	9.53	443	0.017	412	0.0137
			19.05	477	0.0103	444	0.0083					
S6		Horizontal	4.55	440	0.0123	381	0.0179	6.35	507	0.0095	431	0.0176
		Vertical	15.87	482	0.007	444	0.0067	6.35	507	0.0095	433	0.0171

The simple constitutive models representing shear aggregate interlock along cracks and dowel action on reinforcement were adopted as described in Sections 2.4 and 2.5 of this study. A friction coefficient value of $\eta = 0.50$ was used for the analysis of all slender and medium rise wall specimens. Definition of the envelope curves of the peak-oriented shear aggregate interlock and origin-oriented dowel action models were conducted with the constitutive parameters for concrete and reinforcing steel bars, as summarized in Table 3.2.

3.3. Comparison of Model Responses with Test Data

3.3.1. Lateral Load vs. Top Displacement Responses

Comparison of the experimentally-measured and analytically-predicted lateral load vs. top displacement responses for the four relatively slender and five medium rise wall specimens is presented in Figure 3.5 to Figure 3.9. Overall, the FSAFE model replicates the experimentally-obtained load–displacement responses of all specimens, with a reasonable level of accuracy.

Model response predictions are in agreement with test results for relatively slender walls in terms of lateral stiffness, lateral load capacity (excluding TW2 in negative loading direction), and drift capacity of the walls, as well as other important cyclic response characteristics including hysteretic stiffness degradation, plastic (residual) displacements upon unloading to zero load, and pinching behavior. However, the model does not accurately simulate the hysteretic behavioral response characteristics of the specimen R2 although the model well-represents the lateral load capacity for this specimen.

The model accurately predicts the measured lateral load–displacement response of the wall specimen RW2 (Figure 3.5a), although it cannot capture the experimentally-observed degradation in lateral load during the second loading cycle to 2.5% drift in the positive loading direction, which occurred due to initiation of buckling of longitudinal reinforcement in the wall boundary region. The lateral loads applied on the T-shaped wall specimen TW2 are under-predicted by the model (by less than 5%) when the wall flange is in compression, possibly because the model does not consider the out-of-plane flexural stiffness of the flange (Figure 3.5b). In contrast, the model overestimates (by

approximately 20%) the lateral loads applied on the wall when the wall flange is in tension (Figure 3.5b), probably because the model cannot simulate the experimentally-observed out-of-plane instability (global buckling) of the web boundary region of the wall, as also discussed in a subsequent section.

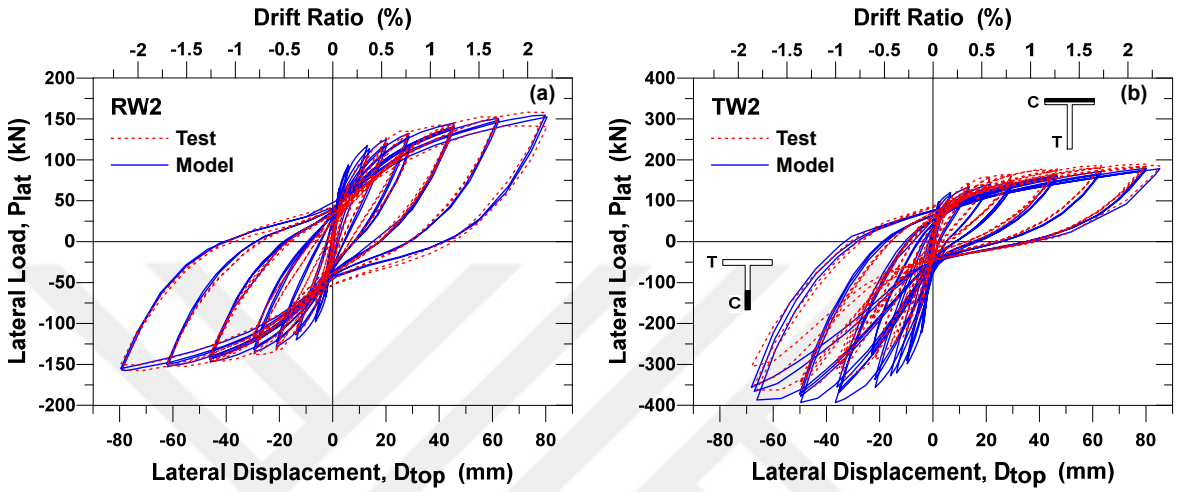

Figure 3.5. Lateral load vs. top displacement responses for specimens: (a) RW2, (b) TW2.

Similarly to specimen RW2, specimen WSH6 showed a predominantly-flexural response during testing. The observed failure mode of the specimen was crushing of confined concrete (caused by rupture of confining hoops) within the boundary region of the wall and buckling of the longitudinal boundary reinforcement, leading to a sudden drop of the lateral load at a drift level of 2.0% in the negative loading direction. As shown in Figure 3.6, the model accurately predicts the experimentally-measured lateral load vs. top displacement response characteristics of this wall, until failure at negative 2.0% drift. However, as expected, the model does not capture the experimentally-observed degradation in lateral load associated with rebar buckling, and therefore overestimates the drift capacity of the wall. Nevertheless, initiation of concrete crushing is reflected in the analysis results, in which a very gradual degradation in lateral load, starting at drift level of approximately 1.5%, is observed.

As shown in Figure 3.7, the experimentally-measured lateral load vs. top displacement response of the wall specimen R2 follows a relatively pinched behavior, the lateral stiffness of the wall undergoes significant hysteretic degradation with increasing

drift, and the wall experiences abrupt strength degradation during loading to a drift ratio of 3.4%. The model, although provides a reasonable estimate of the lateral load capacity of the wall, predicts a hysteretic response that comprises wide load–displacement loops (similar to the cyclic stress–strain behavior of reinforcing steel), with minimal pinching observed at large drift levels only. Specimen R2 is a relatively slender wall, having the second-largest shear span-to-depth ratio among all wall specimens investigated. The nominal shear strength of the wall is more than twice its nominal flexural capacity, and the average shear stress demand on the wall at its lateral load capacity is the lowest among all specimens investigated. Also considering the zero axial load on the wall, it is believed that the flexure-dominated response prediction of the model represents the expected (conventional) behavior of the wall, with yielding of the longitudinal bars in tension, followed by their yielding in compression (upon load reversal) prior to closure of cracks, creating the wide load–displacement loops shown in Figure 3.7.

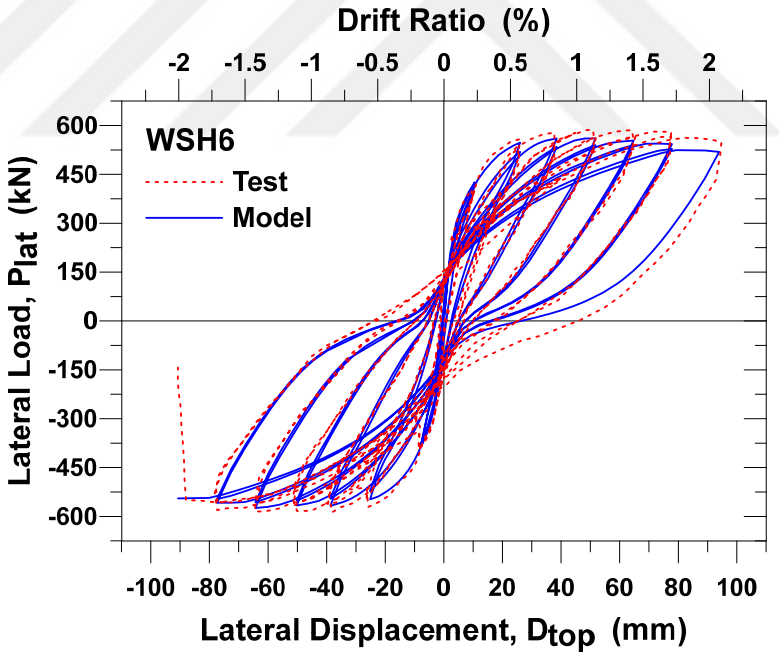

Figure 3.6. Lateral load vs. top displacement responses for specimen WSH6.

The FSAFE model replicates the experimentally-measured lateral load–displacement response of the medium rise walls with reasonable accuracy (Figure 3.8 and Figure 3.9). The model prediction matches the measured response in terms of lateral stiffness, lateral load capacity, and drift capacity of the wall (excluding RW-A20-P10-S38), as well as other

important cyclic response characteristics including hysteretic stiffness degradation, plastic (residual) displacements upon unloading to zero load, and pinching behavior. As also shown in the embedded plots in Figure 3.8a to Figure 3.8d, the model captures the notable contribution of shear deformations to top displacements of the four medium-rise wall specimens that showed shear-flexure coupling behavior, demonstrating the capability of the model in representing the coupled shear-flexural response characteristics of the wall.

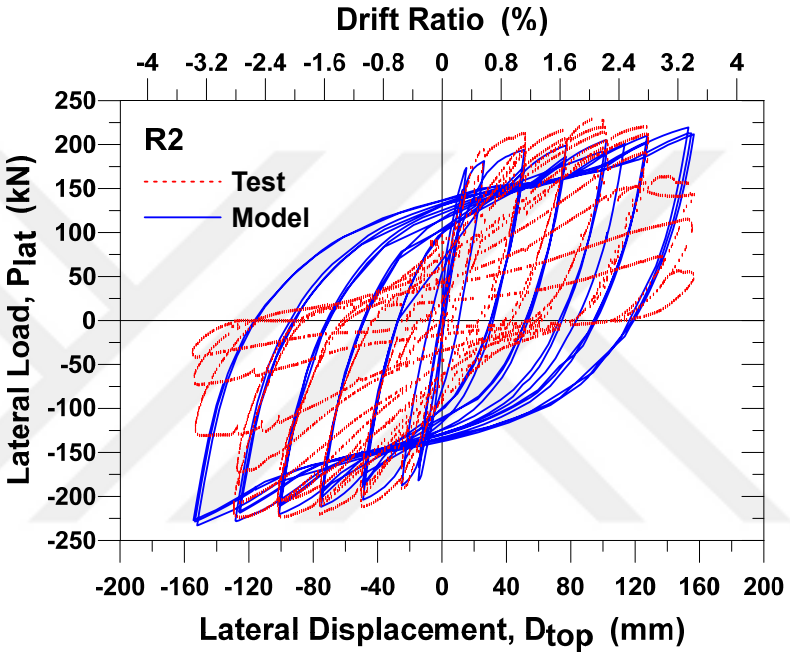

Figure 3.7. Lateral load vs. top displacement response for specimen R2.

Two of the medium rise wall specimens (RW-A20-P10-S38 and RW-A15-P10-S51) experienced degradation in lateral load capacity due to crushing of confined concrete and buckling of longitudinal reinforcement at the wall boundaries, followed by progressive degradation associated with diagonal tension failure along two major diagonal cracks. The incapability of the model in predicting the initiation of lateral load degradation in the response of specimen RW-A20-P10-S38 during the last loading cycle (Figure 3.8a) as well as the inaccuracy of the model in capturing the rate of degradation in the last cycle of the of the lateral load applied on specimen RW-A15-P10-S51 (Figure 3.8c) is probably because rebar buckling behavior is not considered in the present model formulation, whereas for these two specimens, the wall longitudinal reinforcement buckled at failure. The incapability of the model in predicting the abrupt degradation for specimen RW-A20-

P10-S63 (Figure 3.8b) in lateral load during the last loading cycle to 3% drift in the negative loading direction is because lateral instability failures not considered in the present model formulation, including rebar buckling and out-of-plane instability of the compression boundary. During testing, strength loss in the response of the specimen RW-A20-P10-S63 was caused by crushing of concrete at the wall boundary regions, along with crushing along diagonal compression struts near the wall base, leading to out-of-plane buckling of longitudinal boundary reinforcement and lateral instability of the boundary region. Although the model predicts crushing of confined concrete at the wall boundaries and provides a reasonable estimate of the drift capacity of the wall specimen RW-A20-P10-S63 (approximately 2%), it predicts a more gradual degradation in lateral load after 2% drift, and does not capture the sudden and instability-related strength loss observed during the test at negative 3% drift. Similarly to specimen RW-A20-P10-S63, the model does not capture the abrupt degradation in lateral load during the second loading cycle to 3.0% drift in the positive loading direction of the specimen RW-A15-P10-S78 (Figure 3.8d), since the model cannot simulate the out-of-plane buckling of wall boundary reinforcement and the lateral instability of wall the boundary region, which was one of the two experimentally-observed failure modes of this wall, the other being sliding shear adjacent to the wall-pedestal interface. However, the wall drift capacity estimation of the model is again reasonable, at approximately 2.0% drift, since the model captures the crushing of confined concrete in the wall boundary regions, which initiated the experimentally-observed strength degradation.

The medium-rise wall specimen S6 exhibited a shear-flexure interaction response during testing, similarly to other medium rise wall specimens. Failure of the specimen was due to crushing of concrete and out-of-plane buckling of the wall boundary element, creating sudden strength loss during loading to a drift level of 1.6% in the negative loading direction. As illustrated in Figure 3.9, the model accurately simulates the lateral load vs. top displacement response of the wall until failure, but fails to predict the sudden strength loss related to lateral instability of the wall boundary. At the negative 1.6% drift level, mild degradation in lateral load, associated with initiation of crushing of confined concrete within the wall boundary region, is observed in the model response prediction.

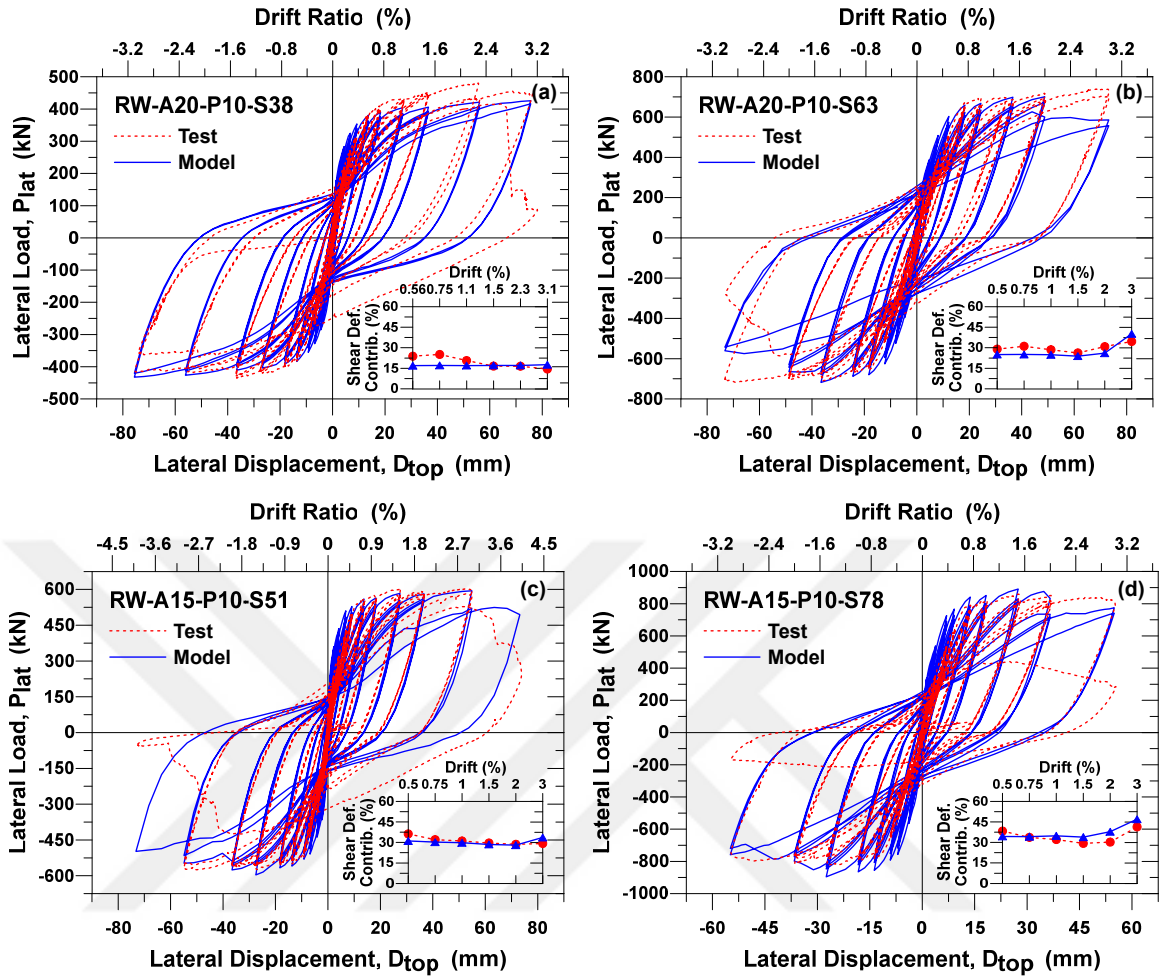

Figure 3.8. Lateral load vs. top displacement responses for specimens: (a) RW-A20-P10-S38, (b) RW-A20-P10-S63, (c) RW-A15-P10-S51, (d) RW-A15-P10-S78.

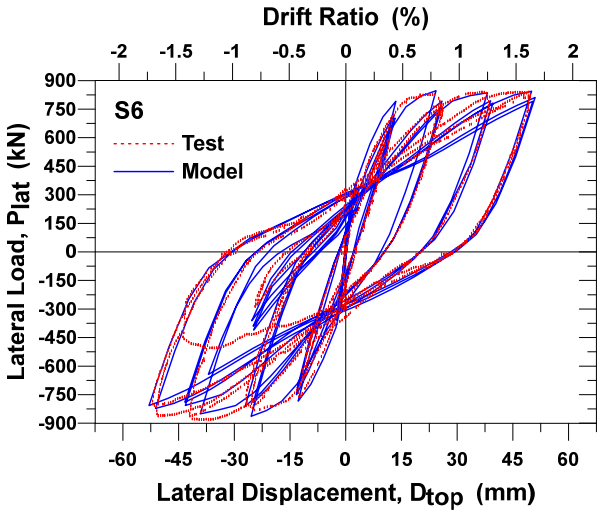

Figure 3.9. Lateral load vs. top displacement responses for specimen S6.

3.3.2. Lateral Load vs. Flexural and Shear Deformation Responses

Comparisons of the experimentally-measured and analytically-predicted flexural and shear deformation components of the lateral load versus top displacement response for relatively slender wall specimens RW2 and TW2 (shear-span-to-depth ratio of 3.0), as well as the medium-rise wall specimens RW-A20-P10-S38 and RW-A20-P10-S63 (shear-span-to-depth ratio of 2.0), RW-A15-P10-S51 and RW-A15-P10-S78 (shear-span-to-depth ratio of 1.5), and S6 (shear-span-to-depth ratio of 1.60) are presented in Figure 3.10 to Figure 3.13, respectively. It can be observed from the results presented in Figure 3.10 to Figure 3.13 that FSAFE modeling approach can capture the development of nonlinear shear deformations, as well as their coupling with nonlinear flexural deformations, throughout the entire cyclic loading history. Simultaneous occurrence of nonlinear shear and flexural deformations (at the same level of lateral load) reveals that shear-flexure interaction behavior is reflected in both analytical and experimental results. Shear and flexural deformations shown in the figures are measured along the bottom 914 mm (i.e., first story height) of specimen RW2 and TW2 and along the entire height of all medium-rise wall specimens. Experimental shear and flexural deformation values are obtained from vertical and diagonal LVDTs mounted on the wall specimens using the procedure described by Massone and Wallace (2004). Shear deformations in the model results were calculated by multiplying the average of the shear strain values obtained for all of the individual model elements that are lined up at the same elevation, with the model element height. These shear deformations were summed up over the model height for obtaining the cumulative shear displacement at a particular elevation of the wall. Flexural displacement predictions of the model were calculated by subtracting shear displacements from total lateral displacement at the same wall elevation.

Model predictions are first compared with the lateral load vs. flexural and shear displacement responses measured at the first story elevation (bottom quarter of wall height) of wall specimen RW2 in Figure 3.10a. Even for the relatively slender wall specimen RW2, for which the contribution of shear deformations to top displacement was measured as approximately 10% (Orakcal and Wallace, 2006), similar to experimental observations, significant nonlinearity in the lateral load vs. shear displacement behavior is predicted by the model along the first story height of the wall where nonlinear flexural deformations are

concentrated. The model slightly underestimates the shear displacements (which is acceptable considering their very small magnitude), but clearly captures the nonlinear shear-flexure interaction behavior observed experimentally even for this slender wall specimen with flexure-dominated behavior. The model also captures the coupling of nonlinear shear and flexural deformations in the response of the T-shaped wall specimen TW2 (Figure 3.10b), although the first-story shear displacement measurements are largely overestimated by the model when the wall flange is in tension. This discrepancy is believed to be mainly due to imperfections in these shear displacement measurements, since the measured shear displacement values (which are of very small magnitude) show inconsistencies throughout the loading history, such as positive shear displacements measured under negative lateral load (Figure 3.10b).

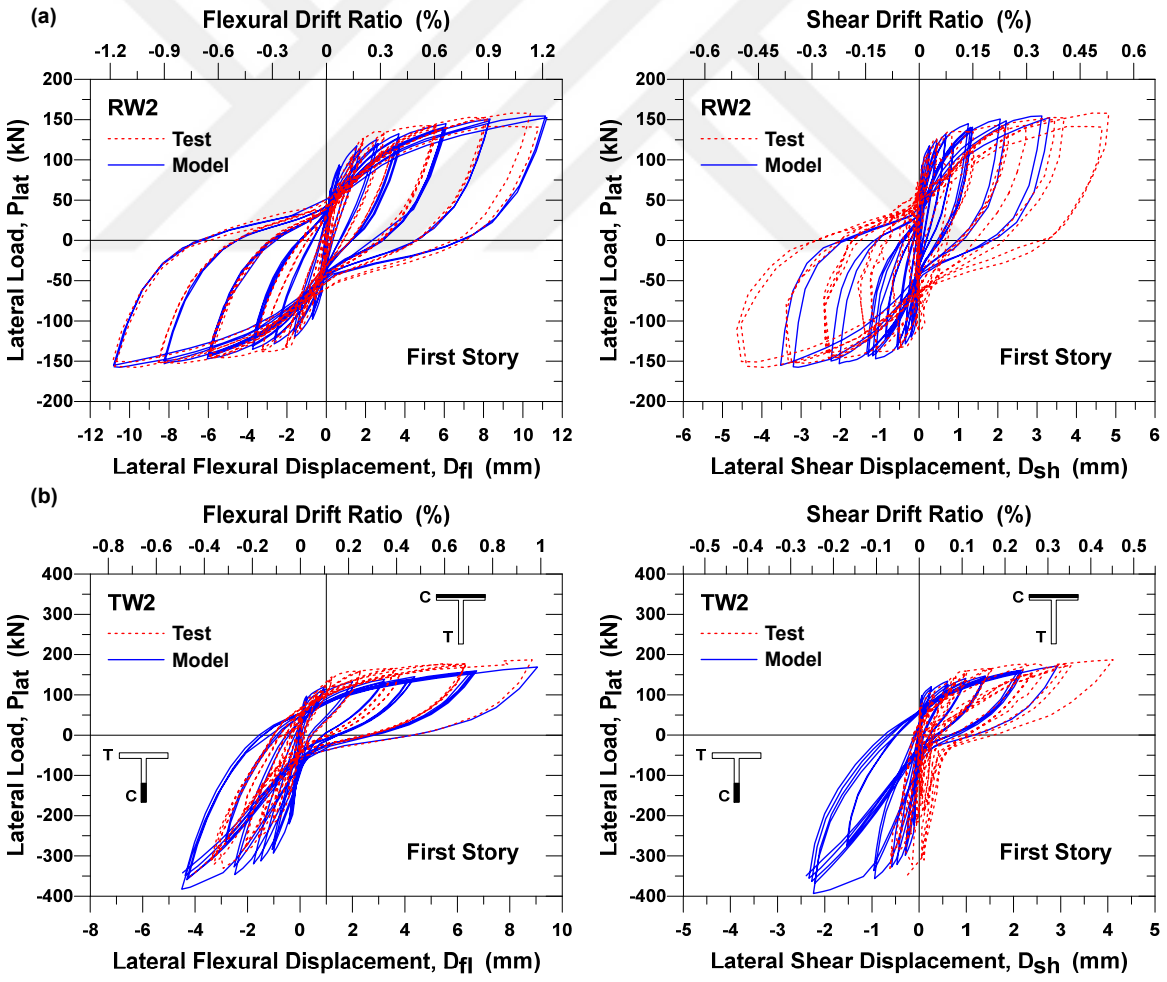

Figure 3.10. Lateral load vs. flexural and shear deformation responses for specimens: (a) RW2, (b) TW2.

For all medium-rise wall specimens, which experienced significant shear-flexure interaction responses, the contribution of shear and flexural deformations to wall lateral displacements were measured along the entire wall height during testing. As shown in Figure 3.11 to Figure 3.13, model predictions for the lateral load vs. top flexural and top shear displacement responses for these five specimens are accurate.

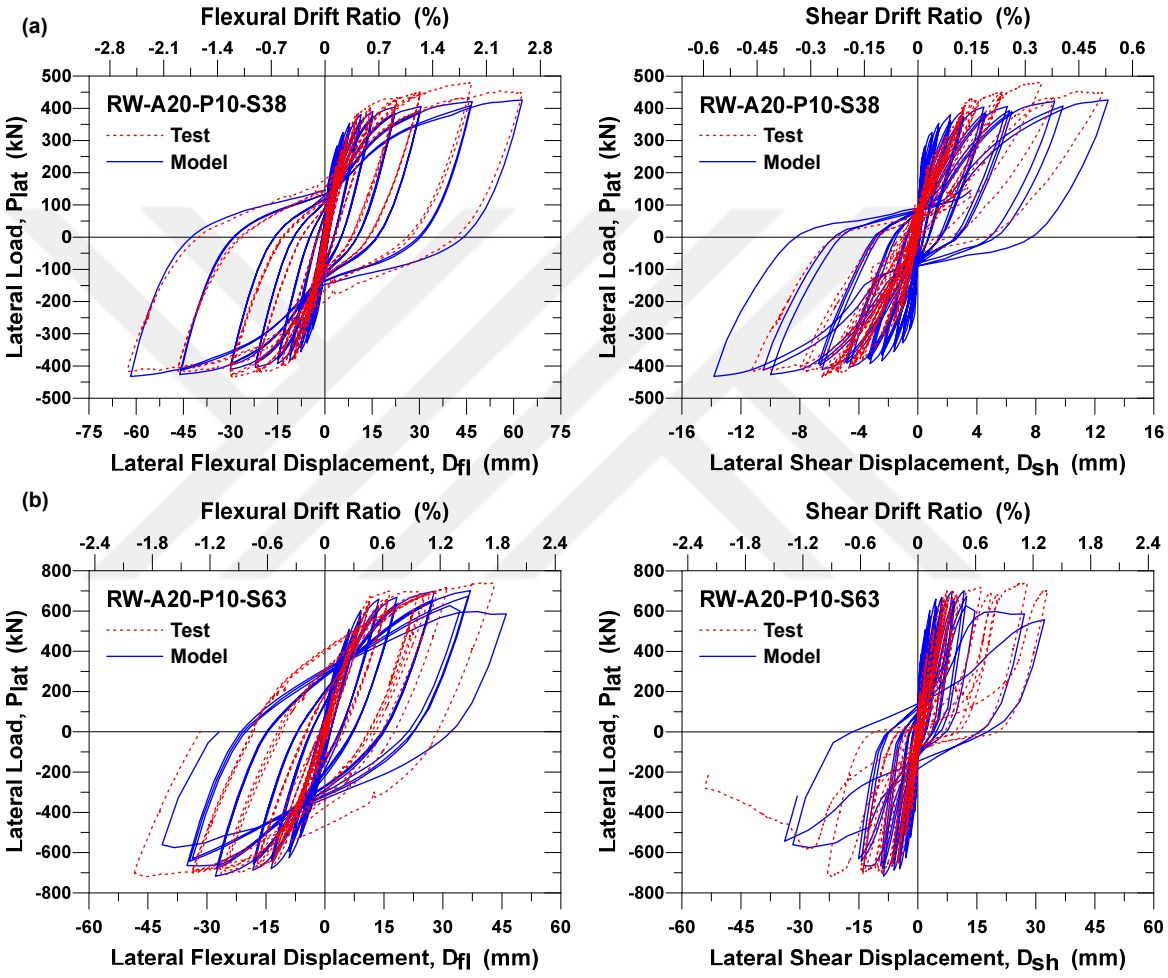

Figure 3.11. Lateral load vs. flexural and shear deformation responses for specimens: (a) RW-A20-P10-S38, (b) RW-A20-P10-S63.

The model successfully replicates the load vs. flexural displacement and the more-pinched load vs. shear displacement response characteristics of these walls, as well as the magnitudes of the flexural and shear components of top displacement. The model also well simulates the flexural initial stiffness and loading/unloading stiffness of medium rise wall specimens whereas shear stiffness predictions of the model at initial drift levels are larger

than experimental results. Medium rise wall specimens with aspect ratio of 2.0 represent flexural dominant responses compared to the wall specimens with aspect ratio of 1.5. The shape of the lateral load versus flexural deformation response of the specimens with higher aspect ratio (Figure 3.11) shows similar trends with the lateral load versus top displacement response of these specimens (Figure 3.8a and Figure 3.8b), indicating that model captures the flexural dominant response of these specimens. The specimen RW-A20-P10-S63 shows higher shear displacements than the specimen RW-A20-P10-S38 as a result of its higher shear stress level although they subjected to equal level of axial load and they have equal aspect ratio. The model is capable of simulating the nonlinear shear and flexural displacements of both specimens with equal aspect ratios but different shear response characteristics.

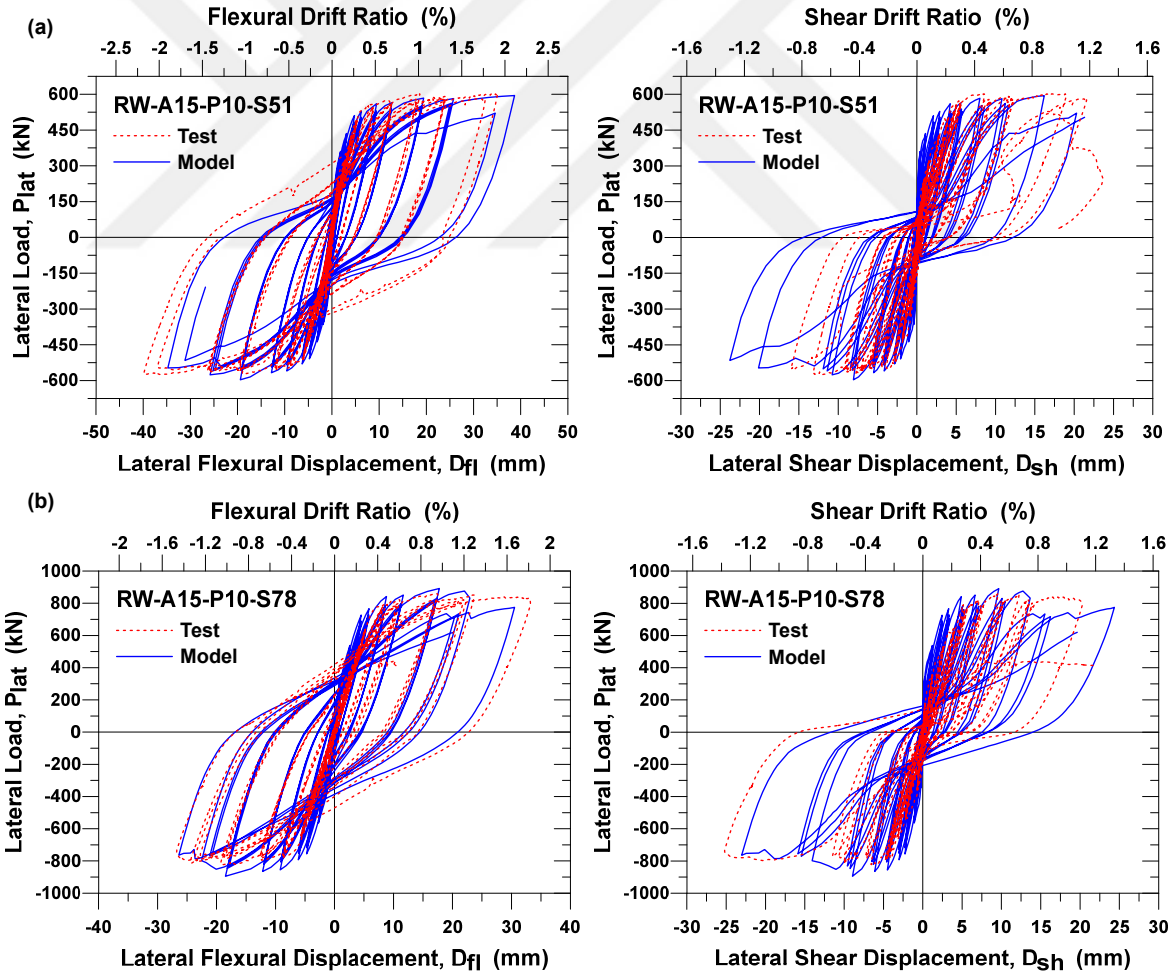

Figure 3.12. Lateral load vs. flexural and shear deformation responses for specimens: (a) RW-A15-P10-S51, (b) RW-A15-P10-S78.

As illustrated in Figure 3.12, lateral load vs. flexural deformation response of wall specimens with aspect ratio of 1.5 represent less pinching than their lateral load vs. top displacement responses, suggesting that flexural deformations are less pronounced for the specimens with aspect ratio of 1.5 compared to the specimens with aspect ratio of 2.0. The model fairly well simulates the shear and flexural displacement components of top displacement thorough the entire loading history. As it is shown in Figure 3.13, model estimations for the lateral load vs. flexural and shear deformation components of top displacement is also accurate for specimen S6, consolidating the reliability of the model in simulating coupled shear and flexural responses of walls.

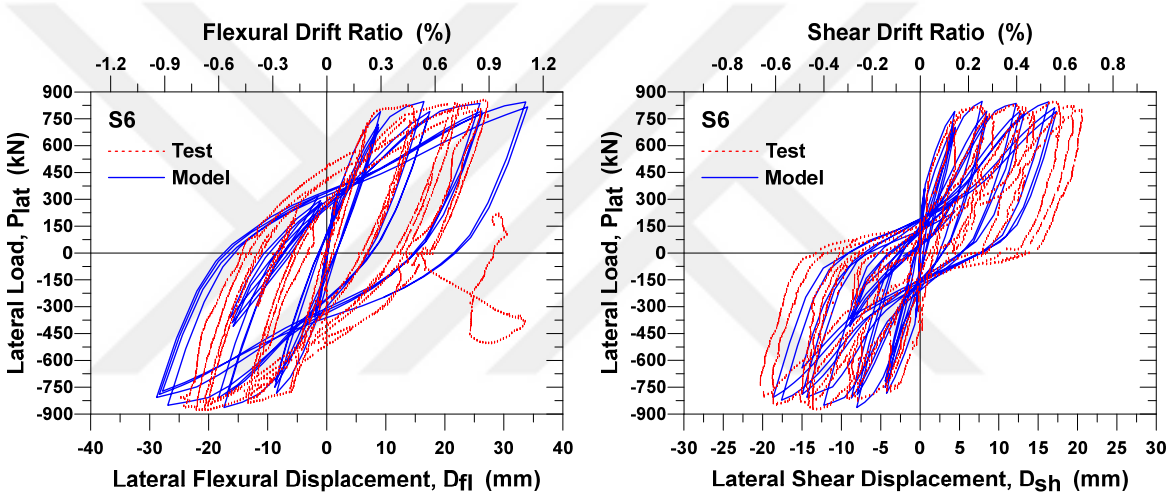

Figure 3.13. Lateral load vs. flexural and shear deformation responses for specimen S6.

3.3.3. Deformation Profiles along Wall Height

Comparison of model results and test measurements for the total lateral displacement, lateral flexural displacement, and lateral shear displacement profiles along the height of specimens RW2, RW-A20-P10-S38, RW-A20-P10-S63, RW-A15-P10-S51, RW-A15-P10-S78 at increasing drift levels, are presented in Figure 3.14 to Figure 3.18. Total, flexural and shear displacement profiles are plotted at peak drift levels in positive and negative loading directions. The total lateral displacement profiles, which follow an approximately linear distribution over wall height, are well-estimated by the model (Figure 3.14a to Figure 3.18a). It must be noted that during the analysis, only top displacement values that were identical to the test were applied on the model. The comparisons

presented in Figure 3.14 to Figure 3.18 are significant, since they demonstrate that the model can capture the coupling of nonlinear shear and flexural deformations (amplification of shear deformations in regions where nonlinear flexural deformations are larger), as well as the distribution of nonlinear flexural and shear deformations (spread of plasticity) along the height of a wall.

The lateral flexural displacement profile of the wall is well-predicted for specimen RW2 (Figure 3.14b), with nonlinear flexural deformations concentrated along the bottom quarter (915mm) of wall height, where flexural yielding was observed. The shape of the shear displacement profile predicted by the model is also representative of test results (Figure 3.14c), although the model slightly underestimates the shear displacements measured along the height of the wall, which is acceptable considering their very small magnitude. It must be mentioned that during testing of this wall, shear deformations were measured along the bottom two quarters of wall height (first two stories) only, and test results shown in Figure 3.14c assume zero shear deformations developing along the top two stories of the wall, whereas model results shown in Figure 3.14c consider shear deformations developing along entire wall height. In both model results and test measurements, shear deformations are amplified along the first story height of the wall, where nonlinear flexural deformations are also concentrated. The model clearly captures the nonlinear shear-flexure interaction behavior observed experimentally even for this slender wall specimen with flexure-dominated behavior, where the contribution of shear deformations to the top displacement of the wall was measured to be as low as 10%.

Comparison of model results and test measurements for the lateral total displacement, lateral flexural displacement and lateral shear displacement profiles along the height of the medium rise wall specimens (RW-A20-P10-S38, RW-A20-P10-S63, RW-A15-P10-S51 and RW-A15-P10-S78) are presented in Figure 3.15 to Figure 3.18. Total, flexural and shear displacements were obtained at 610 mm, 1016 mm, 1422 mm, 1829 mm, and 2438 mm for specimens RW-A20-P10-S38 and RW-A20-P10-S63 while at 610 mm, 1016 mm, 1422 mm, 1829 mm for specimens RW-A15-P10-S51 and RW-A15-P10-S78 above the wall-foundation interface. The lateral flexural displacement profile of the walls (Figure 3.15b to Figure 3.18b) are well-estimated by the model, with nonlinear flexural deformations concentrated along the bottom 610mm of the wall height,

corresponding to a plastic hinge length of half the wall horizontal length (l_w/2). The shapes of the measured and predicted shear displacement profiles are also in agreement (Figure 3.15c to Figure 3.18c), with decreasing shear distortions developing towards the top of the wall, demonstrating that the model captures coupling between nonlinear shear and flexural deformations, since shear deformations are amplified in regions where nonlinear flexural deformations are concentrated. The model also replicates the distribution of nonlinear flexural and shear deformations along the height of the wall, and therefore captures the so-called "spread of plasticity" along wall height. Inaccuracy of the model in predicting the flexural and shear displacement profiles at the last drift levels are probably associated with degradation in lateral load in both model results and test measurements at this drift levels.

3.3.4. Wall Vertical Growth

Figure 3.19 and Figure 3.20 compare model results and test measurements for the wall vertical growth (upward vertical displacement at the geometric centroid of the wall cross-section) vs. the lateral top displacement applied on wall specimens RW-A20-P10-S38, RW-A20-P10-S63, RW-A15-P10-S51 and RW-A15-P10-S78. Vertical growth of a wall is associated with the cumulative effect (along wall height) of the migration of the neutral axis on the wall cross-section (resulting in tensile strains at the wall centroid), which is associated with cracking of concrete and yielding of longitudinal reinforcement, as well as the nonlinear distribution of compressive stresses developing in concrete. Accuracy of the model in representing the experimentally-measured vertical growth behavior of both wall specimens is adequate. For specimen RW-A20-P10-S38 (Figure 3.19a), model results replicate the vertical growth measured at the peak (maximum) lateral displacements applied on the wall, as well as the residual (plastic) vertical growth at zero lateral displacement after unloading from the peak displacements. The model is less accurate in capturing the vertical growth behavior of specimens RW-A20-P10-S63 (Figure 3.19b) especially during the last loading cycles to a drift level of 3.0%, most probably due to initiation of lateral load degradation in the model results at this drift level.

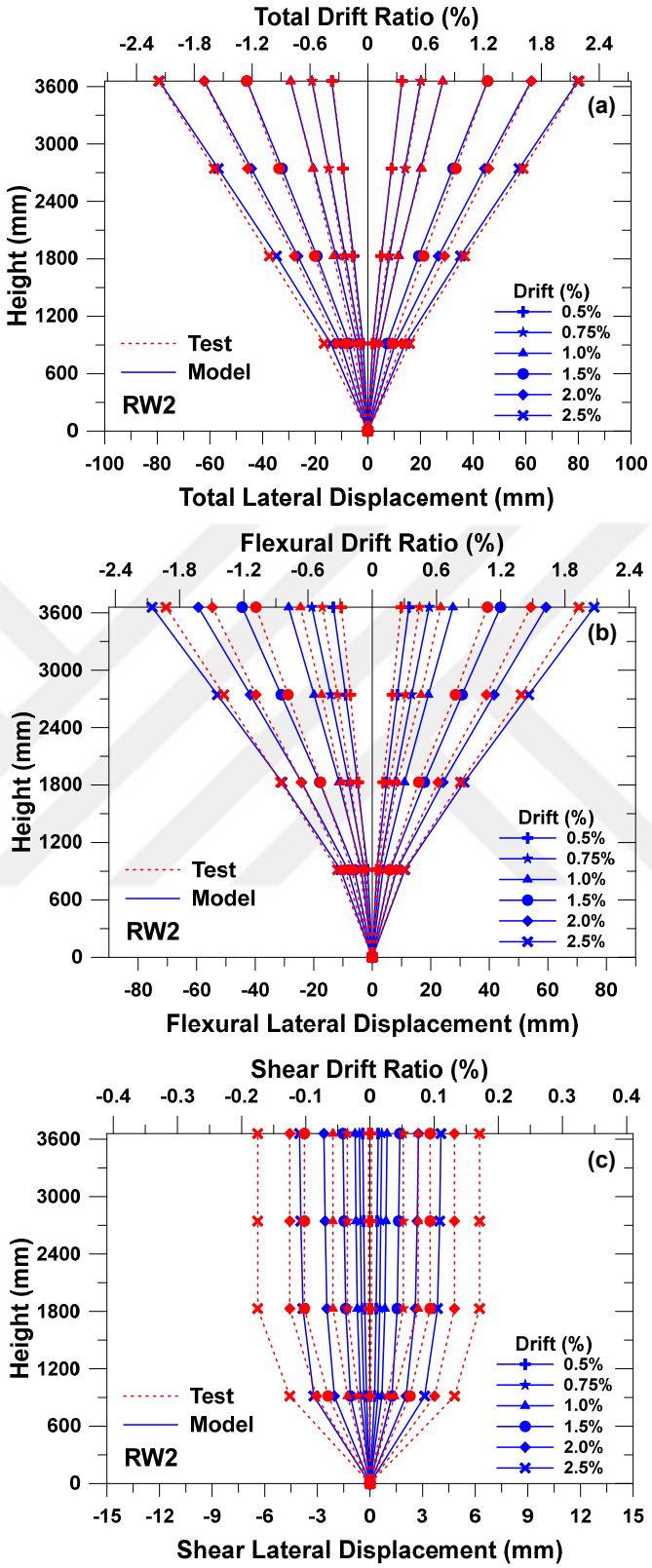

Figure 3.14. Displacement profiles along the height of specimen RW2: (a) total displacement, (b) displacement due to flexural deformation, (c) displacement due to shear deformation.

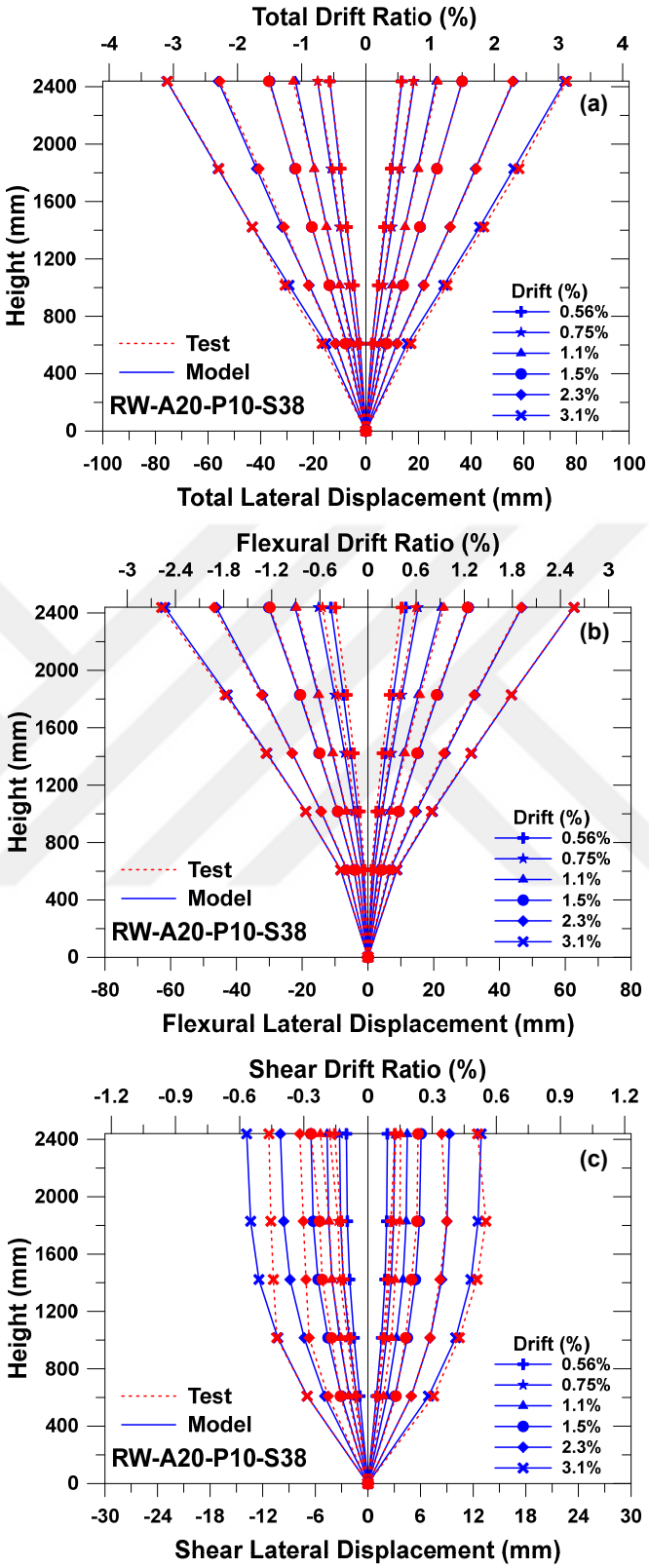

Figure 3.15. Displacement profiles along the height of specimen RW-A20-P10-S38: (a) total displacement, (b) displacement due to flexural deformation, (c) displacement due to shear deformation.

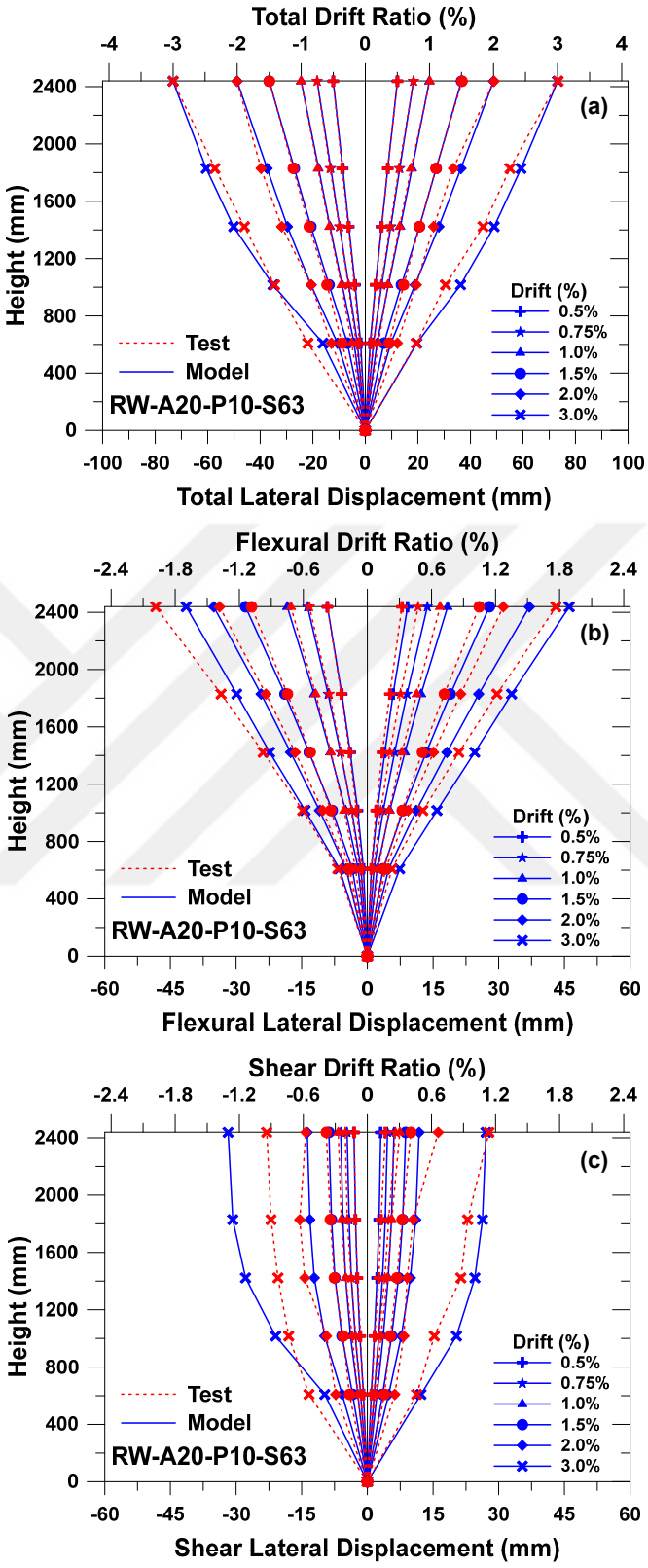

Figure 3.16. Displacement profiles along the height of specimen RW-A20-P10-S63: (a) total displacement, (b) displacement due to flexural deformation, (c) displacement due to shear deformation.

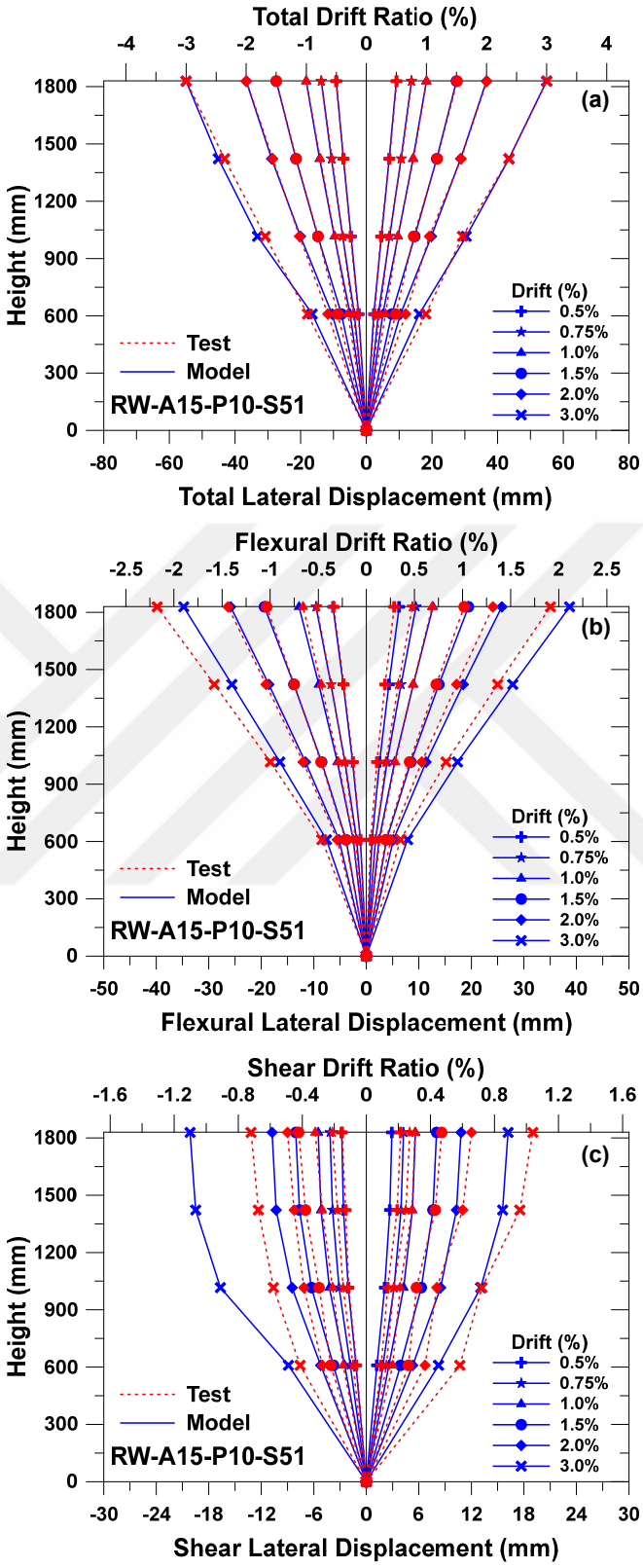

Figure 3.17. Displacement profiles along the height of specimen RW-A15-P10-S51: (a) total displacement, (b) displacement due to flexural deformation, (c) displacement due to shear deformation.

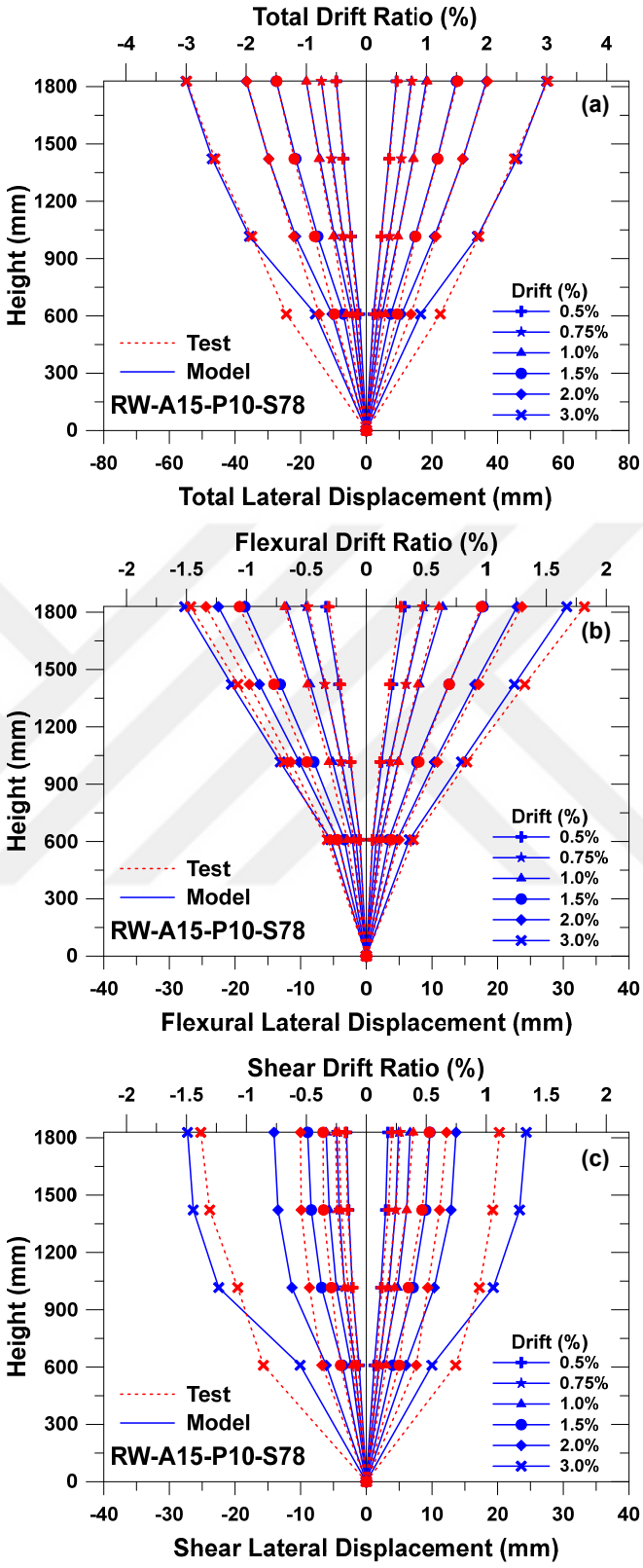

Figure 3.18. Displacement profiles along the height of specimen RW-A15-P10-S78: (a) total displacement, (b) displacement due to flexural deformation, (c) displacement due to shear deformation.

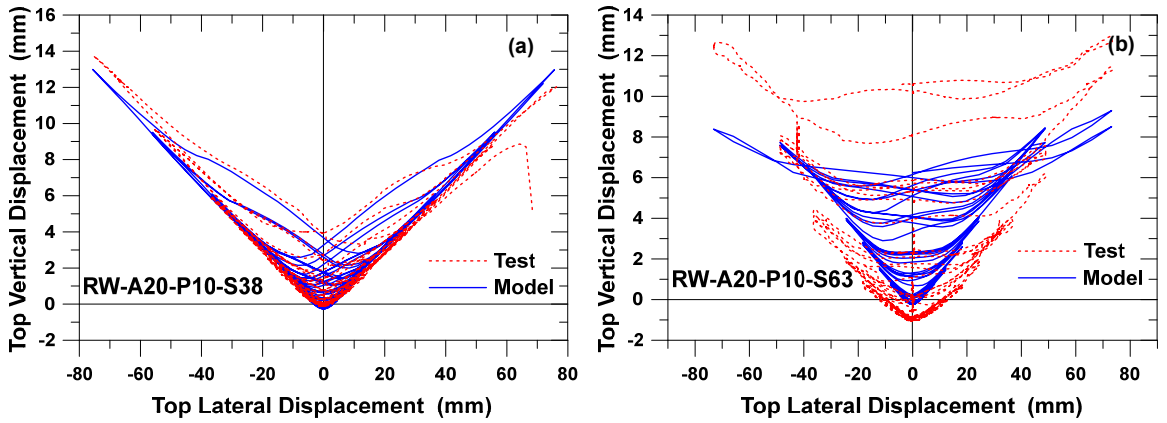

Figure 3.19. Vertical growth vs. top displacement for specimens: (a) RW-A20-P10-S38, (b) RW-A20-P10-S63.

Similar to model results for specimen RW-A20-P10-S63 in predicting wall vertical growth, the model shows discrepancies in wall vertical growth responses between model estimations and test results for specimen RW-A15-P10-S51 in negative load direction (Figure 3.20a), which is again due to degradation in lateral load capacity at this drift level. As shown in Figure 3.20b, the model accurately predicts the vertical growth of the wall not only at the maximum lateral displacements levels applied on the wall, but also the residual (plastic) vertical growth at zero lateral displacement after unloading from the maximum displacements.

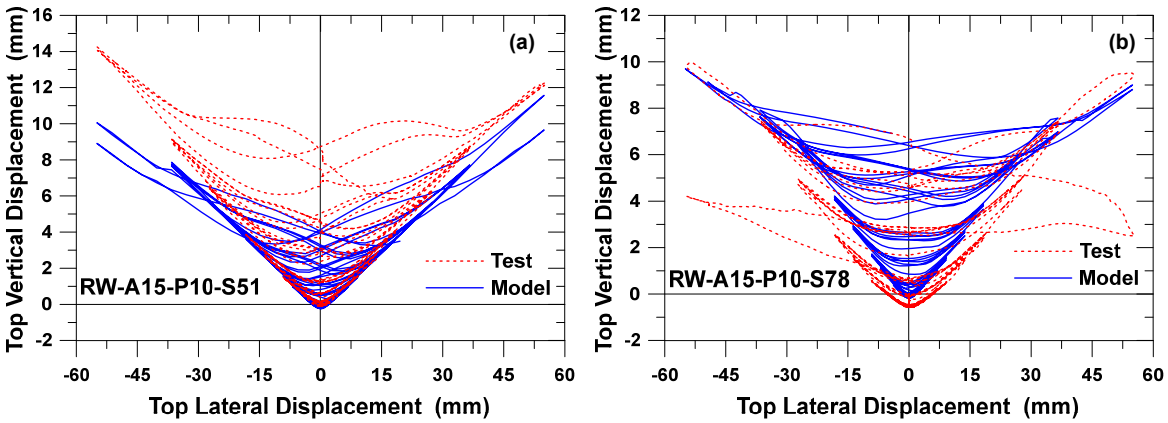

Figure 3.20. Vertical growth vs. top displacement for specimens: (a) RW-A15-P10-S51, (b) RW-A15-P10-S78.

3.3.5. Crack Patterns and Principal Compressive Stress Contours

The experimentally-observed crack patterns on specimens RW2, RW-A20-P10-S38, RW-A20-P10-S63, RW-A15-P10-S51 and RW-A15-P10-S78 are compared with model predictions in Figure 3.21 and Figure 3.22. Since cracking pattern photography of the specimen RW2, obtained at a drift level of 2.0%, (Figure 3.21) is not obviously visible, test results and model predictions are not plotted together. Drift ratios for plotting the cracking patterns were determined in accordance with the availability of the experimentally obtained photographs at higher drift levels. Little should be expected of the model in predicting the actual crack patterns recorded during the tests, since the cracks in the model are inherently discontinuous and crack directions in each model element differ, whereas the cracks propagate in a continuous manner during testing. Nevertheless, Figure 3.21 and Figure 3.22 show that the model provides reasonable estimations of crack orientations for all wall specimens indicating that the cracking criteria and the orthogonal crack assumption in the model formulation are both reasonable. The experimentally-observed cracks are naturally not perpendicular to each other; however, they are plausibly close to being perpendicular. In both test results and model predictions, the cracks are more horizontal at the wall boundaries where flexural (vertical) strains predominate over shear strains, and become more inclined towards the middle of the wall web where shear (diagonal tension) strains are more dominant. As well, the horizontal cracks at wall boundaries at the base of the wall become more inclined as they deviate from the base of wall, since the bending moment on the wall cross-section decreases towards the top of the wall while the shear force remains constant.

For the same specimens, Figure 3.23 and Figure 3.24 show contours of the analytically-predicted principal compressive stresses developing in concrete (also considering shear aggregate interlock stresses along crack surfaces), at the drift ratios approximately corresponds to the experimentally-measured lateral load capacity of these walls in the positive loading direction. All model predictions show concentration of compressive stresses within the wall boundary regions. Figure 3.23 presents the concrete compression distribution in boundary along the height of the wall, which is expected behavior of relatively slender walls. Stress contours obtained using the FSAFE model for medium rise wall specimens (Figure 3.24) indicates that the analytical model predicts a

diagonal compression strut that is oriented from the top left to the bottom right corner of the wall. The analytically predicted diagonal compression strut is consistent with observed experimental behavior of the specimen in which strength degradation was initiated by the crushing of concrete at the wall compression boundary, due to stresses transferred along a diagonal strut.

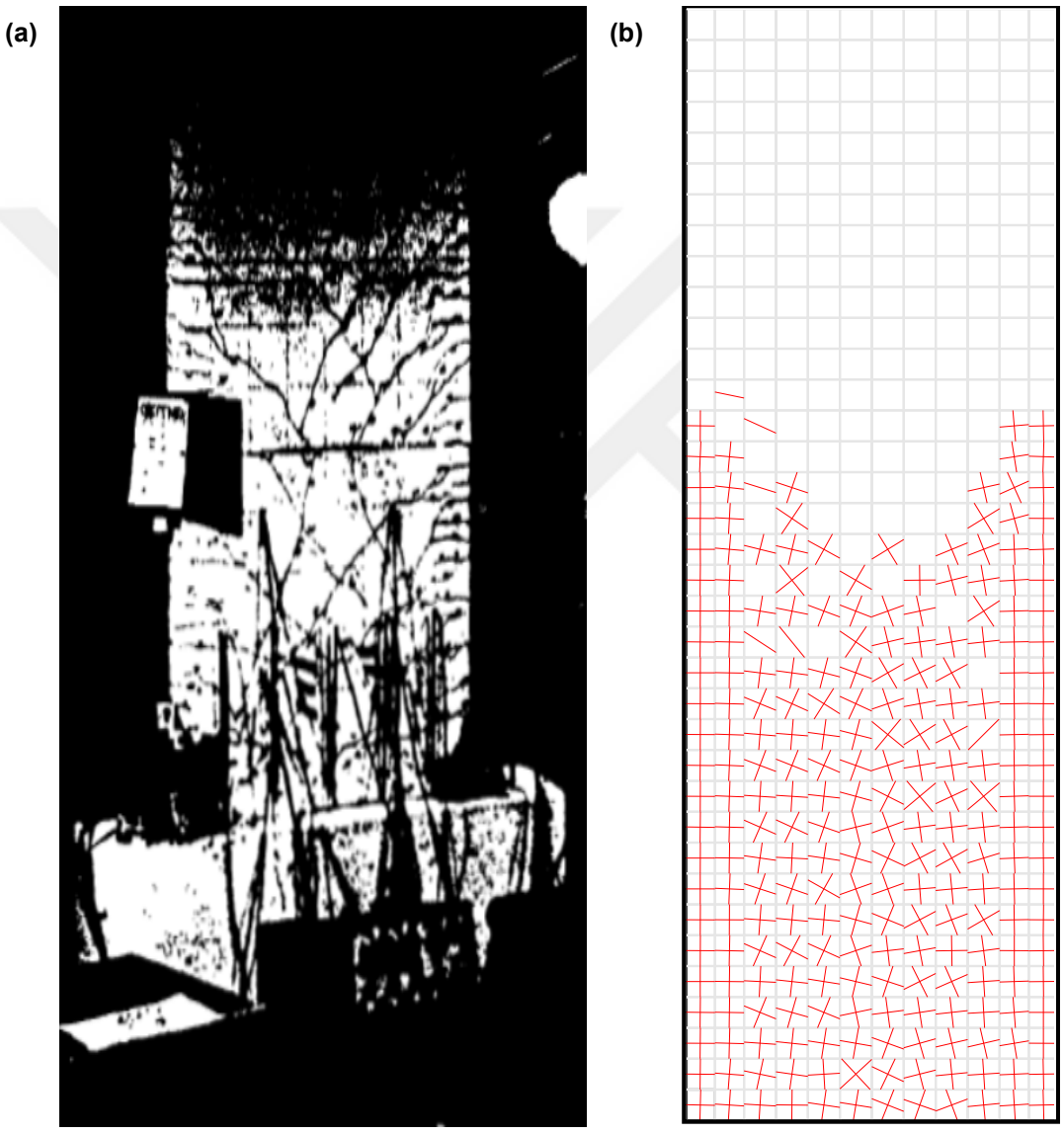

Figure 3.21. Crack patterns for specimen RW2 at 2.0% drift: (a) Test (b) Model.

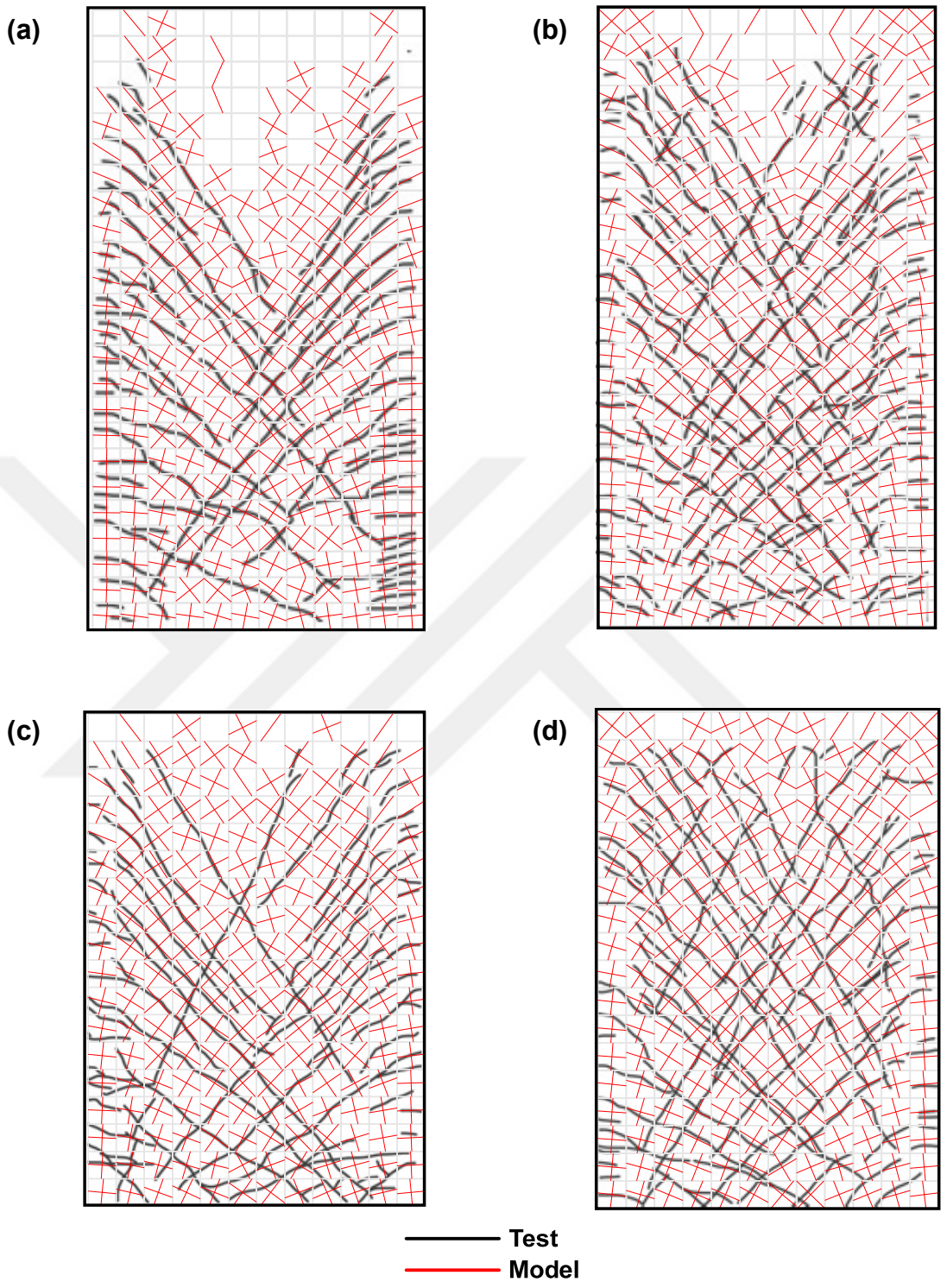

Figure 3.22. Crack patterns for specimens: (a) RW-A20-P10-S38 at 1.5% drift, (b) RW-A20-P10-S63 at 1.5% drift, (c) RW-A15-P10-S51 at 3.0% drift, (d) RW-A15-P10-S78 at 2.0% drift.

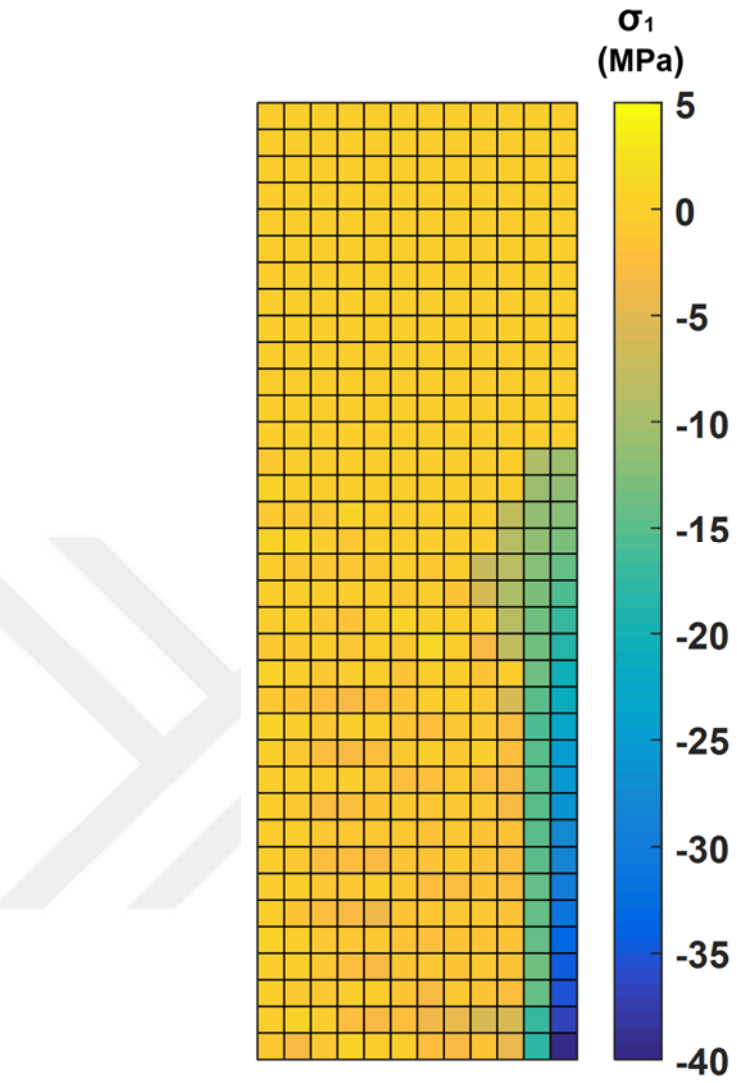

Figure 3.23. Concrete principal compressive stress contours for specimen RW2 at 2.0% drift.

3.3.6. Vertical Normal Strain Profiles at Wall Base

In order to evaluate the accuracy of the model in capturing local deformations on the walls, representative comparisons of model predictions with vertical (longitudinal) strain profiles measured along the base of selected wall specimens at various peak drift levels, is presented in Figure 3.25 and Figure 3.26. It can be observed from the figures that the FSAFE model predicts nonlinear distribution of strains along the wall base, as opposed to typical macroscopic models where the plane-sections assumption enforces a linear strain distribution.

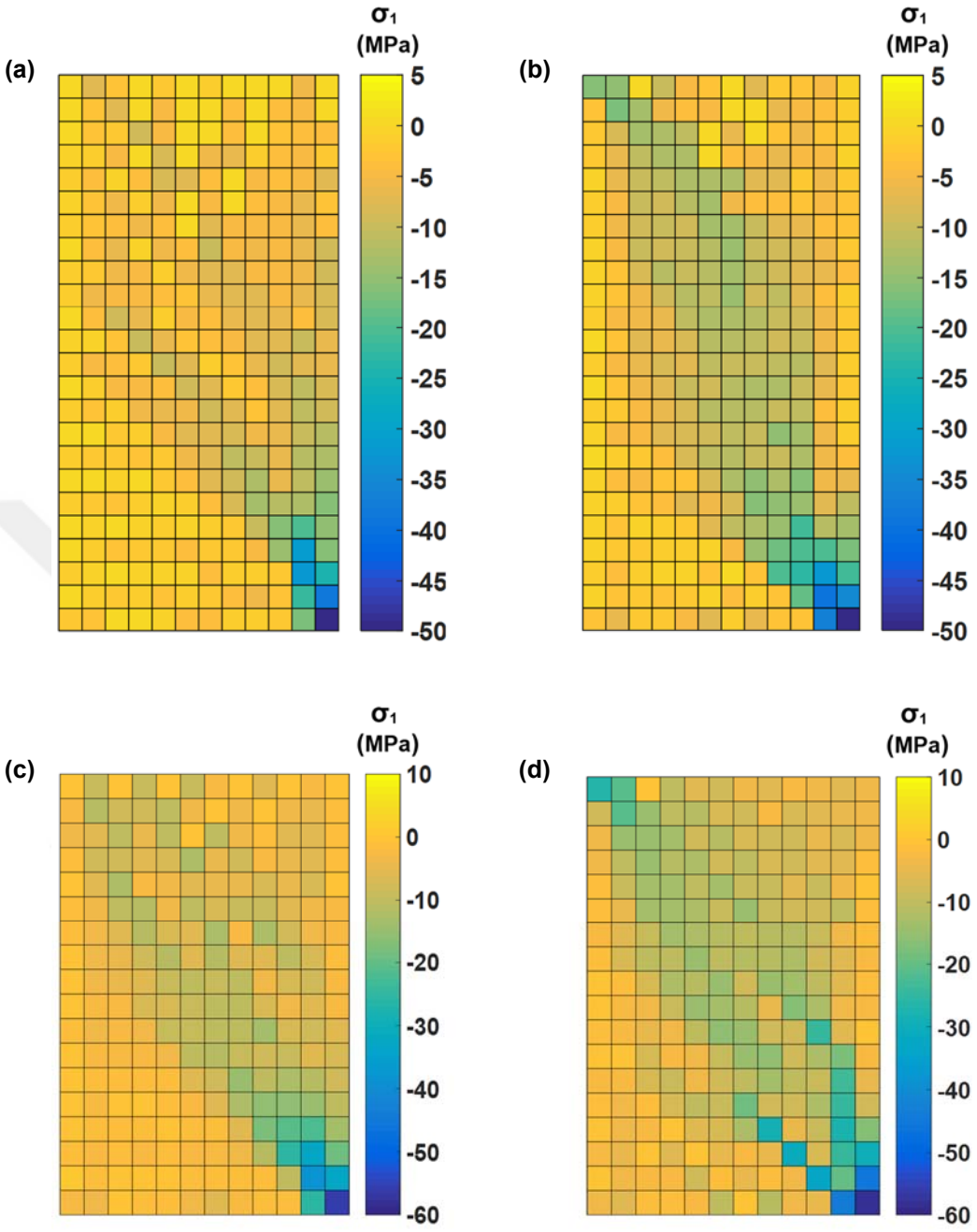

Figure 3.24. Concrete principal compressive stress contours for specimens: (a) RW-A20-P10-S38 at 2.2% drift, (b) RW-A20-P10-S63 at 2.0% drift, (c) RW-A15-P10-S51 at 1.5% drift, (d) RW-A15-P10-S78 at 2.0% drift.

As shown in Figure 3.25 for the relatively slender wall specimen RW2 with flexure-dominated behavior, the model is accurate in predicting both compressive and tensile strains measured at the wall base (with an error margin of approximately 25% in compressive strain predictions) as well as the depth of the neutral axis on the wall cross-

section. This is a significant attribute of the FSAFE model, since previous analytical studies (e.g., Orakcal and Wallace, 2006) have shown that using a fiber-based flexural model formulation for simulating the response of this particular wall specimen results in significant underestimation of compressive strains, with the predicted strains corresponding to approximately one-third of the measured values. Unlike in fiber models, plane sections do not remain plane in the present finite element modeling approach (due to the in-plane shear lag effect resulting from nonlinear shear deformations on the wall), which is more consistent with the experimentally-measured strain profiles, and provides improved predictions of especially compressive strains in concrete, even for such walls with flexure-governed responses.

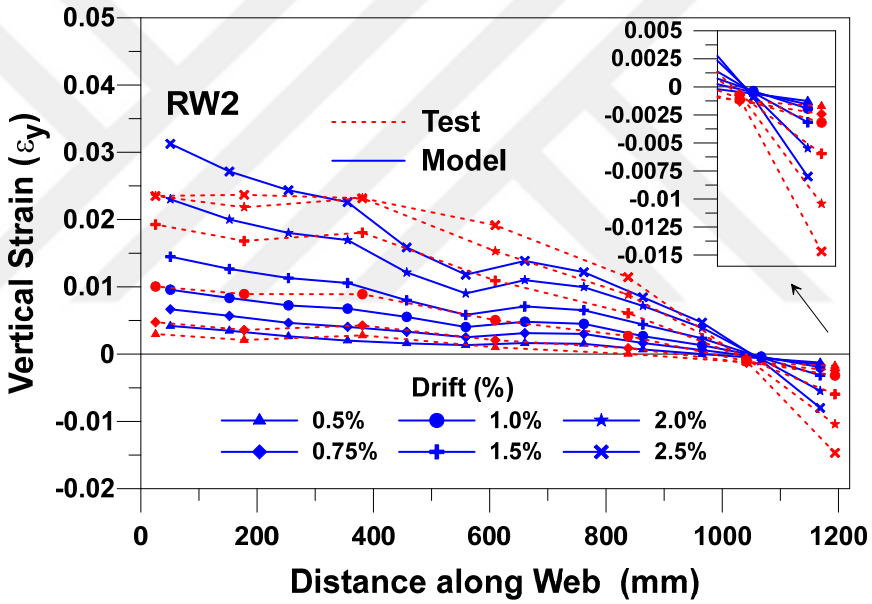

Figure 3.25. Vertical normal strain profiles at wall base for specimen RW2.

For the medium-rise wall specimens RW-A20-P10-S63, RW-A15-P10-S51 and RW-A15-P10-S78 that exhibited coupled nonlinear shear-flexural responses, model estimations for the vertical strain profiles at wall bases are again, representative of test results at various drift levels (Figure 3.26). As illustrated in figures, the model well simulates the distribution of strains along the wall base as well as the maximum compressive and tensile strains at corners of the walls. Additionally, model captures the depth of the neutral axis on the wall cross-section and the nonlinear distribution of the strains along the wall base, which is consistent with the nonlinear behavioral characteristics of walls.

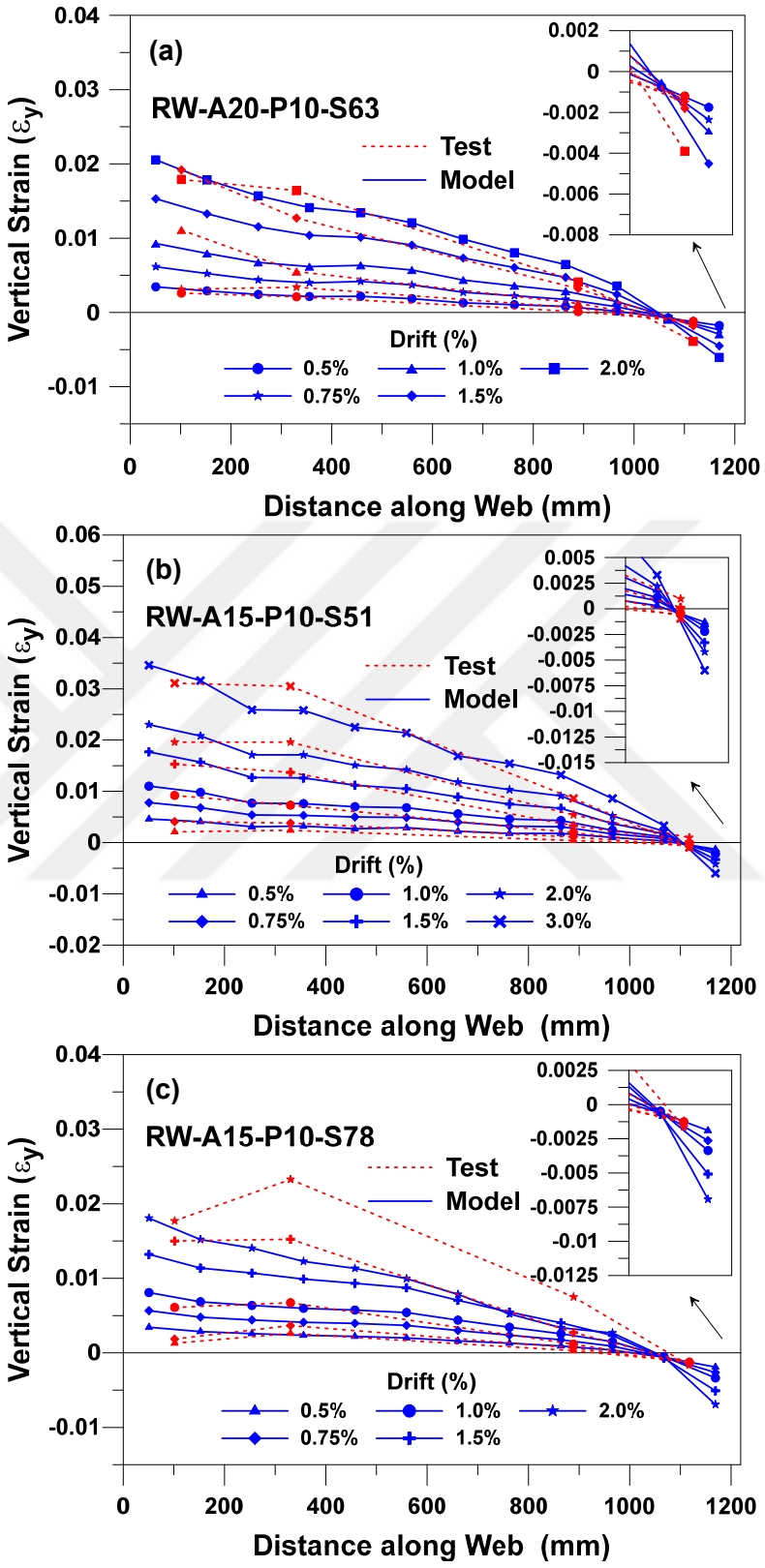

Figure 3.26. Vertical normal strain profiles at wall base for specimens: (a) RW-A20-P10-S63, (b) RW-A15-P10-S51, (c) RW-A15-P10-S78.

In Figure 3.27a and Figure 3.27b, model estimations are compared with the experimentally-measured vertical strain profiles at the base of the T-shaped wall specimen along its web, until a nominal drift level of 1.5% (as measured), in positive (wall flange in compression) and negative (wall flange in tension) loading directions. It must be noted that the drift levels presented in the legends of Figure 3.27a and Figure 3.27b are nominal drift levels, whereas the magnitude of the actual (net) drift ratios that the specimen was subjected to (e.g., shown in Figure 3.5b) become smaller when the contributions of pedestal sliding and rotation to top displacement are removed (see Orakcal and Wallace, 2006). For example, the last loading cycles shown in Figure 3.5b correspond to a nominal drift level of 2.5%. As shown in Figure 3.27a and Figure 3.27b, the model reasonably captures the magnitudes of the measured compressive and tensile strains along the web of this wall specimen also, with an error margin of approximately 25% at the web boundaries, which is again an improvement over results of previous modeling studies (Orakcal and Wallace, 2006) where using a fiber model was shown to underestimate the compressive strains on this wall by as much as 70%. However, the model is not successful in predicting the neutral axis location on the wall cross-section at a nominal drift level of 1.5% in the negative loading direction (Figure 3.27b), at which time the web boundary region of the wall may have started to experience out-of-plane instability.

Comparison of model results and test measurements for the vertical strain profiles at wall base along the flange of specimen TW2 (perpendicular to the loading direction), at increasing peak drift levels in the negative loading direction (flange in tension), up to a nominal drift level of 2.5%, is presented in Figure 3.27c. During testing of this wall, it was possible to measure the strains along the wall flange at also the drift levels of 2.0% and 2.5%, since the flange did not experience significant damage (concrete crushing) throughout the test. As depicted in the figure, the model captures the shear lag effect along the wall flange perpendicular to the loading direction, as the vertical strain magnitudes decrease as one diverges from the web-flange intersection, which is another salient characteristic of the FSAFE model. Model predictions of vertical strains are accurate at nominal drift levels up to 1.5%; however, at drift levels of 2.0% and 2.5%, the model underestimates the tensile strains measured along the flange by as much as 45%.

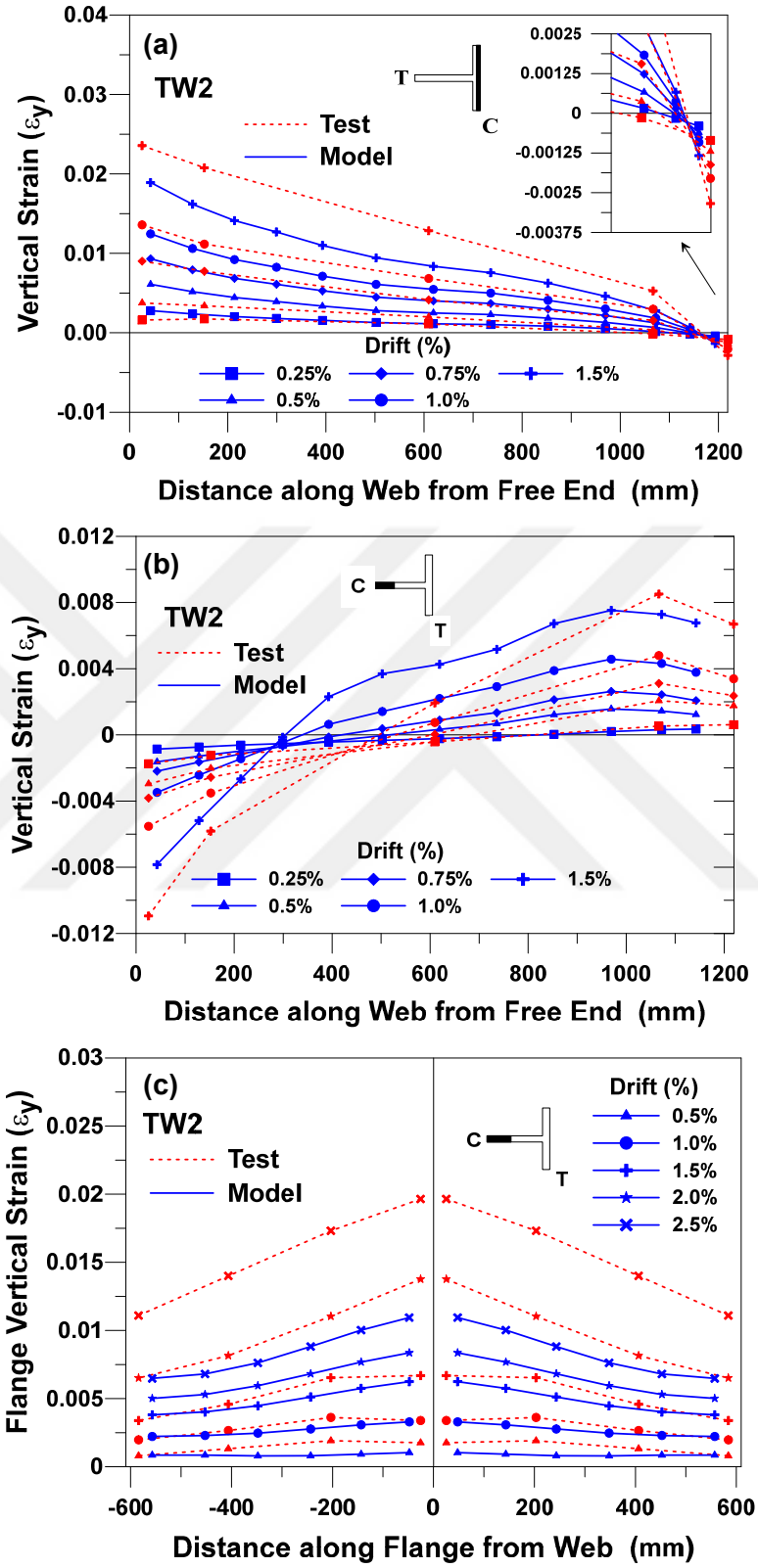

Figure 3.27. Vertical normal strain profiles at wall base for specimen TW2: (a) along the web when the flange is in compression, (b) along the web when the flange is in tension, (c) along the flange when the flange is in tension.

3.3.7. Other Local Response Predictions

Figure 3.28a and Figure 3.28b compare model predictions of the distribution of vertical (longitudinal) strains along the height of the wall, with measurements obtained using mechanical strain gauges mounted on all four corners of the wall specimen, at various drift levels applied in positive and negative loading directions. In Figure 3.29a, the distribution of average curvatures, measured along wall height using LVDT chains attached to the wall boundaries, are compared with model results. Additionally, a comparison of model predictions with test measurements for the cumulative contribution of flexural deformations (relative rotations) measured along wall height to the total flexural displacement at the top of the wall is shown in Figure 3.29b. Finally, model predictions for the ratio of the contribution of shear deformations to the top displacement of the wall to that of flexural deformations, for increasing values of top displacement, are reasonably accurate, as depicted in Figure 3.29c. Comparisons presented in Figure 3.28 to Figure 3.29 clearly demonstrate that the model provides accurate estimations of the distribution of flexural deformations (vertical strains, curvatures, rotations) over the entire wall geometry, indicating that model is reliable in simulating the spreading of flexural plasticity in a wall.

Model estimations for the contribution of shear deformations to the top lateral displacements of the wall specimen S6 (Figure 3.30) is accurate, revealing that the model is consistent in representing coupled shear and flexural responses of medium rise walls.

As illustrated in Figure 3.31, which compares model predictions with test results for the lateral load applied on the wall vs. the shear distortion measured along the bottom 40% of wall height, the model does not capture the large the shear distortions measured during the last three drift levels applied on the wall specimen R2. However, the experimentally-observed behavior and failure mode of this wall was unique. According to test observations provided by Oesterle *et al.* (1976), since zero-axial load applied during the experiment, horizontal cracks on the boundaries did not fully close upon load reversals, increasing the dowel demands on longitudinal bars and resulting in sliding along cracks. The model is not capable of predicting this complex behavioral mode of the specimen R2.

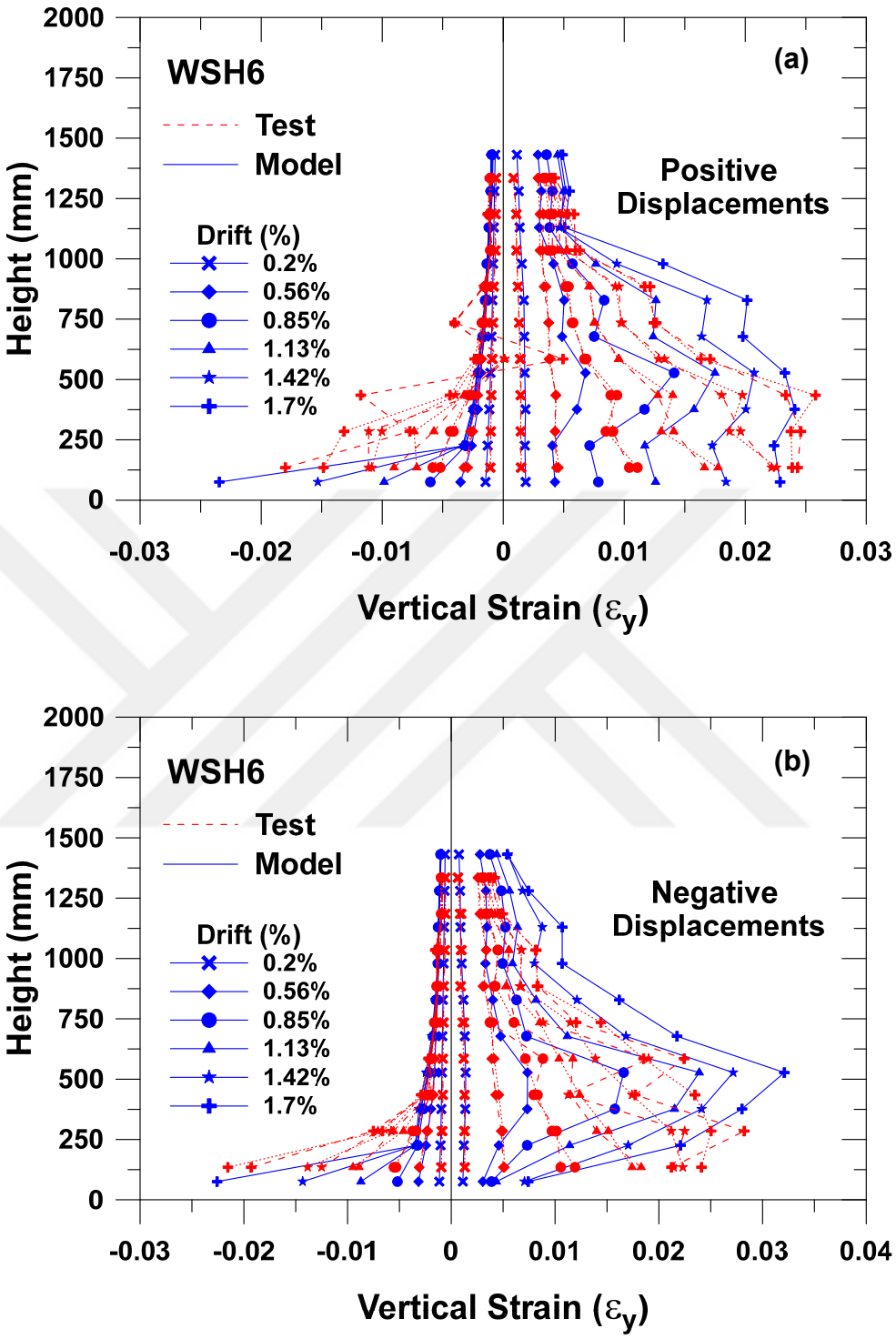

Figure 3.28. Specimen WSH6: (a) vertical strains at wall boundaries along wall height under positive displacements, (b) vertical strains at wall boundaries along wall height under negative displacements.

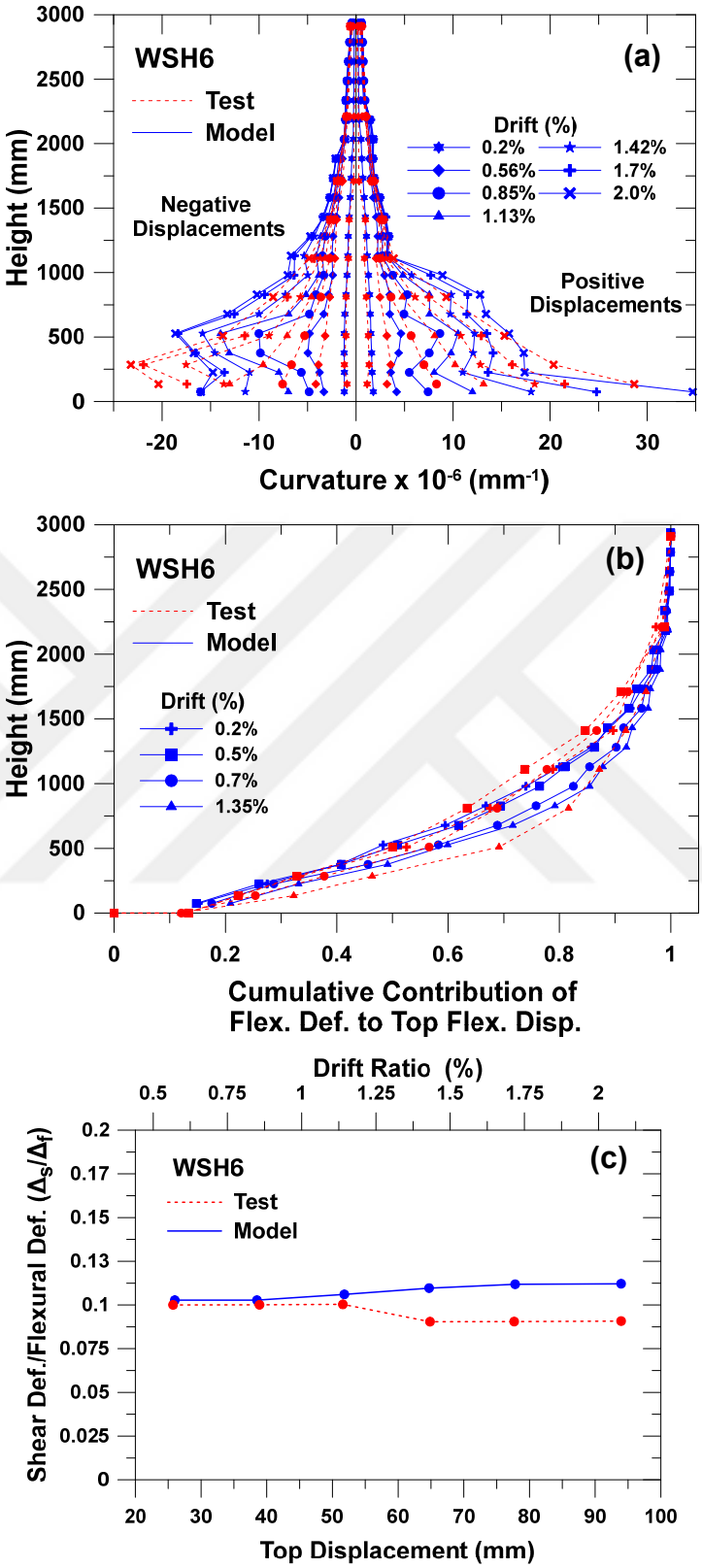

Figure 3.29. Specimen WSH6: (a) curvature profile along wall height, (b) cumulative contribution of flexural deformations along wall height to top flexural displacement, (c) shear deformation to flexural deformation ratio.

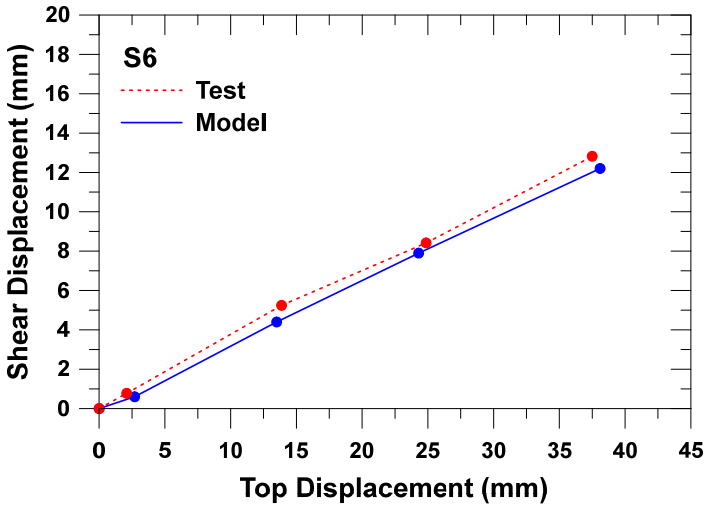

Figure 3.30. Shear deformation contribution to top displacement for specimen S6.

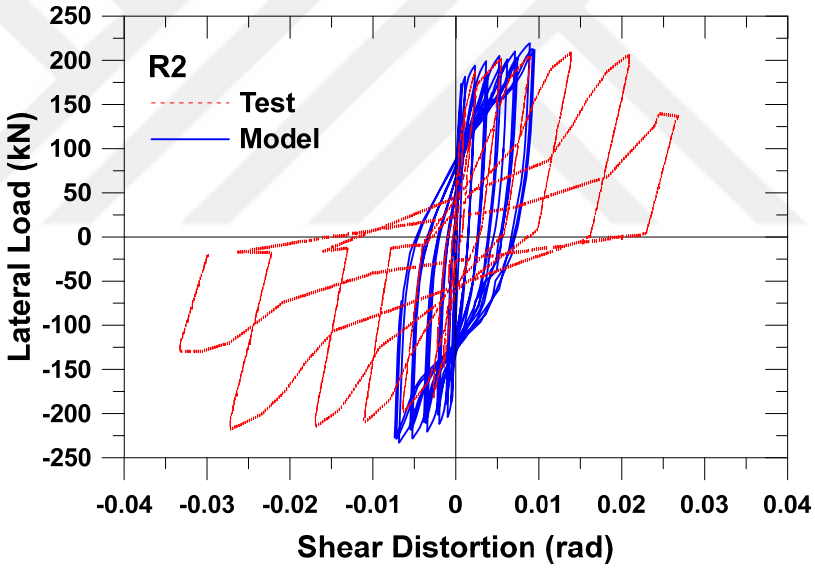

Figure 3.31. Lateral load vs. shear distortion along the bottom 1830mm (40%) of wall height for specimen R2.

3.4. Mesh Sensitivity Analysis

Geometric discretization of the FSAFE model for simulation of the wall specimens analyzed in this study was achieved by standardized approach described in Section 3.2.1. It was observed that using a finer mesh of model elements did not significantly influence the model response predictions, other than the rate of degradation in lateral load after the wall

lateral load capacity is reached. For example, Figure 3.32 to Figure 3.40 show the sensitivity of the model global and local response predictions for specimen RW-A15-P10-S51, to the number of model elements used in the horizontal direction (m) and the number of model elements used in the vertical direction (n) of the wall. Model predictions with coarser (m=6, n=9), medium (m=12, n=18) and finer (m=24, n=36) mesh discretization are compared for inspecting the sensitivity of the model for different number of model elements in horizontal and vertical directions. The medium mesh corresponds to the standard discretization approach used in this study for all wall specimens, whereas results of the model with coarser and finer mesh are also shown for comparison. Although comparison of model predictions with test results using medium (m=12, n=18) mesh discretization for specimen RW-A15-P10-S51 are presented in the previous subsections, comparison of model predictions with medium mesh discretization are again presented in this section for the sake of integrity of the content.

Figure 3.32 and Figure 3.33 show that the lateral load vs. top displacement as well as the lateral load vs. flexural and shear deformation response predictions of the model are not significantly different when the medium and finer mesh are compared, other than a slightly more pronounced rate of degradation in lateral load. However, using coarser mesh leads to initiation of degradation and higher rate of degradation in lateral load capacity compared to medium and finer mesh discretizations as well as less flexural deformations and more shear deformations than test results and model predictions with medium and finer mesh dicretizations. Figure 3.34 to Figure 3.36 compare the model predictions and experimental results for total, flexural and shear deformation profiles along wall height for coarser, medium and finer model discretizations. Although total deformation profiles along wall height for the three different discretizations resemble each other, flexural and shear deformation profiles along wall height differentiate, which may be attributed to the initiation of degradation in lateral load capacity. Figure 3.37 compares the vertical growth vs. top displacement responses of the model and test results for the same mesh discretization. Model predictions are again similar for coarser, medium, and finer mesh discretizations before lateral load degradation starts. Crack orientations and principal concrete compressive stress contours are presented in Figure 3.38 and Figure 3.39, representatively. The magnitude of the principal concrete compressive stress in concrete obtained using a coarser mesh is smaller compared to medium and finer mesh

configurations. Finally, model predictions for vertical strain profiles along the base of the wall for the three different mesh configurations are compared with test results in Figure 3.40. Similarly, refinement of the mesh does not result in noticeably different vertical (longitudinal) strain profiles along the base of the wall when medium and finer mesh configurations are used, except at the highest drift level, due to degradation of lateral load at this drift level. As discussed above, using the medium mesh discretization for the wall specimen RW-A15-P10-S51 provides improved response predictions compared to coarser mesh discretization, and very similar response predictions compared to finer mesh discretization. When computational time and rate of convergence of the model results are also considered, using the medium mesh configuration (the standardized discretization approach used for all wall specimens) is more efficient than the finer mesh configuration. Similar results were obtained for all wall specimens investigated, consolidating the standardized geometric discretization approach used in this study.

3.5. Overview

The aim of this chapter was to provide detailed information on the numerical calibration and experimental validation of the FSAFE model for selected RC wall specimens with flexure controlled or coupled shear flexural responses, where flexural yielding was observed. Test specimens used for verification of the model first introduced and modeling parameters of those specimens obtained based on the as-tested material properties were presented. The analytical model was subjected to the same conditions (test setup and loading protocol) as the experimental programs. Model predictions for relatively slender wall specimens with rectangular and non-rectangular cross sections and medium rise walls with rectangular cross sections were compared with corresponding test results at global and local response levels. Comparison of the lateral load vs. top displacement responses of test results and model predictions were presented. Local response predictions of the model (e.g., vertical normal strain profile, crack patterns) were also compared with corresponding test results to demonstrate the capability of the model for predicting such local responses. In addition, other important response predictions of the model (e.g., curvature distribution along wall height) for three wall specimens from three different experimental programs were presented. Finally, sensitivity of the model predictions to mesh discretization was shown in this chapter.

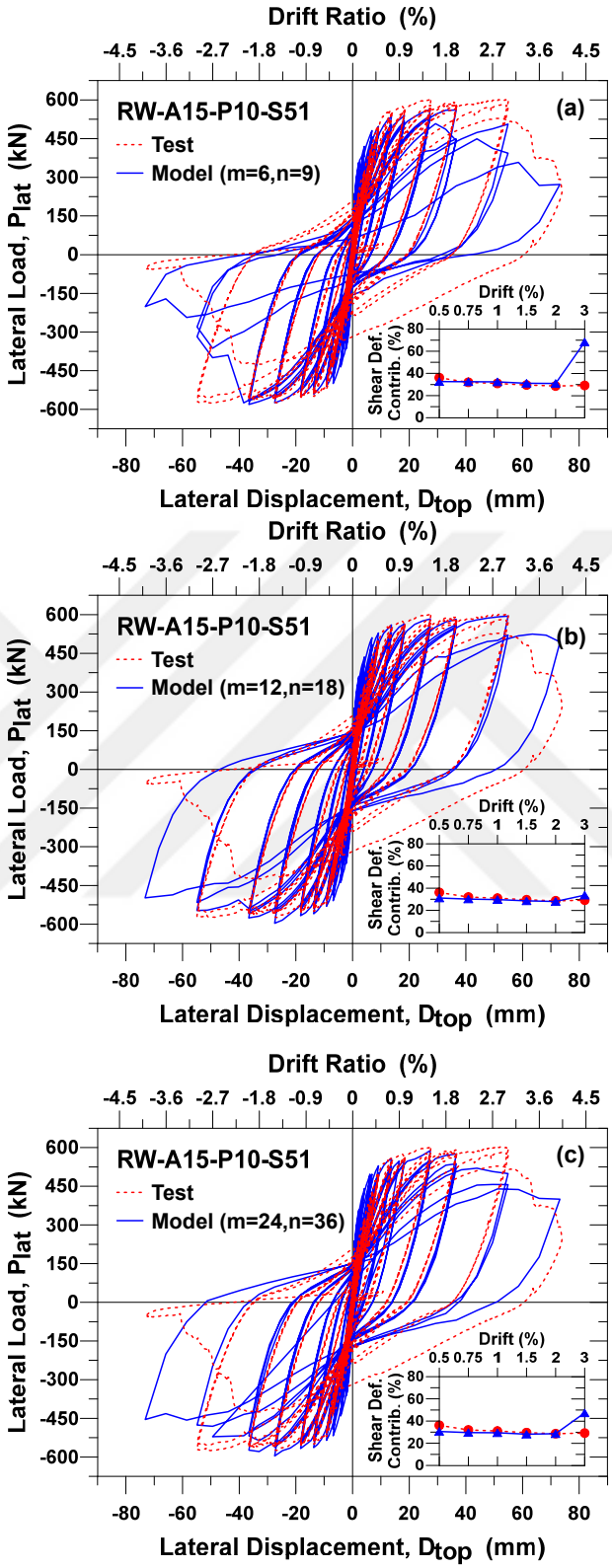

Figure 3.32. Sensitivity of model lateral load vs. top displacement responses to number of model elements used in horizontal (*m*) and vertical directions (*n*): (a) *m*=6, *n*=9 (b) *m*=12, *n*=18, (c) *m*=24, *n*=36.

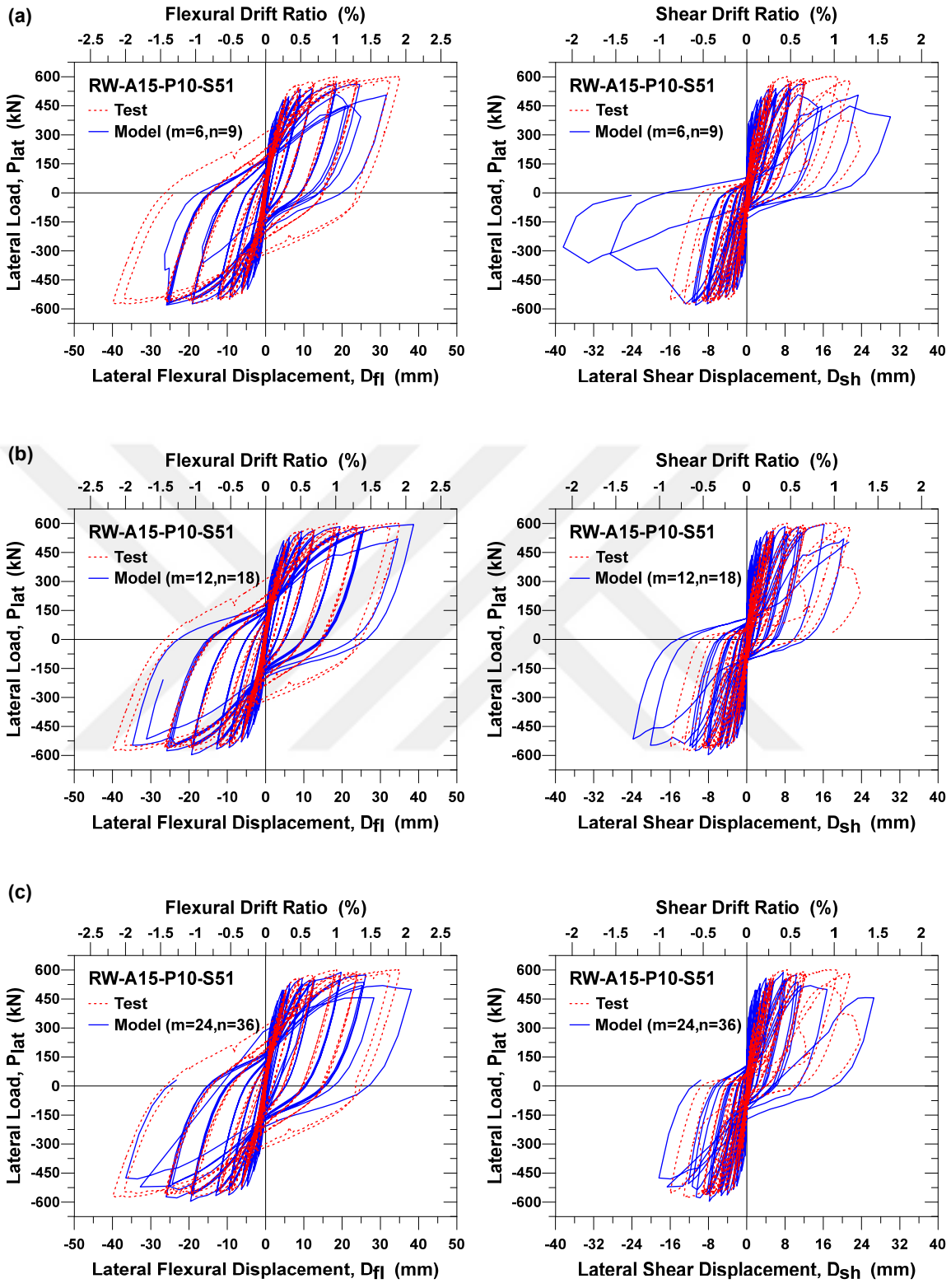

Figure 3.33. Sensitivity of model lateral load vs. flexural and shear deformation responses to number of model elements used in horizontal (m) and vertical (n) directions: (a) m=6, n=9 (b) m=12, n=18, (c) m=24, n=36.

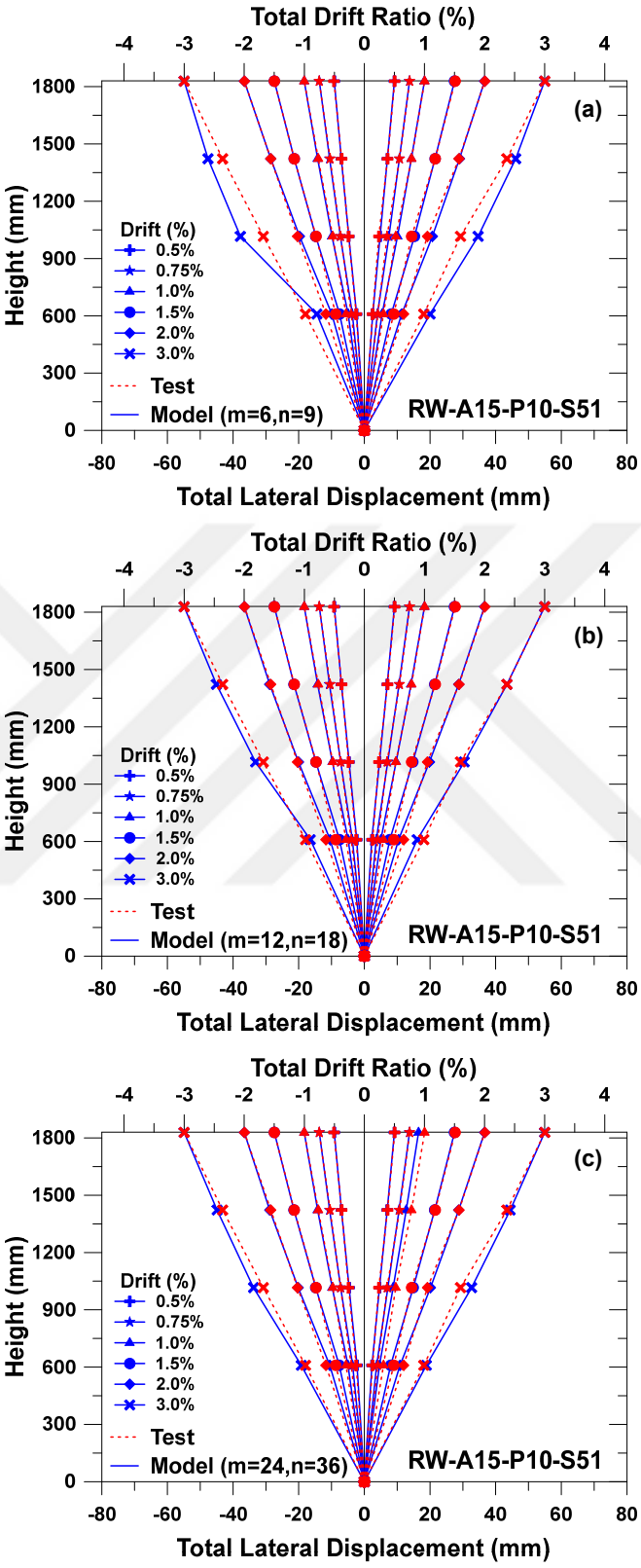

Figure 3.34. Sensitivity of model total displacement profile along wall height responses to number of model elements used in horizontal (m) and vertical (n) directions: (a) m=6, n=9 (b) m=12, n=18, (c) m=24, n=36.

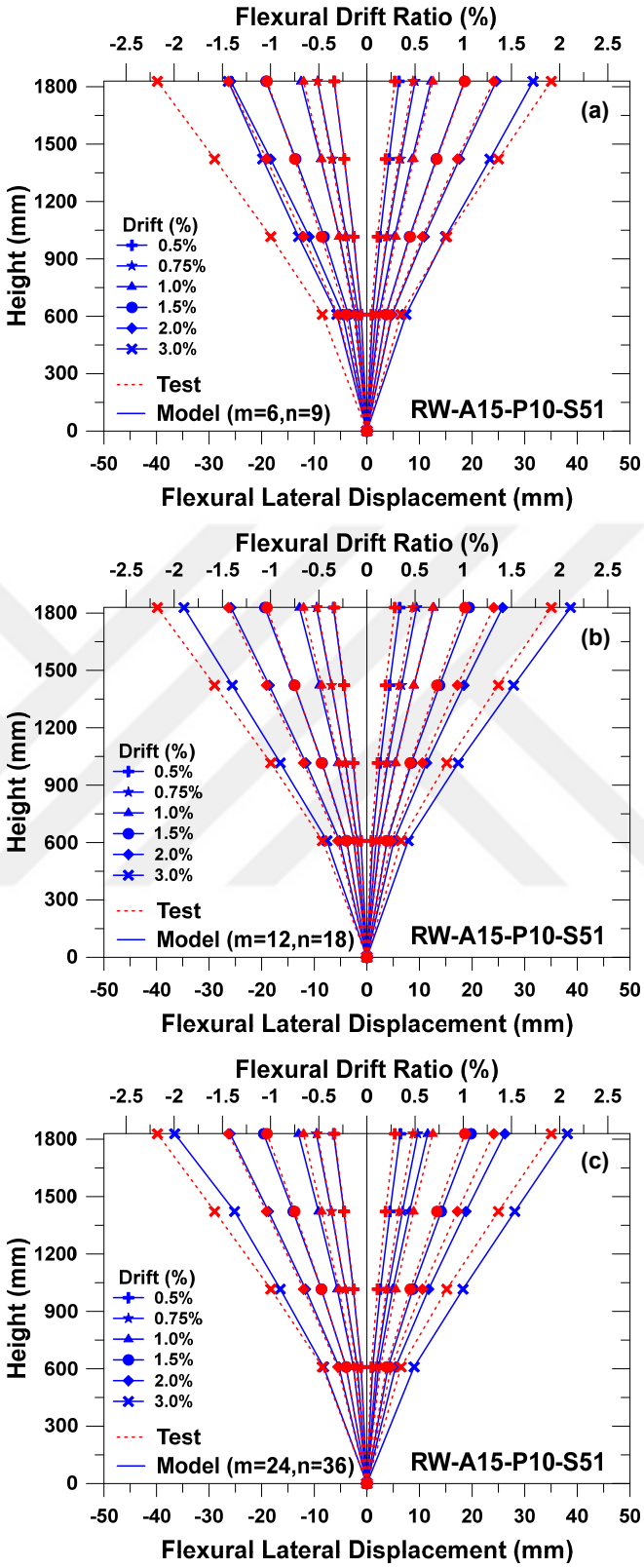

Figure 3.35. Sensitivity of model flexural displacement profile along wall height responses to number of model elements used in horizontal (m) and vertical (n) directions: (a) m=6, n=9 (b) m=12, n=18, (c) m=24, n=36.

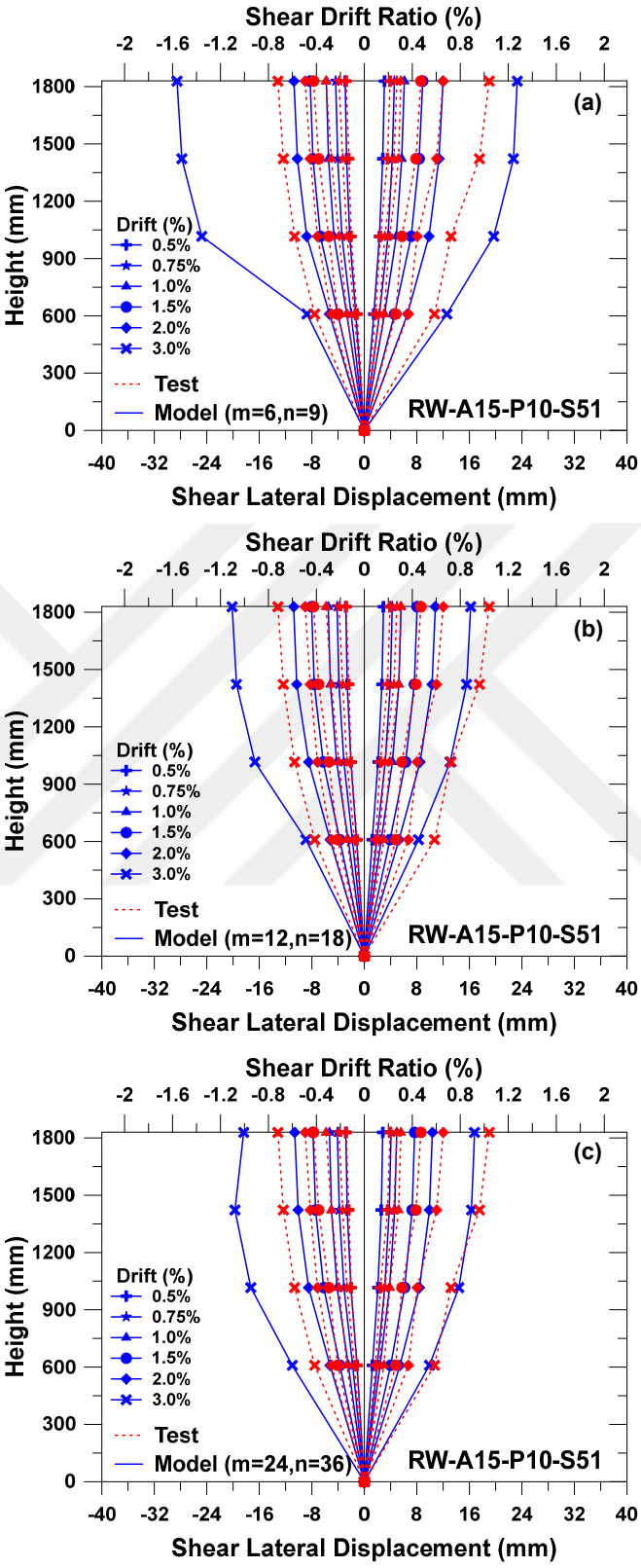

Figure 3.36. Sensitivity of model shear displacement profile along wall height responses to number of model elements used in horizontal (m) and vertical (n) directions: (a) m=6, n=9 (b) m=12, n=18, (c) m=24, n=36.

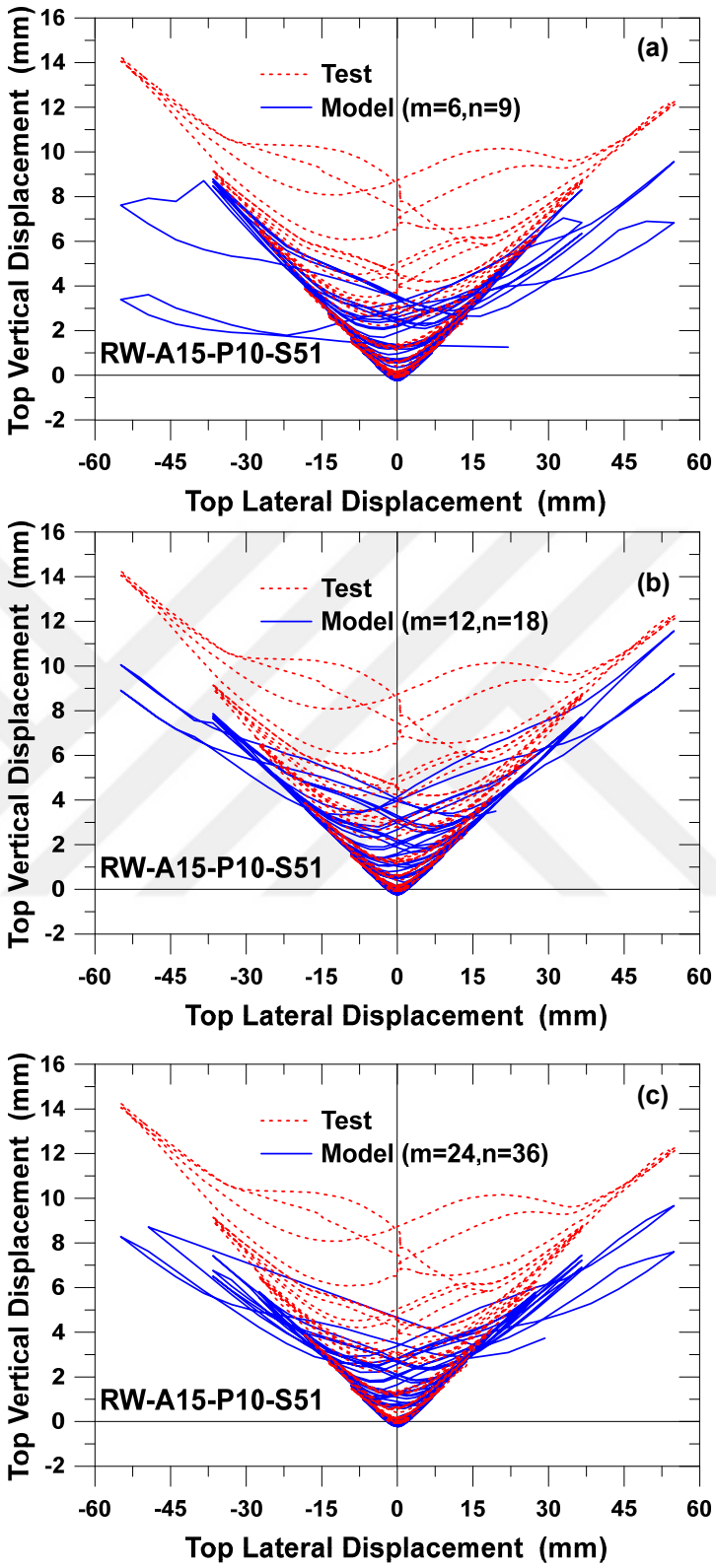

Figure 3.37. Sensitivity of model vertical growth vs. top displacement responses to number of model elements used in horizontal (m) and vertical (n) directions: (a) m=6, n=9 (b) m=12, n=18, (c) m=24, n=36.

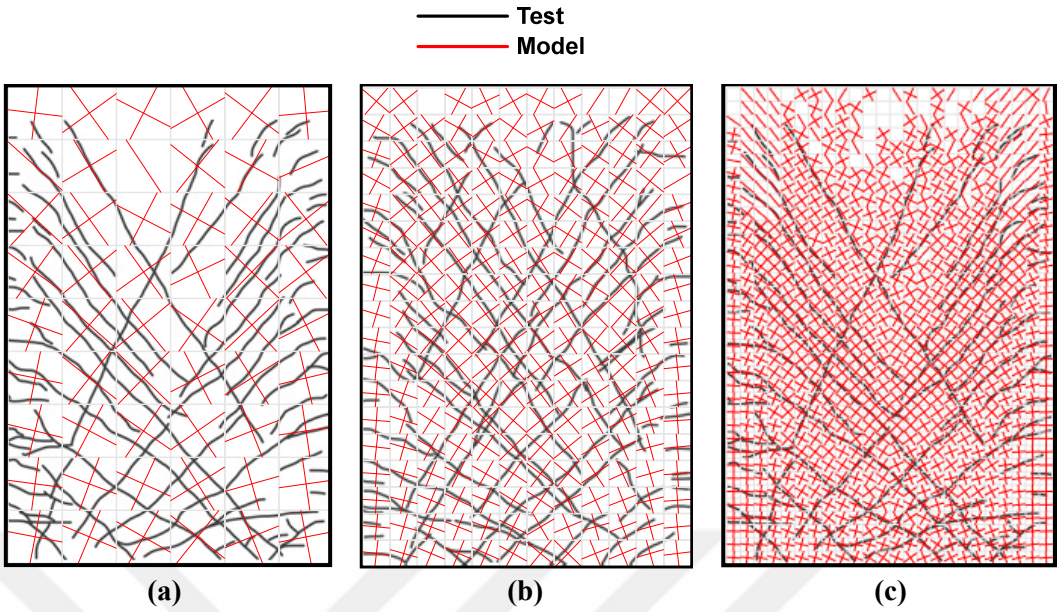

Figure 3.38. Sensitivity of model crack patterns for specimen RW-A15-P10-S51 at 3.0% drift with various model elements in horizontal and vertical directions: (a) *m*=6, *n*=9, (b) *m*=12, *n*=18, (c) *m*=24, *n*=36.

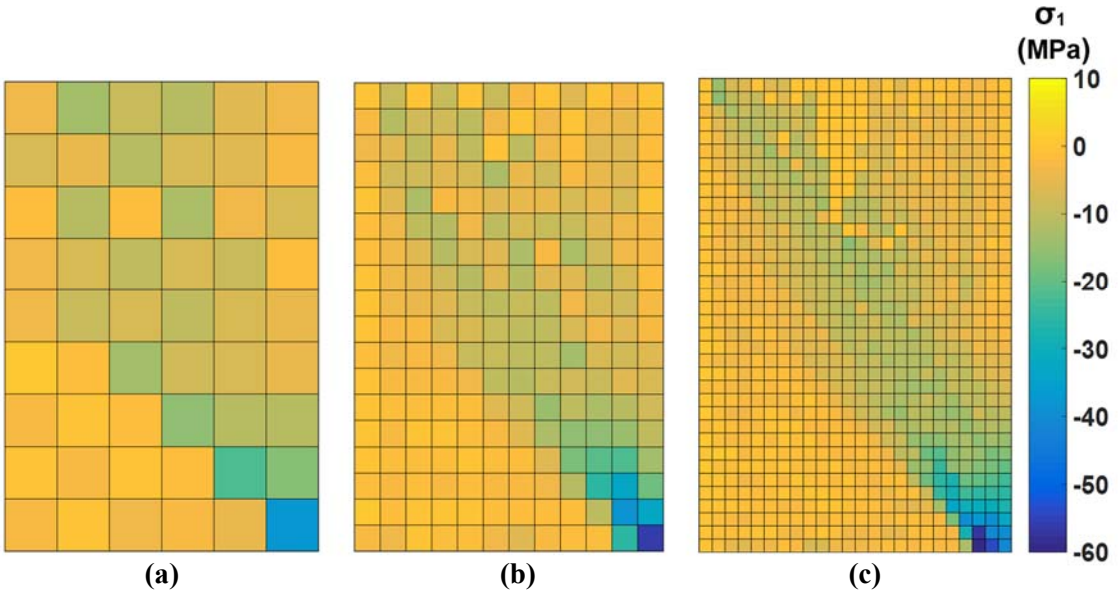

Figure 3.39. Sensitivity of model concrete principal compressive stress contours for specimen RW-A15-P10-S51 at 1.5% drift with various model elements in horizontal and vertical directions: (a) *m*=6, *n*=9, (b) *m*=12, *n*=18, (c) *m*=24, *n*=36.

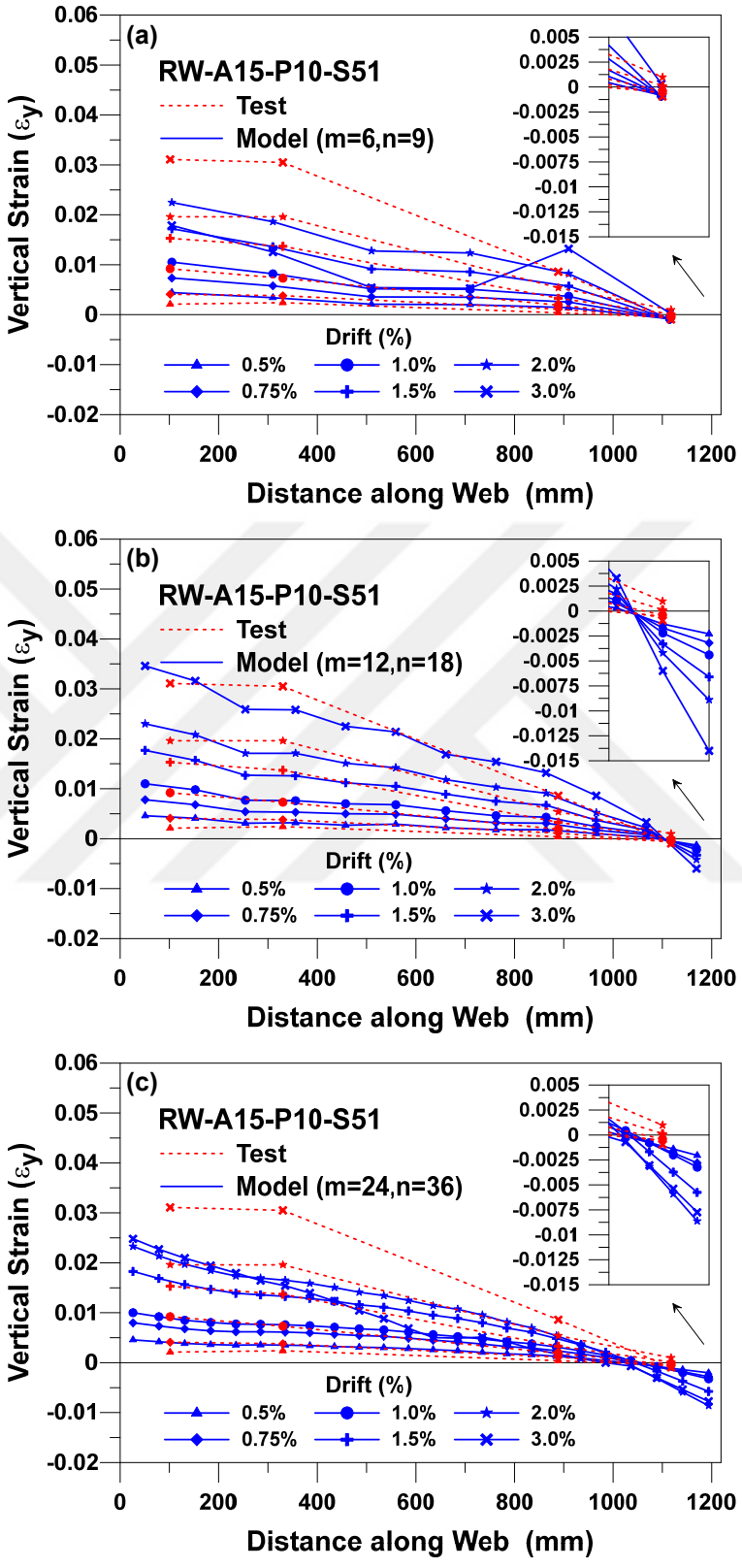

Figure 3.40. Sensitivity of model vertical normal strain profiles at wall base responses to number of model elements used in horizontal (m) and vertical (n) directions: (a) m=6, n=9 (b) m=12, n=18, (c) m=24, n=36.

Comparing the global and local response predictions of the model with test results revealed that the FSAFE model accurately simulates the experimentally-observed responses of relatively slender and medium rise walls. The model also replicates the shear and flexural displacement components of these specimens thorough the entire loading history, demonstrating that the model is capable of simulating the coupled shear and flexural deformations in both slender and medium rise walls. Plots of crack patterns and principal concrete compressive stresses at higher drift levels of one slender (RW2) and four medium rise (RW-A20-P10-S38, RW-A20-P10-S63, RW-A15-P10-S51 and RW-A15-P10-S78) wall specimens showed that the model is again reliable in representing the horizontal cracks at boundaries due to flexural (vertical) strains and diagonal cracks due to interaction of shear (horizontal) and flexural (vertical) strains.

The major limitation of the present model formulation is that it can only capture wall failure modes associated with material stress–strain behavior (e.g., concrete crushing, reinforcement yielding, sliding shear along cracks), and does not consider lateral instabilities (e.g., reinforcement buckling, out-of-plane instability of the wall boundary) in simulating the response of walls. The model provided reasonably accurate load vs. displacement response predictions for wall specimens considered, when the experimentally-observed failure modes of the wall specimens (Table 3.2) were associated with or initiated by crushing of concrete. However, for improving the model accuracy in estimating the drift capacity of the walls, as well as the rate of degradation in lateral load after the capacity is reached, the FSAFE model needs to be extended to also incorporate reinforcement buckling and lateral instability failures in its formulation.

As discussed in this chapter, the relatively low level of model accuracy in simulating both the global (Figure 3.5b) and local (Figure 3.27) response characteristics of specimen TW2 when its flange is in tension, may be attributed to the experimental observation that the web boundary of this wall experienced out-of-plane instability (buckling over several hoop spacings) during the test. The out-of-plane instability was obvious to naked eye at the nominal drift level of 2.5% (Thomsen and Wallace, 2004); however, it is speculated that the instability may have initiated at lower drifts, creating a softening effect on the web boundary of the wall in compression, and thus impairing the correlation between model predictions and test measurements at smaller drift levels also. This observation also

highlights a significant limitation of the present model formulation. It is obvious that the accuracy of the model is subject to improvement upon implementation of constitutive models for representing not only local (rebar) buckling but also global buckling (buckling over multiple tie spacings) behavior in its formulation (e.g., Massone and Moroder, 2009). Consideration of geometric nonlinearity effects in the analysis, possibly using a shell element formulation in which displacements in the out-of-plane direction of the model elements are also considered (e.g., Dashti *et al.*, 2017a) would be a further improvement; however, this would significantly complicate the present model formulation.

Furthermore, test observations reported by Oesterle *et al.* (1976) indicate that due to absence of axial load, flexural cracks on the wall did not fully close upon load reversal, which created significant dowel demands on longitudinal bars and caused sliding along horizontal cracks, amplifying the shear distortion measurements shown in Figure 3.31 and creating the pinching effects on the experimental load–displacement response shown in Figure 3.7. The associated distortion of the longitudinal bars may have impaired uniform crack closure and led to out-of-plane instability of the wall boundary, which initiated at drift levels as low as 1.7%, also due to the relatively low out-of-plane flexural stiffness of the boundary (small wall thickness). The complex behavioral mode and failure mechanism of specimen R2, the main source of which is believed to be the distortion of longitudinal bars as they go from tension to compression, and the related non-uniform crack closure, is naturally not represented in the model response prediction. Out-of-plane instability failures in RC walls (first discussed by Paulay and Priestley, 1993) has recently gained much interest among researchers, especially with damage observations after recent earthquakes (e.g., Elwood 2013, Maffei *et al*. 2014), and has been the subject of both experimental (e.g., Rosso *et al.*, 2016; Dashti *et al.* 2017b, 2018a) and analytical modeling (e.g., Dashti *et al.* 2018b) studies conducted on walls, as well as experimental studies conducted on isolated wall boundary elements (e.g., Welt *et al.* 2017, Rosso *et al.*, 2018). Recent research efforts (e.g., Abdullah and Wallace, 2019) also focus on revision of wall seismic design provisions to consider reduction of wall drift capacity associated in-part with out-of-plane instability of wall boundary regions. Implementation of a behavioral modeling approach in the formulation of the FSAFE model for simulating the lateral instability of wall boundaries can potentially improve the model response predictions, not only for specimen R2 but also the other wall specimens investigated in this study. Test observations

on specimen R2 also highlight the shortcoming that current seismic performance evaluation methods for RC walls do not yet consider the effect of relevant parameters (such as in-plane slenderness and axial load) on development on wall instability failures, which may result in significant differences between observed and expected failure modes.

4. REFINEMENT AND EXPERIMENTAL VALIDATION OF THE MODEL FOR WALLS WITH SHEAR CONTROLLED RESPONSES

4.1. General

In order to prevent brittle failure of structural walls, codes and recommendations require that slender walls be designed to fail in flexure, with adequate shear strength that surpasses nominal flexural capacity. Squat walls (e.g., used in low-rise buildings, parking level of tall buildings) and wall segments between window or door openings, on the other hand, are susceptible to fail in shear, which results in early loss of lateral strength and stiffness. However, relatively limited research has been conducted to investigate the nonlinear hysteretic behavior of squat walls in the literature. Furthermore, current design codes and performance evaluation documents incorporate weaknesses related to shear design of squat walls. For example, calculation of wall shear strength defined in ACI 318-14 does not consider the influence of shear failure modes of squat walls, as experimentally observed in the study by Terzioglu *et al.* (2011, 2018), which include diagonal tension (yielding of horizontal web reinforcement followed by crushing of concrete along diagonal struts) or diagonal compression (crushing of concrete at wall base). Furthermore, the influence of axial load to the shear strength of walls is not considered in the shear strength calculation in ACI 318-14. In nonlinear analysis of tall buildings or performance assessment of current buildings, most commonly used backbone curves for modeling of nonlinear shear behavior are the ones proposed in ASCE 41-17, with the shear strength capacity defined in ACI 318-14. However, effective shear stiffness for simulation of nonlinear shear behavior is not consistent in current design and performance assessment provisions (e.g., effective shear stiffness is provided as $0.5G$ ($0.2E_c$) in LATBSDC (2016)), whereas test results in the literature (e.g., Tran and Wallace, 2015) determined $0.25G$ for shear modulus of medium rise walls (Kolozvari and Wallace, 2016). Nonlinear shear behavior has also been observed in experimental studies on relatively slender walls (Thomsen and Wallace, 2004) and medium-rise walls (Tran and Wallace, 2015). Hence, to characterize and analytically represent the behavior of structural walls under seismic

actions, considering that axial, flexural and shear responses of walls are coupled, is important. Since macroscopic (e.g., plastic hinge, fiber-based) modeling approaches are typically inadequate in accurately representing the coupling of axial, flexural and shear responses of walls, as well as in simulating shear-dominant responses of low-rise walls, using microscopic (finite element) modeling approaches are more appropriate for simulation of the cyclic lateral load behavior of squat walls.

Although, squat walls are used in various building configurations, limited research has been conducted to investigate the nonlinear hysteretic behavior of these walls and numerical modeling of them is scarcely studied. Research studies available in literature for nonlinear finite element modeling of walls with both high and low aspect ratios will be summarized first. Palermo and Vecchio (2007) used VecTor2 (Vecchio, 1989) software as a finite element analysis tool with the Modified Compression Field Theory (Vecchio and Collins, 1986) as a membrane model. For validation of the model, two of the investigated wall specimens were squat walls with rectangular and non-rectangular cross-sections and they were modeled in two-dimension only. Overall, displacements at maximum lateral load of walls were not well represented by the analytical model, which was attributed to the behavior of concrete model employed in the model. Rojas *et al.* (2016) proposed a Quadrilateral Layered Membrane Element with Drilling Degrees of Freedom to predict the nonlinear hysteretic behavior of structural walls with various aspect ratios. Five of the wall specimens investigated for validation of the model was squat walls with rectangular cross-sections and subjected to monotonic loading, one of which had exceptions of being designed with irregular openings and tested under cyclic loading. Strength degradation in lateral load capacity of walls was not presented for monotonically loaded walls. Dashti *et al.* (2017a) conducted a recent study using the commercial software DIANA (2011). Researchers used the rotational total strain crack model available in DIANA (2011) with a curved shell element, which can consider the effect of out-of-plane deformations even for in-plane loading conditions. Only two squat wall specimens with an identical aspect ratio of 1.0 and tested under monotonic loading were investigated in this study. Lateral load-deformation results were not represented by the proposed model beyond degradation in lateral load capacity. As well, lateral load capacity of an axially loaded squat wall specimen was not well represented by the model. The research studies summarized above

did not clearly highlight the applicability of their modeling approaches for simulating behavioral characteristics of wall specimens with shear-controlled responses.

Research efforts available in literature focusing only on the nonlinear response characteristics of low-aspect ratio structural walls can be summarized as follows. Brun *et al*. (2003) proposed a model for simulating the nonlinear response of a flanged squat wall specimen using the finite element code CASTEM (Millard, 1993; Combescure and Pegon, 1994) for the analysis. However, the authors did not model the non-rectangular (flanged) wall specimen in three-dimension; they preferred to use a two-dimensional representation of the wall. Also, degradation in lateral load upon reaching of the capacity was not addressed in the study. Thomson *et al.* (2009) proposed a simplified finite element model for representing the nonlinear behavioral features of squat walls, using the commercial software ABAQUS (Hibbitt, 1993). The model was validated with lateral load vs. top displacement responses of three squat walls, which were analytically described with different modeling parameters. Predictions for one squat wall specimen under monotonic loading, using two different finite element analysis software DIANA (2011) and ABAQUS (Hibbitt, 1993), were compared by Damoni *et al.* (2014). Monotonic envelope and crack pattern of the test result of one squat wall specimen was only compared with model predictions. Delso *et al.* (2015) also used the finite element analysis software ABAQUS (Hibbitt, 1993) with a smeared crack approach to provide finite element model of six shear dominated squat structural wall specimens with non-rectangular and rectangular cross-sections and tested under cyclic loading. Only lateral load-deformation results and failure modes according to principal strains were reproduced by the proposed model. In the aforementioned studies, local response (e.g., average horizontal normal strain, vertical growth) predictions of the models were not provided and limited number of wall specimens was used for validation of the models. Most recently, Epackachi and Whittaker (2018) used the finite element analysis program LS-DYNA (2012a, 2012b) to simulate the cyclic response characteristics of squat walls. Lateral load versus top displacement responses of twenty-two wall specimens with aspect ratios ranging from 0.33 to 1.60 were presented for validation of the model. This study focused on the global nonlinear behavior of all investigated walls and failure mechanisms of selected walls. However, in model formulations of the wall specimens, to predict strength degradation observed in the test results of squat walls, a numerical technique called material erosion was defined with two

different minimum principal strains for three set of experiments. Furthermore, contribution of shear and flexural deformations to top displacements of the model, as well as the local response predictions, were not discussed in this study.

As will be presented in this chapter, the FSAFE model formulation was refined for modeling of squat walls with shear controlled responses, with the implementation of more robust constitutive models for shear aggregate interlock and dowel action models (Vassilopoulou and Tassios, 2003) that also incorporate cyclic degradation parameters (Thermou *et al.*, 2014), as well as by implementation of a rotational spring in the model to simulate strain penetration effects in wall pedestals (Massone *et al.*, 2009), and also with consideration regularization for strain localization effects in the concrete stress vs. strain relationship (Coleman and Spacone, 2001). Representative numerical predictions of the improved FSAFE model for lateral load vs. top displacement responses of squat walls, as well as contributions of flexural and shear deformations on wall lateral displacements and local deformation (e.g., average horizontal normal strains) responses of squat walls with rectangular cross sections are provided. Wall specimens were chosen from two different experimental programs (Orakcal *et al.*, 2009; Terzioglu *et al.*, 2018) to cover a broad range of behavioral characteristics of squat walls, including various shear span-to-depth ratios, reinforcement configurations and axial load levels. Additionally, sensitivity analyses were performed to show the influence of the implemented rotational spring, the regularization method, and mesh discretization to the model predictions, as well as the effect of a pre-defined sliding crack to the response prediction of the specimen that experienced sliding shear failure. The model is further validated by comparing the lateral load capacity, drift capacity, and cumulative energy dissipation capacity predictions with test results for a total of twenty-five squat wall specimens.

4.2. Refinements on the FSAFE Model for Simulation of Squat Walls

4.2.1. Implementation of a Robust Shear Aggregate Interlock Model

As previously described in Chapter 2, in the formulation of the FSAM, together with the strains parallel and perpendicular to the concrete struts, shear strains parallel to the crack directions also develop. The shear aggregate interlock mechanism along crack

surfaces was originally described using the peak-oriented hysteretic model reported in Chapter 2. In the present chapter, a more robust hysteretic shear aggregate interlock model (Vassilopoulou and Tassios, 2003), also including parameters for cyclic degradation (Thermou *et al.*, 2014), is implemented in the model formulation.

The shear aggregate interlock model defined by Vassilopoulou and Tassios (2003) relates the slip along the crack interface to the corresponding shear stress (Figure 4.1) with contribution of resisting mechanisms: frictional resistance along the crack interface due to the resultant compression stress perpendicular to the crack surface and the clamping resistance of the reinforcing bars normal to the crack interface. It is important to mention that shear stress along crack interface stemming from the frictional resistance becomes zero when the cracks are open, similar to shear aggregate interlock model described in Chapter 2. In the refined FSAM, shear strains (γ_{crack}) developed along crack surface are multiplied with the calculated nominal crack spacing (s), as defined in the papers by Vecchio and Collins (1986) and Vecchio (2000), to obtain slip deformations at the crack interface. Slip deformation along the crack interface is given by

$$\Delta_{crack} = \gamma_{crack}\, s \tag{4.1}$$

where the nominal crack spacing (s) is defined as:

$$s = \frac{1}{\frac{\sin\theta}{s_x} + \frac{\cos\theta}{s_y}} \tag{4.2}$$

and in which s_x and s_y are the distance between horizontal reinforcing bars and vertical reinforcing bars, respectively. The originally proposed shear stress capacity of the shear aggregate interlock model (Vassilopoulou and Tassios, 2003) considers the contribution of concrete compressive strength to clamping even if the crack interface is under tension, and a low level of axial compressive stress perpendicular to the crack direction, resulting in a higher clamping shear stress than recommended in ACI 318-14. Hence, in this study, the shear stress capacity is defined as described in Section 2.4, with the following relationship:

$$\tau_{crack,max} = \eta\left\{\sigma_{c\perp} + (\rho f_y)_\perp\right\} \tag{4.3}$$

where $\sigma_{c\perp}$ is the concrete compressive stress and $(\rho f_y)_\perp$ is the clamping stress perpendicular to the crack interface and η is the shear-friction coefficient. Stress vs. slip deformation stiffness of the envelope curve and unloading and reloading paths of the proposed shear aggregate interlock model by Vassilopoulou and Tassios (2003) are directly used in the FSAM, with the exception that the 25% stress offset upon reloading to the previous unloading slip value from the envelope, is omitted (Figure 4.1) in order to make the hysteretic behavior more stable under generalized slip histories.

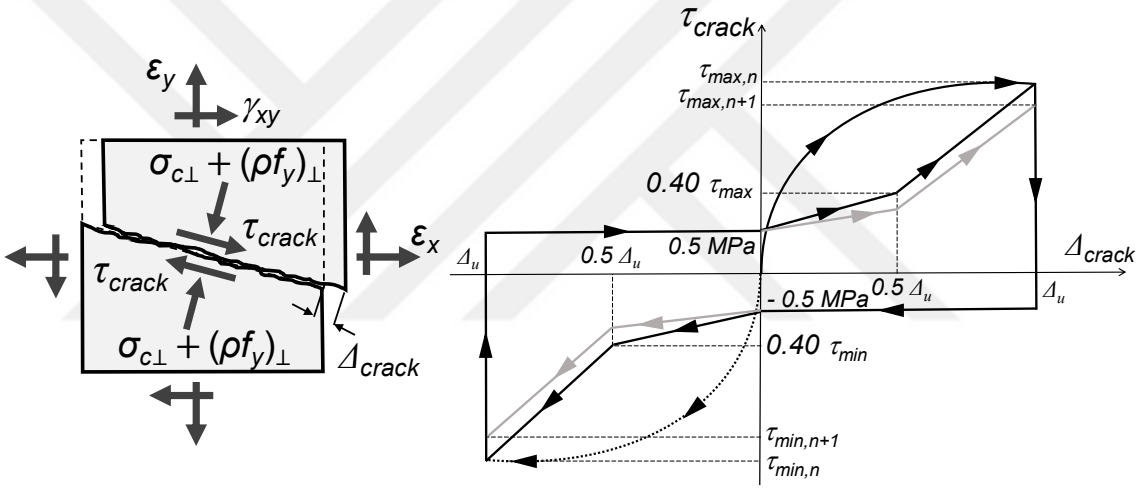

Figure 4.1. Shear aggregate interlock on crack surfaces.

4.2.2. Implementation of a Robust Dowel Action Model

Dowel action behavior of reinforcement in cracked concrete was originally described using the origin-oriented hysteretic model presented in Chapter 2. Contribution of dowel action to the FSAM formulation is refined in this chapter, by implementing the dowel force vs. dowel deformation relationship (Figure 4.2), as described in the study by Vassilopoulou and Tassios (2003). The smeared-stress strain approach proposed by He and Kwan (2001) is still employed for interpretation of the combined effects of shear and tensile stresses along the crack interface. Calculation of the dowel deformations in the orthogonal reinforcing bar directions is achieved similarly to the origin-oriented dowel action model.

The hysteretic rules of the origin-oriented model is modified with the implementation of the dowel action model proposed by Vassilopoulou and Tassios (2003). Dowel deformations for both horizontal and vertical reinforcing bars are used in the hysteretic rules (Figure 4.2) described by Vassilopoulou and Tassios (2003), to calculate the corresponding dowel forces. However, similar to the shear aggregate interlock model described in the previous section, although 30% of force offset upon reloading to the envelope is proposed in the original formulation by Vassilopoulou and Tassios (2003), it is not considered in the present study. The capacity of the dowel force-deformation relationship is defined with the following equation:

$$V_{\text{dow,max}} = 1.30 d_{bar}^2 \sqrt{|f'_c| f_y} \tag{4.4}$$

Using the reinforcement ratio and the smeared stress approach described in Chapter 2, with the corresponding dowel force, dowel stresses perpendicular to the orientation of reinforcing bars are calculated. Dowel stresses are back transformed to the tensile and shear stresses along the crack interface, to be superimposed with the reinforcing steel stresses.

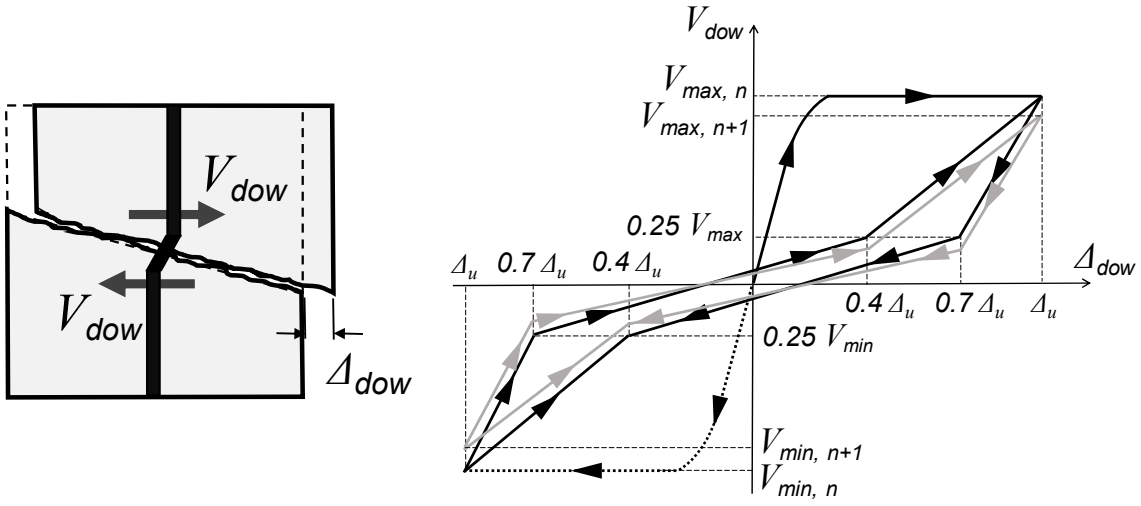

Figure 4.2. Dowel action on reinforcement.

4.2.3. Implementation of Cyclic Degradation Parameters

Cyclic degradation parameters first proposed by Vassilopoulou and Tassios (2003) and modified by Thermou *et al.* (2014) are employed in FSAM for simulating the effects of degradation in interlock stresses and dowel forces under reversed cyclic loading, using the following relationships on the capacity of the shear aggregate interlock and dowel action constitutive models:

$$\tau_{\text{crack,deg}} = 1 - 0.05\alpha\sqrt{\frac{\Sigma\Delta / \left|\Delta_{\max}\right| + 1}{4}}\left(\frac{f'_c}{\sigma_{c\perp}}\right)^{1/2}\left(\frac{\left|\Delta_{\max}\right|}{\Delta_u}\right)^{1/3} \tag{4.5}$$

$$V_{\text{dow,deg}} = 1 - \alpha\frac{1}{7}\sqrt{\frac{\Sigma\Delta / \Delta_{\max} + 1}{4}} \tag{4.6}$$

where $\Sigma\Delta$ and Δ_{max} represent the cumulative slip deformation and maximum slip deformation along the slip reversals, respectively, and Δ_u is defined as equal to 2mm (Vassilopoulou and Tassios, 2003). Cyclic degradation equations described above are chosen since the parameters in the equations are clearly defined and the equations are applicable for indeterminate slip deformation histories along the crack interfaces of the panel elements. In the cyclic degradation parameters ($\tau_{crack,deg}$ and $V_{dow,deg}$), α reflects the degradation parameter and it is used in the present study with a value of 1.0, as it is proposed in the Greek code for cracked interfaces (2013).

4.2.4. Implementation of a Rotational Spring for Strain Penetration

To consider the prevalent effect of the elongation of the bars embedded at the top and bottom pedestals of the wall specimens, which results in a noticeable softening effect on the flexural stiffness of squat walls (the effect is not as noticeable for slender walls), a zero-length rotational spring is also incorporated in the FSAFE model formulation for squat walls at the wall-pedestal interfaces (Figure 4.3). Calculation of the rotational spring stiffness of the wall specimens is performed using the approach proposed by Massone *et al.* (2009), as described in the following paragraphs.

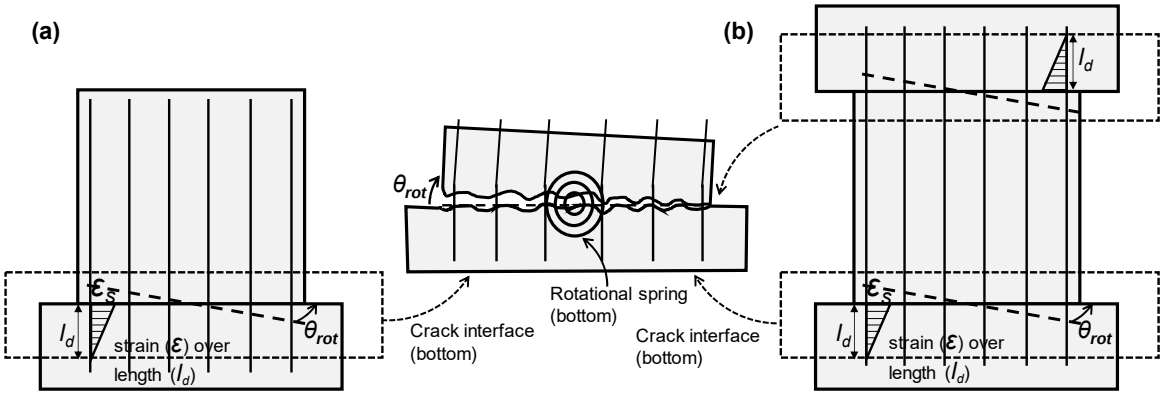

Figure 4.3. Interface crack and rotational spring (Massone *et al*., 2009): (a) single curvature, (b) double curvature.

Along the development length of the embedded bars inside the pedestals, a linear normal strain distribution is assumed, with a maximum tensile strain (ε_s) at the interface and a zero strain at the end of the development length (l_d). Integration of the triangular (linear) strain distribution along the development length gives the cumulative elongation (Δ_{el}) of the reinforcing bars at the wall-pedestal interface, which is further divided by the corresponding distance between neutral axis and reinforcing bar in tension to obtain the rotation (θ_{rot}) at the interfaces, due to the strain penetration effects on these bars, as defined by following equation:

$$\theta_{rot} = \frac{\Delta_{el}}{l_w - c - d'} = \frac{\varepsilon_s \times l_d/2}{l_w - c - d'} \Rightarrow \varepsilon_s = \frac{2 \times \theta_{rot} \times (l_w - c - d')}{l_d} \tag{4.7}$$

where l_w is the length of the wall specimen, c is the neutral axis depth and d' is the distance between steel in tension and the outer face of the wall specimen. Curvature (ϕ) is calculated by the relationship below:

$$\phi = \frac{\varepsilon_s}{l_w - c - d'} \Rightarrow \varepsilon_s = \phi \times (l_w - c - d') \tag{4.8}$$

Equation 4.7 and Equation 4.8 are solved together to determine the relationship between the curvature and rotation at the crack interface as:

$$\frac{2\times\theta_{rot}\times\cancel{(l_w-c-d')}}{l_d}=\phi\times\cancel{(l_w-c-d')} \tag{4.9}$$

$$\phi=\frac{2}{l_d}\times\theta_{rot} \tag{4.10}$$

For definition of the rotational spring stiffness parameters implemented in the FSAFE model, equilibrium of moments obtained from multiplying rotational stiffness (k_θ) with the corresponding rotation (θ_{rot}) and calculated via multiplying the curvature stiffness (k_ϕ) with the corresponding curvature (ϕ) are used. In the following equations, transformation of the curvature stiffness to the rotational spring stiffness is defined:

$$k_\theta\times\theta_{rot}=k_\phi\times\phi \tag{4.11}$$

$$k_\theta\times\cancel{\theta_{rot}}=k_\phi\times\frac{2}{l_d}\times\cancel{\theta_{rot}} \tag{4.12}$$

$$k_\theta=k_\phi\times\frac{2}{l_d} \tag{4.13}$$

4.3. Description of Squat Wall Specimens Used for Model Validation

Two different experimental programs providing test results for low-rise shear-controlled walls, with detailed instrumentation on the wall specimens, were used for validation of the FSAFE model for squat walls. Eleven of the squat wall specimens used for verification of the model, named with the initials SW, were tested by Terzioglu *et al*. (2018). Tests were conducted in an upright position with a fixed bottom pedestal and lateral loading was applied at the top of the specimens with a rigid beam, which was free to rotate. The length of the SW walls was equal to 1500mm and their thickness was 120mm, while wall heights varied. Wall specimens were differentiated by their shear-span-to-depth ratios (0.47, 0.63, 0.65, 1.13 and 1.15), reinforcement configurations in the web and the

boundary regions as well as the material properties of concrete and reinforcing steel bars. Most SW walls were tested under zero axial load, except the two of them were subjected to constant axial load levels of $0.05A_g f'_c$ and $0.10A_g f'_c$ throughout the experiment. The squat wall named as SW-T1-S2-9 was unique among the walls investigated in this study, due to existence of ties in the boundary zones providing confinement effect. A representative figure for the geometry and reinforcement details of two of the eleven wall specimens used for validation of the model is presented in Figure 4.4.

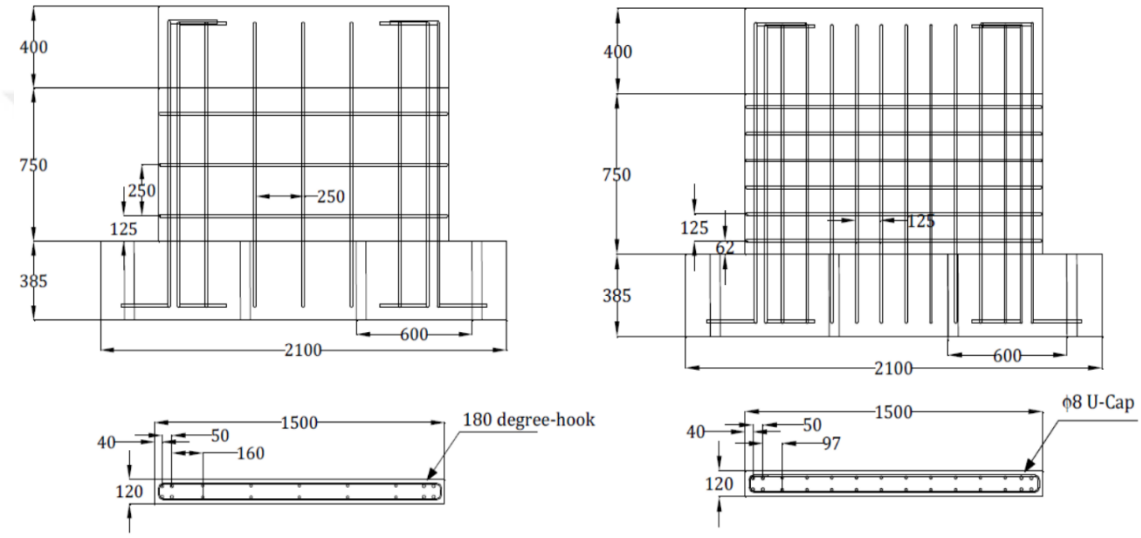

(a) (b)

Figure 4.4. Wall geometry and reinforcement details for specimens (Terzioglu *et al*., 2018): (a) Type 1, (b) Type 2. Note: All units are in mm.

Further validation of the FSAFE model was carried out using the experimental results reported by Orakcal *et al.* (2009) and Massone *et al.* (2009) for fourteen shear-controlled wall specimens, representing wall segments between window opening in a building, including six pier (WP–vertical wall segment) and eight spandrel (WS–horizontal wall segment) specimens. All WP and WS specimens were tested under a zero-rotation restraint enforced at the top of the wall (using two coupled vertical actuators), and cyclic lateral load applied at the mid-height level of the specimens (using an L-shaped steel loading frame), creating a double-curvature loading condition where the bending moment was zero at wall mid-height and reaches maximum values (with reverse signs) at the top and bottom cross-sections of the wall, representing the actual loading condition on wall piers and spandrels in a building perimeter wall with window openings. This loading setup

enforced the shear-span-to-depth ratio of the wall specimens to be equal to half of their aspect ratio. Six of the wall pier and eight of the spandrel type specimens had an equal thickness of 152mm, with lengths of 1370mm and 1520mm, respectively. Wall pier specimens were identical and the variables among them were the level of axial load ($0.00A_g f'_c$, $0.05A_g f'_c$ and $0.10A_g f'_c$), and the concrete compressive strengths ranged from 28.3MPa to 34.0MPa. Wall spandrel specimens were differentiated by reinforcement configurations at boundary and web regions, and with weakened plane joints (WPJ) located at mid-height or at the bottom close to the wall pedestal interface. Weakened plane joints were provided by decreasing the thickness of the wall and cutting the longitudinal reinforcement at a specific location along the height of the wall during construction, representing outdated construction practice in the United States. Figure 4.5 shows the geometry and reinforcement configuration of a typical spandrel specimen and all pier specimens.

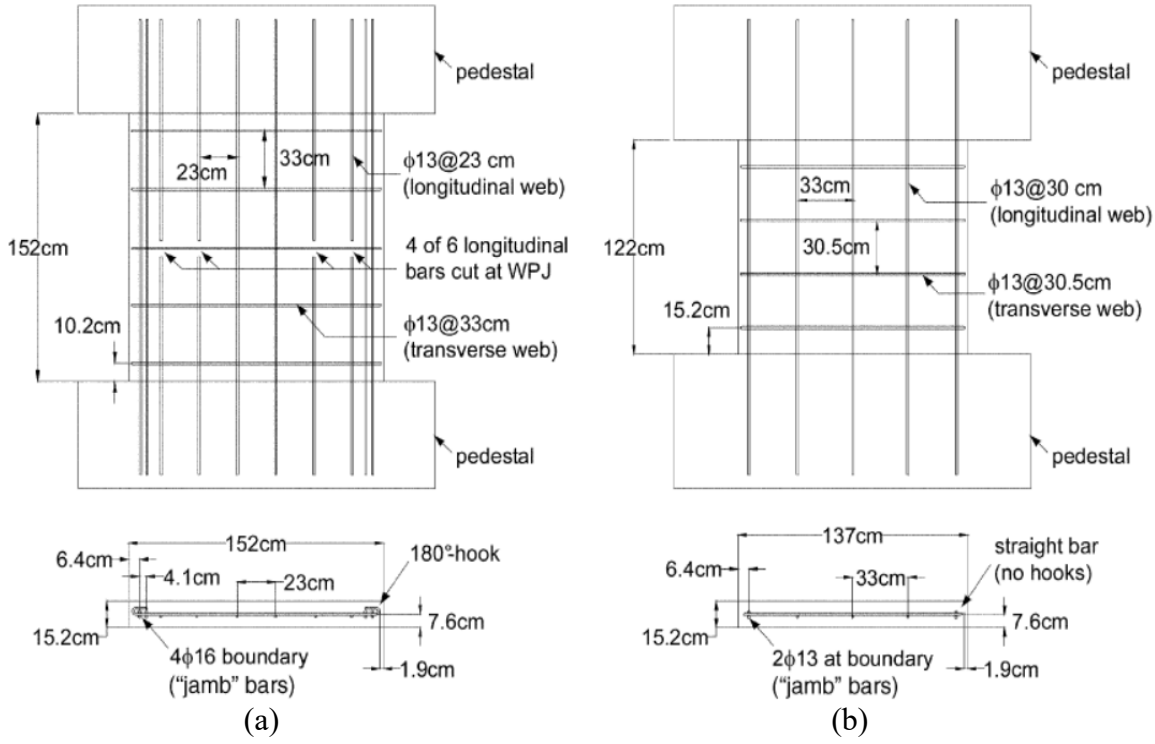

Figure 4.5. Wall geometry and reinforcement details for specimens (Orakcal *et al.*, 2009): (a) wall spandrel (Type 1), (b) wall pier (Type 5).

Geometric dimensions, shear-span-to-depth ratios, concrete compressive strengths, applied constant axial load levels, web and boundary reinforcement configurations, as well

as the yield strengths of reinforcing bars for all squat walls used for verification of the FSAFE model are presented in Table 4.1 and Table 4.2. For calculation of the boundary reinforcement ratios of squat walls with no ties, tributary areas were defined with by considering the side cover thickness on both sides of the boundary reinforcements, as described in ACI 318-14 (Figure 4.6). Web reinforcement ratios were calculated by dividing the total web reinforcement over the remaining tributary area excluding the boundary regions.

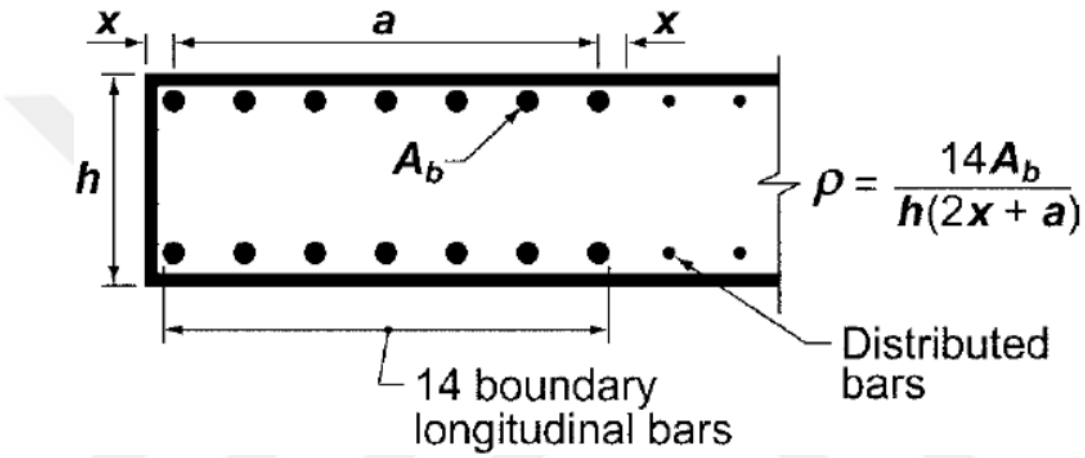

Figure 4.6. Longitudinal reinforcement ratios for typical wall boundary conditions (ACI318-14, 2014).

Shear and flexural capacities of the wall specimens, calculated according to ACI 318-14, using as-tested material properties are listed in Table 4.2. In the WS specimens, due to the WPJs (which leads to decrease in vertical web reinforcement ratio), and in the WP specimens due to the absence of hooks in horizontal web reinforcements, horizontal web reinforcement ratios used in calculation of shear strength were defined according to the restrictions specified in ASCE 41-17. Vertical web reinforcement ratios were reduced to 0.14% for Type 1 and 0.13% for Type 2, 3 and 4 spandrel specimens due to the presence of WPJ. As recommended in ASCE 41-17, the multiplication of the minimum horizontal or vertical web reinforcement ratios with the corresponding yield strengths for calculation of shear strength of walls would be used for all wall spandrel specimens, as well as for the squat wall specimen SW-T5-S1-7 having the only different web reinforcement ratios along horizontal and vertical directions between SW wall specimens. However, the minimum of

both horizontal and vertical reinforcement ratios were smaller than 0.15% for all spandrel specimens. A lower limit of 0.15% for web reinforcement ratios was used for calculation of the shear strength for those specimens as it is described in the commentary of ASCE 41-17 that a reinforcement ratio below the value of 0.15% does not result in a reduction in the shear strength of walls. For shear strength calculation of all WP specimens, horizontal web reinforcement ratio was also defined as 0.15%, due to lack of hooks on the horizontal web reinforcement. Nominal moment capacities calculated per ACI 318-14 of the SW walls were divided by the height of the loading point from the basement, while the total of the nominal moment capacities at the bottom and top of WP and WS specimens were divided by the height of the wall to provide flexural lateral load capacities. Average shear stress levels at the measured lateral load capacities of the walls and the observed failure modes for all walls are also available in Table 4.2.

4.4. Modeling Parameters for Squat Wall Specimens

4.4.1. Model Geometry

Geometric discretization of the squat wall models was performed by first definition of wall boundary lengths, by adding cover thickness on both sides of the longitudinal boundary reinforcement, as defined in ACI 318-14. One model element was defined at each boundary of the wall specimens that did not incorporate confined boundary regions. As a standard discretization approach for modeling of squat walls, mesh dimensions were defined with approximately equal width and height at boundary and web regions, similar to the slender and medium rise walls. For example, for specimen SW-T4-S1-6, boundary dimensions were defined as 130 mm width and 125 mm height, while web dimensions were defined as 124 mm width and 125 mm height. Unlike all other squat wall specimens modeled using one element at each boundary, the boundaries of specimen SW-T1-S2-9 were each defined using two elements, due the relatively larger length of the confined boundary region. Table 4.3 presents the mesh dimensions and number of model elements in both horizontal and vertical directions of all squat wall specimens investigated. Sensitivity of the model responses to number of model elements in horizontal and vertical directions is investigated in Section 4.6.3.

Table 4.1. Properties of squat walls.

Specimen ID	l_w (mm)	h_w (mm)	t (mm)	$\frac{l_w}{t}$	$\frac{h_w}{l_w}$	$\frac{M}{Vl_w}$	$\frac{P_{ax}}{A_g f'_c}$	Web Reinforcement (Transverse/Longitudinal)			Boundary Reinforcement	
								Rebar	ρ_{web} (%)	Longitudinal Cut Bars	Rebar	ρ_b (%)
SW-T2-S1-1	1500	750	120	12.5	0.50	0.63	0.00	ϕ8@125mm	0.68	-	4ϕ16	5.15
SW-T2-S2-3	1500	750	120	12.5	0.50	0.63	0.00	ϕ8@125mm	0.68	-	4ϕ 16	5.15
SW-T2-S3-4	1500	750	120	12.5	0.50	0.63	0.00	ϕ8@125mm	0.68	-	4ϕ 16	5.15
SW-T3-S1-5	1500	750	120	12.5	0.50	0.63	0.00	ϕ8@125mm	0.68	-	2ϕ 8	0.65
SW-T4-S1-6	1500	500	120	12.5	0.33	0.47	0.00	ϕ8@125mm	0.68	-	4ϕ 14	3.95
SW-T5-S1-7	1500	1500	120	12.5	1.00	1.13	0.00	ϕ8@125/250mm	0.68/0.34	-	4ϕ 22	9.75
SW-T6-S1-8	1500	1500	120	12.5	1.00	1.15	0.00	ϕ8@125mm	0.68	-	4ϕ 22	9.75
SW-T1-S2-9	1500	750	120	12.5	0.50	0.65	0.00	ϕ8@250mm	0.34	-	4ϕ 16	5.15
SW-T1-N5-S1-10	1500	750	120	12.5	0.50	0.63	0.05	ϕ8@250mm	0.34	-	4ϕ 16	5.15
SW-T1-N10-S1-11	1500	750	120	12.5	0.50	0.63	0.10	ϕ8@250mm	0.34	-	4ϕ 16	5.15
SW-T1-S1-2	1500	750	120	12.5	0.50	0.63	0.00	ϕ8@250mm	0.34	-	4ϕ 16	5.15
WP-T5-N0-S1	1370	1220	152	9	0.90	0.44	0.00	ϕ13@305/330mm	0.278/0.227	-	2ϕ 13	1.33
WP-T5-N0-S2	1370	1220	152	9	0.90	0.44	0.00	ϕ13@305/330mm	0.278/0.227	-	2ϕ 13	1.33
WP-T5-N5-S1	1370	1220	152	9	0.90	0.44	0.05	ϕ13@305/330mm	0.278/0.227	-	2ϕ 13	1.33
WP-T5-N5-S2	1370	1220	152	9	0.90	0.44	0.05	ϕ13@305/330mm	0.278/0.227	-	2ϕ 13	1.33
WP-T5-N10-S1	1370	1220	152	9	0.90	0.44	0.10	ϕ13@305/330mm	0.278/0.227	-	2ϕ 13	1.33
WP-T5-N10-S2	1370	1220	152	9	0.90	0.44	0.10	ϕ13@305/330mm	0.278/0.227	-	2ϕ 13	1.33
WS-T1-S1	1520	1520	152	10	1.00	0.50	0.00	ϕ13@330/230mm	0.278/0.428	4 of 6[(1)]	4ϕ 16	3.12
WS-T1-S2	1520	1520	152	10	1.00	0.50	0.00	ϕ13@330/230mm	0.278/0.428	4 of 6[(1)]	4ϕ 16	3.12
WS-T2-S1	1520	1520	152	10	1.00	0.50	0.00	ϕ13@330/230mm	0.278/0.400	4 of 6[(1)]	1ϕ13+1ϕ16	1.70
WS-T2-S2	1520	1520	152	10	1.00	0.50	0.00	ϕ13@330/230mm	0.278/0.400	4 of 6[(1)]	1ϕ13+1ϕ16	1.70
WS-T3-S1	1520	1520	152	10	1.00	0.50	0.00	ϕ13@280mm	0.278/0.256	2 of 4[(1)]	2ϕ13	1.33
WS-T3-S2	1520	1520	152	10	1.00	0.50	0.00	ϕ13@280mm	0.278/0.256	2 of 4[(1)]	2ϕ13	1.33
WS-T4-S1	1520	1520	152	10	1.00	0.50	0.00	ϕ13@280mm	0.278/0.256	2 of 4[(2)]	2ϕ13	1.33
WS-T4-S2	1520	1520	152	10	1.00	0.50	0.00	ϕ13@280mm	0.278/0.256	2 of 4[(2)]	2ϕ13	1.33

[(1)] Weakened plane joint at wall mid-height

[(2)] Weakened plane joint at wall-pedestal interface

Table 4.2. Material and response characteristics of squat walls.

Specimen ID	f'_c (MPa)	$f_{y,web}$ (Transverse/Longitudinal) (MPa)	$f_{y,boundary}$ (MPa)	$V_{n,ACI}$ (kN)	$V_{n,ACI\text{-}FLEX}$ (kN)	$\frac{V_{max}}{A_{CV}\sqrt{f'_c}}$	Failure Mode[1]
SW-T2-S1-1	19.3	481	440	656	835	1.03	DC
SW-T2-S2-3	25.8	481	440	759	850	0.73	DC
SW-T2-S3-4	29.0	584	473	805	855	0.84	DC
SW-T3-S1-5	32.1	584	584	846	480	0.38	SS
SW-T4-S1-6	34.8	584	519	881	1180	0.82	DC
SW-T5-S1-7	35.0	584	528	618	785	0.67	DC
SW-T6-S1-8	22.6	584	528	710	870	0.86	DC
SW-T1-S2-9	24.0	584	473	572	690	0.64	DT
SW-T1-N5-S1-10	26.3	584	473	583	825	0.85	DT
SW-T1-N10-S1-11	27.0	584	473	590	970	0.85	DT
SW-T1-S1-2	23.7	481	440	525	690	0.72	DT
WP-T5-N0-S1	29.9	424	424	419	415	0.36	DT
WP-T5-N0-S2	31.0	424	424	424	415	0.28	DT
WP-T5-N5-S1	31.9	424	424	428	741	0.55	DT
WP-T5-N5-S2	32.0	424	424	428	741	0.58	DT
WP-T5-N10-S1	28.3	424	424	411	948	0.68	DT
WP-T5-N10-S2	34.0	424	424	425	1011	0.68	DT
WS-T1-S1	25.5	424	448	441	949	0.54	DT
WS-T1-S2	43.7	424	448	531	967	0.49	DT
WS-T2-S1	31.4	424	448	473	579	0.35	DT
WS-T2-S2	31.0	424	448	471	579	0.38	DT
WS-T3-S1	31.7	352	352	449	358	0.31	DT
WS-T3-S2	33.6	352	352	459	358	0.30	DT
WS-T4-S1	31.9	352	352	450	313	0.25	SS
WS-T4-S2	33.0	352	352	456	313	0.26	SS

[1] DC: diagonal compression; DT: diagonal tension; SS: sliding shear

Table 4.3. Definition of wall geometry.

Specimen ID	Mesh (Element) Dimensions (mm)			Number of Meshes (Elements)		
	Horizontal		Vertical	Horizontal (*m*)		Vertical (*n*)
	Boundary	Web		Boundary	Web	
SW-T2-S1-1	130	124	125	2	10	6
SW-T2-S2-3	130	124	125	2	10	6
SW-T2-S3-4	130	124	125	2	10	6
SW-T3-S1-5	125	125	125	2	10	6
SW-T4-S1-6	130	124	125	2	10	4
SW-T5-S1-7	130	124	125	2	10	12
SW-T6-S1-8	130	124	125	2	10	12
SW-T1-S2-9	97	93	94	4	12	8
SW-T1-N5-S1-10	130	124	125	2	10	12
SW-T1-N10-S1-11	130	124	125	2	10	12
SW-T1-S1-2	130	124	125	2	10	12
WP-T5-N0-S1	128	124	122	2	9	10
WP-T5-N0-S2	128	124	122	2	9	10
WP-T5-N5-S1	128	124	122	2	9	10
WP-T5-N5-S2	128	124	122	2	9	10
WP-T5-N10-S1	128	124	122	2	9	10
WP-T5-N10-S2	128	124	122	2	9	10
WS-T1-S1	168	169	169	2	7	9
WS-T1-S2	168	169	169	2	7	9
WS-T2-S1	128	140	138	2	9	11
WS-T2-S2	128	140	138	2	9	11
WS-T3-S1	128	140	138	2	9	11
WS-T3-S2	128	140	138	2	9	11
WS-T4-S1	128	126	127	2	10	12
WS-T4-S2	128	126	127	2	10	12

4.4.2. Material Model Parameters

As-tested material properties presented in Table 4.2 were adopted for defining the concrete and reinforcing steel stress-strain envelope in the formulation of FSAFE model. Concrete and reinforcing steel modeling parameters for the squat wall specimens were determined similarly to slender and medium rise wall specimens. A brief summary of the main assumptions for assignment of the material parameters of squat wall specimens is presented herein. Monotonic stress-strain envelope of the concrete model by Chang and Mander (1994) was defined in the FSAFE model using the reported concrete compressive stress obtained from the cylinder specimen test results. For the specimens for which only concrete compressive strengths were documented, the ascending region of the envelope of unconfined and confined concrete stress-strain relationship was defined using the empirical equations provided by Chang and Mander (1994) and Mander *et al*. (1988), respectively. The constitutive material model proposed by Saatcioglu and Razvi (1992) was used for definition of the descending slope of the envelope in FSAFE formulation for both the unconfined and the confined concrete models. Stress-strain relationship of concrete in tension was adopted by definition of tensile strength of concrete as $f_t = 0.31\sqrt{f'_c}$ and the cracking strain of concrete as ε_t=0.00008 with the shape of stress-strain model suggested by Belarbi and Hsu (1994) for incorporation of the tension stiffening effects on the smeared stress-strain behavior of concrete in tension. Table 4.4 presents the constitutive modeling parameters for concrete in compression and tension for squat wall specimens. Constitutive modeling parameters for confined concrete shown in Table 4.5 were only used for specimen SW-T1-S2-9, for simulation of the confining effect of the stirrups in wall boundary regions.

For the reinforcing steel, coupon test results were adopted to define the envelope of the Menegotto and Pinto (1973) stress-strain relationship in the formulation of FSAFE model, together with the cyclic stiffness degradation parameters (R_0 = 20, a_1 = 18.5, and a_2 = 0.15) as originally proposed by Menegotto and Pinto (1973). The yield strength and strain hardening ratios in tension were also modified based on the empirical equations defined by Belarbi and Hsu (1994) for consideration of tension stiffening effects on reinforcing steel bars embedded in concrete. Material model parameters for reinforcing steel bars are listed in Table 4.6 and Table 4.7.

Table 4.4. Material model parameters for concrete in compression and tension.

Specimen ID	Concrete in Compression					Concerete in Tension				
	f'_c (MPa)	E_c (MPa)	ε'_c	r	x_{crn}	f_t (MPa)	E_c (MPa)	ε_t	r_t	x_{crp}
SW-T2-S1-1	19.3	25022	0.0021	1.83	1.320	1.37	25022	0.00008	1.26	10000
SW-T2-S2-3	25.8	27900	0.0021	3.09	1.127	1.58	27900	0.00008	1.25	10000
SW-T2-S3-4	29.0	29150	0.0021	3.71	1.098	1.68	29150	0.00008	1.24	10000
SW-T3-S1-5	32.1	30282	0.0021	4.31	1.081	1.76	30282	0.00008	1.24	10000
SW-T4-S1-6	34.8	31213	0.0021	4.83	1.070	1.84	31213	0.00008	1.23	10000
SW-T5-S1-7	35.0	31280	0.0021	4.87	1.069	1.84	31280	0.00008	1.24	10000
SW-T6-S1-8	22.6	26636	0.0021	2.51	1.175	1.49	26636	0.00008	1.25	10000
SW-T1-S2-9	24.0	27153	0.0021	2.74	1.152	1.53	27153	0.00008	1.25	10000
SW-T1-N5-S1-10	26.3	28101	0.0021	3.19	1.121	1.60	28101	0.00008	1.25	10000
SW-T1-N10-S1-11	27.0	28380	0.0021	3.32	1.115	1.62	28380	0.00008	1.25	10000
SW-T1-S1-2	23.7	27026	0.0021	2.68	1.156	1.52	27026	0.00008	1.25	10000
WP-T5-N0-S1	29.9	29486	0.0025	3.88	1.140	1.70	29486	0.00008	1.24	10000
WP-T5-N0-S2	31.0	29889	0.0027	4.09	1.148	1.73	29889	0.00008	1.24	10000
WP-T5-N5-S1	31.9	30211	0.0023	4.27	1.105	1.76	30211	0.00008	1.24	10000
WP-T5-N5-S2	32.0	30247	0.0025	4.29	1.118	1.76	30247	0.00008	1.24	10000
WP-T5-N10-S1	28.3	28885	0.0021	3.57	1.116	1.66	28885	0.00008	1.24	10000
WP-T5-N10-S2	31.4	30033	0.0025	4.17	1.130	1.74	30033	0.00008	1.24	10000
WS-T1-S1	25.5	27778	0.0018	3.03	1.113	1.57	27778	0.00008	1.25	10000
WS-T1-S2	43.7	33996	0.0024	6.55	1.052	2.06	33996	0.00008	1.23	10000
WS-T2-S1	31.4	30033	0.0022	4.17	1.093	1.74	30033	0.00008	1.24	10000
WS-T2-S2	31.0	29889	0.0020	4.09	1.085	1.73	29889	0.00008	1.24	10000
WS-T3-S1	31.7	30140	0.0021	4.23	1.082	1.75	30140	0.00008	1.24	10000
WS-T3-S2	33.6	30805	0.0021	4.60	1.073	1.80	30805	0.00008	1.24	10000
WS-T4-S1	31.9	30211	0.0021	4.27	1.082	1.76	30211	0.00008	1.24	10000
WS-T4-S2	33.0	30598	0.0021	4.48	1.077	1.79	30598	0.00008	1.23	10000

Table 4.5. Material model parameters for confined concrete of specimen SW-T1-S2-9.

Specimen ID	f'_c (MPa)	E_c (MPa)	ε'_c	r	x_{crn}
SW-T1-S2-9	35.3	31386	0.0064	4.93	1.06

Table 4.6. Material model parameters for reinforcing bars in wall boundary regions.

Specimen ID	Horizontal					Vertical				
	ϕ (mm)	Rebar in Compression		Rebar in Tension		ϕ (mm)	Rebar in Compression		Rebar in Tension	
		f_y (MPa)	b	f_y (MPa)	b		f_y (MPa)	b	f_y (MPa)	b
SW-T2-S1-1	8	500	0.0032	443.6	0.0079	16	440	0.0043	406.2	0.0043
SW-T2-S2-3	8	500	0.0032	438.5	0.0092	16	440	0.0043	405.5	0.0045
SW-T2-S3-4	8	575	0.0082	507.7	0.0124	16	525	0.0028	484.6	0.0031
SW-T3-S1-5	8	584	0.0073	514.2	0.0120	8	584	0.0073	514.2	0.0120
SW-T4-S1-6	8	575	0.0082	503.8	0.0133	14	535	0.0046	492.1	0.0049
SW-T5-S1-7	8	575	0.0082	503.6	0.0133	22	550	0.0067	509.3	0.0058
SW-T6-S1-8	8	575	0.0082	512.2	0.0114	22	550	0.0067	509.9	0.0057
SW-T1-S2-9	8	575	0.0082	520.7	0.0096	16	525	0.0028	481.1	0.0040
SW-T1-N5-S1-10	8	575	0.0082	484.5	0.0174	16	525	0.0028	484.8	0.0031
SW-T1-N10-S1-11	8	575	0.0082	483.5	0.0177	16	525	0.0028	484.8	0.0031
SW-T1-S1-2	8	500	0.0032	415.2	0.0150	16	440	0.0043	405.7	0.0044
WP-T5-N0-S1	13	424	0.0060	318.9	0.0270	13	424	0.0060	378.5	0.0094
WP-T5-N0-S2	13	424	0.0060	316.9	0.0276	13	424	0.0060	378.1	0.0096
WP-T5-N5-S1	13	424	0.0060	315.2	0.0281	13	424	0.0060	377.7	0.0097
WP-T5-N5-S2	13	424	0.0060	315.0	0.0281	13	424	0.0060	377.7	0.0097
WP-T5-N10-S1	13	424	0.0060	322.0	0.0261	13	424	0.0060	379.1	0.0092
WP-T5-N10-S2	13	424	0.0060	316.1	0.0278	13	424	0.0060	377.9	0.0096
WS-T1-S1	13	424	0.0080	318.5	0.0287	16	448	0.0068	410.8	0.0071
WS-T1-S2	13	424	0.0080	280.7	0.0399	16	448	0.0068	407.8	0.0079
WS-T2-S1	13	424	0.0080	305.7	0.0325	13-16	448	0.0068	377.7	0.0140
WS-T2-S2	13	424	0.0080	306.5	0.0323	13-16	448	0.0068	377.9	0.0139
WS-T3-S1	13	352	0.0390	243.8	0.0607	13	352	0.0390	308	0.0379
WS-T3-S2	13	352	0.0390	240.1	0.0621	13	352	0.0390	307.1	0.0382
WS-T4-S1	13	352	0.0390	243.4	0.0609	13	352	0.0390	307.9	0.0380
WS-T4-S2	13	352	0.0390	241.3	0.0616	13	352	0.0390	307.4	0.0381

Table 4.7. Material model parameters for reinforcing bars in wall web.

Specimen ID	Horizontal/Vertical				
	ϕ (mm)	Rebar in Compression		Rebar in Tension	
		f_y (MPa)	b	f_y (MPa)	b
SW-T2-S1-1	8	500	0.0032	443.6	0.0079
SW-T2-S2-3	8	500	0.0032	438.5	0.0092
SW-T2-S3-4	8	575	0.0082	507.7	0.0124
SW-T3-S1-5	8	584	0.0073	514.2	0.0120
SW-T4-S1-6	8	575	0.0082	503.8	0.0133
SW-T5-S1-7	8	575	0.0082	503.6	0.0133
SW-T6-S1-8	8	575	0.0082	512.2	0.0114
SW-T1-S2-9	8	575	0.0082	487.9	0.0167
SW-T1-N5-S1-10	8	575	0.0082	484.5	0.0174
SW-T1-N10-S1-11	8	575	0.0082	483.5	0.0177
SW-T1-S1-2	8	500	0.0032	415.2	0.0150
WP-T5-N0-S1	13	424	0.0060	318.9/312.8	0.0270/0.0288
WP-T5-N0-S2	13	424	0.0060	316.9/310.5	0.0276/0.0295
WP-T5-N5-S1	13	424	0.0060	315.2/308.7	0.0281/0.0300
WP-T5-N5-S2	13	424	0.0060	315.0/308.5	0.0281/0.0301
WP-T5-N10-S1	13	424	0.0060	322.0/316.1	0.0261/0.0278
WP-T5-N10-S2	13	424	0.0060	316.1/309.7	0.0278/0.0297
WS-T1-S1	13	424	0.008	318.5/341.5	0.0287/0.0220
WS-T1-S2	13	424	0.0080	280.7/315.2	0.0399/0.0297
WS-T2-S1	13	424	0.0080	305.7/332.5	0.0325/0.0246
WS-T2-S2	13	424	0.0080	306.5/333.1	0.0323/0.0244
WS-T3-S1	13	352	0.0390	243.8	0.0607
WS-T3-S2	13	352	0.0390	240.1	0.0621
WS-T4-S1	13	352	0.0390	243.4	0.0609
WS-T4-S2	13	352	0.0390	241.3	0.0616

Overall, the main difference in the FSAM formulation for walls with flexural or coupled shear-flexural responses and shear-controlled responses is the implementation of more robust shear aggregate interlock and dowel action models that also incorporate cyclic degradation parameters, as well as consideration of strain penetration and strain localization effects in the analysis, as described in the following sections. The capacity equations of the improved shear aggregate interlock and dowel action mechanisms in the

FSAFE model formulation were defined using the as-tested material properties and the cyclic degradation parameters reported in Section 4.2.3. Based on results of preliminary analyses, a friction coefficient value of $\eta = 0.30$ was used for the analysis of all squat wall specimens, as opposed to a friction coefficient of $\eta = 0.50$ that was used for the slender and medium-rise walls. It was observed that model results for slender and medium-rise walls were not noticeably sensitive to the friction coefficient value, whereas optimum results were obtained for all squat wall specimens when a coefficient of $\eta = 0.30$ was used in the model formulation.

4.4.3. Strain Penetration Spring Stiffness

Implementation of rotational strain penetration in the formulation of FSAFE model was conducted as described in Section 4.2.4. Rotational spring stiffness parameters were calculated individually for all of the squat wall specimens, based on their varying flexural stiffness values and anchorage conditions. Moment-curvature analyses were conducted for all squat wall specimens for calculation of the moment-curvature stiffness (k_ϕ). Table 4.8 presents the development length (l_d) of the reinforcing bars at boundaries calculated as defined in ACI 318-14, the moment-curvature stiffness (k_ϕ) obtained from sectional analysis of the wall cross-sections, and the rotational spring stiffness (k_θ) of the strain penetration springs in the wall models, calculated using Equation 4.13.

4.4.4. Regularization of the Constitutive Model for Concrete in Compression

In nonlinear macroscopic and microscopic analysis of the structural walls, sensitivity of the analysis results to the model mesh size is inevitable, particularly in degrading regions of the lateral load vs. displacement response, due to strain localization effects in modeling. Considering that in shear-controlled responses of squat walls, a significant portion of the lateral load vs. displacement response incorporates degradation in lateral load, in order to reduce the unfavorable sensitivity of the analysis results to strain localization effects, the regularization method proposed by Coleman and Spacone (2001) was also incorporated in the formulation of FSAFE model. The regularization technique proposed by Coleman and Spacone (2001) was originally applied for the longitudinal stress-strain behavior of concrete in force-based frame (e.g., fiber) elements; however, in

the present study, this regularization approach was used in the FSAFE model formulation along the strut directions, along which a uniaxial stress-strain relationship is applied for concrete in compression (Figure 4.7).

Table 4.8. Rotational (strain penetration) spring stiffness for wall specimens.

Specimen ID		l_d (mm)	k_ϕ (MNm^2)	k_θ (MNm)
SW-T2-S1-1		497.7	293.1	1178
SW-T2-S2-3		461.4	301.6	1307
SW-T2-S3-4		490.6	305.2	1244
SW-T3-S1-5		236.2	123.5	1046
SW-T4-S1-6		413.3	262.0	1268
SW-T5-S1-7		657.8	453.7	1379
SW-T6-S1-8		741.8	451.8	1218
SW-T1-S2-9		516.6	260.1	1007
SW-T1-N5-S1-10		503.7	307.9	1223
SW-T1-N10-S1-11		500.1	337.8	1351
SW-T1-S1-2		471.5	266.8	1132
WP-T5-N0-S1		293.2	102.2	697
WP-T5-N0-S2		288.0	102.5	712
WP-T5-N5-S1		283.9	168.6	1188
WP-T5-N5-S2		283.5	167.4	1181
WP-T5-N10-S1		301.4	207.6	1378
WP-T5-N10-S2		286.2	209.5	1464
WS-T1-S1		409.9	300.2	1465
WS-T1-S2		313.1	311.7	1991
WS-T2-S1		324.5	180.7	1114
WS-T2-S2		326.6	181.0	1108
WS-T3-S1		230.7	133.2	1155
WS-T3-S2		224.1	134.4	1199
WS-T4-S1	Top	230.0	133.4	1160
	Bottom	230.0	120.6	1049
WS-T4-S2	Top	226.1	134.1	1186
	Bottom	226.1	121.3	1073

With the integration of the compressive stress-strain envelope defined by the Chang and Mander (1994) model, over length of a standard cylinder specimen (L_p), the so-called fracture energy ($G_{f,c}$) for concrete in compression was first calculated (Figure 4.7a) as shown in the following equation:

$$G_{f,c} = \left(\frac{f'_c}{E_c} + \left(\varepsilon_r - \varepsilon'_c \right) \right) f'_c L_p \tag{4.14}$$

where f'_c is the as-tested concrete compressive strength (also as defined in the model with no regularization), E_c is the young modulus of concrete calculated by the equation by Chang and Mander (1994), and ε_r is the strain at which concrete compressive stress reaches zero. Using the lengths of the two orthogonal fixed-struts (L_e) in each of the model elements in FSAFE model, a new descending slope for the uniaxial concrete stress-strain relationship was defined for each strut of model elements, based on the condition that the fracture energy is held constant (Figure 4.7b).

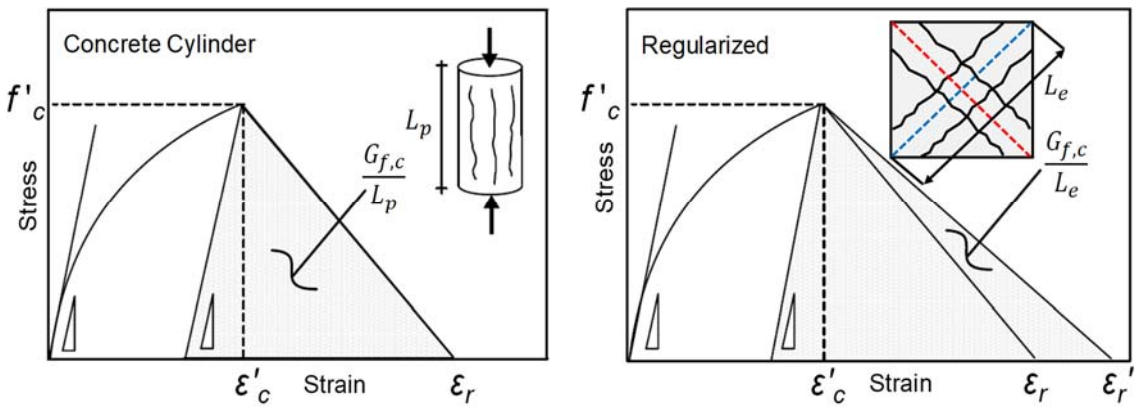

(a) (b)

Figure 4.7. Compression fracture energy for (a) Non-regularized stress-strain model (based on standard cylinder test results), (b) Regularized stress-strain model.

For definition of the new descending (regularized) slope, a new strain parameter at which the concrete compressive stress reaches zero (ε_r') was defined using the following relationship:

$$\varepsilon_r' = \frac{G_{f,c}}{f'_c L_e} - \frac{f'_c}{E_c} + \varepsilon'_c \tag{4.15}$$

Regularization of the stress-strain model for reinforcing steel and of concrete in tension was not employed in the present study for simplicity purposes, and also because they do not directly pertain to localization effects associated with degradation in lateral load.

4.5. Comparison of Model Responses with Test Data

4.5.1. Lateral Load vs. Top Displacement Responses

Comparison of the experimentally-measured and analytically-predicted lateral load vs. top displacement responses of selected ten of the twenty-five shear-controlled wall specimens is presented in Figure 4.8 to Figure 4.10. These ten representative specimens were selected to cover broad range of behavioral characteristics of squat walls, with a variety of shear-to-span-depth ratios, reinforcement configurations, levels of axial load, and loading conditions. Specimens SW-T4-S1-6, SW-T2-S3-4 and SW-T6-S1-8 have aspect ratios of 0.33, 0.50 and 1.00 (shear-span-to-depth ratios of 0.47, 0.63 and 1.15) with boundary reinforcement ratios of 3.95%, 5.15% and 9.75%, respectively. Their web reinforcement ratios are equal and have the highest value of 0.68% among the specimens investigated in the present study, and there is no axial load applied on these specimens. Due to the larger web reinforcement ratios of these three specimens, they experienced diagonal compression failure during the experiments, with crushing of concrete initiating at the bottom corners of the walls and propagating towards the web at wall base. Model predictions for these three specimens that experienced shear stress levels at lateral load capacities that ranged from $0.82\sqrt{f'_c}$ to $0.86\sqrt{f'_c}$, are compared with the experimentally-observed results in Figure 4.8a to Figure 4.8c. The lateral load capacity and stiffness of the wall specimens are well-predicted in both positive and negative loading directions. Degradation in lateral load, degradation in loading/unloading stiffness, ductility and pinching characteristics of the behavior are also represented reasonably well by the FSAFE model. The model provides accurate estimations of the overall response of specimens SW-T4-S1-6 and SW-T2-S3-4. The wall specimen SW-T6-S1-8 experienced sudden strength

degradation in the positive and negative loading directions due to crushing of concrete during the experiment, whereas degradation in the analysis results is more gradual. This abrupt degradation due to crushing of concrete could not be captured by the FSAFE model, probably due to the shape of the concrete stress-strain relationship in its formulation, which incorporates a linear slope in the descending region of the stress-strain relationship after the peak compressive stress is reached.

Specimen SW-T1-S1-2 had an aspect ratio of 0.5 (shear-span-to-depth ratio of 0.63 due to the presence of the loading beam at the top), and there was no axial load applied on this specimen. Specimen SW-T1-S1-2 had half of the web reinforcement ratio and equal boundary reinforcement ratio of specimen SW-T2-S3-4, and experienced diagonal tension failure during the test, with widening of the diagonal cracks due to yielding of horizontal web reinforcement, followed by crushing of concrete along the diagonal cracks. Specimens SW-T1-S2-9 and SW-T1-N10-S1-11 were identical with specimen SW-T1-S1-2, except that specimen SW-T1-S2-9 had boundary regions confined with ties, and specimen SW-T1-N10-S1-11 was tested under a constant axial load level of $0.10A_g f'_c$. Figure 4.8d to Figure 4.8f compare the model predictions with test results for these specimens, which had average shear stress levels at lateral load capacity, ranging from $0.64\sqrt{f'_c}$ to $0.85\sqrt{f'_c}$. The FSAFE model slightly underestimates the lateral load capacities for specimens SW-T1-S1-2 and SW-T1-N10-S1-11, while it overestimates the capacity for the specimen SW-T1-S2-9 in the positive loading direction. However, in the negative loading direction, lateral load capacity estimation of the model matches the experimental results, except for the underestimation for specimen SW-T1-S1-2. It should be mentioned that lateral load vs. top displacement responses measured in the experiments are mostly asymmetrical, whereas they are more symmetrical in the model predictions. Degradation in lateral load of the specimens with zero axial load is well-estimated; however, sudden degradation of the specimen tested under constant axial load is not captured, as is typically the case with the model results. The FSAFE model underestimates the ductility of these walls, whereas degradation of the hysteretic stiffness and pinching behavior are replicated accurately, excluding the specimen SW-T1-S2-9 which showed less pronounced pinching behavior.

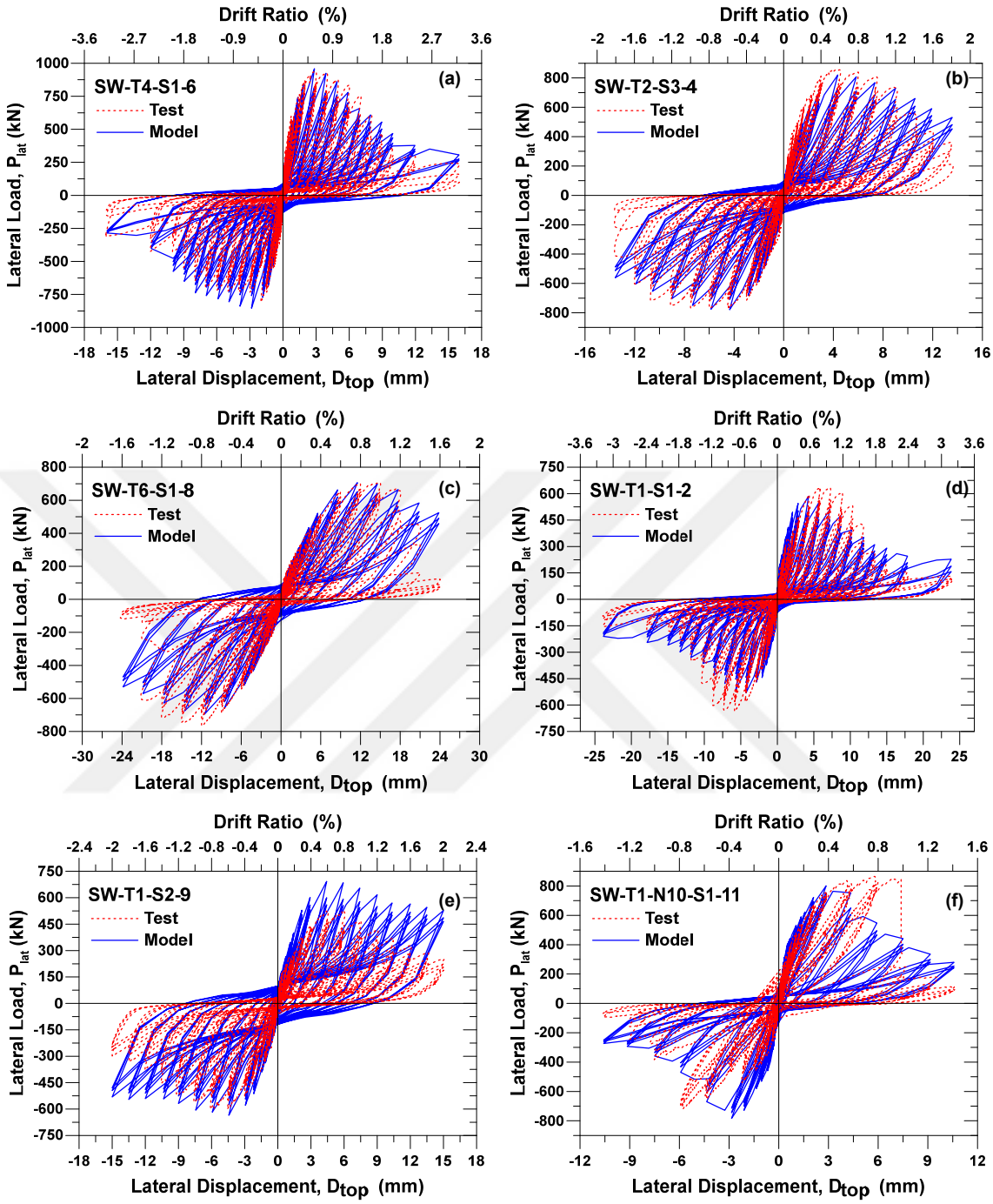

Figure 4.8. Lateral load vs. top displacement responses for specimens: (a) SW-T4-S1-6, (b) SW-T2-S3-4, (c) SW-T6-S1-8, (d) SW-T1-S1-2, (e) SW-T1-S2-9, (f) SW-T1-N10-S1-11.

In Figure 4.9a and Figure 4.9b, representative model predictions are compared with test results for the spandrel type specimens having weakened plane joints at-mid height. These specimens were tested under double curvature loading conditions with zero axial

load. They have smaller web reinforcement ratios compared to the SW wall specimens discussed previously, which resulted in diagonal tension failure during the experiments. Average shear stress demands at lateral load capacity of these specimens were also not as high as the SW specimens. Although they had more complicated configurations, due to the presence of a WPJ and cutting of some of the longitudinal bars at mid-height, the model predicts the lateral load capacity and degradation in lateral load of these spandrel specimens, again with reasonable accuracy. Lateral load capacity of specimen WS-T1-S1 is under-predicted by the FSAFE model in negative direction, due to the unsymmetrical experimental results. Drift capacity prediction of the model for specimen WS-T1-S1 is accurate in the positive loading direction and it is slightly underestimated in the negative loading direction. In the positive loading direction of specimen WS-T2-S1, significant lateral load degradation in the model results starts at drift ratio of 0.8%, whereas in the experiment it starts at drift ratio of 1.2%, which is acceptable for prediction of the drift ratios of shear-controlled walls. However, in negative loading direction, degradation in lateral load capacity initiates later in the model results than test results, which is the opposite of the correlation in the positive loading direction. Degradation to almost 25% of the lateral load capacity in the negative loading direction at the highest drift level is well-captured by the FSAFE model for the specimen WS-T2-S1, which is also a remarkable prediction of the model. Pinching behavior is reasonably reproduced by the model for both of the spandrel specimens presented.

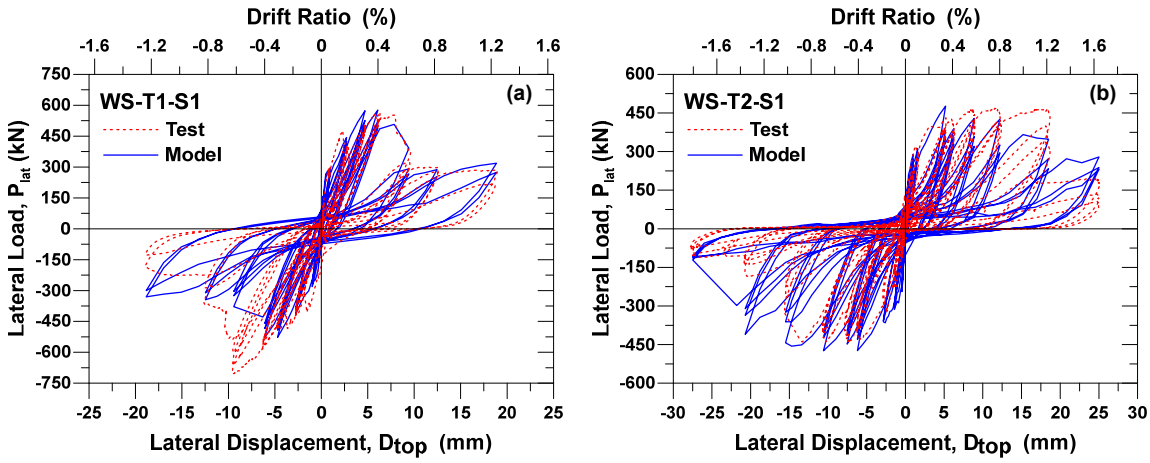

Figure 4.9. Lateral load vs. top displacement responses for specimens: (a) WS-T1-S1, (b) WS-T2-S1.

Finally, comparison of the model lateral load displacement estimations with two pier specimens are presented in Figure 4.10a and Figure 4.10b. Specimens WP-T5-N5-S1 and WP-T5-N10-S1 were tested under double curvature loading conditions and their average shear stress levels at lateral load capacity were $0.55\sqrt{f'_c}$ and $0.68\sqrt{f'_c}$, respectively. Among the shear-controlled specimens investigated, specimen WP-T5-N5-S1, which was subjected to an axial load corresponding to 5% of its axial load capacity, showed diagonal tension failure, as it had smaller web reinforcement ratio, similarly to the spandrel specimens. The model exhibits good accuracy in predicting the lateral stiffness in both positive and negative loading directions and slightly underestimates the lateral load capacity, especially in negative loading direction. Degradation in lateral load, although captured by the model, is more gradual in the analytical results. A similar correlation is obtained for specimen WP-T5-N10-S1, subjected to an axial load corresponding to 10% of its axial load capacity and having identical reinforcement configuration, geometry and failure mode with the specimen WP-T5-N5-S1. For specimen WP-T5-N10-S1, lateral stiffness and lateral load capacity in the positive loading direction are slightly underestimated by the FSAFE model; however, in the negative loading direction they are accurately simulated. Experimentally observed sudden degradation in lateral load is also well captured by the model, although the model again predicts a more gradual degradation.

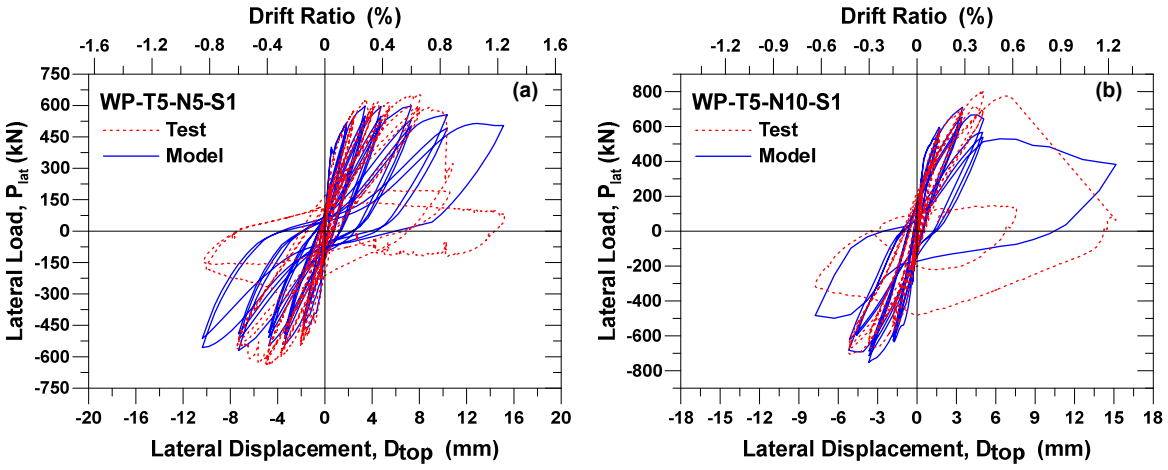

Figure 4.10. Lateral load vs. top displacement responses for specimens: (a) WP-T5-N5-S1, (b) WP-T5-N10-S1.

4.5.2. Lateral Load vs. Flexural and Shear Deformation Responses

Two squat wall specimens with the lowest (SW-T4-S1-6) and the highest (SW-T6-S1-8) aspect ratios are selected for demonstration of the model accuracy for predicting the lateral flexural and shear deformation responses of the walls, due to their significant differences in contribution of flexural and shear deformations to top displacements (Figure 4.11). Comparison of model estimations with test results is provided up to the data point where local deformation measurements were available.

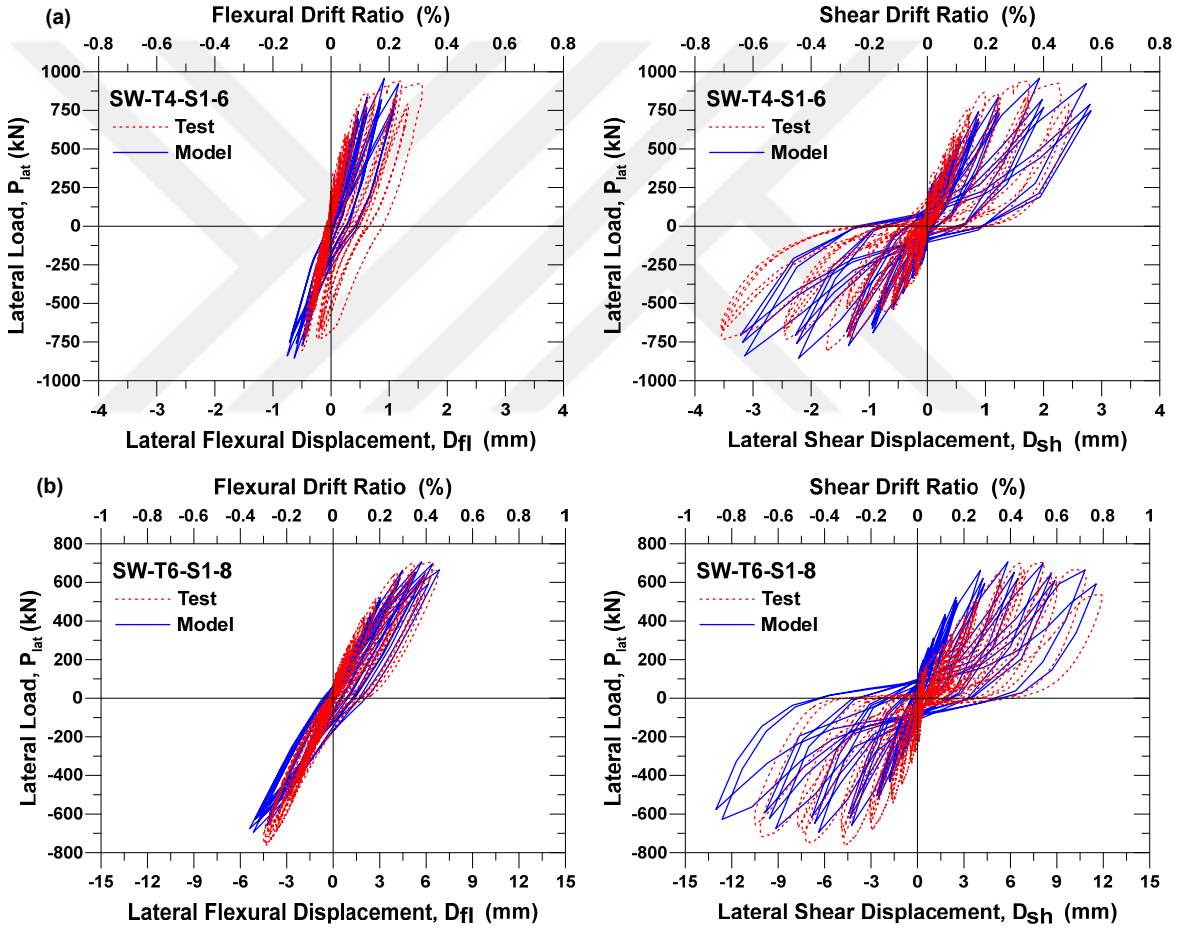

Figure 4.11. Lateral load vs. flexural and shear deformation responses for specimens: (a) SW-T4-S1-6, (b) SW-T6-S1-8.

The model replicates the test observations reasonably well in terms of lateral flexural and shear stiffness values, as well as the lateral load vs. nonlinear shear deformation and approximately linear elastic flexural deformation responses. Flexural stiffness values of the

walls are slightly under-predicted for both specimens, whereas shear stiffness values for the specimen with the lowest aspect ratio in both loading directions as well as the specimen with the highest aspect ratio in the positive loading direction are accurately represented. However, in the negative loading direction of the specimen with the highest aspect ratio, the shear stiffness is slightly overestimated. Average shear to flexural deformation ratio of the specimen with the lowest aspect ratio is approximately 3.0, whereas for the specimen with the highest aspect ratio, it is approximately 2.0, in both test results and model estimations, impressing the capability of the FSAFE model in predicting contributions of the shear and flexural deformations to top displacement. Discrepancies between the model predictions and test results, especially in the negative loading directions of the lateral load vs. flexural and shear deformations responses, are again due to the asymmetrical responses measured during the experiments.

4.5.3. Local Responses

Other representative comparisons of experimentally-observed and analytically-predicted local responses, including shear displacement profiles along the height of the walls, vertical growth vs. top displacement response, average horizontal normal strain profiles along the height of the walls, as well as principal concrete compressive stress contours and crack orientations, for two shear-controlled squat wall specimens are presented in Figure 4.12 to Figure 4.17. Again, test results and model predictions are compared up to the data point where local deformation measurements were available.

Total lateral displacement and flexural displacement profiles along wall height were not reported for the WS and WP specimens, whereas for the SW specimens, none of the displacement or deformation profiles along wall height were reported. Hence, limited experimental data is available for validation of the model predictions for the distribution of total, flexural, and shear displacement profiles along wall height. Figure 4.12 compares the measured and predicted lateral shear displacement profiles along wall height for two of the axially loaded WP specimen at increasing drift levels. Variations between the model predictions and test results at the last drift level is due to the experimentally-observed abrupt degradation at drift level of 0.6% for the specimen WP-T5-N5-S1, and at the drift level of 0.4% for the specimen WP-T5-N10-S1 in the negative loading direction (see also

Figure 4.10a and Figure 4.10b). Model estimations show similar trends with the experimental results for both specimens, which indicates the capability of the model in predicting the distribution of the shear deformation profiles along the height of squat walls.

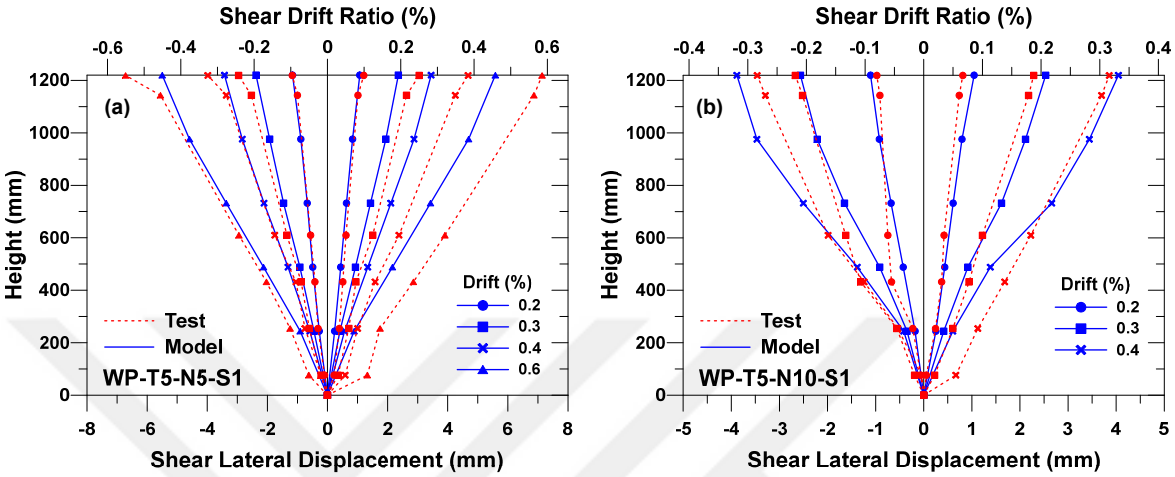

Figure 4.12. Shear displacement profile along the height of the specimens: (a) WP-T5-N5-S1, (b) WP-T5-N10-S1.

Experimentally-measured top lateral displacement vs. top vertical displacement (wall vertical growth) responses of two wall specimens are compared with the model predictions in Figure 4.13. Experimental vertical growth data was available only for the WS and WP specimens. The FSAFE model adequately simulates the vertical growth measurements for specimens WP-T5-N5-S1 and WS-T2-S1. Top vertical displacements at peak lateral displacements and at zero lateral displacements are well-predicted by the model, indicating that the model is capable for simulating the neutral axis migration along the wall cross-section due to cracking of concrete and yielding of wall longitudinal reinforcement. Experimentally-observed vertical growth response of the specimen WP-T5-N5-S1, which was tested under an axial load corresponding to 5% of its axial load capacity, is lower than that of the specimen WS-T2-S1 tested under zero axial load. The model also successfully captures the more pronounced vertical growth behavior of the specimen WS-T2-S1 with zero axial load, as compared to specimen WP-T5-N5-S1.

Test measurements and model predictions for the distribution of average (across wall length) horizontal normal strain values along wall height, at increasing drift levels, are

compared in Figure 4.14. These two shear-critical specimens were selected for evaluation of the capability of the model for representing the experimentally-observed failure mode of the wall, whether it is diagonal compression or diagonal tension. Although typically undervalued in modeling studies, horizontal normal strains are significant response quantities for RC walls–shear-critical walls in particular. These strains are direct indications of whether the horizontal web reinforcement (shear reinforcement) of the wall yields or not, which further determines whether the wall will undergo diagonal tension failure (where the diagonal cracks widen and the softened concrete crushes along diagonal struts) or diagonal compression failure (where the diagonal cracks do not widen and crushing of concrete is typically at the base of the wall under combined shear and flexural effects), respectively (Terzioglu *et al.*, 2018).

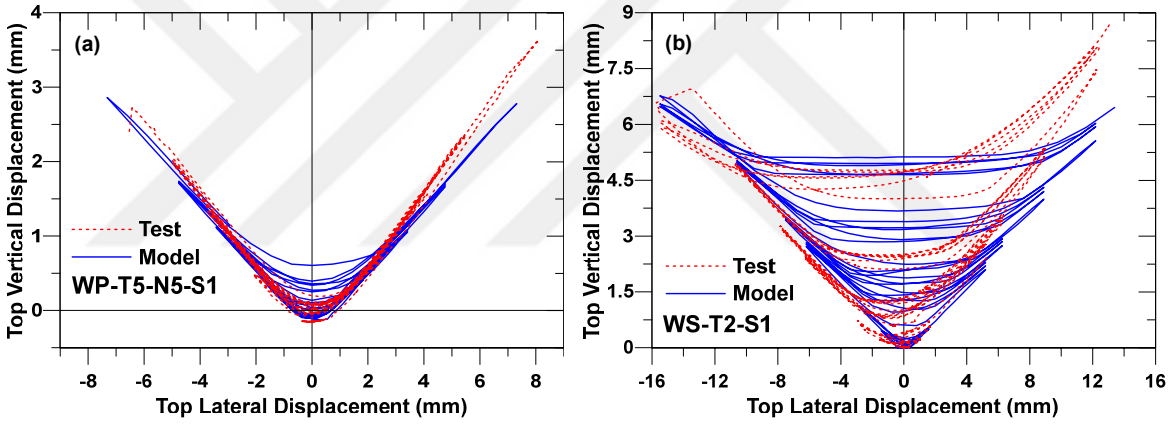

Figure 4.13. Vertical growth vs. top displacement for specimens: (a) WP-T5-N5-S1, (b) WS-T2-S1.

The strain distributions that are plotted in Figure 4.14 for various drift levels before significant degradation in lateral load is observed, indicate that in both model results and test measurements, the average horizontal normal strains tend to increase from near-zero values at the top and bottom of the walls towards their maximum values at wall mid-height, due to the lateral constraining effect of the top and bottom pedestals of the walls, as well as diagonal cracking behavior. As well, the magnitudes of strains predicted by the model are in reasonable agreement with the experimentally-measured values, indicating that the model is also reliable for predicting yielding of horizontal web reinforcement, which influences the wall shear capacity and failure mode. The model predicts that the web

reinforcement of specimen SW-T2-S3-4 will not yield when the wall reaches lateral load capacity (Figure 4.14a), whereas that of specimen SW-T1-N10-S1-11 will yield (Figure 4.14b). These predictions are consistent with the measured strains on the walls, as well as their experimentally-observed failure modes, where SW-T2-S3-4 failed in diagonal compression, while SW-T1-N10-S1-11 suffered with diagonal tension failure. Considering that current code provisions (e.g. ACI 318-14) for wall shear strength typically do not differentiate between whether the wall shear reinforcement yields or not, capability of the FSAFE model in predicting the pre-yield or post-yield horizontal normal strain levels on walls under high shear demands is another important model attribute that may be used towards improvement of code provisions or performance assessment guidelines related to the nonlinear shear behavior of walls.

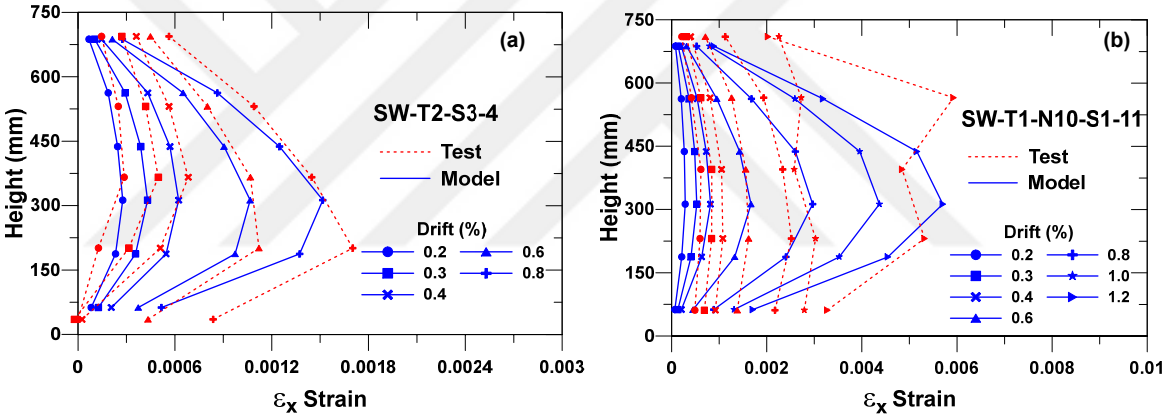

Figure 4.14. Average horizontal normal strain profiles along wall height for specimens: (a) SW-T2-S3-4, (b) SW-T1-N10-S1-11.

For illustrative purposes, Figure 4.15a and Figure 4.15b present stress contours for the principal compressive stresses in concrete (also incorporating shear aggregate interlock stresses on crack surfaces) predicted by the model for the wall specimens that experienced diagonal compression and diagonal tension failures, at their lateral load capacity. The diagonal struts, formation of which constitutes the primary shear resisting mechanism of squat walls with shear controlled responses, can be clearly observed in the principal compressive stress contours. Concentration of stress contours at the bottom right corner for the specimen SW-T2-S3-4 (Figure 4.15a) as well as at the top left and bottom right corners

for the specimen WP-T5-N10-S1 (Figure 4.15b) demonstrate the capability of the FSAFE model for simulating the diagonal compression and diagonal tension failures, respectively.

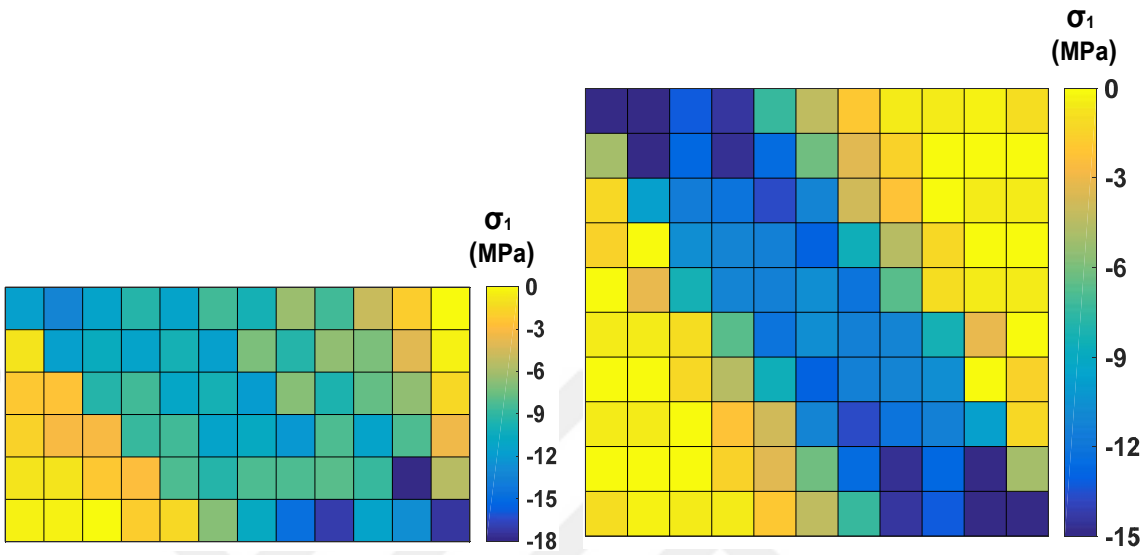

(a) (b)

Figure 4.15. Concrete principal compressive stress contours for specimens: (a) SW-T2-S3-4 at 0.6% drift, (b) WP-T5-N10-S1 at 0.4% drift.

Again, for illustrative purposes, Figure 4.16 and Figure 4.17 show representative crack orientations (with solid lines representing open cracks and dashed lines representing closed cracks) predicted by the model and experimentally-recorded crack patterns for two wall specimens with aspect ratios of 1.0 and 0.5, at the drift level corresponding to their lateral load capacity in the positive loading direction. As shown in the figures, the cracks are mostly diagonal within the web region of the walls, representing formation of a diagonal strut under shear-dominated behavior. However, they tend to be more horizontal at the base of the walls and at the wall boundaries, where flexural deformations are somewhat more influential. Although the predicted and recorded crack patterns are considerably different (which should be expected since the cracks observed during the tests propagate in a continuous manner whereas the cracks predicted by the model are inherently discrete), similar trends in the crack orientations can be observed in both model and test results.

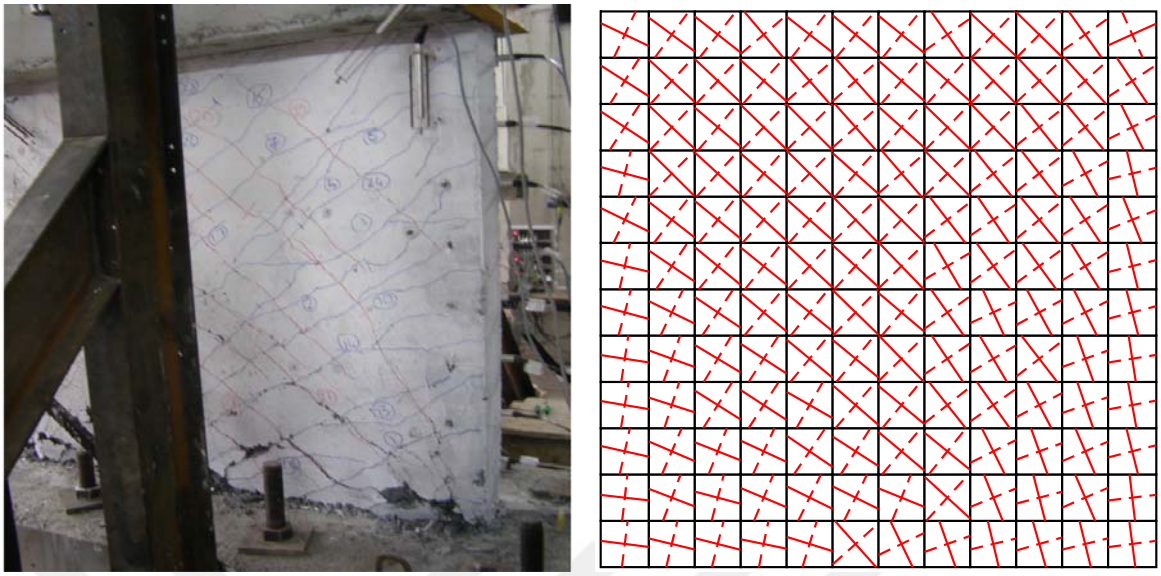

(a) (b)

Figure 4.16. Open and closed crack orientations for specimen SW-T6-S1-8 at 0.8% drift: (a) Test, (b) Model.

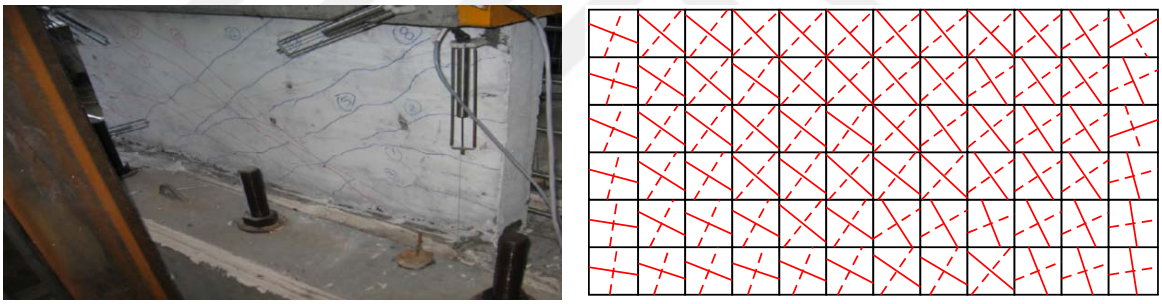

(a) (b)

Figure 4.17. Open and closed crack orientations for specimens SW-T2-S3-4 at 0.6% drift: (a) Test, (b) Model.

4.6. Parametric Sensitivity Studies on Model Results

4.6.1. Consideration of a Rotational Strain Penetration Spring

Reduction in the initial lateral stiffness of the squat walls, due to the elongation (strain penetration) of reinforcing bars embedded in the bottom and top pedestals, has been considered by adding a zero-length rotational spring in the formulation of FSAFE model, with calculated rotational spring stiffness parameters for each of the squat wall specimens.

Lateral load vs. top displacement responses of two specimens are presented in Figure 4.18 for showing the improving effect of the incorporation of rotational spring in the FSAFE model formulation. It is important to state that in demonstration of the influence of the rotational spring in the analysis predictions, lateral load vs. top displacement responses are plotted up to small drift levels to highlight the contribution of rotational spring on the initial stiffness (Figure 4.18).

Before the implementation of the rotational spring in the model formulation, the model overestimates the experimentally-observed stiffness of the specimens SW-T6-S1-8 and WS-T1-S1, as illustrated in Figure 4.18. However, when a zero-length rotational spring is employed, the model shows a very good correlation with the experimental results, in terms of the lateral stiffness of the specimen SW-T6-S1-8 in both positive and negative loading directions (Figure 4.18a), while it also improves the model stiffness estimations for the specimen WS-T1-S1 in both directions (Figure 4.18b). Comparison of model results with and without consideration of the rotational spring reveals that employment of a zero-length rotational spring improves the model accuracy in predicting the initial lateral stiffness of squat walls. It must be mentioned that for slender and medium-rise walls, the influence of the rotational spring on stiffness prediction of the model is not as noticeable, since slender and medium-rise walls are more flexible and the contribution of strain penetration effects on their lateral stiffness is less pronounced.

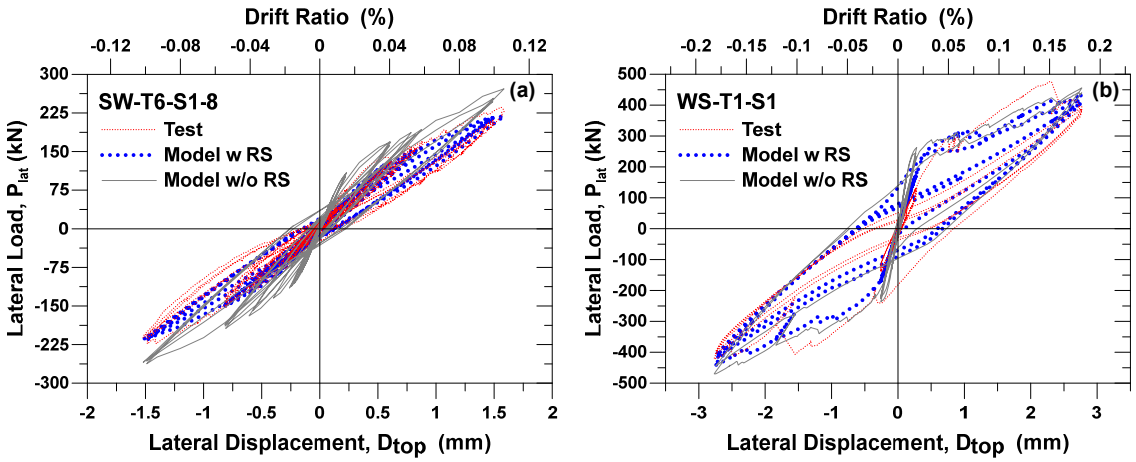

Figure 4.18. Sensitivity of the model results to consideration of rotational spring for the specimens: (a) SW-T6-S1-8, (b) WS-T1-S1.

4.6.2. Consideration of a Regularization Method to Minimize Strain Localization

For improving the sensitivity of the model results on the mesh size, especially related to the negative slope of the degrading region of the lateral load vs. displacement response of squat walls investigated, a regularization method was employed in the model formulation, via modifying the descending slope of the envelope of concrete stress-strain relationship under compression, as described in Section 4.4.4. Figure 4.19 compares the lateral load vs. top displacement predictions of the regularized and non-regularized models with test results for two representative specimens. These two specimens were selected to illustrate the impact of the regularization method employed in the model formulation to the ductility and lateral load degradation characteristics of the squat wall specimens.

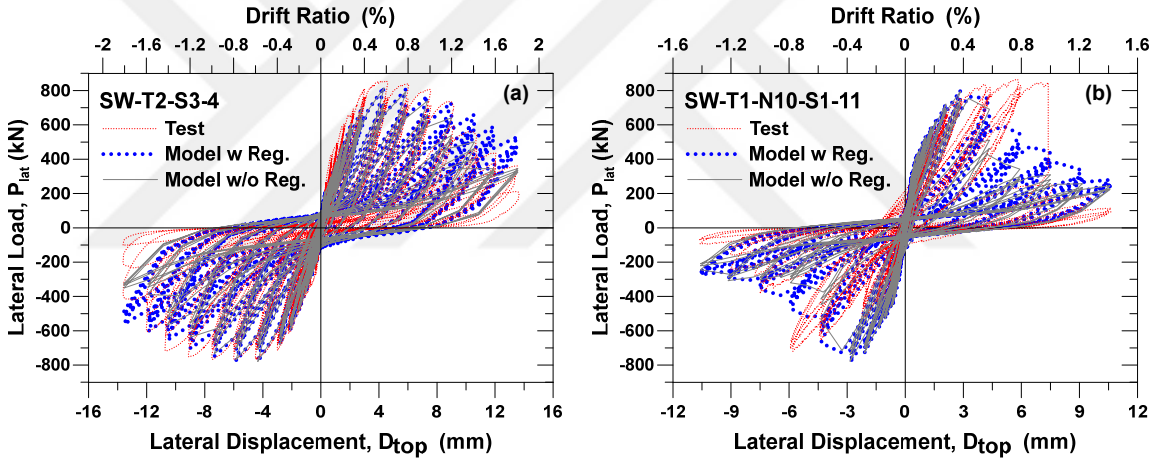

Figure 4.19. Sensitivity of the model results to consideration of regularization for specimens: (a) SW-T2-S3-4, (b) SW-T1-N10-S1-11.

With incorporation of the regularization method, the model better-represents the ductility characteristic of the wall specimen SW-T2-S3-4, which was tested under zero axial load, up to drift levels at which severe degradation was observed in lateral load (Figure 4.19a). The improving effect of employment of the regularization method in the FSAFE model formulation to the initiation of degradation and rate of degradation in lateral load are more noticeable (Figure 4.19b) for specimen SW-T1-N10-S1-11, which was subjected to an axial load level of 10% $A_g f'_c$, with a drift capacity of 0.8% in positive and negative loading directions. Comparison of the numerical estimations with the

experimental results proves that consideration of the regularization method moderately improves the model accuracy. Accordingly, the regularization method described in Section 4.4.4. was considered in modeling of all the squat wall specimens investigated in the present study.

4.6.3. Mesh Sensitivity Analysis

Following consideration of strain localization effects and implementation of a zero-length rotational (strain penetration) spring in FSAFE model formulation, mesh sensitivity analyses were also conducted representatively for two specimens to investigate the effect of mesh size on the model response predictions. Mesh sensitivity analysis was performed for two representative specimens from the two different experimental programs. Global and local response predictions of the model for specimens SW-T2-S3-4 and WP-T5-N5-S1, with three different mesh discretizations along the wall height and width, are compared in Figure 4.20 to Figure 4.29. Although comparison of model predictions with test results using medium (m=12, n=6 for specimen SW-T2-S3-4; m=11, n=10 for specimen WP-T5-N5-S1) mesh discretization were presented in the previous sections, they are presented again herein for comparison purposes.

As shown in Figure 4.20 and Figure 4.21, model predictions with different mesh discretizations (number of model elements) show similar trends before lateral load degradation starts for both specimens. However, using a coarser mesh (m=7, n=3 for specimen SW-T2-S3-4; m=7, n=5 for specimen WP-T5-N5-S1) in the model, results in overestimation of the lateral load capacity for specimen SW-T2-S3-4 (Figure 4.20a) and not capturing the initiation of degradation in lateral load for both specimens (Figure 4.20). Comparison of the results for medium and finer (m=24, n=12 for specimen SW-T2-S3-4; m=22, n=30 for specimen WP-T5-N5-S1) mesh configurations reveals similar model predictions in terms of lateral load capacity and drift capacity. Furthermore, using a coarser mesh leads to slightly higher flexural deformations and smaller shear deformations compared to model predictions with medium and finer mesh configurations (Figure 4.22 and Figure 4.23). Comparison of the model predictions and experimental results for the shear deformation profiles along wall height and vertical growth vs. top displacement responses for coarser, medium and finer mesh discretizations are presented in Figure 4.24

and Figure 4.25. Since only shear deformation profiles were available for the wall pier and spandrel specimens, model predictions for specimen SW-T2-S3-4 is not shown. Shear deformation profiles along wall height predicted by the model with medium and finer mesh discretizations are identical; however, model predictions with the coarser mesh discretization are slightly different than the medium and finer mesh discretizations, similarly to the trend in shear and flexural deformation contributions (Figure 4.23). Model predictions for wall vertical growth also shows the same trend for coarser, medium and finer mesh discretizations (Figure 4.25).

Figure 4.26 and Figure 4.27 compare the average horizontal normal strain profiles predicted by the model at various drift levels for specimens SW-T2-S3-4 and WP-T5-N5-S1. Again, model predictions with medium and finer mesh discretizations are almost equal to each other and close to test results, whereas model estimations with the coarser mesh discretization underestimates test measurements. Finally, Figure 4.28 and Figure 4.29 present crack orientations and principal concrete compressive stress contours for specimen SW-T2-S3-4 at the drift level of 0.6%. Crack orientations do not differentiate significantly in the model predictions; however, model predictions for the magnitude and distribution of principal compressive stresses in concrete differ. In conclusion, similarly to the case of slender and medium rise walls, considering computational time and convergence of the model results; the medium mesh discretization approach (described in Section 4.4.1) is applied for all squat walls investigated in the present study, as a standardized geometric discretization procedure.

4.6.4. Effect of Predefining a Sliding Crack for the Wall with Sliding Shear Failure

In the model results presented in the previous sections for squat walls, wall specimens that experienced sliding failure at the wall-pedestal interface were not included. This is because concrete cracks in the FSAFE model formulation are inherently discrete, and formation of a continuous sliding shear crack at the pedestal interface of the wall, and the subsequent sliding shear type of wall response cannot be simulated by the model. However, as a final sensitivity study, one of the three specimens that experienced sliding shear failure (Table 4.2) along the wall bottom pedestal interface is scrutinized herein. Two different model predictions for the specimen SW-T3-S1-5 are presented in Figure 4.30.

The specimen is first modeled using the standard FSAFE model formulation with the rotational strain penetration spring and regularization for strain localization, similarly to all other squat wall specimens investigated.

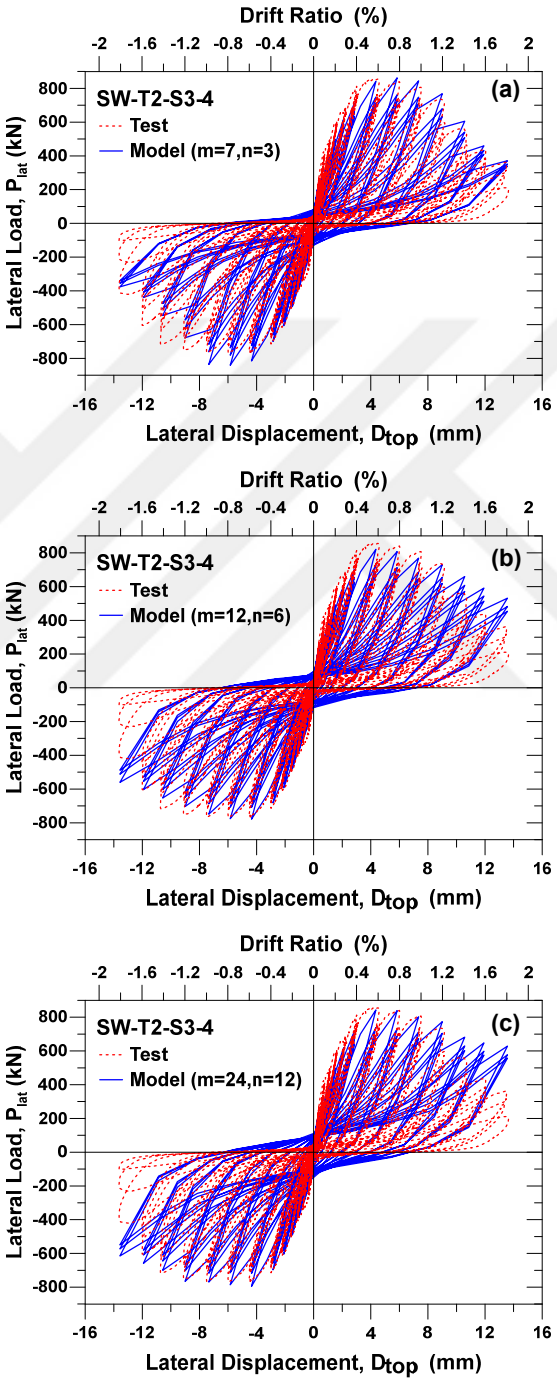

Figure 4.20. Sensitivity of model lateral load vs. top displacement responses to number of model elements used in horizontal (*m*) and vertical (*n*) directions for specimen SW-T2-S3-4: (a) *m*=7, *n*=3 (b) *m*=12, *n*=6, (c) *m*=24, *n*=12.

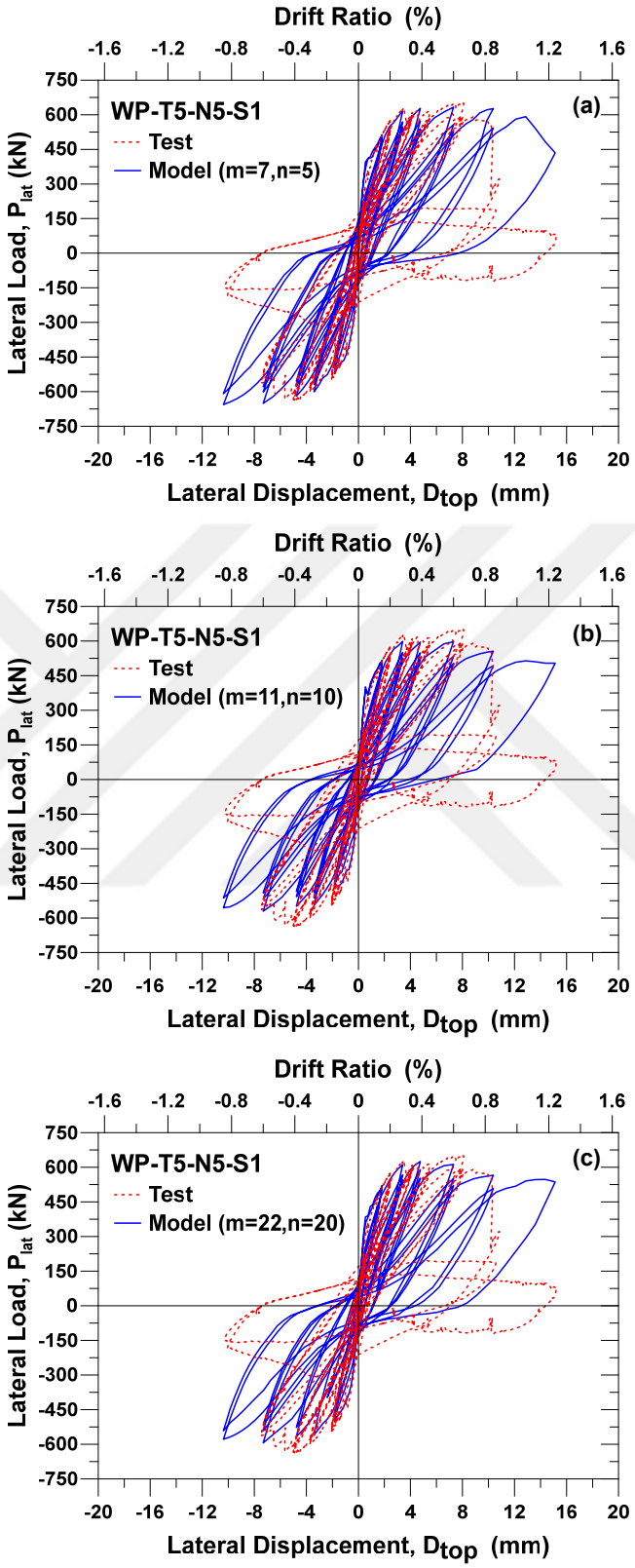

Figure 4.21. Sensitivity of model lateral load vs. top displacement responses to number of model elements used in horizontal (*m*) and vertical (*n*) directions for specimen WP-T5-N5-S1: (a) *m*=7, *n*=5 (b) *m*=11, *n*=10, (c) *m*=22, *n*=20.

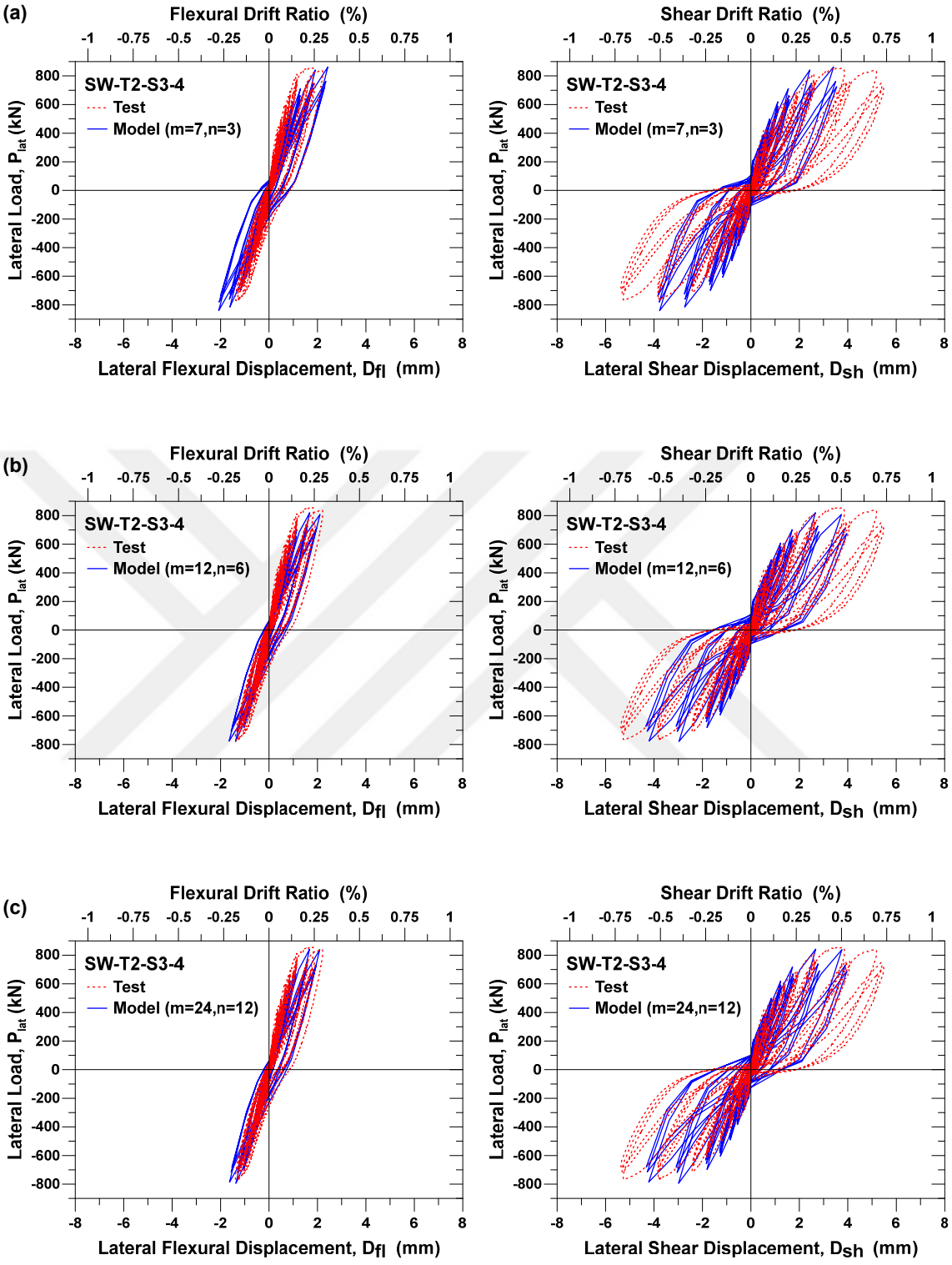

Figure 4.22. Sensitivity of model lateral load vs. flexural and shear deformation responses to number of model elements used in horizontal (*m*) and vertical (*n*) directions for specimen SW-T2-S3-4: (a) *m*=7, *n*=3, (b) *m*=12, *n*=6, (c) *m*=24, *n*=12.

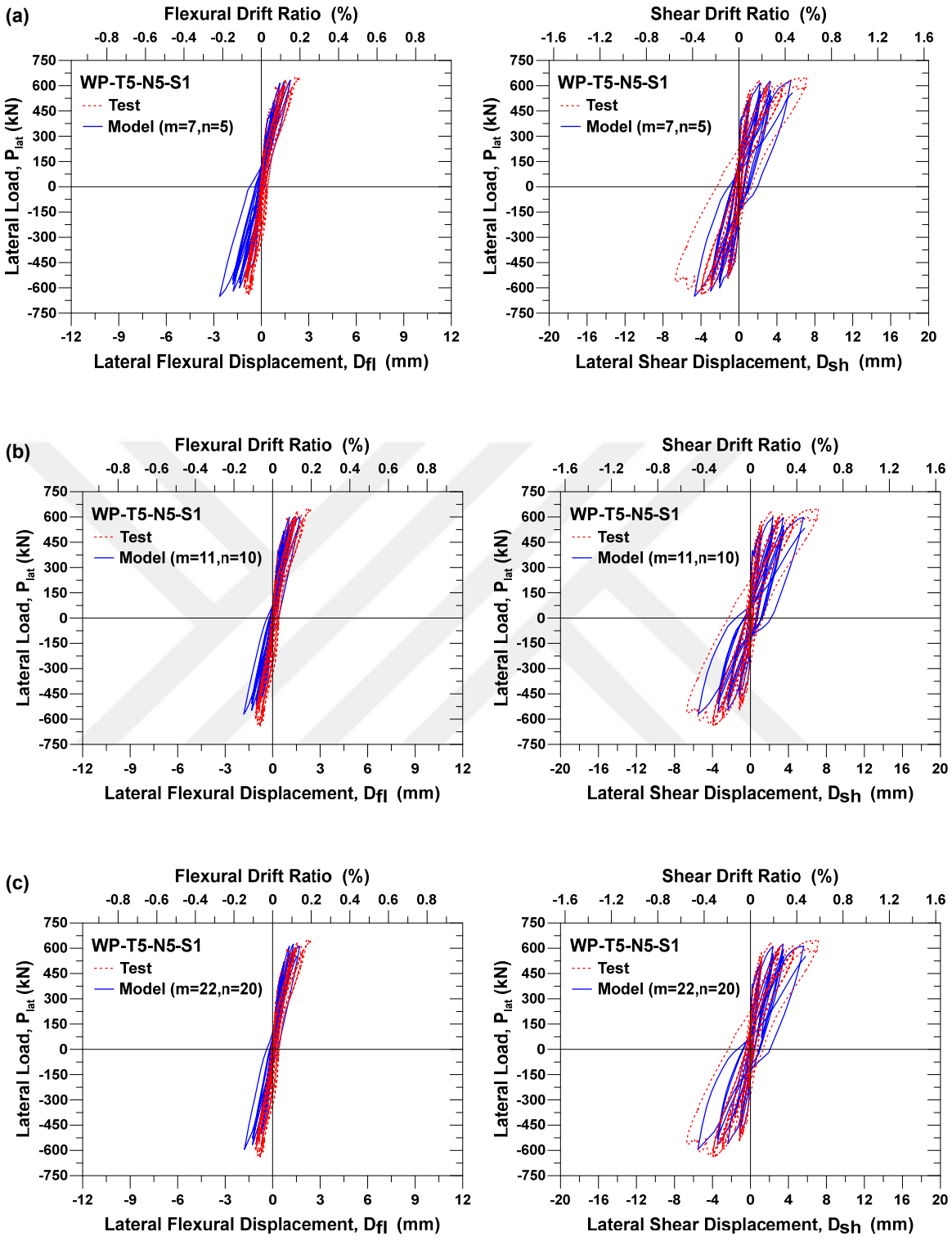

Figure 4.23. Sensitivity of model lateral load vs. flexural and shear deformation responses to number of model elements used in horizontal (*m*) and vertical (*n*) directions for specimen WP-T5-N5-S1: (a) *m*=7, *n*=5, (b) *m*=11, *n*=10, (c) *m*=22, *n*=20.

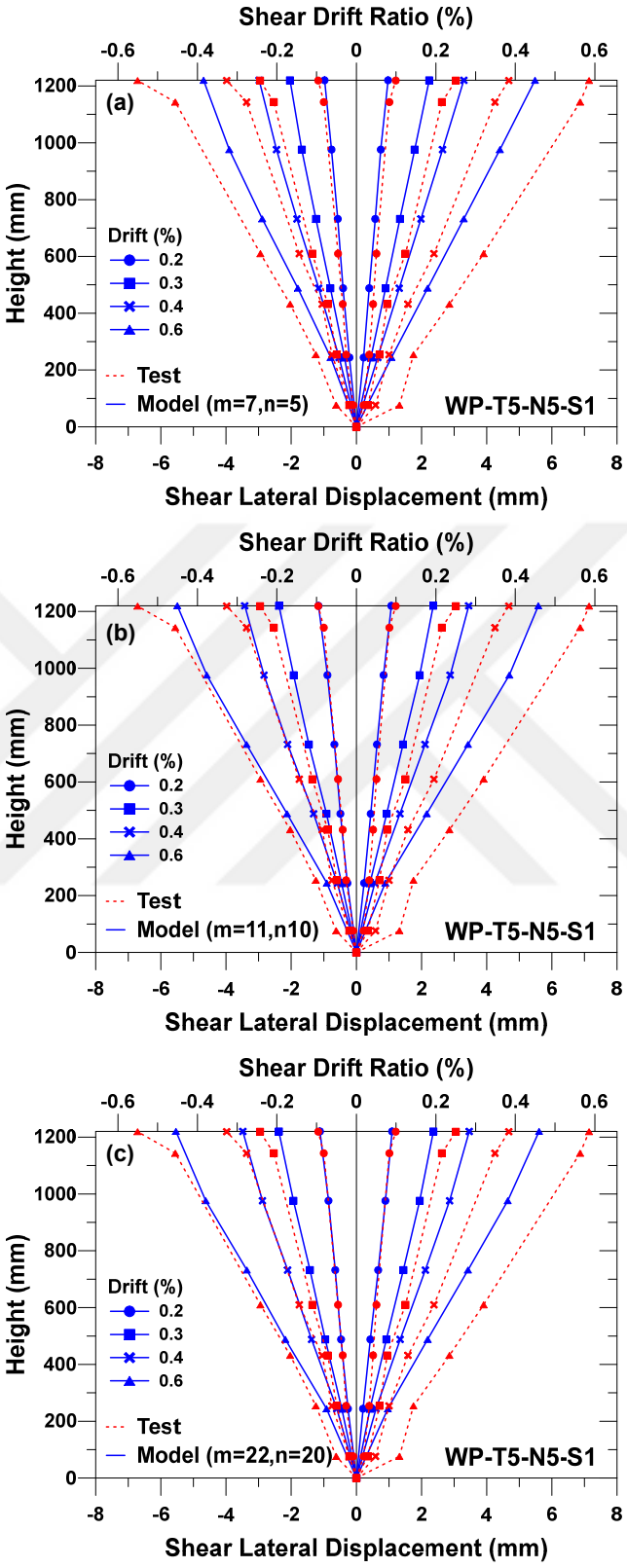

Figure 4.24. Sensitivity of model shear displacement profile along wall height responses to number of model elements used in horizontal (m) and vertical (n) directions for specimen WP-T5-N5-S1: (a) m=7, n=5, (b) m=11, n=10, (c) m=22, n=20.

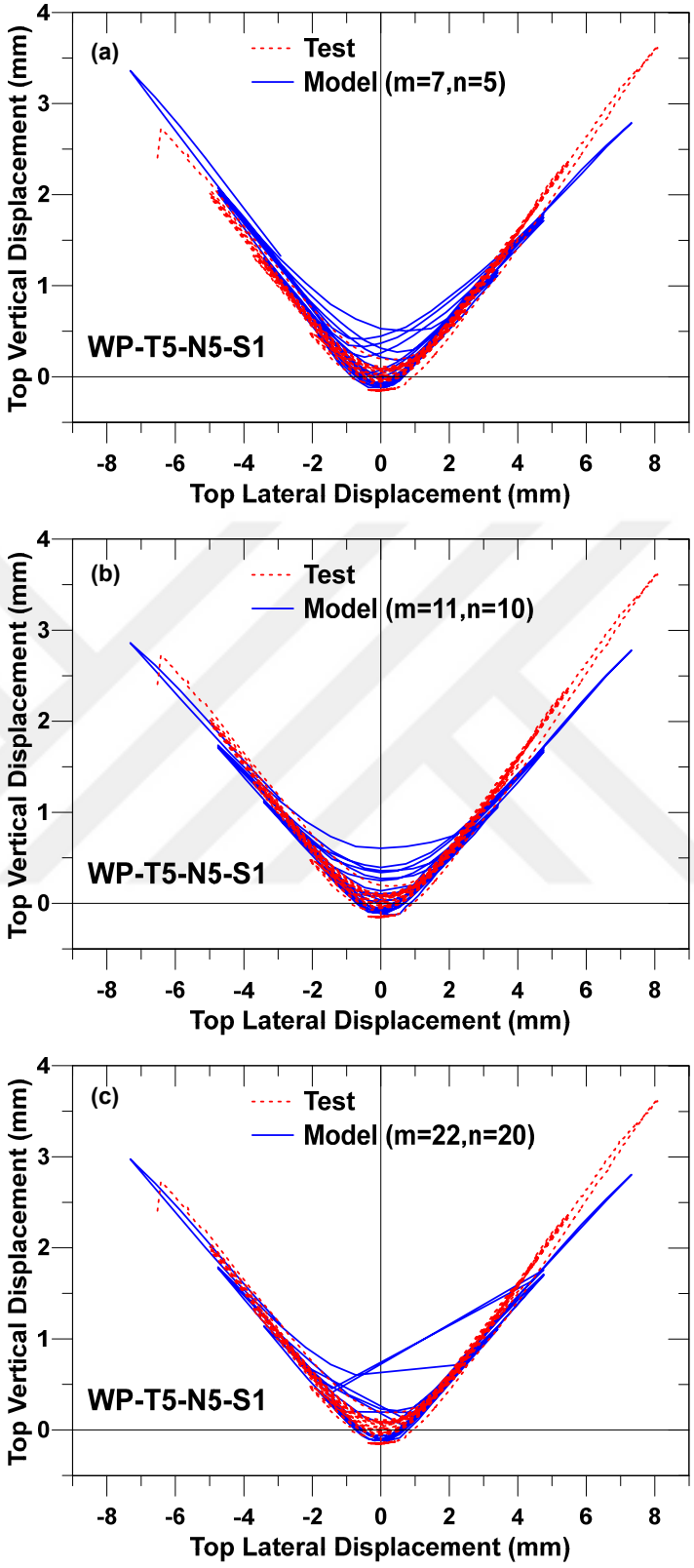

Figure 4.25. Sensitivity of model vertical growth vs. top displacement responses to number of model elements used in horizontal (m) and vertical (n) directions for specimen WP-T5-N5-S1: (a) m=7, n=5, (b) m=11, n=10, (c) m=22, n=20.

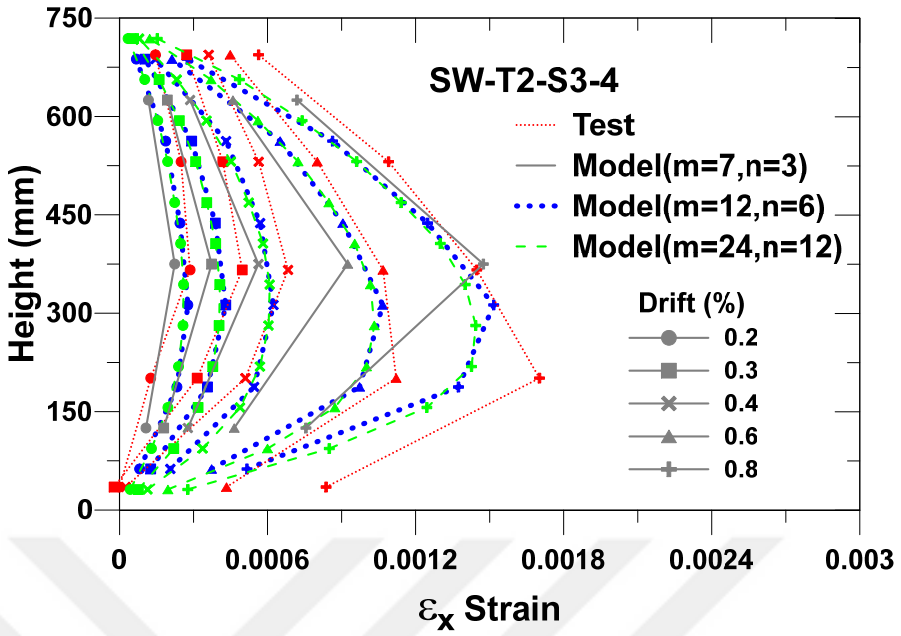

Figure 4.26. Sensitivity of model average horizontal normal strain profiles along wall height responses to number of model elements used in horizontal (*m*) and vertical (*n*) directions for specimen SW-T2-S3-4.

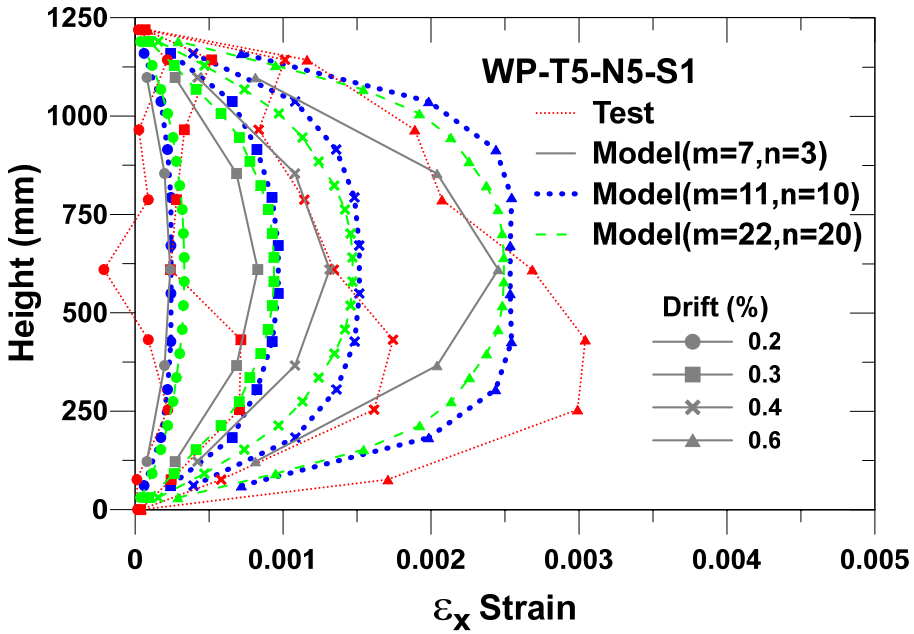

Figure 4.27. Sensitivity of model average horizontal normal strain profiles along wall height responses to number of model elements used in horizontal (*m*) and vertical (*n*) directions for specimen WP-T5-N5-S1.

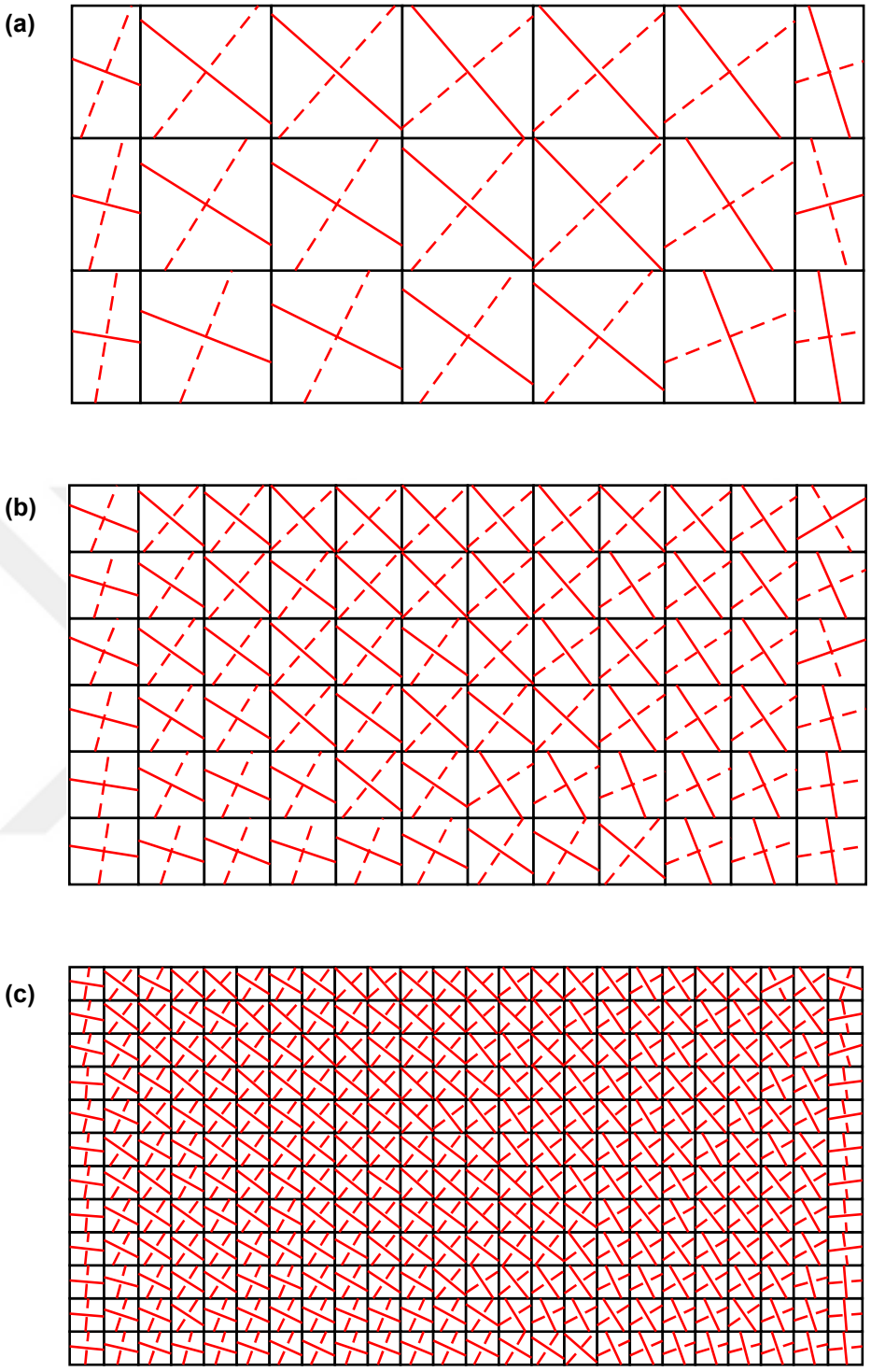

Figure 4.28. Sensitivity of model crack patterns for specimen SW-T2-S3-4 at 0.6% drift with various model elements in horizontal and vertical directions: (a) m=7, n=3, (b) m=12, n=6, (c) m=24, n=12.

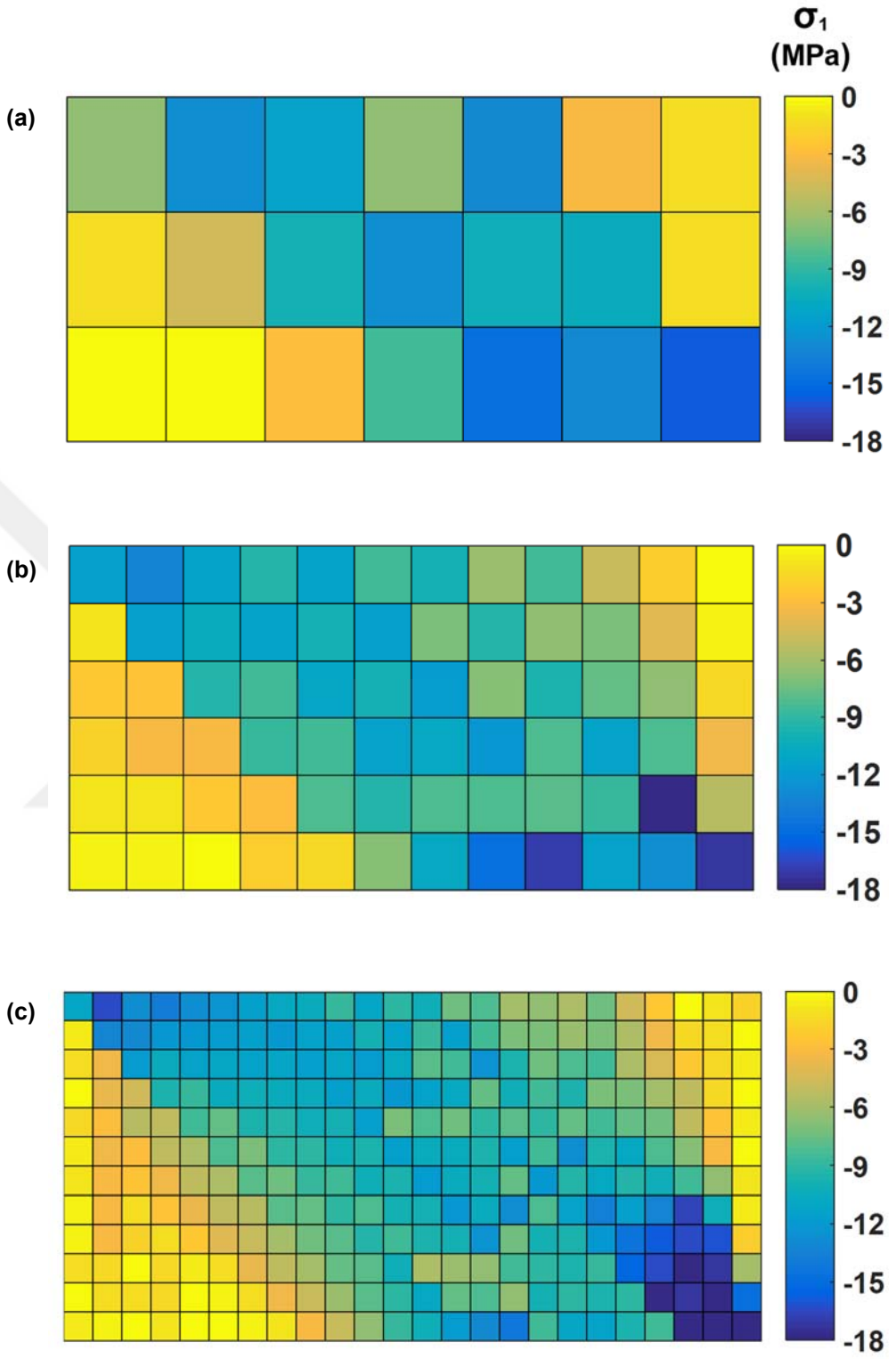

Figure 4.29. Sensitivity of model concrete principal compressive stress contours for specimen SW-T2-S3-4 at 0.6% drift with various model elements in horizontal and vertical directions: (a) *m*=7, *n*=3, (b) *m*=12, *n*=6, (c) *m*=24, *n*=12.

As illustrated in Figure 4.30a, the standard model captures the lateral load capacity of the wall in the positive loading direction while it largely overestimates the capacity in the negative loading direction. However, and more importantly, the model cannot capture the experimentally-observed pronounced pinching behavior of the wall, as well as the degradation in lateral load (Figure 4.30a), since the model predicts a coupled shear-flexural behavior, whereas the experimentally-observed behavior was sliding shear at the wall-pedestal interface. Therefore, for illustrative purposes, the model formulation is manipulated such that a "horizontal" crack is enforced on all of the bottommost model elements (for simulating the experimentally-observed sliding shear crack at the interface), in order to study whether or not it would be possible to obtain improved model predictions upon such manipulation. Figure 4.30b compares the response prediction of the model with the enforced horizontal crack along the wall base, with test results. The manipulated model under-predicts the lateral load capacity in the positive loading direction; however, it overestimates the capacity in the negative loading direction. Considering the average of the positive and negative loading directions, the lateral load capacity prediction of the model can be deemed reasonable. However, other hysteretic response characteristics of the wall, including pinching behavior, ductility, degradation in lateral load, and loading/reloading stiffness characteristics are all well-captured by the manipulated model, compared to the standard model formulation. Therefore, it can be stipulated that although the FSAFE model cannot capture global sliding shear failures in walls (due to its inherent discrete crack formulation), the shear aggregate interlock and dowel action models incorporated in the model formulation, in terms of their capacities (e.g., a friction coefficient of $\eta = 0.30$) and hysteretic rules, are reliable, since shear aggregate interlock and dowel action mechanisms dominate the response of the manipulated model for specimen SW-T3-S1-5. In fact, this observation has resulted in selection of a friction coefficient of $\eta = 0.30$ for all of the squat wall specimens analyzed in this study, as opposed to a friction coefficient of $\eta = 0.50$ that was used for modeling of slender and medium-rise walls (Chapter 3). It must be mentioned that using a friction coefficient of $\eta = 0.30$ for the slender and medium-rise wall specimens did not significantly alter the model results for the slender and medium-rise wall specimens, other than minor differences in the local response predictions.

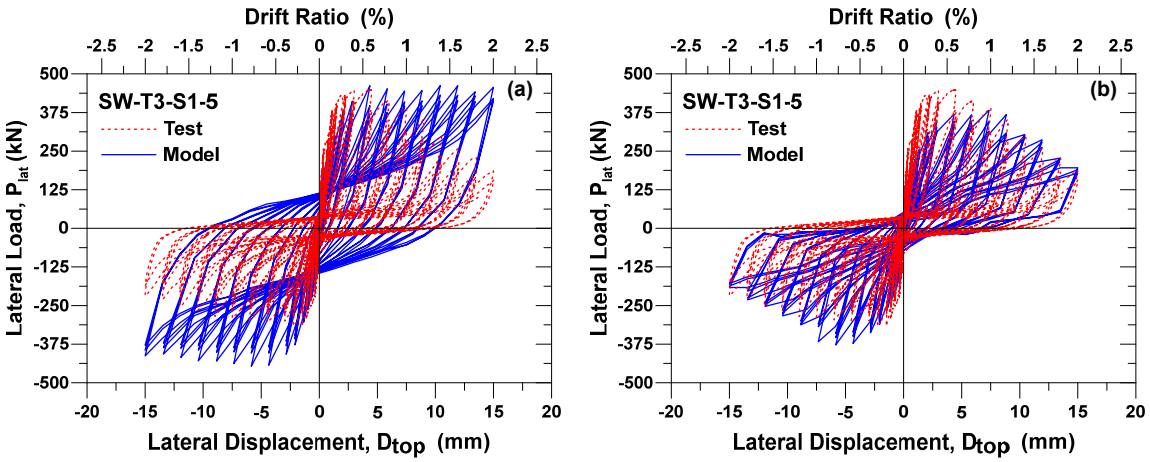

Figure 4.30. Lateral load vs. top displacement response for specimen SW-T3-S1-5: (a) sliding shear crack not enforced (b) sliding shear crack enforced.

4.7. Global Response Predictions of the Model for the Entire Squat Wall Database

Model accuracy in predicting the global lateral load vs. top displacement responses of all twenty-five shear-controlled squat wall specimens considered in this study is evaluated herein, via presenting the measured-to-predicted lateral load capacity, lateral displacement (drift) capacity and cumulative hysteretic energy dissipation capacity ratios. Lateral load capacity was defined as the maximum of the predicted or measured lateral loads, averaged in the positive and negative loading directions. The wall lateral drift capacity (Δ_u) was defined as the measured or predicted drift levels corresponding to 80% of the lateral load capacities of the walls upon degradation (Figure 4.31), also averaged in positive and negative loading directions. A similar definition of wall drift capacity was employed in the study by Pugh *et al.* (2015). Calculation of the measured (Figure 4.32a) and predicted (Figure 4.32b) cumulative hysteretic energy dissipation capacities of all specimens (cumulative area under the load vs. displacement loops) was performed up to a limiting drift level, since calculating the energy dissipation capacity up to very large drift levels is not very meaningful since such large drift levels correspond to unrealistically-severe damage states (see also Figure 4.8 to Figure 4.10). Considering the collapse-prevention-level drift capacities defined in ASCE 41-17 for shear-controlled walls (1.0% for walls with negligible axial load and 0.75% for specimens subjected to axial load), the measured and predicted cumulative hysteretic energy dissipation capacities were calculated up to a drift level of 1.20% for the specimens tested under zero axial load, and 0.80% for

specimens subjected to constant axial load during the tests. Hysteretic energy dissipation capacities in the test results and model predictions were calculated for each of the applied drift levels and loading cycles separately as shown in Figure 4.32, and summed over all loading cycles and drift levels for obtaining the cumulative dissipation capacity.

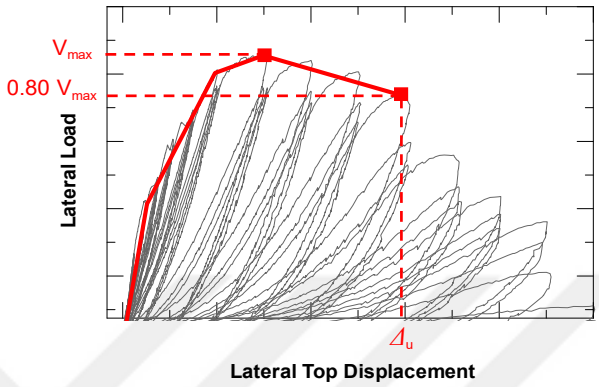

Figure 4.31. Description of the significant parameters in lateral load vs. top displacement envelope.

Figure 4.33 to Figure 4.35 show the measured-to-predicted lateral load capacity, lateral drift capacity, and cumulative hysteretic energy dissipation capacity ratios, with regards to three different important aspects that govern shear-controlled squat wall behavior, including failure mode, shear span-to-depth ratio, and axial load level, for scrutinizing the accuracy of the global response predictions of the FSAFE model for all of the squat wall specimens considered.

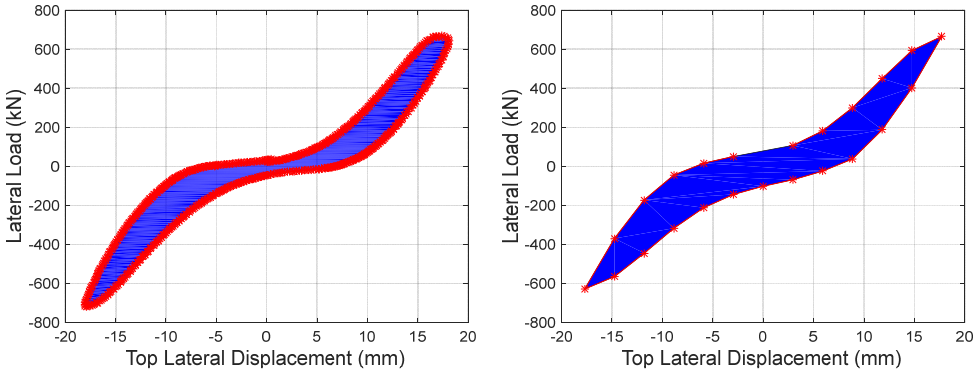

(a) (b)

Figure 4.32. Hysteretic energy dissipation capacity of specimen SW-T6-S1-8 for the first loading cycle to 1.2% drift: (a) Test, (b) Model.

Measured-to-predicted lateral load capacity ratios are reasonable (Figure 4.33). Average of the normalized ratios for the specimens that failed in diagonal tension is 1.06, whereas it is 1.04 for the specimens that experienced diagonal compression failure and 0.94 for the specimens that showed sliding shear failure. Overall, the FSAFE model slightly underestimates the experimentally-measured lateral load capacities of specimens that experienced diagonal compression tension failures, and slightly overestimates that of specimens that suffered sliding shear failure (with no manipulation of a sliding shear crack in the model formulation). Since limited experimental data was available for specimens with shear-span-to-depth ratios of 0.47, 0.65, 1.13 and 1.15, one ratio is presented for each. However, for shear-span-to-depth ratios of 0.44, 0.50 and 0.63, model accuracy was evaluated with a sufficient number of experimental data. Comparison of the lateral load capacity predictions of the model when the specimens are categorized according to their axial load levels is shown in Figure 4.33c. For the specimens subjected to zero axial load, average of the measured-to-predicted ratios is 1.03, whereas it is 1.12 and 1.06 for the specimens with axial load levels of $0.05A_g f'_c$ and $0.10A_g f'_c$, respectively. Although variation in experimental data in terms of the shear-span-to-depth ratio and axial load level is limited, it can be deduced from the comparisons that the model is capable of reproducing the experimentally-observed lateral load capacities of the walls with an acceptable margin of error. Overall average of the measured-to-predicted lateral load capacity ratios for all walls is 1.04 with a coefficient of variation of 0.1.

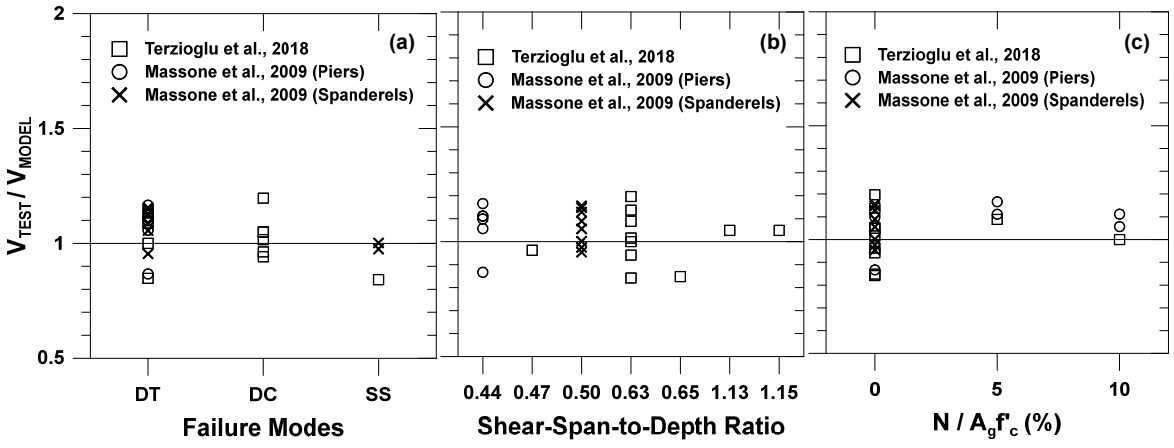

Figure 4.33. Comparison of lateral load capacities for squat walls with: (a) different failure modes, (b) different shear-span-to-depth ratios, (c) different levels of axial load.

In design, and evaluation of walls using performance-based design approaches, drift (or chord rotation) capacity of shear-controlled walls (e.g., as defined in ASCE 41-17), is the governing parameter. However, accurately predicting the drift capacities of shear-controlled walls is very challenging, due to their large stiffness and non-ductile behavior. Figure 4.34 shows the measured-to-predicted drift capacity ratios of the squat walls investigated, where the drift capacity is defined at 20% loss of lateral load capacity, categorized similarly to the lateral load capacity ratios. Average of the measured-to-predicted drift capacity ratios obtained for the specimens that failed in diagonal tension, diagonal compression, and sliding shear are 0.98, 0.99 and 0.72, respectively. With an average $\Delta_{u,test}/\Delta_{u,model}$ ratio of 0.90, the model overestimates the drift capacity of the specimens having a shear-to-span-depth ratios below 0.50. In contrast, the model underestimates the drift capacity of the specimens with shear-to-span-depth ratios above 0.50, with an average $\Delta_{u,test}/\Delta_{u,model}$ ratio of 1.06. In terms of the level of axial load, the average of the measured-to-predicted drift capacity ratios is 0.95 for specimens tested under zero axial load, whereas the average value is 1.02 for specimens subjected to axial load during testing. Although the error margin in the drift capacity predictions of the model can be significant (Figure 4.34), the overall average of the measured-to-predicted drift capacity ratios for all specimens is 0.96 with a coefficient of variation of 0.34, indicating that the FSAFE model is capable of providing reasonable predictions of the drift capacity of squat walls with shear-controlled responses.

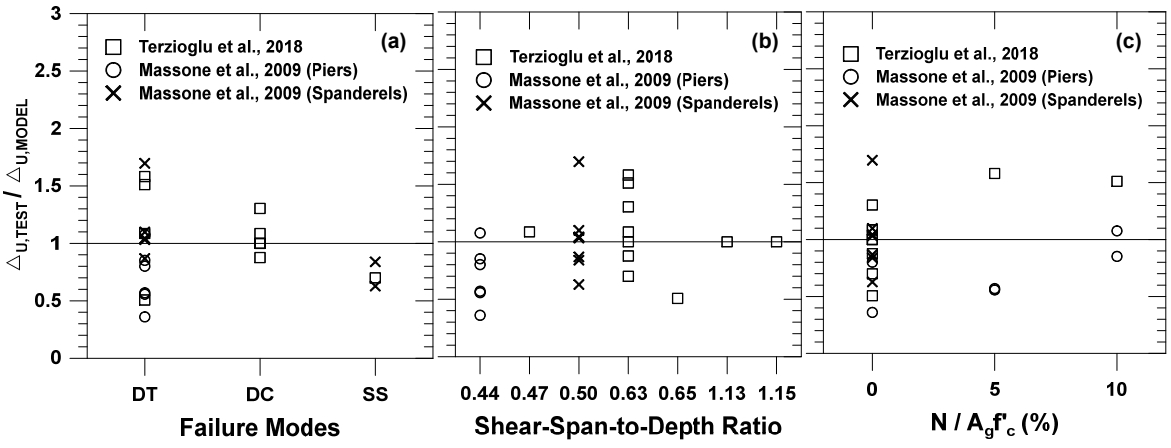

Figure 4.34. Comparison of drift capacities for squat walls with: (a) different failure modes, (b) different shear-span-to-depth ratios, (c) different levels of axial load.

Final validation of the model accuracy in predicting global response characteristics of squat walls is conducted by comparing the cumulative hysteretic energy dissipation capacities of the test measurements and model predictions, up to a drift level of 1.20% for the specimens with zero axial load and 0.80% for the specimens with axial load (Figure 4.35). Comparing the average of the cumulative hysteretic energy dissipation ratios, the model slightly under-predicts the energy dissipation capacities of specimens that suffered diagonal tension failure, and slightly overestimates the capacities of specimens with diagonal compression and sliding shear failures. Specimens with a shear-span-to-depth ratio below 0.50, the average value of the measured-to-predicted cumulative energy dissipation ratios is 1.02, whereas for those above 0.50 the average ratio is 0.87, revealing that the model provides more accurate predictions of the energy dissipation ratios of walls with shear-span-to-depth ratios below 0.5. The average of the energy dissipation capacities is underestimated for the specimens with zero axial load, with an average measured-to-predicted ratio of 0.89, and is overestimated for the axially loaded specimens, with a ratio of 1.17. Average of the measured-to-predicted cumulative energy dissipation ratios for all twenty-five specimens is 0.96, with a coefficient of variation of 0.21, which is reasonable considering the non-ductile response characteristics of shear-controlled squat walls.

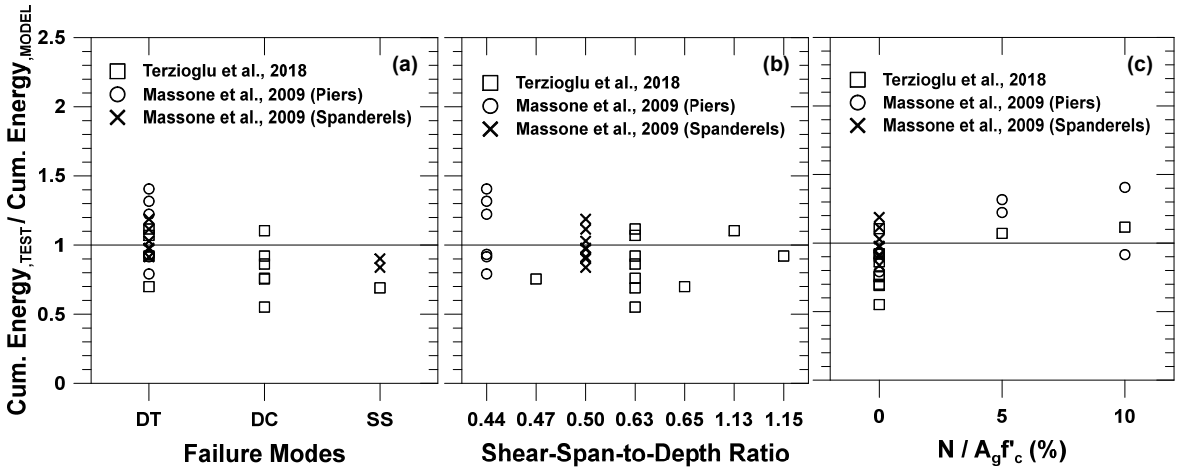

Figure 4.35. Comparison of cumulative hysteretic energy dissipation capacities for squat walls with: (a) different failure modes, (b) different shear-span-to-depth ratios, (c) different levels of axial load.

4.8. Overview

The intent in this chapter was to improve the FSAFE model formulation, by implementing more refined constitutive models for shear aggregate interlock and dowel action mechanisms that also include cyclic degradation parameters, by implementation of a rotational spring to simulate strain penetration effects, and by consideration of a regularization method for minimizing strain localization effects, as well as to extensively validate the improved model against test results on wall specimens with shear controlled responses. A description of all squat wall specimens used for validation of the model was first presented. The modeling approach used for these specimens, including the geometric discretization method used and the material modeling parameters selected, was described. Validation of the FSAFE model for important global and local response characteristics of representative wall specimens was systematically presented. Crack patterns and principal concrete compressive stress contours predicted by the model were also provided for evaluating the stress transfer mechanisms in the model results. Parametric sensitivity studies were conducted for demonstrating the influence of the implementation of the rotational spring in FSAFE model, consideration of a regularization method in the concrete stress-strain relationship under compression, as well as the model mesh discretization approach used. Furthermore, model results for one of the wall specimens that experienced sliding shear failure was scrutinized, with and without enforcement of a horizontal sliding shear crack the wall base in the model formulation. Finally, results of model validation studies for the global lateral load vs. top displacement responses of all twenty-five squat wall specimens was presented, where the experimentally-measured lateral load capacity, drift capacity, and cumulative hysteretic energy dissipation capacity of all specimens were compared to the analytical predictions.

It was observed that the FSAFE model, with the improvements presented in this chapter, provides reasonably accurate response predictions also for squat wall specimens with shear-controlled responses. However, the sudden and abrupt degradation in lateral load observed in the test results of some of the specimens is not captured by the model; a more gradual degradation in is observed in the analytical responses. The FSAFE model replicates the approximately linear elastic lateral load vs. flexural deformation behavior, and the highly-nonlinear and pinched lateral load vs. shear deformation responses of squat

walls. Considering model predictions for the average horizontal normal strain distributions along wall height, crack patterns, and principal concrete compressive stress contours, it is verified that the FSAFE model is capable of simulating the failure modes of the shear-controlled walls. Measured-to-predicted ratios have an average of 1.04 and a coefficient of variation of 0.10, for the lateral load capacity of all twenty-five wall specimens, and an average of 0.96 and a coefficient of variation of 0.34 for their drift capacity, demonstrating that the model, on average, is reliable in simulating the global lateral load vs. displacement characteristics (or backbone curves) of squat walls with shear-controlled responses. Furthermore, with an average of 0.96 and a coefficient of variation of 0.21 for the measured-to-predicted cumulative hysteretic energy dissipation capacity ratios of all wall specimens investigated, the FSAFE model is shown, on average, to be capable of simulating the hysteretic energy dissipation characteristics of walls with shear-dominated responses also.

5. SUMMARY AND CONCLUSIONS

5.1. Summary

A novel finite element model formulation (named as the Fixed Strut Angle Finite Element–FSAFE–Model) was proposed in this study for simulating the nonlinear response of RC walls under cyclic lateral loads. The constitutive behavior of the model elements follow a fixed-crack-angle approach, in which normal stresses in concrete are calculated along the fixed crack directions. Relatively simple behavioral models for shear-aggregate-interlock effects along crack surfaces and dowel action on reinforcing bars were first implemented in the model formulation, for representing shear stress transfer mechanisms across cracks. The model was validated against test results at global and local response levels on nine densely-instrumented wall specimens selected from the literature, with various configurations and response characteristics, including slender walls with flexure-dominated responses and medium-rise walls with coupled shear and flexural responses. Sensitivity of the analytical results on mesh discretization of the model was also presented for a representative wall specimen.

The FSAFE model formulation was subsequently improved for simulation of shear-controlled wall responses, via refinement of the constitutive models for shear aggregate interlock effects and dowel action (also incorporating cyclic degradation parameters), as well as by implementation of a zero-length rotational spring to include strain penetration effects in wall pedestals, and incorporation of a stress-strain regularization method to minimize strain localization effects in the analysis. Model predictions were validated against test results on twenty-five shear-critical wall specimens with various configurations, tested as part of two different experimental programs. Sensitivity of model results to incorporation of the rotational strain penetration spring, implementation of the regularization method, and to model mesh discretization was investigated. Furthermore, sensitivity of the model results to predefinition of a sliding crack at the wall-pedestal interface was investigated, for a wall specimen that experienced sliding shear failure at the interface. Analysis results for representative squat wall specimens were compared with experimental measurements at both global and local response levels. For all twenty-five

squat wall specimens in the experimental database, model estimations and test results for important global response parameters (lateral load capacity, lateral displacement capacity, cumulative hysteretic energy dissipation capacity) were also compared.

5.2. Conclusions on FSAFE Model Characteristics

5.2.1. Walls with Flexural or Coupled Shear Flexural Responses

Based on the comprehensive correlation studies conducted between model predictions and experimental results for slender and medium-rise walls designed to yield in flexure, the following conclusions on important attributes of the FSAFE model were reached:

- Despite its relatively simple formulation, the FSAFE model was shown to be reasonably accurate in predicting the experimentally-observed response features of the wall specimens investigated except one (specimen R2). The model captured the experimentally-measured load-displacement response characteristics of most of the walls, including their lateral stiffness, lateral load capacity, drift capacity, hysteretic stiffness degradation, and pinching behavior. The model reasonably captured the drift capacity of three of the wall specimens only (RW-A20-P10-S63, RW-A15-P10-S51, RW-A15-P10-S78, and S6), although with much more gradual lateral load degradation in the analysis results. For all specimens, the model could not simulate the experimentally-observed abrupt degradation in lateral load, since instability failures related to buckling of reinforcement or out-of-plane instability of the wall boundary region are not considered in its formulation, which is also the reason why the model was incapable of predicting the drift capacity of specimens RW2, TW2, RW-A20-P10-S38, WSH6, and R2.

- Prior to their experimentally-observed instability failures, local response characteristics of all wall specimens excluding R2, including the contribution of shear and flexural deformations to lateral displacement, distribution of shear and flexural deformations along wall height, crack orientations on the walls, vertical growth behavior of the walls and the vertical normal strain profiles measured along

the base of the walls were all well-estimated by the model. Simulation of nonlinear shear-flexure interaction behavior and capturing of the nonlinear flexural strain gradient along wall length, which creates increased compressive strain demands on concrete and leads to reduction in wall drift capacity, are significant strengths of the FSAFE model over typical fiber-based models used for walls that are expected to yield in flexure. Model predictions are not always 100% accurate, as should not be expected from a relatively simple model formulation, considering the idealizations used in representation of the mechanical behavior as well as the high level of variability in material behavior.

- Significant attributes of the FSAFE model pertaining to seismic design and performance-assessment of walls include: (i) successful representation of the shear-flexure interaction behavior observed experimentally in both slender and medium-rise walls designed to fail in flexure, (ii) capturing of the nonlinear distribution of vertical normal strains across both rectangular and non-rectangular wall cross-sections in parallel and perpendicular directions to loading (plane sections not remaining plane due to shear lag effects), as well as (iii) providing improved predictions for the compressive strains in concrete (as opposed to fiber-based models). These features constitute the obvious strengths of the FSAFE model over existing approaches used for modeling of walls in current performance-based seismic design applications.

- The major shortcoming of the present model formulation is lack of consideration of lateral instabilities in simulating the response of walls. The inadequacy of the present model in capturing the experimentally-observed response of Specimen R2, which experienced initiation of lateral instability in the wall boundaries at early drift levels, due to the zero axial load level and the large in-plane slenderness of the wall, highlights the potential of such an approach towards improving the capabilities of the model. Such improvements would also enhance the accuracy of the model in predicting local responses (e.g., vertical strains) at or close to failure.

5.2.2. Walls with Shear Controlled Responses

Based on the numerous correlations studies conducted between model results and test measurements for squat walls, the following conclusions on significant features of the FSAFE model for walls with shear controlled responses were derived:

- The model was shown to provide fairly-well predictions of the lateral stiffness, lateral load capacity, ductility, pinching, as well as the degradation lateral load and unloading/reloading stiffness of the shear critical wall specimens investigated. The capability of the model to incorporate the influence of axial load in lateral load capacity of the shear critical walls was also confirmed through the wall specimens considered, six of which was subjected to axial load whereas the remaining wall specimens were tested under zero axial load. The model provided reasonable estimates for the approximately linear elastic flexural and highly nonlinear shear deformation responses of squat walls (as opposed to flexure-dominated response characteristics of slender and medium-rise walls) as well as vertical growth characteristics, and the profile of shear displacements and the distribution of average horizontal normal strains along the height of the walls. Reasonable model results were also obtained for the distribution of compressive stresses in concrete, and the orientation of the cracks developing in walls with shear-dominant responses.

- Parametric sensitivity analysis were also conducted on selected specimens for assessing the dependency of model results on implementation of a zero-length rotational strain penetration spring implemented in the model assembly, the regularization method employed to minimize strain localization effects, the mesh discretization approach used in modeling of wall specimens, and pre-definition of a horizontal crack at the wall base for wall specimen that experienced sliding shear failure at the wall-pedestal interface. Implementation of a rotational spring for simulation of strain penetration behavior improved the model accuracy in capturing the initial stiffness of the squat walls. Incorporation of a stress-strain regularization method on concrete in compression for reducing the strain localization effects on the analysis predictions resulted in improved predictions of the rate of lateral load degradation in the global response of the wall specimens, enhancing the accuracy in

the ductility predictions of the FSAFE model. Comparison of model results with coarser, medium and finer mesh discretizations revealed that the differences in analysis results when medium and finer mesh discretizations are used, are not remarkable. Pre-definition of a horizontal crack at the base of the wall model for the wall specimen that experienced sliding shear failure at the wall-pedestal interface resulted in reasonable predictions for the lateral load capacity and other important hysteretic response characteristics (e.g., degradation in lateral load and stiffness, pinching), and also validated the value selected for the coefficient of friction to be applied across crack surfaces, which was also used in modeling of all squat wall specimens.

- Furthermore, model estimations for all twenty-five shear-controlled squat wall specimens were presented in terms of measured-to-predicted lateral load capacity, drift capacity and cumulative hysteretic energy dissipation capacity ratios. Lateral load capacity predictions of the model are in good agreement with experimental results, with an average value of measured-to-predicted ratios of 1.04. Admissible variations between the drift capacity predictions and test results can be attributed to the variations in the degrading slope of the concrete stress-strain relationship used in the formulation of FSAFE model, due to its dominating effect on the rate of lateral load degradation in the load-displacement response of shear-controlled brittle wall responses. Discrepancies between model results and test measurements associated with the cumulative energy dissipation capacity of the walls can also be attributed to the brittle response characteristics of the wall specimens considered.

- It is significant that the model prediction for the lateral load capacity of the axially-loaded wall specimens with shear-dominant behavior is reasonably accurate, since the model is apparently successful in capturing the influence of the axial load on the response characteristics of shear-controlled walls. Considering that current seismic design codes and performance assessment guidelines neglect the influence of axial load in wall shear strength calculations, (e.g., the ACI318-14) shear strength equation underestimates the lateral load capacity of this wall by approximately 35% (Orakcal *et al*., 2009), mainly due to lack of experimental data on walls failing in shear,

availability of a modeling approach that considers axial/shear interaction is promising towards improvement of code provisions on wall shear strength.

5.3. Suggested Improvements and Recommendations for Future Studies

(i) The accuracy of the model in predicting the lateral load capacity and drift capacity of walls, as well as the rate of degradation in lateral load after the capacity is reached, are subject to improvement upon implementation of constitutive models in its formulation for representing both local and global (over several hoop spacings) (e.g., Dhakal and Maekawa 2002) buckling behavior of reinforcement, and/or possible consideration of geometric nonlinearity effects in the analysis, using model elements that also incorporate out-of-plane displacement degrees of freedom.

(ii) For improving the model accuracy in predicting wall responses experienced lateral instability during experiments, a behavioral modeling approach to incorporate this instability-related softening behavior at wall boundaries (e.g., based on test observations by Welt *et al*. 2017, which show that previously-applied tensile strains on a wall boundary element can reduce its confined compressive strength by as much as 50% due to lateral instability) can be implemented in the formulation of the FSAFE model.

(iii) The FSAFE model has been validated in this study for wall specimens having concrete compressive strengths between 19MPa and 56MPa. Although the constitutive concrete material model by Chang and Mander (1994) used in the model formulation had also been validated for high-strength concrete, shear aggregate interlock characteristics of high-, ordinary-, and low-strength concrete may differ. The coefficient of friction used for simulating shear aggregate interlock remains to be an ad-hoc parameter in the model formulation that is expected to be sensitive to also the size and shape of the aggregates used in the concrete mixture. Future studies can address possible correlations between the friction coefficient and characteristics of concrete used in wall construction.

(iv) The FSAFE model can be validated for RC walls with non-rectangular cross-sections tested under bi-directional loading, for analytical investigation of shear-lag effects in non-rectangular walls, as well as their nonlinear torsional response characteristics.

(v) Further validation of the FSAFE model can be conducted for RC walls with openings, as well as for walls incorporating inclined reinforcing bars.

Overall, with the features described and the potential improvements identified in this study, the FSAFE model is presented as a relatively simple yet accurate modeling approach for simulating the nonlinear seismic behavior for RC walls with flexural, coupled shear-flexural, and shear controlled responses, at both global and local response levels. The FSAFE model is a feasible candidate to be used in modeling of structural walls in improved seismic response simulation studies for building systems, aimed towards enhancement of performance-based seismic design and assessment procedures.

REFERENCES

Abdullah, S.A. and J.W. Wallace, 2019, "Drift Capacity of RC Structural Walls with Special Boundary Elements", *ACI Structural Journal*, Vol. 116, No. 1, pp. 183-194.

ACI Committee 318, 2014, *Building Code Requirements for Structural Concrete (ACI-318) and Commentary*, American Concrete Institute, Farmington Hills, ML.

ASCE/SEI Seismic Rehabilitation Committee, 2014, *Seismic Evaluation and Retrofit of Existing Buildings,* ASCE/SEI41-13*,* American Society of Civil Engineers, Reston, VA.

Belarbi, A. and T.T.C. Hsu, 1994, "Constitutive Laws of Concrete in Tension and Reinforcing Bars Stiffened By Concrete", *ACI Structural Journal*, Vol. 91, No. 4, pp. 465-474.

Belarbi, A. and T.T.C. Hsu, 1995, "Constitutive Laws of Softened Concrete in Biaxial Tension-Compression", *ACI Structural Journal*, Vol. 92, No. 5, pp. 562-573.

Brun, M., J.M. Reynouard, and L. Jezequel, 2003, "A Simple Shear Wall Model Taking Into Account Stiffness Degradation", *Engineering Structures*, Vol. 25, pp. 1-9.

Chang, G.A. and J.B. Mander, 1994, *Seismic Energy Based Fatigue Damage Analysis of Bridge Columns: Part I-Evaluation of Seismic Capacity*, NCEER Technical Report No. NCEER-94-0006, National Center for Earthquake Engineering Research, State University of New York at Buffalo, NY, USA.

Clarke, M.J. and G.J. Hancock, 1990, "A Study of Incremental-Iterative Strategies for Non-Linear Analyses", *International Journal for Numerical Methods in Engineering*, Vol. 29, pp. 1365-1391.

Coleman, J. and E. Spacone, 2001, “Localization Issues in Force-Based Frame Elements”, *ASCE Journal of Structural Engineering*, Vol. 127, No. 11, pp. 1257–1265.

Combescure, D. and P.A. Pegon, 1994, “A Fiber Model Accounting for Transverse Shear in CASTEM 2000”, JRC-Special Publication.

Computers and Structures Inc., 2006, *Perform Components and Elements for Perform 3D and Perform Collapse, Version 4*, Computers and Structures Inc., Berkeley, California.

Damoni, C., B. Belletti, and R. Esposito, 2014, “Numerical Prediction of The Response of A Squat Shear Wall Subjected to Monotonic Loading”, *European Journal of Environmental and Civil Engineering*, Vol. 18, No. 7, pp. 754-769.

Dashti, F., R.P. Dhakal, and S. Pampanin, 2017a, “Numerical Modeling of Rectangular Reinforced Concrete Structural Walls”, *ASCE Journal of Structural Engineering*, Vol. 143, No. 6, p. 04017031.

Dashti, F., R.P. Dhakal, and S. Pampanin, 2017b, “Tests on Slender Ductile Structural Walls Designed According to New Zealand Standard”, *Bulletin of the New Zealend Society for Earthquake Engineering*, Vol. 50, No. 4, pp. 504-516.

Dashti, F., R.P. Dhakal, and S. Pampanin, 2018a, “Evolution of Out-of-Plane Deformation and Subsequent Instability in Rectangular RC Walls under In-Plane Cyclic Loading: Experimental Observation”, *Earthquake Engineering & Structural Dynamics*, Vol. 47, No. 15, pp. 2944-2964.

Dashti, F., R.P. Dhakal, and S. Pampanin, 2018b, “Validation of a Numerical Model for Prediction of Out-of-Plane Instability in Ductile Structural Walls under Concentric In-Plane Cyclic Loading”, *ASCE Journal of Structural Engineering*, Vol. 144, No. 6, p. 04018039.

Dazio, A., K. Beyer, and H. Bachmann, 2009, “Quasi-static Cyclic Tests and Plastic Hinge Analysis of RC Structural Walls”, *Engineering Structures*, Vol. 31, pp. 1556-1571.

Delso, M.J., R.S. Dunham, D.R. Parker, and R.J. James, 2015, "Nonlinear analysis of squat RC walls using three-dimensional continuum finite element models", *Proceedings*, *Second ATC and SEI Conference on Improving the Seismic Performance of Existing Buildings and Other Structures*, San Francisco, CA, USA, pp. 36-46.

Dhakal, R.P. and K. Maekawa, 2002, "Modeling for Postyield Buckling of Reinforcement", *ASCE Journal of Structural Engineering*, Vol. 128, No. 9, pp. 1139-1147.

DIANA, T.N.O., 2011, *Finite Element Analysis User's Manual-Release 9.4.4*, The Netherlands.

Elwood, K.J., 2013, "Performance of Concrete Buildings in the 22 February 2011 Christchurch Earthquake and Implications for Canadian Codes", *Canadian Journal of Civil Engineering*, Vol. 40, No. 8, pp. 759-776.

Epackachi, S. and A.S. Whittaker, 2018, "A Validated Numerical Model for Predicting The In-Plane Seismic Response of Lightly Reinforced, Low-Aspect Ratio Reinforced Concrete Shear Walls", *Engineering Structures*, Vol. 168, pp. 589-611.

Filippou, F.C., E.G. Popov, and V.V. Bertero, 1983, *Effects of Bond Deterioration on Hysteretic Behavior of Reinforced Concrete Joints*, EERC Report No. UCB/EERC-83/19, University of California, Berkeley.

Fischinger M., K. Rejec, and T. Isakovic, 2012, "Modeling Inelastic Shear Response of RC Walls", *Proceedings, 15th World Conference on Earthquake Engineering*, Lisbon, Portugal, No. 2120.

Fischinger, M., T. Vidic, J. Selih, P. Fajfar, H.Y. Zhang, and F.B. Damjanic, 1990, "Validation of a Macroscopic Model for Cyclic Response Prediction of RC Walls", *Computer Aided Analysis and Design of Concrete Structures*, Vol. 2, pp. 1131-1142.

Gérin, M. and P. Adebar, 2009, “Simple Rational Model for Reinforced Concrete Subjected to Seismic Shear”, *ASCE Journal of Structural Engineering*, Vol. 135, No. 7, pp. 753-761.

Greek Code for Interventions (KANEPE), 2013, *Earthquake Planning and Protection Organization*, Council of Europe European Centre on Preventing and Forecasting of Earthquakes, Athens.

Gullu, M. F., 2013, *Finite Element Modeling Of Reinforced Concrete Structural Walls*, M.S. Thesis, Boğaziçi University.

He, X.G. and A.K.H. Kwan, 2001, “Modeling Dowel Action of Reinforcement Bars for Finite Element Analysis of Structures”, *Computers and Structures*, Vol. 79, No. 6, pp. 595-604.

Hibbitt, K., 1993, *ABAQUS/Standard User's Manual*, *Version 5.3*, Pawtucket, RI: Hibbitt, Karlsson & Sorensen. Inc.

Hsu, T.T.C., 1988, “Softened Truss Model Theory for Shear and Torsion”, *ACI Structural Journal*, Vol. 85, No. 6, pp. 624-635.

Hsu, T.T.C., and L.X. Zhang, 1997, “Nonlinear Analysis of Membrane Elements by Fixed-Angle Softened-Truss Model”, *ACI Structural Journal*, Vol. 94, No. 5, pp. 483-492.

Hsu, T.T.C., and R.R.H. Zhu, 2002, “Softened Membrane Model for Reinforced Concrete Elements in Shear”, *ACI Structural Journal*, Vol.99, No. 4, pp. 460–469.

Jiang, H. and Y. Kurama, 2010, “Analytical Modeling of Medium-Rise Reinforced Concrete Shear Walls”, *ACI Structural Journal*, Vol. 107, No 4. pp. 400-410.

Kabeyasawa, T., H. Shiohara, S. Otani, and H. Aoyama, 1983, “Analysis of the Full-Scale Seven-Story Reinforced Concrete Test Structure”, *Journal of the Faculty of Engineering*, The University of Tokyo (B), Vol. 37, No. 2, pp. 431-478.

Kolozvari, K., C. Arteta, M. Fischinger, S. Gavridou, M. Hube, T. Isaković, L. Lowes, K. Orakcal, J. Vásquez, and J.W. Wallace, 2018a, "Comparative Study of State-of-the-Art Macroscopic Models for Planar Reinforced Concrete Walls", *ACI Structural Journal*, Vol. 115, No. 6, pp. 1637-1657.

Kolozvari, K. and J.W. Wallace, 2016, "Practical Nonlinear Modeling of Reinforced Concrete Structural Walls", *ASCE Journal of Structural Engineering*, Vol. 142, No.12, p. G4016001.

Kolozvari, K., K. Orakcal, and J.W. Wallace, 2018b, "New Opensees Models for Simulation Nonlinear Flexural and Coupled Shear-Flexural Behvior of RC Walls and Columns", *Computers and Structures*, Vol. 196, pp. 246-262.

Kolozvari, K., K. Orakcal, and J. W. Wallace, 2015a, "Modeling of Cyclic Shear-Flexure Interaction in Reinforced Concrete Structural Walls. I: Theory", *ASCE Journal of Structural Engineering*, Vol. 141, No. 5, p. 04014135.

Kolozvari, K., T. Tran, K. Orakcal, and J.W. Wallace, 2015b, "Modeling of Cyclic Shear-Flexure Interaction in Reinforced Concrete Structural Walls. II: Experimental Validation", *ASCE Journal of Structural Engineering*, Vol. 141, No. 5, p. 04014136.

Los Angeles Tall Buildings Structural Design Council, 2015, *An Alternative Procedure for Seismic Analysis and Design of Tall Buildings Located in the Los Angeles Region*, Los Angeles Tall Buildings Structural Design Council, California.

LSTC, LS-DYNA, 2012a, *Keyword User's Manual, Volume I, Version 971 R6.0.0*, Livermore, CA, USA.

LSTC, LS-DYNA, 2012b, *Keyword User's Manual, Volume II, Version 971 R6.0.0*, Livermore, CA, USA.

Lu, Y., and R.S. Henry, 2017, "Numerical Modelling of Reinforced Concrete Walls with Minimum Vertical Reinforcement", *Engineering Structures*, Vol. 143, pp. 330–345.

Luu, C.H., Y.L. Mo, and T.T.C. Hsu, 2017, "Development of CSMM-Based Shell Element for Reinforced Concrete Structures", *Engineering Structures*, Vol. 132, pp. 778-790.

Maffei, J., P. Bonelli, D. Kelly, D.E. Lehman, L. Lowes, J. Moehle, K. Telleen, J.W. Wallace, and M. Willford, 2014, *Recommendations for Seismic Design of Reinforced Concrete Wall Buildings Based on Studies of the 2010 Maule, Chile Earthquake*, Nist No. NISTGCR 14-917-25, National Institute of Standards and Technology, California.

Mander, J.B., M.J.N Priestley, and R. Park, 1988, "Theoretical Stress-Strain Model for Confined Concrete", *ASCE Journal of Structural Engineering*, Vol. 114, No. 8, pp. 1804-1826.

Mansour, M.Y. and T.T.C. Hsu, 2005, "Behavior of Reinforced Concrete Elements under Cyclic Shear", *ASCE Journal of Structural Engineering*, Vol. 131, No. 1, pp. 44-53.

Mansour, M.Y., T.T.C. Hsu, and J.Y. Lee, 2002, "Pinching Effect in Hysteretic Loops of R/C Shear Elements", *ACI Special Publication*, Vol. 205, pp. 293-322.

Massone, L.M. and D. Moroder, 2009, "Buckling Modeling of Reinforcing Bars with Imperfections", *Engineering Structures,* Vol. 31, No. 3, pp. 758–767.

Massone, L. M. and J.W. Wallace, 2004, "Load-Deformation Responses of Slender Reinforced Concrete Walls", *ACI Structural Journal*, Vol. 101, No. 1, pp. 103–113.

Massone, L.M., K. Orakcal, and J.W. Wallace, 2009, "Modeling of Squat Structural Walls Controlled by Shear", *ACI Structural Journal*, Vol. 106, No. 5, pp. 646–655.

MatLab M., 2012, *The language of technical computing*, The MathWorks, Inc., Massachusetts USA.

McKenna F., G.L. Fenves, M.H. Scott, and B. Jeremic, 2000, *Open System for Earthquake Engineering Simulation (OpenSees)*. Pacific Earthquake Engineering Research Center, University of California, Berkeley, California.

Menegotto, M. and E. Pinto, 1973, "Method of Analysis for Cyclically Loaded Reinforced Concrete Plane Frames Including Changes in Geometry and Non-Elastic Behavior of Elements under Combined Normal Force and Bending", *Proceedings*, *IABSE Symposium on Resistance and Ultimate Deformability of Structures Acted on by Well-Defined Repeated Loads*, Lisbon, Portugal.

Millard, A., 1993, CASTEM 2000, *Manuel D'utilisation*, Report CEA/LAMS No. 93/0007, Saclay, France.

Mo, Y.L., J. Zhong, and T.T.C. Hsu, 2008, "Seismic Simulation of RC Wall-Type Structures", *Engineering Structures*, Vol. 30, pp. 3167-3175.

Murray, Y.D., 2007, *Users Manual for LS-DYNA Concrete Material Model 159*, No. FHWA-HRT-05-062, United States, Federal Highway Administration Office of Research, Development, and Technology.

Oesterle R.G., A.E. Fiorato, L.S. Johal, J.E. Carpenter, H.G. Russel, and W.G. Corley, 1976, *Earthquake Resistant Structural Walls - Tests of Isolated Walls*, Report to National Science Foundation, Grant No. GI-43880, Research and Development Construction Technology Laboratories Portland Cement Association, Skokie, Illinois.

Ohmori, N., T. Takahashi, N. Inoue, K. Kurihara, and S. Watanabe, 1989, "Experimental Studies on Nonlinear Behaviors of Reinforced Concrete Panels Subjected to Cyclic in-plane Shear", *Proceedings of AIJ*, Vol. 403, pp. 105-117.

Orakcal, K., D. Ulugtekin and L.M. Massone, 2012, "Constitutive Modeling of Reinforced Concrete Panel Behavior under Cyclic Loading" *Proceedings, 15th World Conference on Earthquake Engineering*, Lisbon, Portugal, No. 3573.

Orakcal, K. and J.W. Wallace, 2006, "Flexural Modeling of Reinforced Concrete Walls – Model Calibration", *ACI Structural Journal*, Vol. 103, No. 2, pp. 196-206.

Orakcal, K., J.W. Wallace, and J.P. Conte, 2004, "Flexural Modeling of Reinforced Concrete Walls – Model Attributes", *ACI Structural Journal*, Vol. 101, No. 5, pp. 688-699.

Orakcal, K., L.M. Massone, and J.W. Wallace, 2006, *Analytical Modeling of Reinforced Concrete Walls for Predicting Flexural and Coupled - Shear - Flexural Responses*, PEER Report No. EEC-9701568, Pacific Earthquake Engineering Research, Berkeley.

Orakcal, K., L.M. Massone, and J.W. Wallace, 2009, "Shear Strength of Lightly Reinforced Wall Piers and Spanderels", *ACI Structural Journal*, Vol. 106, No. 4, pp. 455-465.

Palermo, D. and F.J. Vecchio, 2003, "Compression Field Modeling of Reinforced Concrete Subjected to Reversed Loading: Formulation", *ACI Structural Journal*, Vol. 100, No. 5, pp. 616-625.

Palermo, D. and F.J. Vecchio, 2007, "Simulation of Cyclically Loaded Concrete Structures Based on The Finite-Element Method", *ASCE Journal of Structural Engineering*, Vol. 133, No. 5, pp. 728-738.

Panagiotou M., J.I. Restrepo, M. Schoettler, and G. Kim, 2012, "Nonlinear Cyclic Truss Model for Reinforced Concrete Walls", *ACI Structural Journal*, Vol. 109, No. 2, pp. 205-214.

Pang, D. and T.T.C. Hsu, 1995, "Behavior of Reinforced Concrete Membrane Elements in Shear", *ACI Structural Journal*, Vol. 92, No. 6, pp. 665-677.

Pang, D. and T.T.C. Hsu, 1996, "Fixed Angle Softened Truss Model for Reinforced Concrete", *ACI Structural Journal*, Vol. 93, No. 2, pp. 197-207.

Paulay, T. and M.J.N. Priestley, 1993, "Stability of Ductile Structural Walls", *ACI Structural Journal*, Vol. 90, No. 4, pp. 385-392.

Petrangeli, M., P.E. Pinto, and V. Ciampi, 1999, “Fiber Element for Cyclic Bending and Shear of RC Structures. I: Theory”, *ASCE Journal of Engineering Mechanics*, Vol. 125, No. 9, pp. 994-1001.

Pugh, J.S., L.N. Lowes, and L.E. Lehman, 2015, “Nonlinear Line-Element Modeling of Flexural Reinforced Concrete Walls”, *Engineering Structures*, Vol. 104, pp. 174-192.

Rejec, K., 2011, *Inelastic Shear Behaviour of RC Structural Walls under Seismic Conditions (in Slovenian)*, Ph.D. Thesis, University of Ljubljana, Slovenia.

Rojas F., J.C. Anderson, and L.M. Massone, 2016, “A Nonlinear Quadrilateral Layered Membrane Element with Drilling Degrees of Freedom for The Modeling of Reinforced Concrete Walls”, *Engineering Structures*, Vol. 124, pp. 521-538.

Rosso, A., J.P. Almeida, and K. Beyer, 2016, “Stability of Thin Reinforced Walls under Cyclic Loads: State-of-The-Art and New Experimental Dindings”, *Bulletin of Earthquake Engineering*, Vol. 14, No. 2, pp. 455-484.

Rosso. A., L.A. Jiménez-Roa, J.P. Almeida, A.P.G. Zuniga, C.A. Blandon, R.L. Bonett, and K. Beyer, 2018, “Cyclic Tensile-Compressive Tests on Thin Concrete Boundary Elements with a Single Layer of Reinfocement Prone to Out-of-Plane Instability”, *Bulletin of Earthquake Engineering*, Vol. 16, No.2, pp. 859-887.

Saatcioglu, M. and S. Razvi, 1992, “Strength and Ductility of Confined Concrete”, *ASCE Journal of Structural Engineering*, Vol. 118, No. 6, pp. 1590-1607.

Stevens, N.J., M. Uzumeri, and M.P. Collins, 1991, “Reinforced Concrete Subjected to Reversed Cyclic Shear-Experiments and Constitutive Model”, *ACI Structural Journal*, Vol. 88, No. 2, pp. 135-146.

Tassios, T.P. and E.N. Vintzēleou, 1987, “Concrete-to-Concrete Friction”, *ASCE Journal of Structural Engineering*, Vol. 113, No. 4, pp. 832-849.

Terzioglu, T., 2011, *Experimental Evaluation Of The Lateral Load Behavior Of Squat Structural Walls*, M.S. Thesis, Boğaziçi University.

Terzioglu, T., K. Orakcal, and L.M. Massone, 2018, "Cyclic Lateral Load Behavior of Squat Reinforced Concrete Walls", *Engineering Structures*, Vol. 160, pp. 147-160.

Thermou, G. E., V.K. Papanikolaou, and A.J. Kappos, 2014, "Flexural Behaviour of Reinforced Concrete Jacketed Columns under Reversed Cyclic Loading" *Engineering Structures*, Vol. 76, pp. 270-282.

Thomsen, J.H. and J.W. Wallace, 1995, *Displacement-Based Design of Reinforced Concrete Structural Walls: An Experimental Investigation of Walls with Rectangular and T-Shaped Cross-Sections*, Report No. CU/CEE-95/06, Department of Civil Engineering, Clarkson University, Postdam, New York.

Thomsen, J.H. and J.W. Wallace, 2004, "Displacement-Based Design of Slender Reinforced Concrete Structural Walls-Experimental Verification", *ASCE Journal of Structural Engineering*, Vol. 130, No. 4, pp. 618-630.

Thomson, E.D., M.E. Perdomo, R. Picón, M.E. Marante, and J. Flórez-López, 2009, "Simplified Model for Damage in Squat RC Shear Walls", *Engineering Structures*, Vol. 31, pp. 2215-2223.

Tran, T.A., 2012, *Experimental and Analytical Studies of Moderate Aspect Ratio Reinforced Concrete Structural Walls*" Ph.D. Thesis, Department of Civil Engineering, University of California, Los Angeles.

Tran, T.A. and J.W. Wallace, 2015, "Cyclic Testing of Moderate-Aspect-Ratio Reinforced Concrete Structural Walls", *ACI Structural Journal*, Vol. 112, No. 6, pp. 653-666.

Tsai, W.T., 1988, "Uniaxial Compressional Stress-Strain Relation of Concrete", *ASCE Journal of Structural Engineering*, Vol. 114, No. 9, pp. 2133-2136.

Ulugtekin, D., 2010, *Analytical Modeling of Reinforced Concrete Panel Elements under Reversed Cyclic Loadings*, M.S. Thesis, Boğaziçi University.

Vallenas, J.M., V.V. Bertero, and E.P. Popov, 1979, *Hysteretic Behavior of Reinforced Concrete Structural Walls*, Report to National Science Foundation, Report No. UCB/EERC-79/20, College of Engineering, University of California, Berkeley, California.

Vásquez, J.A., J.C. de la Llera, and M.A. Hube, 2016, "A Regularized Fiber Element Model for Reinforced Concrete Shear Walls", *Earthquake Engineering & Structural Dynamics*, Vol. 45, No. 13, pp. 2063-2083.

Vassilopoulou I. and T.P. Tassios, 2003, "Shear Transfer Capacity along A RC Crack under Cyclic Sliding", *Proceedings of fib Symposium Concrete Structures in Seismic Regions*, Athens, Greece.

Vecchio, F.J., 1989, "Nonlinear Finite Element Analysis of Reinforced Concrete Membranes", *ACI Structural Journal*, Vol. 86, No. 1, pp. 26–35.

Vecchio, F.J., 1999, "Towards Cyclic Load Modeling of Reinforced Concrete", *ACI Structural Journal*, Vol. 96, No. 2, pp. 193-202.

Vecchio, F.J., 2000, "Disturbed Stress Field Model for Reinforced Concrete: Formulation", *ASCE Journal of Structural Engineering*, Vol. 126, No. 9, pp. 1070-1077.

Vecchio, F.J. and M.P. Collins, 1986, "The Modified Compression-Field Theory for Reinforced Concrete Elements Subjected to Shear", *ACI Structural Journal*, Vol. 83, No. 2, pp. 219-231.

Vecchio, F.J. and M.P. Collins, 1993, "Compression Response of Cracked Reinforced Concrete", *ASCE Journal of Structural Engineering*, Vol. 119, No. 12, pp. 3590-3610.

Vintzēleou, E.N. and T.P. Tassios, 1986, "Mathematical Models for Dowel Action under

Monotonic and Cyclic Conditions", *Magazine of Concrete Research*, Vol. 38, No. 134, pp. 13-22.

Vulcano, A. and V.V. Bertero, 1986, "Nonlinear Analysis of RC Structural Walls", *Proceedings, 8th European Conference on Earthquake Engineering*, Lisbon, Portugal, Vol. 3, pp. 1-6.

Vulcano, A., V.V. Bertero, and V. Colotti, 1988, "Analytical Modeling of RC Structural Walls", *Proceedings*, *9th World Conference on Earthquake Engineering*, Tokyo-Kyoto, Japan, Vol. 6, p. 41-46.

Welt, T.S., L.M. Massone, J.M. LaFave, D.E. Lehman, S.L. McCabe, and P. Polanco, 2017, "Confinement Behavior of Rectangular Reinforced Concrete Prisms Simulating Wall Boundary Elements", *ASCE Journal of Structural Engineering*, Vol. 143, p. 401620.

Zhu, R.R.H. and T.T.C. Hsu, 2002, "Poisson Effect in Reinforced Concrete Membrane Elements", *ACI Structural Journal*, Vol. 99, No. 5, pp. 631-640.

Zhu, R.R.H. and T.T.C. Hsu, J.Y. Lee, 2001, "Rational Shear Modulus for Smeared-Crack Analysis of Reinforced Concrete", *ACI Structural Journal*, Vol. 98, No. 4, pp. 443-450.